Progress in Energy and Combustion Science 91 (2022) 100993

Contents lists available at ScienceDirect

Progress in Energy and Combustion Science

journal homepage: www.elsevier.com/locate/pecs

Numerical approaches for thermochemical conversion of char

Nils Erland L. Haugen [a,b,*], Brandon Ka Yan Loong [c], Reginald E. Mitchell [c]

[a] Department of Energy and Process Engineering, Norwegian University of Science and Technology, Trondheim, Norway
[b] Department of Thermal Energy, SINTEF Energy Research, Trondheim, Norway
[c] Department of Mechanical Engineering, Stanford University, USA

ARTICLE INFO

Keywords:
Char
combustion
gasification
thermal annealing
ash vaporization
fragmentation
numerical models

ABSTRACT

This paper gives a review of the current state of the art for numerical simulations of char conversion. In particular, it presents models that have been developed to describe the physical and chemical phenomena that characterize thermochemical char conversion. All particle sizes are covered, ranging from pulverized particles to wood logs. The aim of the paper is to give the reader the required starting point in order to develop his own simulation tool. Two fundamentally different approaches are studied in detail, namely the resolved particle approach and the point particle approach. In the resolved approach, both the char particle itself and the surrounding boundary layer is resolved. This means that heat, mass and momentum transfer are accurately handled. For the point particle approach, which is computationally much cheaper, one has to rely on suitable models to estimate for example the heat, mass and momentum transfer. Finally, the paper also gives detailed descriptions of how to handle ash inclusions in the char in addition to particle fragmentation and thermal annealing.

1. Introduction

The combustion and gasification characteristics of the chars from coal and biomass have received considerable attention owing to greenhouse gas emission concerns and mandates. Efforts to mitigate these concerns require changes to process operating conditions that result in low emissions of such atmospheric pollutants as the oxides of nitrogen and sulfur, NOx and SOx, respectively. Char conversion is the rate-limiting step in nearly all coal and biomass utilization technologies. In pulverized coal applications, the ratio of characteristic devolatilization times to char oxidation times is of the order 0.1 and in fluidized-bed applications, this ratio is of the order 0.01 [1]. Biomass has considerably larger volatile matter contents than coals and as a consequence, devolatilization times are longer with biomass materials than with coals and with some biomass materials, char oxidation may start before devolatilization has completely ended. The ratio of characteristic devolatilization times and combustion times for biomass is provided in the study undertaken by Li *et al.* [2]. For particles from ~100 to 1500 μm in diameter burning in air at 1173 K, the ratio is reported to be in the range ~0.5 to ~0.7 for the woody biomass studied. For coals, the ratio was in the range 0.1 to 0.2, consistent with the findings of Smith [1] . Consequently, accurate prediction of the performances of coal- and biomass-fired combustors and gasifiers requires the accurate characterization of the physical and chemical processes that take place during the char conversion process. This paper is concerned with the various models that have been developed to describe the physical and chemical phenomena that characterize thermochemical char conversion. Many of the simplifying assumptions that are used to yield a solvable set of governing equations are assessed.

The prediction of char conversion rates in combustors and gasifiers requires models that predict the gas phase temperature and composition profiles established inside these devices as well as models that predict the initial char structure, which depends on devolatilization behaviors. This paper does not address predicting pyrolysis or devolatilization behaviors of coals and biomass materials. Papers concerned with modeling coal and biomass devolatilization are available in the published literature [3–12]. The devolatilization models fall into two categories - kinetics-based models (in which one, two or multiple independent, irreversible, first-order reactions are used to describe the release rates of gases, tars and char) [3,7,11,12] or structural-based models (in which the chemical structure of the carbonaceous material is used to formulate expressions for the yields of gases, tars and char) [4–6, 8–10] . For char particles smaller than about 150 microns in size, devolatilization is essentially complete before the onset of significant char conversion but for larger particles, char conversion models must be initiated during the devolatilization process. The current review is applicable to all sizes of chars, from pulverized particles to wood logs and even forest fires.

* Corresponding author: Nils Erland L. Haugen
E-mail address: nils.e.haugen@sintef.no (N.E.L. Haugen).

https://doi.org/10.1016/j.pecs.2022.100993
Received 16 March 2021; Received in revised form 14 January 2022; Accepted 23 January 2022
Available online 2 May 2022

Nomenclature

Variable Description Units

A	Pre-exponential factor in Arrhenius expression for reaction rate coefficient reaction dep.
A_a, A_{ov}	Power-law kinetics: pre-exponential factor in Arrhenius expression for apparent or overall rate coefficient model dep.
a_c	Volatile mineral condensation coefficient (see Eq. (201))
A_c	External surface area of grid cell m^2
A_E	Pre-exponential factor in Arrhenius expression for rate coefficient for a desorption reaction with activation energy E mol m^{-2} s^{-1}
A_{int}	Power-law kinetics: pre-exponential factor in Arrhenius expression for intrinsic reaction rate coefficient model dep.
$A_{k,f}$	Pre-exponential factor for rate constant $k_{k,f}$ Reaction dep.
A_p	Geometric external surface area of particle m^2
A_{pore}	Cross sectional area of a pore m^2
A_R	Aspect ratio of a non-spherical particle, the ratio of the lengths of the particle's major to minor axis m^2
b_{ij}	Elements of the particle fragmentation progeny matrix
Bi	Biot number
C_D	Drag coefficient
C_i	Concentration of species i in reaction k mol m^{-3}
$C_{i,k}$	Fraction of particles that leave the size bin per unit time owing to a reduction in diameter below the lower bin cutoff due to char reactivity (see Eq. (168))
C_g	Gas concentration within pore mol m^{-3}
$c_{p,char}$	Heat capacity of char J kg^{-1} K^{-1}
c_{pg}	Heat capacity of the gas J kg^{-1} K^{-1}
$c_{p,MO}$	Heat capacity of mineral oxide inclusion J kg^{-1} K^{-1}
$c_{p,p}$	Effective heat capacity of the particle J kg^{-1} K^{-1}
$c_{p,solid}$	Heat capacity of solid material
$C_{s,i}$	The area-specific concentration of species i adsorbed on a surface mol m^{-2}
d_{char}	Char particle diameter m
d_{coal}	Coal particle diameter m
d_{crit,MO_n}	Critical cluster size for volatile mineral species nucleation (see Eq. (200)) m
d_{equiv}	Diameter of a spherical particle having the same volume as the non-spherical particle m
d_I	Mean diameter of mineral inclusions inside the char particle m
$\mathscr{D}_i$	Bulk diffusivity of species i m^2 s^{-1}
$D_{i,k}$	Fraction of particles that leave density class per unit time owing to a reduction in apparent density due to char reactivity (see Eq. (168))
$\mathscr{D}_{i,ash}$	Diffusivity of species i in ash layer m^2 s^{-1}
$\mathscr{D}_{i,eff}$	Effective diffusion coefficient of species i in porous material m^2 s^{-1}
$\mathscr{D}_{Kn,i}$	Knudsen diffusivity of species i m^2 s^{-1}
d_{MO}	Diameter of a single mineral inclusion embedded in char particle core m
$\mathscr{D}_{MS_i,eff}$	Effective diffusion coefficient of volatile mineral species in pores of particle corem^2 s^{-1}
d_p	Diameter of particle m
$d_{p,t}$	Diameter of particle at time t m
$d_{pc,t}$	Diameter of carbonaceous core of particle at time t m
$\mathscr{D}_{pore,i,eff}$	Effective diffusion coefficient of species i in a given pore with constant cross section m^2 s^{-1}
D_{th}	Gas thermal diffusivity m^2 s^{-1}
$\overline{d}_p$	The volume-mean diameter of mineral oxide particles outside the char particle's outer surface at time t (see Eq. (223)) m
E_a, E_a'	Apparent activation energy, power-law kinetics J $(mol)^{-1}$
E_{ave}	The mean value of the activation energy distribution for modeling desorption reactions J $(mol)^{-1}$
E_d	Activation energy for a desorption reaction (see Eq. (171)) J $(mol)^{-1}$
E_{int}	Intrinsic activation energy, power-law kinetics J $(mol)^{-1}$
$E_{k,f}$	Activation energy for rate constant $k_{k,f}$ J $(mol)^{-1}$
E_{ov}	Apparent activation energy under Zone II conditions J $(mol)^{-1}$
$\boldsymbol{F}$	Forces due to particle collisions in particle momentum equation (Eq. (5)) N
$F(E_d)$	Active site distribution function in thermal annealing model (see Eq.(171))
$f(E_d)$	Distribution of annealing activation energies in the thermal annealing model (see Eq.(175))
f_g	Correction to particle response time for non-Stokesian flow (see Eq. (33))
f_{MM}	Mass fraction of mineral matter in receded core volume that appends to the exterior ash layer
f_r	Pore surface roughness factor
f_{shed}	Mass fraction of mineral matter in receded core volume that is shed from particle
$f(E,\ t)$	Distribution function describing the adsorbed oxygen concentration on the carbonaceous surface
$f_c(\varphi_i,m)$	Effectiveness factor-Thiele modulus correction function
$\boldsymbol{g}$	Gravitational constant m s^{-2}
$\Delta\widehat{G}_R$	Gibbs function change for mineral vaporization reaction J $(mol)^{-1}$
ΔG_v	Change in the Gibbs free energy for volatile mineral droplet formation per unit volume J m^{-3}
h	Enthalpy J kg^{-1}
h_{char}	Enthalpy of gaseous phase that leaves the char particle (see Eq. (52)) J kg^{-1}
h_{f0}	Enthalpy of formation at reference temperature and pressure J kg^{-1}
H	Heat transfer coefficient for single film model W m^{-2} K^{-1}
H_0	Heat transfer coefficient for a spherical particle without a Stefan flow W m^{-2} K^{-1}
$\boldsymbol{J}_i$	Diffusive flux of species i kg m^{-2} s^{-1}
$j_{i,r_{pc}}$	Molar flux of reactive gas i at the outer surface of the particle core mol m^{-2} s^{-1}
K	Permeability of the porous particle material (see Eq. (16)) m^2
k_a, k_a'	Apparent reaction rate coefficients, power-law kinetics s^{-1} $(atm)^{-n}$
k_{AKM}	Reaction rate coefficient for the apparent kinetic model s^{-1}
$k_{AV\text{-}ER}$	Reaction rate coefficient for the Avrami-Erofeev reaction model s^{-1}
k_B	Boltzmann constant J K^{-1}
$K_{C,k}$	Equilibrium constant for reaction k
k_{eff}	Effective reaction rate coefficient for a desorption reaction employing the distributed activation energy approach s^{-1}
k_{frag}	Fragmentation rate constant m^{-2} s^{-1}
k_{im}	Mass transfer coefficient mol m^{-2} s^{-1}
k_{int}	Intrinsic reaction rate coefficients, power-law kinetics kg m^{-2} s^{-1} $(atm)^{-m}$
k_k, $k_{k,f}$	Rate constant of reaction k in forward direction Reaction dep.
$k_{k,r}$	Rate constant of reaction k in reverse direction Reaction dep.
k_{ov}	Overall apparent reaction rate coefficient for the removal of carbon from a surface kg m^{-2} s^{-1} $(atm)^{-n}$
K_p	Equilibrium constant
Kn	Knudsen number (Kn = mean free path/characteristic length)

l_{shape}	Shape factor in the grain model of internal surface area
L_{pore}	Mean length of pores in char m
m	Mass kg
m	Intrinsic reaction order with respect to the reactive gas partial pressure, power-law kinetics; the true reaction order
m_{ash}	Mass of the ash in the char particle kg
$\widehat{M}_C$	Molar mass of carbon kg (kmol)$^{-1}$
m_{char}	Mass of char in a particle kg
$\dot{m}_{char}$	Char consumption rate kg s^{-1}
$\dot{m}_{diff,i}$	Mass diffusion rate of species i in a pore kg s^{-1}
$\widehat{M}_i$	Molar mass of species i kg (kmol)$^{-1}$
m_{MO}	Mass of mineral oxide inclusions in char particle core kg
$\dot{M}_{MOvap,t}$	Rate at which all vaporized mineral oxides leave particle core at time t kg s^{-1}
$\widehat{M}_{MS_i}$	Molecular weight of volatile mineral species i kg (mol)$^{-1}$
m_{MO_n}	molecular mass of mineral oxide species kg (molecule)$^{-1}$
m_p	Mass of particle kg
$\dot{m}_{reac,i}$	Mass consumption rate of species i in a pore kg s^{-1}
$\dot{m}_{tot,i}$	Total mass diffusion rate of species i at a pore inlet kg s^{-1}
m_{solid}	Total mass of solid particle material (char plus ash) kg
$n,\quad n'$	Apparent reaction order with respect to the reactive gas partial pressure, power-law kinetics
n''	Oxygen reaction order associated with the heterogeneous CO/CO_2 molar product ratio
n'''	Reaction order associated with the Avrami-Erofeev reaction model
N_{AV}	Avogadro's number molecule (mol)$^{-1}$
N_{dens}	Number of apparent density classes considered
N_i	Number of moles of species i adsorbed on a surface
N_I	Total number of inclusions in the char particle's core
$\dot{n}_i$	Molar flux of gaseous species i at the external particle surface mol m^{-2} s^{-1}
$\dot{n}_{i,k}$	Molar flux of gaseous species i due to reaction k mol m^{-2} s^{-1}
n_p	Number of pores per unit particle volume
N_r	Number of heterogeneous reactions occurring on the solid surface
$N_{reac\ \ des}$	Number of desorption reactions in the heterogeneous reaction mechanism
N_s	Number of reactant species (gas and adsorbed) involved in heterogeneous reactions (used in Eq. (7))
N_s	Number of gas phase species
$\dot{n}_{total}$	Total molar flux of gaseous species mol m^{-2} s^{-1}
N_{size}	Number of size bins describing the fragmentation size distribution
$n(u)$	The number of volatile mineral oxide particles in the boundary layer per unit volume having volume u
Nu	Nusselt number
N_{CO}/N_{CO_2}	Heterogeneous molar product ratio of CO to CO_2
P	Total pressure Pa
$P_{g,s}$	Partial pressure of reactive gas at the outer surface of char particle atm
P_i	Partial pressure of species i Pa
$P_{i,j,k,m}$	Elements in the apparent density tensor that describes variations in fragmentation with particle density
P_{MS_i}	Partial pressure of mineral species i at the mineral inclusion Pa
$P^{eq}_{MS_i}$	Equilibrium partial pressure of mineral species i at the surface of a vaporizing mineral inclusion inside the char particle Pa
$P^{*}_{MO_n}$	Saturation partial pressure of volatile mineral species at conditions in the particle's boundary layer Pa
P_{ref}	Reference pressure for equilibrium calculation bar
Q_{conv}	Overall particle energy release rate due to convection kJ s^{-1}
$q_{gas\ -\ reac}$	Energy released as heat due to gas-phase homogeneous reaction kJ m^{-3} s^{-1}
q_{rad}	Energy flux from particle surface due to radiation kJ m^{-2} s^{-1}
Q_{rad}	Overall particle energy release rate due to radiation kJ s^{-1}
q_{reac}	Energy released as heat due to heterogeneous reaction kJ m^{-3} s^{-1}
Q_{reac}	Overall particle energy release rate due to heterogeneous reaction kJ s^{-1}
$q_{reac,k}$	Heat of reaction for reaction k kJ (mol)$^{-1}$
r	radius m
$R_a,\ R'_a$	The rate of change in the fraction of the initial char mass remaining (defined in Eq. (73)) s^{-1}
R_c	Intrinsic reactivity of char kg m^{-2} s^{-1}
$\dot{R}_{condensation}$	Rate of condensation of volatile mineral species in the particle's boundary layer mol m^{-3} s^{-1}
R_{ext}	Intrinsic char reactivity evaluated at the conditions existing at the external surface of the char particle kg m^{-2} s^{-1}
$\widehat{R}_i$	Molar reactivity of gaseous species i mol m^{-2} s^{-1}
R_{int}	Intrinsic char reactivity evaluated at the conditions inside the particle kg m^{-2} s^{-1}
$\widehat{\Re}_k$	Molar reaction rate of reaction k mol m^{-2} s^{-1}
$\dot{r}_{condensation,MO_n}$	Condensation rate in the particle's boundary layer for a mineral droplet having diameter d_{MO_n} mol s^{-1}
$\dot{R}_{nucleation}$	Rate of nucleation of volatile mineral species in the particle's boundary layer mol m^{-3} s^{-1}
$\dot{r}_{nucleation,MO_n}$	Rate of homogeneous nucleation of volatile mineral droplet in the particle's boundary layer nuclei m^{-3} s^{-1}
R_{ov}	Area-specific rate of carbon removal kg m^{-2} s^{-1}
r_{pore}	Mean radius of pores in particle m
r_p	Particle radius m
$\dot{R}_{reaction}$	Rate of reaction of volatile mineral particles in the particle's boundary layer mol m^{-3} s^{-1}
$\widehat{R}_u$	Universal gas constant J (mol)$^{-1}$ K^{-1}
Re_p	Particle Reynolds number
S	Number of active sites in the thermal annealing model (see Eq. (173))
$\overline{\overline{\mathbf{S}}}$	Strain tensor s^{-1}
S_d	Total surface site density sites m^{-2}
S_g	Mass specific internal surface area m^2 kg^{-1}
$S_{i,k}$	Fraction of particles per unit time of size $d_{p,i}$ and apparent density $\rho_{p,k}$ that fragment (see Eq. (168)) s^{-1}
S_t	Total surface area of a surface m^2
S_v	Volume specific internal surface area m^2 m^{-3}
Sh	Sherwood number
t	time s
T	Temperature K
T_{BL}	Temperature of the effective boundary layer K
T_g	Gas temperature K
T_p	Particle temperature K
T_{rad}	Effective radiating temperature of the surroundings K
$\boldsymbol{u}$	Fluid velocity vector m s^{-1}
$\boldsymbol{u_s}$	Superficial gas velocity within the particle pores m s^{-1}
$\boldsymbol{v}$	Fluid velocity vector m s^{-1}
V	Volume m^3
V_{ash}	Volume occupied by ash material m^3
V_c	Volume of grid cell in the resolved particle approach m^3
$V_{char\ pores}$	Total volume occupied by the pores in the char m^3
V_{MO}	Volume of the mineral oxide inclusions inside particle core m^3

v_{MO_n}	molecular volume of a droplet of the mineral oxide species that condenses in the particle's boundary layer m^3 (molecule)$^{-1}$
V_{obj}	Total volume of the char particle, including char, ash, and pores m^3
V_p	Volume of a char particle m^3
$V_{true,char}$	Volume occupied by solid carbonaceous material m^3
$\overline{v}_t$	The average volume of mineral oxide particles outside the char particle's outer surface at time t (see Eq. (222)) m^3
$\dot{W}_g$	Source term in continuity equation (Eq. (1)) due to interaction with unresolved point particles (defined in Eq. (50)) kg m^{-3} s^{-1}
$\dot{W}_h$	Source term in energy equation (Eq. (3)) due to interaction with unresolved point particles (defined in Eq. (52)) J m^{-3} s^{-1}
$\dot{W}_i$	Source term in species conservation equation (Eq. (4)) due to interaction with unresolved point particles (defined in Eq. (53)) kg m^{-3} s^{-1}
$\dot{w}_{i,j}$	Production rate of gas phase species i due to heterogeneous reactions on particle j in the point particle approach kg s^{-1}
$\dot{W}_u$	Source term in momentum equation (Eq. (2)) due to interaction with unresolved point particles kg m^{-2} s^{-2}
x_c	Char conversion
$X_{i,s}$	Mole fraction of species i at external particle surface
$X_{i,\infty}$	Mole fraction of species i in bulk field
Y_{ash}	Mass fraction of ash in char particle
Y_i	Mass fraction of species i
Y_{MO}	Mass fraction of mineral matter in the core of the particle
z	Length along a pore m
z_{ij}	Number of collisions between volatile mineral oxide particles per unit time per unit volume (see Eq. (209))

GREEK

α	Mode of conversion parameter governing particle apparent density (see Eq. (130))
α'	Parameter in expression for α_I (see Eq. (149))
α_c	Mass accommodation factor associated with the rate of volatile mineral condensation (see Eq. (204))
α_I	Parameter in the expression for the vaporization effectiveness factor that accounts for Stefan flow effects (see Eq. (148))
a_{MO_n}	Activity of the solid or liquid mineral oxide
β	Mode of conversion parameter governing particle size (see Eq. (131))
$\beta(u, v)$	Collision frequency function - the rate of collisions per mineral oxide particle per unit volume
γ	Bin diameter ratio parameter in the fragmentation model (see Eq. (159))
γ	Volume change upon reaction at outer surface of particle core
δ	Thickness of ash layer surrounding char particle m
ε_p	Char particle emissivity
ζ	Temperature exponent in expression for the approximate mass transfer coefficient (see Eq. (129))
η	Effectiveness factor
η_i	Effectiveness factor for species i
η_{vap}	Effectiveness factor for vaporization in mean-field theory
Θ	Porosity of the porous char particle
Θ_{ash}	Porosity of the ash layer surrounding the char particle core
θ_c	Pore constriction factor
Θ_i	Fraction of carbon sites occupied by adsorbed species i
θ_{therm}	Correction term that accounts for the effects of Stefan flow
Λ	Thiele modulus for a non-spherical particle (see Section 3.7.3)
λ_{gas}	Thermal conductivity of a gas W m^{-1} K^{-1}
λ_{th}	Effective thermal conductivity of the porous material W m^{-1} K^{-1}
μ	Dynamic viscosity Pa s
ν	Kinematic viscosity m^2 s^{-1}
ν_i	Moles reactant species i consumed per mole of carbon gasified
$\nu'_{i,k}$	Stoichiometric coefficient of reactant species i in reaction k
$\nu''_{i,k}$	Stoichiometric coefficient of product species i in reaction k
ξ_n	Total area-specific concentration of all carbon sites mol m^{-2}
ρ	Density kg m^{-3}
ρ_{ash}	Apparent density of the ash kg m^{-3}
ρ_{char}	Apparent density of char kg m^{-3}
ρ_g	Average gas density kg m^{-3}
ρ_{MM}	Apparent density of mineral matter in the ash layer kg m^{-3}
ρ_{MO}	Apparent density of mineral oxide inclusions kg m^{-3}
ρ_{pc}	Apparent density of ash-containing char particle core kg m^{-3}
ρ_{solid}	Apparent density of particle, including char and ash kg m^{-3}
$\rho_{true,char}$	True (skeletal) density of the char particle kg m^{-3}
σ	Stefan-Boltzmann constant W m^{-2} K^{-4}
σ_d	The standard deviation of the activation energy distribution when modeling a desorption reaction J (mol)$^{-1}$
σ_{MO_n}	Specific surface tension of a droplet of the mineral oxide species that condenses in the particle's boundary layer kg s^{-2}
τ	Pore tortuosity factor: ratio of the actual diffusive path length to a straight path length
τ_p	Particle response time s
τ_{St}	Particle response time for Stokesian flow s
$\overline{\overline{\tau}}$	Stress tensor Pa
φ_I	Thiele modulus for vaporization: $\phi_I = (d_P/d_I)\sqrt{3\varphi_I}$
$\varphi_{L,i}$	Thiele modulus
$\varphi_{Ste,t}$	Stefan flow constant (see Eq. (117))
ϕ_I	Volume fraction of inclusions inside particle
χ	The double integral defined in Eq. (220)
ψ	Structural parameter in the random pore model (RPM)
$\psi(\eta)$	Non-dimensional size distribution of mineral oxide particles outside the particle's outer surface (see Eq. (215))
ω, ω^*	Parameters in the fragmentation rate expression (see Eq. (167))
$\dot{\omega}_i$	Source term of species i due to gas phase reactions kg m^{-3} s^{-1}

The equations presented apply to chars exposed to both oxidizing and reducing environments and hence, char reactivity to O_2, H_2O and CO_2 must be modeled. Approaches that assume power-law kinetics are briefly discussed but since high levels of CO and/or H_2 may be present in the environments of interest, approaches that account for the inhibiting effects of these gases on gasification rates are also presented and discussed. Attention is given to multi-step heterogeneous reaction models in which Langmuir-Hinshelwood type reaction mechanisms are used to describe the overall adsorption-desorption process.

Consideration is given to the most detailed simulation approach, where both the gas phase and the char are completely resolved. Numerical treatment requires discretization of both the volume of gas within the containing reactor walls and the volume within the outer surfaces of the char particles. This permits direct account for variations in gas composition and temperature inside particles, which is especially important for large particles.

Equations are also presented for cases in which the char particles are not resolved but treated as point-sources in the flow field. These equations reveal the coupling between the solid and gas phases; the assumptions that investigators have used to model this coupling are highlighted. This approach is commonly referred to as the "point-particle approach" (PPA) since as far as the fluid solver is concerned, the particles are treated as infinitely small points that do not occupy any volume. In this approach, all coupling between the fluid and solid is handled through models, this is the case for *e.g.* momentum, mass and heat transfer. The effects of turbulence on char conversion rates is

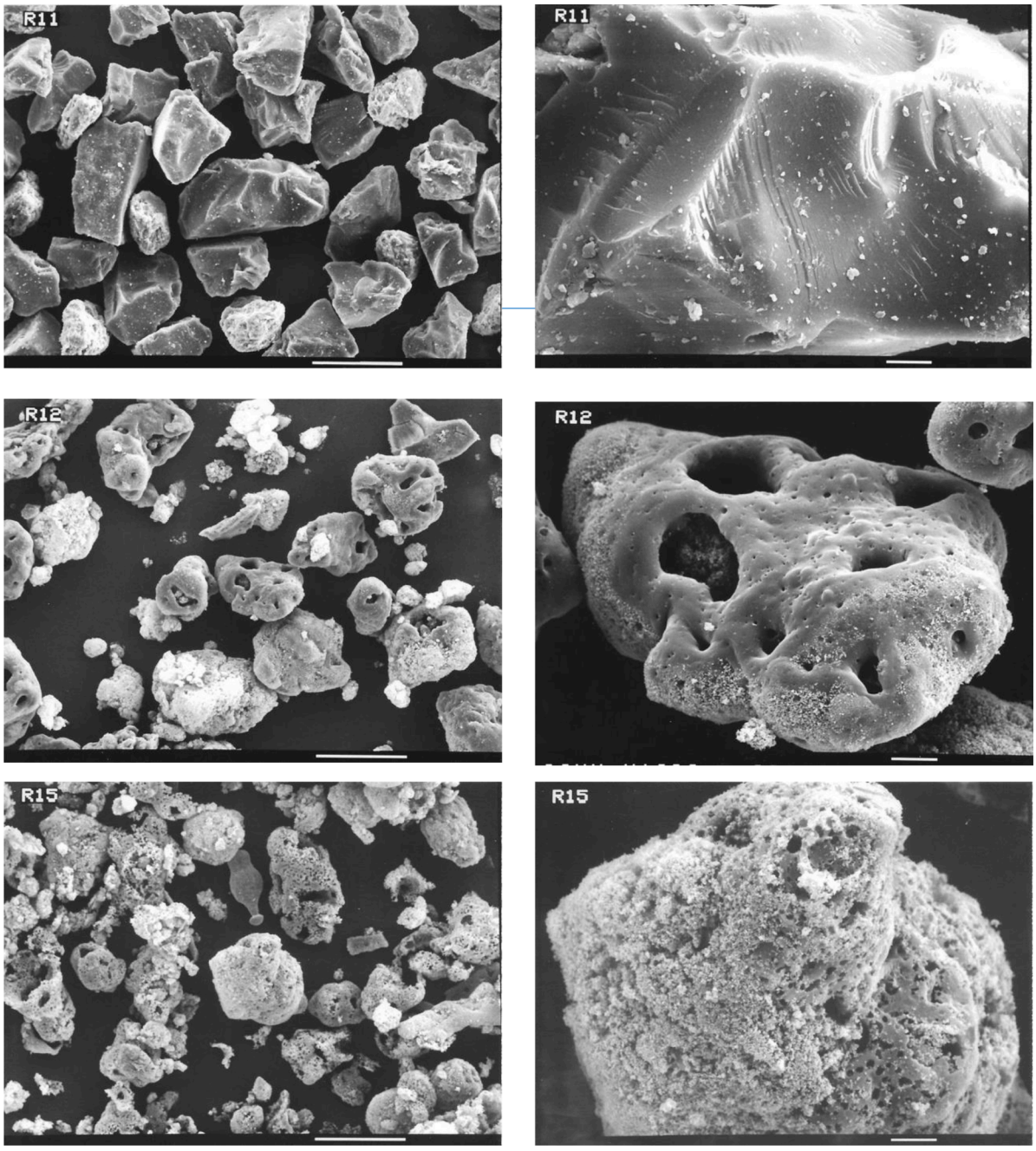

Fig. 1. Scanning electron micrographs of Pittsburgh #8 coal/char particles [14]. The bar in the micrographs on the left denotes 100 μm. In addition to the raw coal (upper row), chars with two different residence times are shown: $\mathbf{t_{res}} = 47$ ms (middle row) and $\mathbf{t_{res}} = 117$ ms (lower row). The raw coal particles, nominally 100 μm in diameter, were injected into a laminar flow reactor having 12% oxygen, by volume, at 1 atm. The gas temperature in the reactor decreased from ~1710 K at 47 ms to ~1532 K at 117 ms.

discussed in light of both Reynolds-averaged Navier-Stokes (RANS) and large eddy simulation (LES) turbulence modeling approaches. Results of direct numerical simulations (DNSs) are presented to illustrate the impact of these approaches on char conversion rates and overall conversion times. In these point-particle approximations, sub-models for the mode of burning govern the changes in char size and apparent density during mass loss; non-uniform composition and temperature profiles inside particles are accounted for via the Thiele modulus/effectiveness factor approach.

During the course of char conversion, individual particles experience variations in gas-phase temperature and composition that impact the conversion rates of the char owing to variations in the transport rates of reactive gases through particle pores and variations in heterogeneous reaction rates on pore surfaces. The sizes and apparent densities of the char particles also vary, as do the specific surface areas of the char. These physical properties of the char impact conversion rates and must be accurately characterized for accurate prediction of char conversion times. In addition, ash transformations in particles vary as the relative effects of ash vaporization, diffusion, and film development change due to the particle surroundings. Ash film development influences the rates of diffusion of reactive gases to char surfaces and hence, impacts char conversion rates. Ash film diffusion could enhance catalytic effects, thereby impacting overall char conversion times.

Fragmentation also occurs during the thermochemical conversion of char. Whereas percolative type fragmentation may be dominant during devolatilization, breakage and attrition type fragmentation are more important during char conversion [13]. Fragments are not only smaller in size than their parent particles; they can also have higher or lower apparent densities. These physical changes must be characterized in order to accurately predict char conversion rates.

In Fig. 1, the temporal evolution of a pulverized coal exposed to hot combustion products is shown. As exposure time increases, the particles become more porous and the number of smaller particles increases, most likely a consequence of fragmentation. The large holes at the outer surfaces of particles were created when volatile matter escaped the particles during devolatilization. Some particles appear to have large void volumes within their outer surfaces. The small white particles on the surfaces of the larger particles in the photos are ash, which means that for this coal in these conditions, there was no build-up of ash-film.

In general, the mode of conversion of a char particle can be divided into three different zones (or regimes), depending on the relationship between the rates of diffusion and reaction of the reactant species. Zone I conversion is defined as when reactant diffusion rates are much faster than consumption rates. This means that the reactant concentration within the char particle is spatially uniform. For this mode of conversion, which is kinetically controlled, the apparent density of the char particle will be reduced while its radius is unchanged. Zone III conversion is defined as the opposite extreme, when chemical reaction rates are much faster than diffusion rates. For this mode, all reactant species are consumed as soon as they reach the external surface of the char. Hence, the reactant concentration inside the particle is essentially zero, and the particle loses mass by reducing its radius while having a constant apparent density. For the intermediate regime, referred to as Zone II, the rate of diffusion is not too different from the kinetic rate. This means that the reactant concentration is higher at the particle surface than in its interior, but the reactant concentration in the interior is still non-zero. The particle will therefore lose mass both due to changes in apparent density and radius.

The main aim of this paper is first to present a comprehensive overview of the full spectrum of different numerical methods and models available for simulating char conversion. This includes a thorough presentation of the methodologies themselves, together with the associated evolution equations and the most relevant model and constitutive equations. From this, the reader should be able to implement and use the full range of different numerical methods and models for char conversion. Then, instead of stating that one method is better than the other, we try to guide the reader to which methods should be used for a given problem. This could be, for example, problems involving the conversion of billions of micrometer-sized particles in pulverized burners, millions of centimeter-sized particles in fluidized beds or a few decimeter sized wood logs in wood stoves. For all of these problems, one can try to obtain as much detail as possible of individual particles by resolving the smallest scale of the char particle and the fluid in its immediate surroundings, or, towards the other extreme, one can aim at simulating a full-sized industrial combustion chamber by using state-of-the-art modelling to account for the effects of individual particles. As such, this paper aims at being the starting point for anyone intending to perform numerical simulations involving char conversion.

2. Governing equations

In this section, we first present the governing equations for the gas phase outside the outer surface of a solid object. Then, equations for the interior of a resolved solid object, including both solid and gaseous volumes within the porous solid, are given. Finally, the equations for a non-resolved solid are shown based on the point particle approximation.

2.1. Fluid Equations

In the following, it is assumed that the char particles are embedded in a gaseous phase. The gaseous fluid is described by the continuity equation

$$\frac{\partial \rho}{\partial t} + \nabla\cdot(\rho \boldsymbol{u}) = \dot{W}_g, \tag{1}$$

which yields an expression for the time evolution of the gas density (ρ), where $\boldsymbol{u}$ is the fluid velocity vector. Furthermore, the momentum equation is given by

$$\frac{\partial \rho \boldsymbol{u}}{\partial t} + \nabla\cdot(\rho \boldsymbol{u}\boldsymbol{u}) = \nabla\cdot\bar{\bar{\tau}} + \dot{\boldsymbol{W}}_u \tag{2}$$

where the stress tensor $\bar{\bar{\tau}}$, is expressed as: $\bar{\bar{\tau}} = -P\cdot\bar{\bar{\mathbf{I}}} + \mu\bar{\bar{\mathbf{S}}}$. Here, P is the fluid pressure, $\bar{\bar{\mathbf{I}}}$ is the identity matrix, μ is the dynamic viscosity, ν is the kinematic viscosity (ν=μ/ρ), and $\bar{\bar{\mathbf{S}}}$ is the strain tensor $\bar{\bar{\mathbf{S}}} = [(\nabla \boldsymbol{u} + (\nabla \boldsymbol{u})^T) - \frac{2}{3}\mathrm{I}\,(\nabla\cdot\boldsymbol{u})]$. When it comes to conservation of energy, there are a number of different energy equations one can choose to solve. Here, we have chosen total enthalpy. The equation for total enthalpy (h) is given by

$$\frac{\partial \rho h}{\partial t} + \nabla\cdot(\rho \boldsymbol{u} h) = \nabla\cdot(\rho D_{th}\nabla h) + \dot{W}_h, \tag{3}$$

where D_{th} is the thermal diffusivity. Gas temperature is calculated from the relation $h = h_{f0} + \int_{T_{ref}}^{T} c_{p,g}\, dT$, where h_{f0} is the enthalpy of the gas mixture at the reference temperature and pressure, 298 K and 1 atm, respectively, and $c_{p,g}$ is the constant pressure specific heat of the gas. Finally, the evolution equation for the mass fraction Y_i of species i reads

$$\frac{\partial \rho Y_i}{\partial t} + \nabla\cdot(\rho Y_i \boldsymbol{u}) = \nabla\cdot\boldsymbol{J}_i + \dot{\omega}_i + \dot{W}_i, \tag{4}$$

where $\dot{\omega}_i$ is the source term due to gas-phase reactions and $\boldsymbol{J}_i$ is the diffusive flux of species i, given by

$$\boldsymbol{J}_i = \rho \mathscr{D}_i \nabla Y_i$$

Here, $\mathscr{D}_i$ is the molecular diffusivity of the species. It should be noted that the diffusive flux has been significantly simplified here by assuming the mixture averaged approximation and by neglecting several terms/

effects that are known to influence the species diffusion under certain conditions. Since the mixture average approximation does not guarantee mass conservation, a correction velocity may be introduced both in the energy and species conservation equations to overcome this limitation. Alternatively, the diffusive flux may be calculated by the use of full multicomponent diffusion instead of the mixture average approximation. The reader is referred to Hirschfelder *et al.* [15] for a more accurate expression of the diffusive flux. The source terms in Eqs. (1) - (4), $\dot{W}_g$, $\dot{W}_u$, $\dot{W}_h$ and $\dot{W}_i$, are due to the interaction with any unresolved (point) particles. For resolved particles, these source terms are omitted and the exchange between solid and fluid phases are handled through appropriate boundary conditions.

2.2. Resolved particles

In order to obtain the best description of a solid carbonaceous object, the solid object should be resolved by a large number of small grid cells. The evolution of the relevant parameters will then be calculated for every cell within the object. The solid object will be connected to the surrounding fluid phase through appropriate boundary conditions. This is commonly referred to as resolved particle DNS (RP-DNS). A number of papers have been devoted to numerical simulations of such resolved reacting particles [16-41] or surfaces [16]. Only some of these papers include conversion of the carbonaceous part of the solid [16-18, 20-24, 26-30, 32,36-39, 41-43] while the remaining ones only consider devolatilization and/or drying. Most of the papers that do consider conversion of the carbonaceous part of the solid do *not* consider carbonaceous conversion on the *internal porous* surface of the char, but rather allocate all char conversion to the *external* particle surface [16,18,20,23,24, 28-30, 42]. This means that apparent heterogeneous kinetics is required. For this kind of kinetics, the Arrhenius parameters are dependent on the exact conditions of interest, such as fluid temperature and particle size. In order to account for the internal char conversion within the porous structure, one can try to resolve the porous structure on the numerical mesh [26,27,36,37,40]. This can be done by making the pores as long radial wedges [37], channels between almost rectangular blocks of solid [27], spherical cavities [36], or voids between a large number of densely packed carbonaceous spheres [26]. It is interesting to see that one can now start to simulate particles with resolved pores in this way, but as the achievable pore size distribution is far from realistic (only the largest pores can be resolved on the grid), it is not clear what the benefit of resolving the pores is. A more numerically efficient and probably also more accurate approach is to treat the carbonaceous solid as a porous media [17,32]. In this approach, the carbonaceous part of the particle is handled through a statistical description of the pore size distribution and tortuosity. This latter approach yields the best trade-off between accuracy and CPU cost and is recommended for accurate simulations of char conversion. This is also the approach that will be described below.

When the primary focus is on the interior of the char, it is quite common to assume the char to be a perfectly spherical particle embedded in an infinitely large quiescent fluid [44-48]. Under these assumptions, it is sufficient to discretize the particle in the radial direction only. This will be referred to as the resolved-particle in quiescent fluid (RP-QF) approach. Such a discretization is illustrated in Fig. 2 but in this rendition, the boundary layer surrounding the particle is discretized as well. If the surrounding fluid has a velocity relative to the particle, only radial discretization is not sufficient. Instead, the surrounding fluid has to be discretized in all spatial dimensions. For particles larger than about 150 μm, homogeneous reaction in the boundary layer may be significant and should be taken into account for accurate predictions of char particle mass loss rates. Resolving the boundary layer accomplishes this end. For smaller particles, conversion of CO to CO_2 in the boundary layer is negligible and the single-film model (see Section 3.3.2) applies; the gas phase does not have to be resolved. Instead, models for mass and heat transfer can be used as boundary conditions.

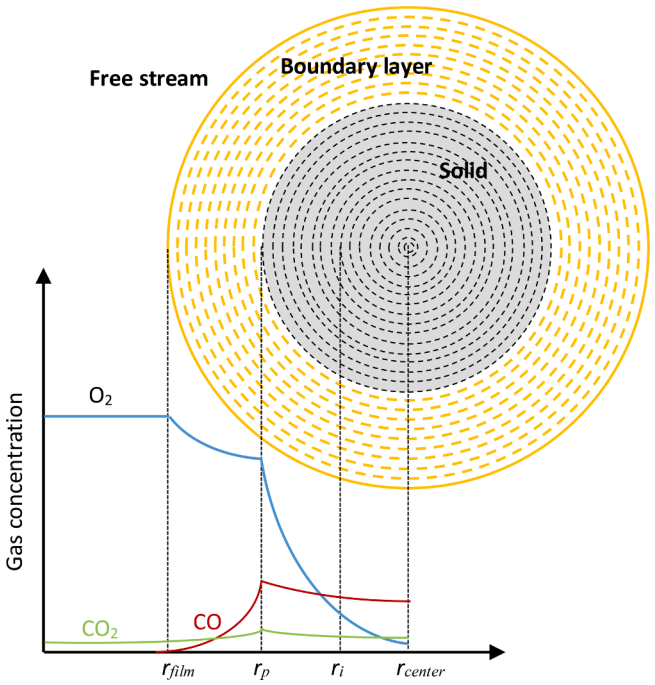

Fig. 2. Illustration of the resolved particle and its resolved boundary layer. The particle volume is discretized into a number of concentric spherical shells, where the volume of shell i is $v_i = (4\pi/3)(r_{i+1}^3 - r_i^3)$. The governing species and energy conservation equations are applied to each volume element in order to determine the species concentrations and particle temperatures at each radial position. Resolving the boundary layer permits homogeneous reaction in the boundary layer to be included in the calculation. There is no need to resolve the boundary layer when homogeneous reaction is assumed to be negligible in the boundary layer. Models for mass and heat transfer across the boundary layer can be used to relate conditions at the particle's outer surface (i.e., at r_p) to conditions in the free-stream (i.e., at r_{film}).

The simplified one-dimensional approach described above has the advantage that it is very fast, since it does not solve for the fluid, and the solid is treated along one dimension only. This means that it may be an ideal strategy to use the RP-QF approach either when very detailed heterogeneous kinetics are being used (since detailed kinetics is much more time consuming than its global counterpart), or when a large number of particles with large Biot numbers have to be treated. The Biot Number (defined as $Bi = HL/\lambda_{th}$, where H is the convective heat transfer coefficient, λ_{th} is the thermal conductivity of the particle and L is a characteristic length, taken as the volume of the particle divided by its external surface area), is used to describe the distribution of energy (or temperature) inside the particle over time. For small Biot numbers, the temperature distribution during transients within the particle can be taken as uniform. A large number of particles with large Biot numbers have to be treated, for example, in grate firing of solid fuels, where the evolution of every individual fuel particle is tracked. It is important to realize that the RP-QF framework is applicable only for cases that are strictly spherically symmetric. This is not the case for example for grate firing, but the method is still used [49] since the error introduced is less than the error associated with using the point particle approach for particles with large Biot numbers.

In the following, we will present the relevant evolution equations for fully resolved particles in a resolved fluid. The evolution of the particle velocity ($\boldsymbol{v}$) is found by integrating all surface and volume forces acting on the particle, such that

$$m_p \frac{d\boldsymbol{v}}{dt} = \int_s \bar{\bar{\tau}} \cdot \boldsymbol{n} dA + \left(\int_V \rho_{solid} dV - V_p \rho \right) \boldsymbol{g} + \boldsymbol{F}. \quad (5)$$

Here, $\boldsymbol{n}$ is the normal vector to the surface, dA is a small surface element, $\boldsymbol{g}$ is the gravitational acceleration, ρ_{solid} is the apparent density of the solid material (including both char and ash), $\boldsymbol{F}$ includes forces due to particle collisions while m_p and V_p are the mass and volume of the solid object, respectively. The position of the center of the object is given by $\boldsymbol{x}$. Knowing the velocity of the solid object, the evolution equation for its position is given by

$$\frac{d\boldsymbol{x}}{dt} = \boldsymbol{v}. \tag{6}$$

Let us now consider a set of N_{reac} heterogeneous reactions for the char, where the molar reaction rate of reaction k is given by

$$\widehat{\Re}_k = k_{k,f}\Pi_{i=1}^{N_s} C_i^{\nu'_{i,k}} - k_{k,r}\Pi_{i=1}^{N_s} C_i^{\nu''_{i,k}}. \tag{7}$$

In this equation, $k_{k,f}$ is the rate constant for the forward direction of reaction k, N_s is the number of reactant species (gaseous and adsorbed) involved in the heterogeneous reactions, C_i is the concentration of reactant species i, and $\nu'_{i,k}$ and $\nu''_{i,k}$ are the stoichiometric coefficients of species i on the reactant and product sides, respectively, of reaction k. The rate constant for the reverse direction of reaction k is determined from the forward rate constant and the equilibrium constant for the reaction, $K_{C,k}$ ($k_{k,r} = k_{k,f} / K_{C,k}$). The rate constant of the forward direction of reaction k is given by

$$k_{k,f} = A_{k,f}\exp\left(-\frac{E_{k,f}}{\widehat{R}_u T_p}\right), \tag{8}$$

where $A_{k,f}$ and $E_{k,f}$ are the corresponding pre-exponential factor and activation energy, respectively, and $\widehat{R}_u$ is the gas constant. More details about the heterogeneous chemical kinetics are found in Section 3.2. The concentration of species i is calculated by

$$C_i = \frac{P_i}{\widehat{R}_u T}, \tag{9}$$

where P_i is the partial pressure of species i and T is the gas temperature. The gas temperature inside a char particle can to a good approximation be set equal to the particle temperature for thermally thin particles, or to the local particle temperature for thermally thick particles.

Based on the above, the reactivity of gaseous species i is given by

$$\widehat{R}_i = \sum_{k=1}^{N_{reac}} \widehat{\Re}_k\left(\nu''_{i,k} - \nu'_{i,k}\right) \tag{10}$$

where N_{reac} is the number of heterogeneous reactions. The intrinsic reactivity of the char can be described as

$$R_c = \widehat{M}_C \cdot \sum_{k=1}^{N_{reac\_des}} \widehat{\Re}_k \tag{11}$$

where $\widehat{M}_C$ is the molar mass of carbon and N_{reac_des} is the number of desorption reactions, reactions in which a gaseous species is released from the solid surface, extracting a carbon atom from the carbonaceous matrix in the process. When it is assumed that all adsorbed species maintain steady-state concentrations, char reactivity can be determined from the reactivities of the gas phase species.

$$(R_c)_{ss} = \sum_{i=1}^{N_{spec\_gas}} \widehat{R}_i \widehat{M}_i. \tag{12}$$

See Appendix A for a discussion of char reactivity based on heterogeneous reaction mechanisms.

The evolution of the apparent char density is given by

$$\frac{\partial \rho_{char}}{\partial t} = -\rho_{char} R_c S_g. \tag{13}$$

Here, S_g is the mass specific internal surface area of the char. For a resolved particle, which is discretized in the radial direction, the outermost shell of grid cells requires some special treatment. For this shell, reaction at the external surface area must be added to that on internal surfaces to yield the evolution of the apparent char density in the grid cell. Thus,

$$\frac{\partial \rho_{char}\left(r = r_p\right)}{\partial t} = -\rho_{char} R_c S_g - \frac{A_c \Theta}{V_c} R_{c,s} = -R_{c,s}\left(\rho_{char} S_g R_c \Big/ R_{c,s} + \frac{\Theta}{\Delta r}\right). \tag{14}$$

In the equation above, which is only applicable for the outermost grid cell, A_c is the external surface area of the grid cell while $V_c \approx A_p \Delta r$ is the volume of a grid cell with thickness Δr. Also in the above equation, Θ is the porosity of the material in the shell, R_c is the intrinsic char reactivity evaluated at conditions existing in the outermost shell, and $R_{c,s}$ is the char reactivity evaluated at conditions existing at the external surface of the particle.

The internal surface area will be discussed in more detail in Section 3.1.2. In the above expression, the apparent density of char is given as ρ_{char}, which varies with mass loss as discussed in Section 3.3.3.

It is customary to consider a char particle as a porous solid material. The continuity equation, which handles the evolution of the gas density within the pores of the char, is then given by

$$\frac{\partial \Theta \rho_g}{\partial t} + \nabla \cdot \left(\rho_g \boldsymbol{u}_s\right) = \dot{\omega}_g \tag{15}$$

where ρ_g is the average density of the gaseous phase, $\boldsymbol{u}_s$ is the superficial velocity of the gas and $\dot{\omega}_g$ represents all sources of gas. The superficial velocity of the gas within the pores can be obtained by solving the momentum equation, but since fluid motion in a porous medium like char will never be turbulent or show any significant recirculation *etc.*, it is more common to use Darcy's law to solve for the superficial fluid velocity:

$$\boldsymbol{u}_s = -\frac{K}{\mu}\nabla P, \tag{16}$$

where, K is permeability, μ is dynamic viscosity and P is pressure, which is obtained from the relevant equation of state.

The mass fraction of gas-phase species i is governed by the following transport equation

$$\frac{\partial \Theta \rho_g Y_i}{\partial t} + \nabla \cdot \left(\rho_g Y_i \boldsymbol{u}_s\right) = \nabla \cdot \left(\rho_g \mathscr{D}_{i,eff} \nabla Y_i\right) + \dot{\omega}_i + \dot{W}_i. \tag{17}$$

Here, $\dot{\omega}_i$ represents gaseous sources of species i and $\dot{W}_i$ represents sources of gas-phase species i due to interactions with the solid phase. Following an approach similar to that of Satterfield [50], the effective diffusivity of species i, $\mathscr{D}_{i,eff}$, is expressed in terms of the bulk and Knudsen diffusion coefficients for the species, $\mathscr{D}_i$ and $\mathscr{D}_{Kn,i}$, respectively, and is given by

$$\mathscr{D}_{i,eff} = \left(\frac{\Theta \theta_c}{\tau}\right)\left(\frac{1}{\mathscr{D}_i} + \frac{1}{\mathscr{D}_{Kn,i}}\right)^{-1} \tag{18}$$

where the Knudsen diffusion coefficient for species i depends on the mean pore radius and molecular weight of the diffusing species [50]:

$$\mathscr{D}_{Kn,i} = \left(\frac{2 r_{pore}}{3}\right)\sqrt{\frac{8\widehat{R}_u T_p}{\pi \widehat{M}_i}}. \tag{19}$$

In Eq. (18), τ is the tortuosity factor and θ_c is the pore constriction factor, factors that account for the fact that pores are not straight nor of constant cross section. The tortuosity factor is the ratio of the length of the actual diffusive paths through the porous material to the length of a straight path through the material. Values for tortuosity between three and seven are reasonable for chars; a value of three is predicted for

randomly oriented, long cylindrical pores [50]. The constriction factor accounts for the variations in pore cross-sectional area normal to the diffusional path and is a function of the ratio of the smallest to largest cross-sectional pore area. Its value is between zero and one, the lower the value the greater the impact of bottleneck-type pores on limiting diffusive flow through the porous system. In Satterfield [50], the constriction factor and tortuosity factor are combined into one factor and is called the "tortuosity factor". The ratio τ/θ_c (termed "τ" in Satterfield), is a measure of the tortuous paths and varying cross-sections of the pores through which gases diffuse.

Constriction factors for coal and biomass chars have not yet been determined. These factors cannot be determined directly; they must be deduced from the determinations of tortuosity, porosity and effective transport properties. Values for θ_c are available for selected electrode materials. Constriction factors in the range 0.15 to 0.23 have been determined for various electrode microstructures with porosities near 50% [51]. In a study to analyze the microstructures of porous lithium-ion electrolytes [52], constriction factors were found to decrease from about 0.75 to 0.5 as the porosity of the electrolyte increased from about 25% to 55%.

Attempts to predict the constriction factor for a porous network from pore size distributions have been undertaken. Münch and Holzer [53] defined the constrictivity β as $\beta = (r_{min50}/r_{max50})^2$, where r_{min50} and r_{max50} are the 50%-quantiles of a continuous pore size distribution (c-psd) and a mercury-intrusion-porosimetry pore size distribution (MIP-psd), respectively. The c-psd, which assumes that the porous structure is a single continuum, independent of possible connectivities, is calculated either from a three-dimensional synthetic microstructural model of the porous material of interest or from a three-dimensional image of the porous material (measured via nano-tomography, for example). Processing of the analytical microstructures using an algorithm that calculates the amount of the total pore volume that can be filled with circles and spheres of a specific pore radius leads to the determination of the volume fraction of pores of all sizes considered [53]. The volume fractions in the smallest of pores of the three-dimensional microstructural model can be determined in this manner. Mercury cannot penetrate the smallest pores of materials (without employing high intrusion pressures that might compress the sample being tested) and hence, a measured MIP-psd is strongly influenced by narrow constrictions along the intrusion pathways. If mercury intrusion porosimetry is not performed, a MIP-psd can be simulated for the microstructural model or nano-tomographic image using c-psd techniques [53]. Forty-three synthetic microstructures were examined by Stenzel *et al.* [54] in efforts to determine a correlation between intrinsic and effective transport properties. For each microstructure, Θ, τ and β were determined. An optimization algorithm revealed that all three parameters were needed to derive an adequate correlation between effective and intrinsic thermal conductivities. The correlation was validated using data obtained with porous nickel-phase solid oxide fuel cell anodes. Values determined for β (nominally, the same as the constriction factor) were in the range 0.2 to 0.4. A number of different ways to define constrictivity exists that are based on c-psd and MIP-psd. This study supports the use of using the radius at the 50% quantile of the c-psd to determine the average size of bulges (r_{max}) along the tortuous path and the radius at the 50% quantile of the MIP-psd to define the average size of bottlenecks (r_{min}) along the path when determining the constriction factor. This technique has not yet been used to determine such factors for chars produced from coals or biomass. This study supports the use an equation of the type given by Eq. (18) to relate effective and intrinsic diffusivities in that all three parameters (Θ, τ and θ_c) are used in the correlation.

Recent coal char combustion modelers [55,56] have also proposed using the pore-size-distribution to estimate the effective diffusion coefficient for coal chars. In their approach, the ratio τ/θ_c is replaced by the ratio τ/f, where f is the fraction of the total porosity in the feeder pores of the char. The total porosity of a char particle consists of the porosity in the micropores ($d_{pore} < 20$Å), the mesopores (20 Å $< d_{pore} <$ 500 Å) and the macropores ($d_{pore} > 500$Å). The feeder pores are in the macropore range. It is these larger pores that feed reactive gases into the smaller pores where char conversion is most appreciable. Sun and Hurt [56] assume that the pore structure conforms to the pore tree model of Simons [57], where macropores feed mesopores and mesopores feed micropores and where the long-path-length transport to the interior of the char particle is via the macropores. As such, any variations in pore cross section in the micropore and mesopore size ranges insignificantly impact mass transport inside the particle. Consequently, in this approach, only the macropore size range needs to be considered when modeling pore diffusion — Knudsen diffusion is neglected. Note that for a specified particle porosity, the larger the fraction of pores in the macropore size range (the larger f), the less the impact of variations in cross sectional area on the transport property and conversely, the smaller the fraction of macropores (the lower f), the greater the impact of variations in cross sectional area on transport properties. Thus f accounts for variations in pore cross sections in essentially the same manner that the constriction factor does. Sun and Hurt [56] recommend a value of 6 for the ratio τ/f, a value that suggests that $\theta_c = 0.5$ when pores are randomly oriented, cylindrical and relatively long. In the absence of experimental data, a value of 0.5 is recommended for θ_c for coal and biomass chars.

Knudsen diffusion accounts for the effect of finite mean free path of gas molecules and is important in the transport of molecules in the small pores of char particles where molecules collide with pore walls as often as they collide with each other. The mean pore size, r_{pore}, is discussed in more detail in Section 3.1.1. Since the pores are very small, the fluid and the solid are typically assumed to be in thermal equilibrium inside the particle, *i.e.*; for a tiny porous volume inside the particle, the fluid and solid within this small volume have the same temperature. This means that a single equation for temperature is sufficient to obtain accurate results:

$$\left(\Theta\rho_g c_{p,g} + \rho_{solid} c_{p,solid}\right)\frac{\partial T}{\partial t} + \rho_g c_{p,g}\boldsymbol{u}_s\cdot\nabla T = \nabla\cdot(\lambda_{th}\nabla T) + q_{gas-reac} + q_{reac}. \tag{20}$$

In the above equation, c_p is the heat capacity at constant pressure, λ_{th} is the effective thermal conductivity of the porous material (including the gas within the pores and the solid), $q_{gas\ -\ reac}$ is the energy released as heat due to gas-phase, homogeneous chemical reaction, and q_{reac} is the energy released as heat by the heterogeneous chemical reactions at the internal surfaces of the char. It is expressed as

$$q_{reac} = \sum_{k=1}^{N_{reac}} \widehat{\Re}_k q_{reac,k} S_g \rho_{char} \tag{21}$$

where the quantity $q_{reac,k}$ represents the heat of reaction for reaction k. For the outermost shell, in the same way as for Eq. (14), account must be made for the presence of the outer external surface. Hence, for the outermost shell,

$$q_{reac} = \sum_{k=1}^{N_{reac}} \left(\widehat{\Re}_k q_{reac,k} S_g \rho_{char} + \left(\Theta\widehat{\Re}_k q_{reac,k}\right)_s \Big/ \Delta r\right) \tag{22}$$

where in the first term of the summation, reaction rates are calculated at the conditions associated within V_{shell} and in the second term, the reaction rates are calculated at the conditions existing at the outer surface. Since thermal equilibrium between solid and gas is assumed, the energy released during reaction is heating both the solid and the gas.

2.2.1. Boundary conditions

All the above equations must be solved for the interior of the char, while at the interface between the char particle and the embedding fluid (the external char surface), appropriate boundary conditions must be applied. For a particle at rest, the gas phase velocity at the particle surface must equal the superficial velocity of the gas just inside of the

boundary, *i.e.*;

$$\boldsymbol{u}|_{gas,s} = \boldsymbol{u}_s|_{char,s} \tag{23}$$

where $\boldsymbol{u}_s$ is given by Eq. (16). If the particle is not at rest, the velocity of the particle surface (including both translation and rotation) must be added to the right-hand side of the above equation. The gas phase density at the surface is calculated directly from Eq. (1), eliminating the need for a boundary condition for density.

The boundary is assumed to be an infinitely thin layer around the particle. This means that the relevant boundary condition for temperature and species is to set the heat and mass flux gradients to zero at the boundary. Consequently, the heat and mass fluxes from the particle interior to the particle surface should be equal to the heat and mass fluxes from the particle surface to the surrounding gas. Based on this, the following expression should be used for the temperature boundary condition:

$$\lambda_{th}\nabla T|_{solid,s} = q_{rad} + \lambda_{gas}\nabla T|_{gas,s} \tag{24}$$

where

$$q_{rad} = \sigma\epsilon_p\left(T_{rad}^4 - T_{solid,s}^4\right). \tag{25}$$

The term $\nabla T|_{solid,s}$ is the temperature gradient of the solid evaluated at the surface based on temperature inside the solid, while $\nabla T|_{gas,s}$ is the corresponding gradient evaluated in the gas phase. In the above equation, σ is the Stefan-Boltzmann constant, ε_p is the emissivity of the particle surface, T_{rad} is the effective radiative temperature of the surroundings, and $T_{solid,s}$ is the temperature of the particle surface. In addition, the solid and gaseous temperatures at the surface must be equal, *i.e.*:

$$T|_{solid,s} = T|_{gas,s}. \tag{26}$$

Correspondingly, the boundary condition for gas phase species k is given by

$$D_{i,eff}\nabla Y_i|_{solid,s} = D_i\nabla Y_i|_{gas,s} \tag{27}$$

and

$$Y_i|_{solid,s} = Y_i|_{gas,s}. \tag{28}$$

Spherical-symmetric particle in non-resolved fluid

When the spherical-symmetric approximation (RP-QF) is applied, the particle is resolved only along the radial direction, and the fluid is not resolved at all. Models for mass and heat transfer are then used as boundary conditions. In such cases, the right-hand side of Eq. (24) should be substituted with

$$F_{temp} = \frac{\mathrm{Nu}\ \lambda_{gas}}{d_p}\left(T_{g,\infty} - T_{g,s}\right) + q_{rad} \tag{29}$$

where Nu is the Nusselt number and d_p is the particle diameter. Similarly, the right-hand side of Eq. (27) should be substituted by

$$F_{spec,i} = \frac{\mathrm{Sh}\ D_i}{d_p}\left(Y_{i,\infty} - Y_{i,s}\right) \tag{30}$$

where Sh is the Sherwood number. In the above equations, $T_{g,\infty}$ and $Y_{i,\infty}$ are the gas temperature and mass fraction of species i, respectively, in the ambient. When calculating the Nusselt and Sherwood numbers, account should be made for the effects of Stefan flow (see Section 3.3.2 and/or refs. [58-60]).

2.3. The point particle approximation

In principle, one would always solve for the above set of equations for all particles, *i.e.,* resolving the particles on the computational mesh. This does, however, become prohibitively time consuming when a large number of particles are involved. For small particles, which have radii that are significantly smaller than the mesh size used to solve for the surrounding fluid, the point particle approximation can be used. In this approximation, the particles are considered as points as far as the fluid solver is concerned. This means that the particles do not displace any fluid, but they do still act as sources of mass, momentum, species, and heat. Since the particles are not resolved on a numerical mesh, appropriate models are used to represent the physical processes inside the particles and at the boundary between the particles and the fluid. For cases where the volume fraction of solid particles cannot be neglected, for example in dense beds, the fluid displacement will be accounted for through the introduction of a solid volume fraction term in the fluid equation. A schematic diagram of point-particles in a flow field is shown in Fig. 3, with radial gas concentration profiles emphasized for a single point-particle.

In contrast to the resolved particle approach, in which all scales of the fluid are resolved, including the boundary layer around the particles (RP-DNS), the point particle approach may be used in combination with three different levels of fluid solvers that *do not* resolve the particle boundary layer. These three different levels refer to solvers where 1) all scales of the fluid (carrier-phase) are resolved in a point particle DNS (PP-DNS) [61-69], 2) the largest turbulent scales are resolved in a LES [70] or 3) no turbulent scales are resolved (but modelled) in a RANS solver [71]. For LES solvers, semi-industrial furnaces may be simulated while for PP-DNS, only smaller cases can be handled. Some examples are laboratory jet flames [62-64], low Reynolds number shear layers [66, 67], isotropic turbulence [69] or laminar flows [65,68]. Out of these, only some include char reactions [62-64, 66,68,69], and it is only the work of Kruger *et al.* [69] that has its primary interest on the char conversion process. Keeping in mind that char conversion is the rate limiting process for most industrial plants, it is clear that there is a need for a more concentrated effort on the conversion of char.

The resonance scale of the turbulence is defined as the time scale that equals the response time of the particles. If the resonance scale of the turbulence is resolved in the fluid solver, the relevant interactions between particles and fluid are properly handled. This is the case for DNS and well resolved LES simulations. In the opposite case, where the resonance scales of the fluid are not resolved, which is the case for RANS and coarse grained LES simulations, the particle-turbulence interaction must be accounted for through models. There are two primary effects that these models must account for: 1) a turbulent fluid will cause embedded particles to form clusters with high number-density of particles, surrounded by voids where there are essentially no particles. Within these clusters, the particles will consume the reactant gas, while there are still large amounts of reactant gas in the voids outside the clusters. This yields a net reduction in the heat and mass transfer rates to the particles. In addition, the models must also account for the fact that 2) the small-scale turbulence (scales smaller than the resonance scale) will yield a relative velocity between the particles and the fluid. This relative difference results in increased heat and mass transfer rates between particles and fluid. The reader is referred to the work of Haugen and collaborators for appropriate models that account for both of these effects [69,72-74].

Particles embedded in a turbulent flow will disperse due to turbulent eddies. This is because the particles follow the path of the larger turbulent eddies. In particular, all eddies larger than the resonance scale will transport the particles, while the smaller eddies will typically be too fast to yield any significant transport. Instead, the smaller eddies will result in a net relative velocity between the particles and the fluid. For the special case of tracer particles (no inertia), even the smallest eddies will contribute to the dispersion while the relative velocity will be zero. Since the turbulence itself is not resolved in RANS models, an appropriate model is required in order to emulate turbulent dispersion. Such a model typically works by giving the particles random kicks that result in a reasonable dispersion. This will, however, result in large relative

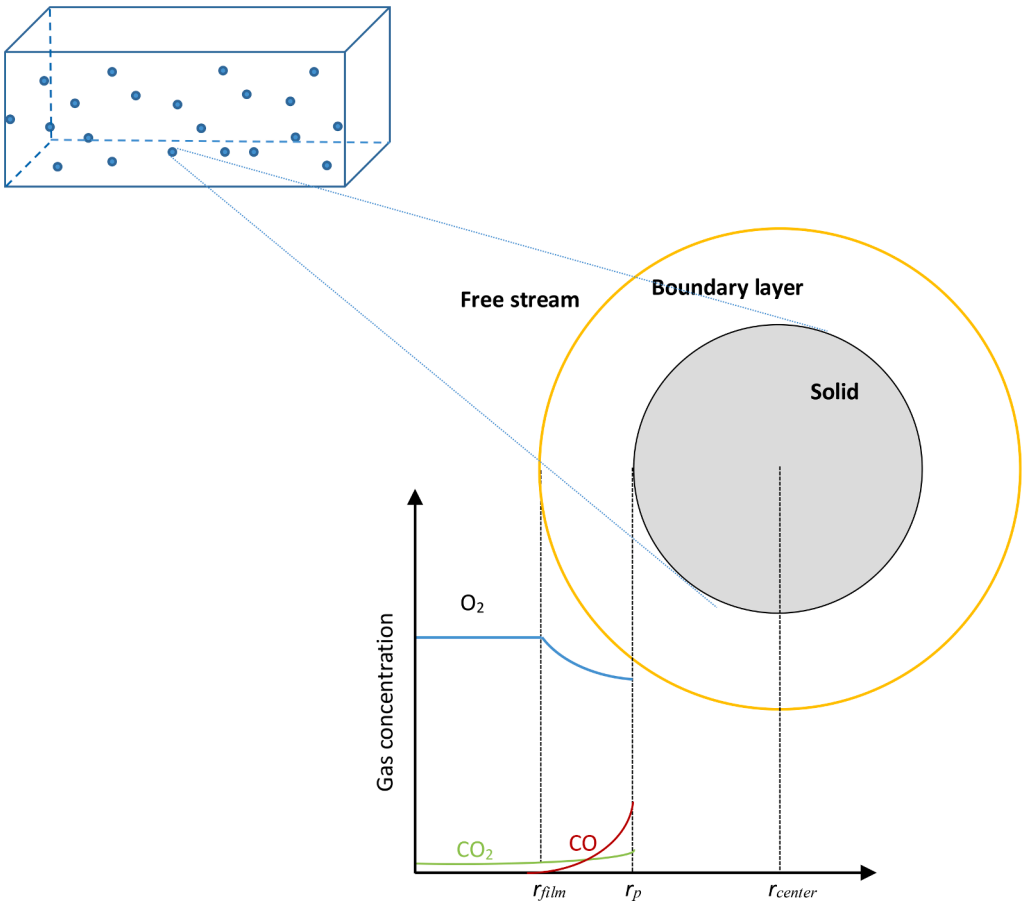

Fig. 3. Illustration of the point-particle. Each point-particle is treated as a sink for reactant species and a source for reaction products. The point-particle absorbs energy from the flow field in gasification environments and releases energy to the flow field in combustion and oxy-combustion environments. Only average particle conditions are determined, but gradients in reactant concentration are accounted for through the effectiveness factor.

velocities between the particles and the fluid – even for tracer particles. This is not physical and may result in an over-estimation of the heat and mass transfer between particle and fluid since these depend on the relative velocity. It is therefore important to realize that the typical turbulent dispersion models implemented in RANS simulation tools may not necessarily result in reasonable heat and mass transfer, even though the dispersion characteristics of the particles are correctly reproduced. A first study of the effect of turbulence on the mass transfer to char particles in RANS simulations is presented in Karchniwy *et al.*[71].

Integrating Eq. (5) over the particle yields the following expression for the particle velocity evolution in the point particle approximation if forces due to particle collisions are omitted

$$m_p\frac{d\boldsymbol{v}}{dt}=\frac{1}{2}\rho C_D A_p|\boldsymbol{u}-\boldsymbol{v}|(\boldsymbol{u}-\boldsymbol{v})+\left(m_p-\rho V\right)\boldsymbol{g}=\frac{m_p}{\tau_p}(\boldsymbol{u}-\boldsymbol{v})+\left(m_p-\rho V\right)\boldsymbol{g}. \tag{31}$$

Here and in the following, subscript p refers to particle-integrated quantities, while C_D is the drag coefficient; $A_p=\pi r_p^2$ is the cross-sectional area of the particle; $m_p=\rho_p{\cdot}\pi d_p^3/6$ is the mass of the particle, ρ_p being the apparent particle density; $d_p=2r_p$ is the particle diameter; and τ_p is the particle response time. The drag coefficient will decrease for increasing Stefan flow velocity and this decrease becomes relevant for very large Stefan flows. A model for the drag coefficient as a function of Stefan flow velocity has been developed by Jayawickrama *et al.* [75].

For Stokesian flow (*i.e.*, when the particle Reynolds number is small), the response time is given by $\tau_{St}=\frac{\rho_p d_p^2}{18\nu\rho}$. If the particle Reynolds number is above unity, a correction to this equation is required, such that a general expression for the particle response time is given by

$$\tau_p=\tau_{St}f_g \tag{32}$$

where f_g is a correction that is different from unity for non-zero particle Reynolds numbers. A popular correction function, which is valid for $Re_p<1000$, is given by [76,77]

$$f_g=\left(1+0.15Re_p^{0.687}\right)^{-1}. \tag{33}$$

The equation for particle position, as given by Eq. (6), is unchanged for the point particle approximation.

It is important to realize that the reactant distribution within the particle is unknown for the point particle approximation. This means that Eq. (7) cannot be integrated directly to yield the particle averaged molar reaction rate of reaction k. Instead, the average reactant concentration in the particle ($C_{i,p}$) is defined such that the particle-averaged reaction rate of reaction k is given by

$$\widehat{\Re}_{k,p}=k_{k,f}\Pi_{i=1}^{N_s}C_{i,p}^{\nu'_{i,k}}-k_{k,r}\Pi_{i=1}^{N_s}C_{i,p}^{\nu''_{i,k}}. \tag{34}$$

In the point-particle approach, temperature gradients inside particles are neglected. Particles are assumed to be thermally thin (small Biot number), yielding a single temperature for the entire particle, and reaction rate coefficients are evaluated at this temperature. The particle-averaged reaction rate is defined based on the integral of the resolved reaction rate of reaction k over the entire volume (V_p) of the particle:

$$\widehat{\Re}_{k,p} = \frac{1}{V_p}\int_{V_p} \widehat{\Re}_k \, dV, \tag{35}$$

where $\widehat{\Re}_k$ is found from Eq. (7). In order to find the average reactant concentration, the effectiveness factor for species i (η_i) is utilized, which is defined such that

$$C_{i,p} = \eta_i \cdot C_{i,s} \tag{36}$$

where $C_{i,s}$ is the concentration of species i at the surface of the particle. (See Section 3.3.1 for a discussion of alternative definitions of the effectiveness factor.) Based on this, Eq. (34) can now be re-written to yield

$$\widehat{\Re}_{k,p} = k_{k,f}\Pi_{i=1}^{N_s}\left(\eta_i C_{i,s}\right)^{\nu'_{i,k}} - k_{k,r}\Pi_{i=1}^{N_s}\left(\eta_i C_{i,s}\right)^{\nu''_{i,k}}. \tag{37}$$

This is formally correct only for first order reactions and homogeneous internal surface area, but it is commonly used for other cases as well. The calculation of species surface concentrations will be discussed in Section 3.3.2 while the effectiveness factor will be discussed in more detail in Section 3.3.1.

In analogy with Eq. (10), which gives the reactivity of species i at a given grid cell within the resolved particle, the following equation for the overall reactivity of species i for the entire particle is defined:

$$\widehat{R}_{i,p} = \sum_{k=1}^{N_{reac}} \widehat{\Re}_{k,p}\left(\nu''_{i,k} - \nu'_{i,k}\right). \tag{38}$$

In the same way, the reactivity of the particle (analogous to Eq. (11)) can be defined as:

$$R_{c,p} = M_C \cdot \sum_{k=1}^{N_{reac\_des}} \widehat{\Re}_{k,p}\ , \tag{39}$$

where N_{reac_des} is the number of desorption reactions that release a carbon atom from the surface.

The evolution of the particle mass can now be found by considering mass loss on both internal and external particle surfaces:

$$\frac{dm_p}{dt} = \left(\frac{dm_p}{dt}\right)_s + \left(\frac{dm_p}{dt}\right)_{int} = -\left(A_p \cdot R_{c,s} + S_g m_p \cdot R_{c,p}\right). \tag{40}$$

where $R_{c,s}$ is the intrinsic reactivity evaluated at conditions existing at the external surface of the particle. Rearranging the right-hand-side yields

$$\frac{dm_p}{dt} = -\left(1 + \frac{S_g m_p}{A_p}\frac{R_{c,p}}{R_{c,s}}\right)\cdot A_p \cdot R_{c,s}. \tag{41}$$

Realizing that particle reactivity is maximum on its external surface, the effectiveness factor can be expressed as $\eta = R_{c,p}/R_{c,s}$, and the particle mass loss rate can be rewritten as

$$\frac{dm_p}{dt} = -\left(1 + \frac{S_g m_p}{A_p}\cdot\eta\right)\cdot A_p \cdot R_{c,s}. \tag{42}$$

Since $m_p = \rho_{char} \cdot V_p$, the mass rate expression can be written as

$$\frac{dm_p}{dt} = -\left(1 + \frac{S_g \cdot \rho_{char} \cdot V_p}{A_p}\cdot\eta\right)\cdot A_p \cdot R_{c,s} = -\left(1 + \frac{S_g \cdot \rho_{char} \cdot d_p \cdot \eta}{6}\right)\cdot A_p \cdot R_{c,s}. \tag{43}$$

The second term in the parenthesis of the above expression is dominant except for situations when carbon conversion rates are very near the diffusion-limited rates (*i.e.,* when η approaches zero). For $\eta > \sim 0.001, \eta > \sim 0.001$, unity in the parenthesis term of Eq. (43) can be neglected, and since $R_{c,s} = R_{c,p}/\eta$, the equation simplifies to

$$\frac{dm_p}{dt} = -S_g \cdot \rho_{char} \cdot V_p \cdot R_{c,p} = -S_g \cdot m_p \cdot R_{c,p}. \tag{44}$$

Given the change in particle mass, as obtained from Eq. (43), it is not known if the change in mass will be due to a reduction in particle radius or density – or both. This is determined by the mode of conversion, which will be discussed in Section 3.3.3.

By assuming that the particle is thermally thin, (rendering a constant temperature throughout the particle), the temperature evolution, as presented in Eq. (20), can be integrated together with the boundary condition given in Eq. (24) to yield

$$\frac{dT_p}{dt} = \frac{1}{m_p c_{p,solid}}\left(Q_{reac} + Q_{rad} + Q_{conv}\right) \tag{45}$$

where the reactive heating of the entire particle (Q_{reac}) is expressed as

$$Q_{reac} \sum_{k=1}^{N_{reac}} \widehat{\Re}_{k,p}\ q_{reac,k}\ S_t. \tag{46}$$

Here, S_t is the total particle surface area, internal plus external surface area ($S_t = m_p S_g + A_p$). The radiative heating (Q_{rad}) is given by

$$Q_{rad} = \int_{A_p} q_{rad} dA \tag{47}$$

while the convective heating (Q_{conv}) is found from

$$Q_{conv} = HA_p\left(T_p - T_g\right), \tag{48}$$

where H is the convective heat transfer coefficient. It is important to note that one should use the thermally thin approximation only when the Biot number, which is given by

$$Bi = \frac{H\ V_p}{A_p\ \lambda_{gas}}, \tag{49}$$

is smaller than 0.1. If the thermally thin approximation cannot be used, the point particle approximation is not applicable. Hence, for large Biot numbers, the particle has to be resolved with one of the resolved particle approaches presented in Section 2.2: RP-DNS or RP-QF. For spherical particles, the particle volume and external surface area are given by $V_p = \frac{4}{3}\pi r_p^3$ and $A_p = 4\pi r_p^2$, respectively. The heat transfer coefficient, H, models the heat transfer through the boundary layer around the particle. This is not trivial since the boundary layer is associated with an outflow due to the heterogeneous reactions (Stefan flow), and since there may be gas phase reactions within the boundary layer. On top of this, the particle typically has a velocity relative to the fluid. The heat and mass transfer coefficients will be handled in detail in Section 3.3.2. The heat and mass transfer models will also be affected by the way the remaining ash is treated. Whether the remaining ash is assumed to form a dense ash layer around the particle, redistribute within the remaining char, or just fall off, may have a dramatic effect on transport to and from the particle. The ash treatment is presented in Section 3.4.

Wood logs have large Biot numbers and due to the internal structure of a wood stove, their boundary layers cannot be modelled using traditional models for heat and mass transfer through boundary layers. When simulating conversion of wood logs, one therefore has to use some version of the resolved particle approach [48].

The source terms in the fluid equations due to point particles can be found by summing the contributions from all particles N_p within a given grid cell with volume δV, such that

$$\dot{W}_g = \frac{1}{\delta V}\sum_{j=1}^{N_p}\frac{dm_{p,j}}{dt}. \tag{50}$$

This is the source term in the continuity equation (Eq. (1)); the evolution of the particle mass is given by Eq. (43). The source term in the momentum equation (Eq. (2)) contains two terms, the first is due to momentum added to the fluid because of mass transport from the particles,

while the second is due to the drag between the particles and the fluid. Hence, the momentum source term is given by

$$\dot{\boldsymbol{W}}_u = \frac{1}{\delta V} \sum_{j=1}^{N_p} \left(\boldsymbol{v}_j \frac{dm_{p,j}}{dt} + \frac{m_{p,j}}{\tau_{p,j}} \left(\boldsymbol{u} - \boldsymbol{v}_j \right) \right). \tag{51}$$

The source term in the enthalpy equation is given by

$$\dot{W}_h = \frac{1}{\delta V} \sum_{j=1}^{N_p} \left(\frac{dm_{p,j}}{dt} h_{char} - Q_{cond} \right) \tag{52}$$

where h_{char} is the enthalpy of the gaseous phase that leaves the particle. Here, it is assumed that the solid and the gas within the pores of the solid are in thermal equilibrium, which means that the temperature of the gaseous reaction products entering the gas phase has the same temperature as the particle. This may not be a good approximation for small particles. A certain fraction of the heat of reaction may then be directly transferred to the gas phase while the remaining part is heating the solid. This fraction is commonly set to 0.3 [78], but particle specific values have also been proposed [79]. Finally, the source of species i is found from

$$\dot{W}_i = \frac{1}{\delta V} \sum_{j=1}^{N_p} \left(\dot{w}_{i,j} + Y_i \frac{dm_{p,j}}{dt} \right) \tag{53}$$

where $\dot{w}_{i,j}$ is the production rate of gas phase species i due to heterogeneous reactions on particle j.

A point particle will always be associated with one single fluid grid cell. If the source of a given quantity from the particle is large compared to the rate by which the quantity is transported away from the grid cell by advection and/or diffusion, there will be a strong accumulation of this quantity in the grid cell. Too strong accumulations will yield numerical instabilities that eventually may result in the code crashing. The natural reflex of researchers working with numerical flow simulations is to increase resolution when such strong spikes in any quantity give numerical issues. This will, however, only make things worse, since transferring the entire source term to an even smaller grid cell will yield an even stronger relative accumulation. The solution to this problem is therefore to distribute the sources over several neighboring grid cells. A common approach is to use a Gaussian profile as the distribution function, such that the further from the particle a cell is, the less of its source it will get. This is a very straightforward approach that is easy to implement. The width of the Gaussian profile cannot be determined on physical grounds, though. So, it is typically made wide enough to get rid of the sharpest gradients. Another problem with this approach is that for a three-dimensional solver, the number of receiving grid points increases very quickly when the width of the Gaussian distribution function increases. A width of just a few grid points will quickly start to slow down the code due to the large number of cells that must be called for every particle. An alternative to this approach, which is more physically sound and also faster already for relatively small widths, is to add a diffusing step to the source before it is added to the evolution equation. This method was found by Kruger *et al.* [69] to yield very good results, both regarding accuracy and calculation efficiency.

In the previous paragraph, we discussed the issue of strong particle source terms in relatively small grid cells. In the other extreme, when the grid cells are much larger than the particles, the source terms from the particle will be distributed homogeneously over a very large volume (the volume of the grid cell). This resembles an artificially large diffusion coefficients, which may result in failed gas-phase ignition. One possible solution to this can be to use the double-film model, where the flame is a part of the film model (see Section 3.3.2 for a discussion of the double film model).

3. Physio-chemical modelling

3.1. Porosity and internal surface area

All chars are porous, which means that a certain fraction of their volume is made up of pores, while the rest is solid material. The porosity is defined as

$$\Theta = \frac{V_{pore}}{V_p}, \tag{54}$$

where V_{pore} is the total volume of all the pores within the reference volume V_p. Here, and in the following, we make the following assumptions [80]:

1 Pores are the volumes between the ill-fitted building blocks that make up the solid structure.
2 The pore structure of a char particle is homogeneous throughout.
3 The pore structure is continuous and interconnecting
4 Any surface in a char particle (either the external surface or any imaginary one drawn in the interior of the particle) consists of a fraction Θ of pore mouths and a fraction $(1 - \Theta)$ of solid material.
5 The pores are cylindrical with a mean radius r_{pore} and a mean length L_{pore}

The above assumptions mean that the relationship between the pore parameters and the porosity is given by

$$n_{pore} L_{pore} \pi r_{pore}^2 = \Theta \tag{55}$$

where n_{pore} is the number density of pores (number of pores per unit volume). Similarly, for the surface area density (S_v in m^2/m^3), it is also true that

$$S_v = S_g \rho_{char} = (1 - \Theta) f_r n_{pore} L_{pore} 2\pi r_{pore} \tag{56}$$

where S_g is the mass specific surface area and the term inside the parentheses on the right-hand-side is due to pores intersecting each other [80], which yields a reduction in surface area, while f_r is a roughness factor that accounts for the fact that the pore surface area is increased by the roughness of the pore walls. By combining the above two equations, one can solve for the mean pore radius

$$r_{pore} = \frac{2\Theta(1 - \Theta) f_r}{S_g \rho_{char}} \tag{57}$$

and the average pore length times the number density of pores

$$L_{pore} n_{pore} = \frac{\left(S_g \rho_{char} \right)^2}{4\pi\Theta(1 - \Theta)^2 f_r^2}. \tag{58}$$

Typical values for Θ and f_r in chars are ½ and 2, respectively, which means that the product $(1 - \Theta) f_r \approx 1$. This explains why it is rather common to define the mean pore radius as

$$r_{pore} = \frac{2\Theta}{S_g \rho_{char}}. \tag{59}$$

Based on the work by Wheeler [80], the number of pore mouths per unit geometric external area is $n_p = \Theta / (\sin(\alpha_{pore}) \pi r_{pore}^2)$, where α_{pore} is the average angle of intersection of pores with the external surface. Wheeler argued that pores could run perpendicular to the external surface, parallel to the external surface or at any angle α_{pore} to it. If α_{pore} has the approximately random value of 45°, then the number of pore mouths per unit external geometric area is $n_p = \Theta / (\sqrt{2}\, \pi r_{pore}^2)$. Since $n_{pore} = n_p A_p / V_p$, when Eq. (57) is used for the mean pore radius, the number of pore mouths per unit particle volume can be expressed as

$$n_{pore} = \frac{\left(S_g \rho_{char}\right)^2}{\sqrt{2}\ 4\pi\ \Theta(1-\Theta)^2\ f_r^2} \left(\frac{A_p}{V_p}\right),$$

where A_p is the geometric external surface area of the particle. Employing this expression for the pore number density in Eq. (58) results in the following expression for the average pore length

$$L_{pore} = \sqrt{2}\ V_p \Big/ A_p.$$

For a number of char particles (*e.g.,* cenospheres), assumption number 2 above is not valid for the particle as a whole. Since the pore structure of the *carbonaceous* part of the particle is homogeneous, the equations above are still expected to be valid for the carbonaceous material forming the shell around the central void.

The surface area of char is typically determined by utilizing the Brunauer–Emmett–Teller (BET) theory, where the physical adsorption of a given molecular species on the char surface is measured. Several different species, such as CO_2, N_2 or O_2, can be used for the experimental measurements. The result does, however, depend on which species is used. For a typical coal char, the measured surface area is smaller (20-100 m^2/g) when N_2 is used as the adsorbed gas compared to when CO_2 is used (200-500 m^2/g). This means that CO_2, despite the fact that it is a larger molecule, accesses smaller pores than N_2 does. This is commonly explained by the capillary effect of CO_2, which allows it to penetrate smaller pores than N_2. Hence, measurements with CO_2 include the surface area of all pores down to micropores while measurements with N_2 only include pores down to mesopores. For oxidation reactions, the relevant adsorbing gas is O_2, but due to its high reactivity with the solid material it is not convenient to use for BET measurements. Any heterogeneous reaction mechanism is developed based on the given surface area measurements, which means that if CO_2 is used to obtain the surface area of the char, the calculated reactivities will be lower than if N_2 is used. When calculating char reactivity with a given intrinsic heterogeneous mechanism, it is therefore crucial that the surface area of the char is measured with the same absorbing gas as was used to obtain the heterogeneous mechanism.

In theory, a surface-area based reaction mechanism includes both the internal *and* the external surface area when calculating the reaction rates. In reality, since the internal surface area is many orders of magnitude larger than the external surface area, the external surface area can be neglected. It is therefore important to distinguish between an apparent chemical mechanism, based on the external surface area, and internal-surface-area based mechanisms, based on the internal surface area.

3.1.1. Porosity evolution

The volume of the ash-containing porous char particle is composed of the volume occupied by the solid, carbonaceous material ($V_{true,char}$), the volume occupied by the ash (V_{ash}) and the volume oocupied by the pores in the char ($V_{char\ \ pores}$): $V_{obj} = V_{true,char} + V_{ash} + V_{char\ \ pores}$. The volume occupied by the solid carbonaceous material can be expressed in terms of the true density of the char ($\rho_{true,char} = m_{char}/V_{true,char}$) and the volume occupied by the ash can be expressed in terms of the apparent density of the ash ($\rho_{ash} = m_{ash}/V_{ash}$). When the expression for the total volume is divided by V_{obj}, the following equation is derived:

$$1 = \frac{m_{char}/\rho_{true,char}}{V_{obj}} + \frac{m_{ash}/\rho_{ash}}{V_{obj}} + \frac{V_{char\ pores}}{V_{obj}}. \tag{60}$$

The apparent density of the ash-containing porous char particle is $\rho_{char} = m_{char}/V_{obj}$. Employing this expression in the first term of the right-hand-side of Eq. (60) and using it to eliminate V_{obj} in the second term results in

$$1 = \frac{\rho_{char}}{\rho_{true,char}} + \frac{m_{ash}\rho_{char}}{m_{char}\rho_{ash}} + \Theta$$

where the final term in Eq. (60) is identified as the porosity of the porous char, *i.e.*, $\Theta = \frac{V_{char\ pores}}{V_{obj}}$. Rearranging the equation, solving for porosity yields

$$\Theta = 1 - \frac{\rho_{char}}{\rho_{true,char}} - \frac{\rho_{char} m_{ash}}{\rho_{ash} m_{char}}.$$

Denoting the mass fraction of ash in the particle by Y_{ash}, then $m_{ash} = Y_{ash} m_{solid}$ and $m_{char} = (1 - Y_{ash}) m_{solid}$ and hence, the above expression for char porosity can be expressed as

$$\Theta = 1 - \frac{\rho_{char}}{\rho_{true,char}} - \frac{\rho_{char} Y_{ash}}{\rho_{ash}(1 - Y_{ash})}. \tag{61}$$

During char conversion, the apparent density of the char follows the mode of conversion relations (see Section 3.3.3) and since the ash inclusions only lose mass from their outer surfaces, their apparent densities are constant. Thus, this equation permits the char porosity at any time to be determined from the instantaneous values of the apparent density of the char and the ash mass fraction. For an ash-free char particle, Eq. (61) reduces to the expected relation.

In the Zone II conversion regime in which both particle apparent density and size decrease during mass loss (see Sections 1 and 3.3.3 for more information on the different zones of conversion), the porosity will vary throughout the char, with the highest porosity closer to the external surface. This is not a problem for the resolved particle approach, where this variation is indeed resolved by the computational mesh, such that the porosity within any computational cell can be considered as uniform. For the point particle approach, however, this spatial variation is not resolved, which means that the reported porosity is averaged over the entire particle. This shortcoming of the point particle approach means that the diffusion of species through the outer volumes of the particle is underestimated, since the local porosity in these volumes is higher than the mean value that is actually used to calculate the pore diffusivity.

3.1.2. Evolution of internal surface area

The internal surface area of a char will change as char conversion proceeds. Two common models describing this change are the grain model [81,82] and the random pore model [81,83-85]. In the grain model, which presumes the porous carbon particle to be a collection of grains of various shapes and sizes, the volume specific internal surface area (in m^2/m^3) is given by

$$S_v = S_{v,0}(1 - x_c)^{l_{\text{shape}}}, \tag{62}$$

where l_{shape} is the grain shape factor, a factor that depends on the geometry of the grains, while the char conversion is defined as

$$x_c = 1 - \frac{m_{char}}{m_{char,0}} \tag{63}$$

where $m_{char,0}$ is the initial mass of the char. Theoretically, for flat-plate grains, $l_{\text{shape}} = 0$, for cylindrical grains, $l_{\text{shape}} = \frac{1}{2}$ and for spherical grains, $l_{\text{shape}} = \frac{2}{3}$. In practice, the value used for l_{shape} is determined by fitting

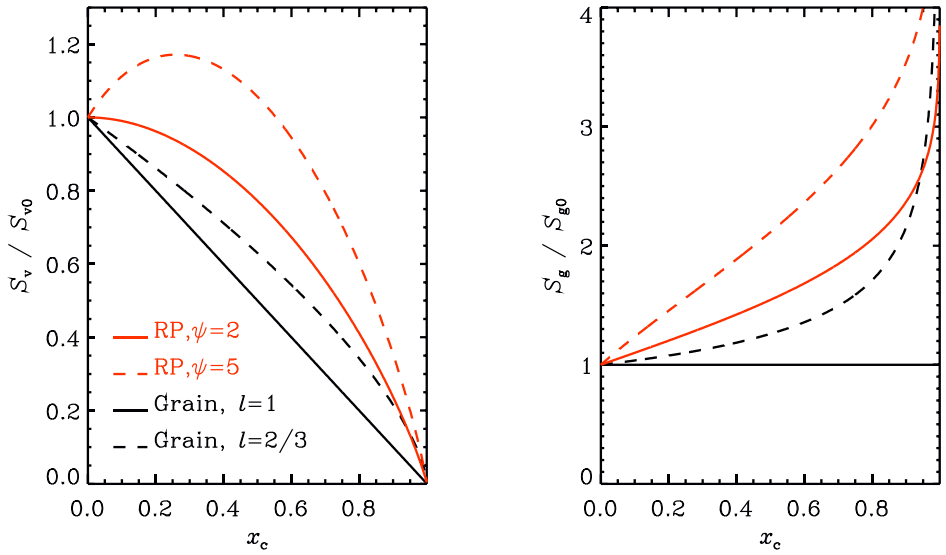

Fig. 4. Volume specific (left) and mass specific (right) surface area as a function of conversion for the random pore model (RP) and the grain model (Grain) with different parameters.

carbon conversion data. For $l_{\text{shape}} = 1$, the model corresponds to the homogeneous reaction model [86] in which particle shape and pore structure remain uniform and constant during carbon conversion. Sometimes, this model is referred to as the volume reaction model (VRM) or volumetric model. For $l_{\text{shape}} = \frac{2}{3}$, spherical grains are assumed to continuously shrink in size during carbon conversion, causing the particle diameter to shrink while apparent density remains constant.

This model is sometimes referred to as the shrinking core model (SCM). The grain model predicts a decrease in the total surface area per unit particle volume with increasing mass loss over the full range of carbon conversion (see black lines in Fig. 4). This yields a carbon conversion rate that decreases with mass loss over the lifetime of the particle, a characteristic not observed experimentally. The early work of Dutta *et al.* [87,88] clearly demonstrate that in the initial stages of carbon conversion ($x_c \lesssim 0.4 x_c <\sim 0.4$), reaction rate profiles exhibit a maximum. Despite this, some researchers (*e.g.* [89]) have found that the grain model adequately describes their char combustion data up to 50% char conversion.

For the random pore model (RPM), which is based on overlapping pore evolution, the volume specific internal surface area is

$$S_v = S_{v,0}(1 - x_c)\sqrt{1 - \psi \ln(1 - x_c)} \tag{64}$$

where ψ is a structural parameter, having values ranging from 0 to about 25. Bhatia and Perlmutter [81] give an expression for the structural parameter, ψ, but in practice it is typically determined by fitting carbon conversion data. Typical values are in the range 5 to 20, the larger the value, the less the porosity of the solid particle material. For $\psi > 2$, the random pore model predicts an initial increase in the surface area per unit volume. The conversion corresponding to the peak of surface area, $x_{c,peak}$, varies with the structural parameter as

$$x_{c,peak} = 1 - \exp\left(\frac{1}{\psi} - \frac{1}{2}\right). \tag{65}$$

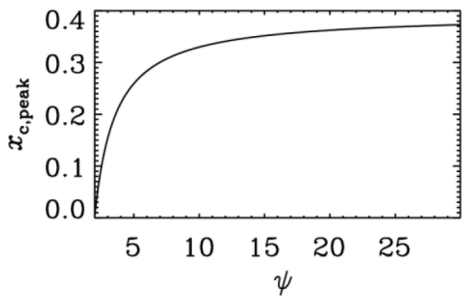

Fig. 5. Conversion where the volume specific surface area has its maximum as a function of the structural parameter.

This is shown graphically in Fig. 5 where it is noted that the initial increase in surface area density continues until larger conversion for larger values of ψ. It can also be observed, as predicted by Dutta *et al.* [87,88], that the surface area continues to increase for conversions as large as 0.4 if ψ is large enough. The increase in surface area with conversion is reflective of the opening of initially closed pores, exposing new pore surfaces for reaction while the decrease in surface area throughout the remainder of carbon conversion is due to pore growth and coalescence. The grain and random pore models yield similar x_c-t profiles when $m = 1$ and $\psi = 0$, as demonstrated, for example, by Bhatia and Perlmutter [81] and by Raghunathan and Yang [90]. In Fig. 4, both the volume specific and the mass specific surface areas are shown as a function of conversion for the random pore and the grain models. From the left-hand panel, we can see that the volume specific surface area is monotonically decreasing with conversion for all cases except for the random pore models with larger values of ψ. For the RP model with $\psi = 5$, the volume specific surface area is increasing until conversion is 0.26, after which it starts to decrease. From the right-hand panel of Fig. 4, it can be observed that the mass specific surface area is increasing with conversion for all models except for the grain model with $m = 1$, which has a constant specific surface area.

Although the grain and random pore models were developed for steam and CO_2 gasification, both models have been applied to combustion. In recent years, most researchers have applied the random pore model to describe conversion rates for both combusting and gasifying coal and biomass char particles (*e.g.*, [84,91-98]). Fermoso *et al.*, [99] demonstrated that the random pore model better described steam gasification data compared to the grain model for the chars of two coals, two biomass materials and a petroleum coke. Lu and Do [100] found that both models adequately described conversion rate data for chars having high ash-contents. Some biomass chars and alkali catalyzed carbons exhibit a maximum in reactivity in the high conversion range, a feature not predicted by the random pore or grain models. Duman *et al.* [101] modified the random pore model to include an additional conversion term to account for such behavior. The random pore model is conceptually more correct than the grain model, since it accounts for the

non-monotonic evolution of the internal particle surface area, a phenomenon observed with most coal and biomass char particles. Consequently, the random pore model is recommended for use to account for the evolution of internal surface area during char conversion in both combustion and gasification environments. It should be emphasized, however, that model selection should be based on the quality of the fits to experimental data.

BET surface area measurements yield the mass specific surface areas of a given particle (S_g, in m^2/kg), which are related to the volume specific surface area through the apparent density of the particle: $S_v = \rho_{char} S_g$. Hence, it follows that

$$\frac{S_g}{S_{g0}} = \frac{S_v}{S_{v0}} \frac{\rho_{char,0}}{\rho_{char}} = \sqrt{1 - \psi \ln(1 - x_c)} \,. \tag{66}$$

Note that when applying the random pore model to a combusting or gasifying carbon particle, the mass specific surface area of the particle increases throughout carbon conversion (see the right-hand panel of Fig. 4).

3.1.3. Adsorbed species concentrations

For adsorption-desorption reaction models, one must know the surface concentration, or site fraction, of any adsorbed species participating as a reactant in the reactions. The number of moles of species i that is adsorbed on a surface of total area S_t is given by

$$N_i = C_{s,i} \cdot S_t \tag{67}$$

where $C_{s,i}$ is the surface concentration (in mol/m^2) of adsorbed species i. The above equation can now be differentiated with respect to time to yield the evolution equation for the surface concentration of adsorbed species i as

$$\frac{dC_{s,i}}{dt} = \frac{1}{S_t}\frac{dN_i}{dt} - \frac{C_{s,i}}{S_t}\frac{dS_t}{dt} = \widehat{R}_i - \frac{C_{s,i}}{S_t}\frac{dS_t}{dt}. \tag{68}$$

The surface concentration of free carbon sites is given by $C_{s,free} = \xi_n - \sum_{i \neq free} C_{s,i}$ where ξ_n is the total surface concentration of all carbon sites.

Instead of the surface concentration, it is often convenient to define the adsorbed species site fraction as

$$\Theta_i = \frac{C_{s,i}}{\xi_n}. \tag{69}$$

For a total of N_{ads} adsorbed species, where a free carbon site is considered as an adsorbed species, it is then clear that

$$\sum_{i=1}^{N_{ads}} \Theta_i = 1. \tag{70}$$

Eq. (68) can now be re-written as

$$\frac{d\Theta_i}{dt} = \frac{\widehat{R}_i}{\xi_n} - \frac{\Theta_i}{S_t}\frac{dS_t}{dt}.$$

The total surface concentration of all carbon sites is expected to be of similar magnitude for all chars. It is calculated from the total surface site density (S_d, total number of carbon sites per unit area) of the carbonaceous material and Avogadro's number (N_{AV}): $\xi_n = S_d/N_{AV}$. Its value is of the order 10^{-7} kmol/m^2.

Measurements of the surface site density (the total number of carbon sites per unit area) of a char are scarce; few values can be found in the literature. Coal and biomass chars are amorphous carbons and as such, there is no well-defined surface within the solid material on which to base density functional theory estimations of the surface site density. Consequently, there are few DFT estimates of the surface site density of chars. Tsuge *et al.* [102] report the surface site density of an amorphous diamond-like carbon surface to be in the range $1.5 - 3 \times 10^{19}$ sites/m^2, a value close to that reported for diamond ($\sim 2 \times 10^{19}$ sites/m^2 [103]). Amorphous carbons have less development of structural anisotropy with more disordered and defective structures than crystalline carbons like diamond – their site densities should be higher than that for diamond. HRTEM fringe image analyses of coal chars indicate that their graphene patterns are shorter and more isotropic than they are in graphite and that the extent of crystalline order and the size and linearity of lamellar features are less [104,105]. Such effects increase the number of carbon atoms per unit area – the surface site density of coal and biomass chars should be higher than that of graphite. Reports of measurements of the surface site density of graphite are also difficult to find in the literature. A value of 3.82×10^{19} sites/m^2 was calculated via DFT employing properties of the graphite (0001) surface [106].

By considering the area occupied by a subset of the fused hexagonal rings on the graphene layers in graphite, a site density of $\sim 4 \times 10^{19}$ sites/m^2 can be estimated for its surface site density. There are no pristine graphene surfaces in coal and biomass chars. Any surfaces that are present are not as smooth nor as uniform, reflective of more disorder in the amorphous carbon structure. In addition, the graphene patterns on the surfaces are not all oriented in the same direction and the fused rings are not all the same. Smaller rings tend to increase the number of atoms per unit area. Consequently, the surface site density of a graphene layer should represent the lower limit for the surface site density of an amorphous solid such as a coal or biomass char. The relatively low value determined by Tsuge *et al.* [102] is a consequence of the solid used in their study having a diamond-like structure, although amorphous. Coal and biomass chars should have surface site densities higher than 4×10^{19} sites per m^2.

An upper limit for the surface site density of a char can be estimated based on measurements of its mass specific surface area, S_g. For a char sample, the total number of carbon atoms per unit volume is $\rho_{char} N_{AV}/\widehat{M}_C$, where ρ_{char} is the apparent density of the char, N_{AV} is Avogadro's number and $\widehat{M}_C$ is the molar mass of carbon. The number of surface carbon atoms/molecules per unit volume is $\rho_{char} S_g S_d$, where S_d is the surface site density (in #-sites/m^2). The fraction of the total carbon atoms in any char sample that are surface carbon atoms is therefore $S_g S_d \widehat{M}_C / N_{AV}$. Setting this relation to unity and solving for S_d yields its maximum possible value: $S_{d,max} = N_{AV}/\widehat{M}_C S_g$. If this were the value used for the surface site density, all the carbon atoms would be surface carbons, an unreasonable scenario – there would be no bulk carbons to expose when adsorbed species desorb. As an example, for a char having a specific surface area of $S_g = 450$ m^2/g, $S_{d,max} = 1.11 \times 10^{20}$ sites/m^2.

Based on the above discussion, it is expected that for coal and biomass chars, 4×10^{19} sites/m^2 $< S_d < N_{AV}/\widehat{M}_C S_g$, where S_g is the specific surface area of the char. In the work of Mitchell and co-workers (*e.g.*, see [98,107,108]), a value of 6.5×10^{19} sites/m^2 was used for the surface site density of coal and biomass chars.

3.2. Carbon particle reaction models

The chemical kinetic mechanisms developed to date to predict the mass loss rate and off-gas composition of a carbon particle of specified diameter exposed to an environment of specified temperature, pressure and gas composition can be divided into two groups: apparent particle reaction rate models and intrinsic particle reaction rate models. With apparent reaction rate models (sometimes referred to as global, overall or macroscopic particle reaction rate models), carbon conversion rates are expressed in terms of the overall effects of mass transport and the chemical reactivity of the particle material. Only the size and apparent density of the particle are used when describing the particle's physical state. Processes that govern mass transport and heterogeneous chemical reaction inside the particle are not considered individually. With intrinsic reaction rate models (sometimes referred to as microscopic particle reaction rate models), carbon conversion rates are expressed as separate functions of mass transport effects and the intrinsic reactivity of

the carbonaceous particle material, which depends solely on chemical reaction effects. Such carbon particle material properties as total surface area, porosity, size, and apparent density are used when describing the physical state of the particle and characterizing the effects of mass transport through particle pores.

With apparent reaction rate models, power-law kinetics are usually used to describe carbon reactivity whereas with intrinsic reaction rate models, both power-law kinetics and kinetics based on heterogeneous reaction mechanisms are used to describe carbon reactivity. Power-law kinetics have no fundamental basis but as has been shown by Hurt and Haynes [109], power-law kinetics can yield carbon conversion rates that mimic the conversion rates obtained with detailed adsorption/desorption reaction mechanisms when a broad distribution function is used to describe the distribution of activation energies for adsorption and/or desorption reactions. Surface heterogeneity is given as a reason for needing broad distribution functions for adsorption and desorption processes. Employing an adsorption/desorption turnover model for carbon oxidation developed by Haynes [110], Hurt and Haynes [109] found that increased surface coverage of adsorbed species leads to decreased adsorption rates, and that decreased surface coverage of adsorbed species leads to decreased desorption rates. Consequently, during char conversion, the steady-state coverage of adsorbed species, which occurs when adsorption and desorption rates are equal, never reaches a limiting value of adsorption control or desorption control but instead, maintains intermediate values over wide ranges of oxygen partial pressure. Hurt and Haynes [109] noted that char reaction occurs in a stable regime of mixed adsorption/desorption control that can be approximated using n^{th}-order kinetics.

3.2.1. Apparent particle reaction rate models

Several researchers [*e.g.*, [111-120]] define an overall reaction rate R_{ov} (in kg/m^2/s), the rate of removal of carbon per unit external surface area of the particle (A_p), as follows:

$$R_{ov} \equiv -\frac{1}{A_p}\frac{dm}{dt} = -\left(\frac{1}{\pi d_p^2}\right)\frac{dm}{dt}\ . \tag{71}$$

Once these overall reaction rates are determined for particles burning under selected conditions of gas temperature, pressure and composition, they are correlated with temperature and reactive gas partial pressure, assuming power-law kinetics:

$$R_{ov} = k_{ov} P_{g,s}^{n}. \tag{72}$$

Here, k_{ov} is the overall reaction rate coefficient (in kg/m^2/s/atm^n), $P_{g,s}$ is the partial pressure of the reactive gas at the outer surface of the carbon particle, and n is the apparent reaction order with respect to the reactive gas partial pressure. The overall reaction rate coefficient is expressed on an external surface area basis. Arrhenius parameters that describe the rate coefficient are found by fitting experimental data: $k_{ov} = A_{ov}\ \exp(-E_a/\widehat{R}_u T_P)$.

Sometimes Eq. (71) is rearranged to yield the following expression for the mass loss rate in terms of the overall reaction rate coefficient and its Arrhenius parameters:

$$-\frac{dm}{dt} = A_p\ R_{ov} = A_p\ k_{ov}\ P_{g,s}^{n} = A_p\ A_{ov}\ \exp(-E_a/\widehat{R}_u T_P)\ P_{g,s}^{n}.$$

In this approach, the product $A_p\ A_{ov}$ is considered as a single parameter when fitting experimental data to determine kinetic parameters, and the mass loss rate is written as

$$-\frac{dm}{dt} = A_{ov}^{'}\ \exp(-E_a/\widehat{R}_u T_P)\ P_{g,s}^{n}$$

where $A_{ov}^{'} = A_p\ A_{ov}$. Several researchers have taken this approach, see for example, references [121-123]. Note that overall particle reaction rates are classified as apparent reaction rates, being void of any description of the effects of heterogeneous reaction inside the particle.

Some researchers [*e.g.*, [105,124-128]] define an apparent reaction rate, R_a (in s^{-1}), expressed by either of the following relations:

$$R_a \equiv -\left(\frac{1}{m_0}\right)\frac{dm}{dt} \qquad \text{or} \qquad R_a^{'} \equiv -\left(\frac{1}{m}\right)\frac{dm}{dt} \tag{73}$$

In the first of these relations, m_0 is the initial mass of the carbon particle and R_a represents the rate of change in the fraction of the initial mass remaining. In the second relation, $R_a^{'}$ represents the rate of change in the fraction of the instantaneous mass remaining. In both cases, the apparent reaction rate is correlated with temperature and reactive gas partial pressure as shown in Eq. (74):

$$\begin{aligned} R_a &= k_a \cdot P_{g,s}^{n'} = A_a\ \exp(-E_a/\widehat{R}_u T_p)\cdot P_{g,s}^{n'} \\ \text{and}\quad R_a^{'} &= k_a^{'}\cdot P_{g,s}^{n'} = A_a^{'}\ \exp(-E_a^{'}/\widehat{R}_u T_p)\cdot P_{g,s}^{n'} \end{aligned} \tag{74}$$

where k_a and $k_a^{'}$ are the temperature dependent apparent reaction rate coefficients (which are expressed in Arrhenius form) and n' is the apparent reaction order with respect to the reactive gas partial pressure. Like the overall reaction rate coefficients, once the apparent reaction rate coefficients are determined for particles burning under selected conditions of gas temperature, pressure and composition, they are correlated with temperature and reactive gas partial pressure to determine the apparent pre-exponential factor, activation energy and reaction order. The kinetic parameters for the apparent reaction rate coefficients are expected to vary with carbon type. Also, parameters determined for pulverized fuel sizes may differ from parameters determined for millimeter size particles, in the same way as parameters obtained under zone I conditions may differ from those obtained under zone II or III conditions.

The rate equations shown in Eqs. (72) and (74) are examples of power-law kinetics. Owing to an undefined reaction mechanism, the reaction order is used to describe the dependence of the rate on the reactant gas concentration (or partial pressure).

Note that carbon particle temperatures are needed in order to evaluate apparent reaction rate coefficients employing apparent activation energies and pre-exponential factors. These are calculated from carbon particle energy balances that require the determination of energy release rates, which depend on the ΔH_R of the global carbon consumption reactions. The fraction of the carbon converted to CO depends upon temperature, increasing with increasing temperature. In many studies, the molar CO/CO_2 heterogeneous product ratio is expressed in Arrhenius form: $N_{CO}/N_{CO_2} = A_{CO}\exp(-E_{CO}/\widehat{R}_u T)$, (*e.g.*, see [115,129-131]). The investigations of Tognotti *et al.* [132] demonstrate that this ratio has a slight dependence on the oxygen concentration, decreasing with increasing oxygen concentration (or partial pressure) at fixed particle temperature. To capture this effect, some researchers include an oxygen dependence on the molar CO/CO_2 ratio, multiplying the Arrhenius expression by $P_{O_2}^{n''}$, where n'' is the reaction order. The results of investigations by Day *et al.* [133] suggest that the molar CO/CO_2 ratio also depends on the water partial pressure (or concentration), slightly decreasing with increasing P_{H_2O}. A discussion of Arrhenius fits to experimentally observed product distributions during carbon oxidation is given below, in Section 3.2.2.2.1.

The predictions for R_{ov}, R_a and $R_a^{'}$ are most accurate in conditions in which the reaction rate coefficients were determined. If determined under Zone I burning conditions (when burning rates are chemically-limited), inaccurate predictions will result if applied to particles burning under Zone II conditions (when burning rates are limited by the combined effects of mass diffusion and chemical reaction). The reverse is also true. This is a shortcoming of using apparent or overall particle reaction rate models. If carbon particles are burning under Zone III conditions, when burning rates are limited by the diffusion of reactants to the outer surfaces of particles, reliable parameters that describe the reaction rate coefficients cannot be obtained from analysis of the data.

The contributions of chemical reaction effects to particle reactivities are insignificant when conversion rates are diffusion limited.

When power-law kinetic expressions are employed, predicted conversion rates are most inaccurate when predictions are for environments having pressures that differ greatly from the pressures used in the experiments to obtain data from which the kinetic parameters were derived. If kinetic parameters were adjusted to obtain predictions that agree with data obtained in experiments performed at 1 atm, the model is not likely to accurately predict conversion rates in environments at 20 atm. This could be a consequence of chemical reaction rates increasing with increasing pressure and diffusional transport rates decreasing with increasing pressure, these opposing effects not being properly captured employing power-law kinetics.

Several investigators have used power-law kinetics to correlate their mass loss data obtained with coal and biomass chars exposed to oxygen. Data analyses yielded reaction orders in the range 0 to 1, with orders greater than 0.6 associated mostly with combustion tests performed at temperatures less than 1000 K, when particles were burning under Zone I conditions. For studies performed at temperatures higher than 1000 K when particles burn under Zone II conditions in oxygen-containing environments, apparent reaction orders ranged from fractional values (*e.g.,* [114,115,118,134-136]) to 1 (*e.g.,* [111,121,126,137-140]), with most being fractional orders. Some of the fractional orders are below a value of 0.5, however based on the work of Thiele [141], apparent reaction orders should be greater than 0.5. The work of Murphy and Shaddix [142] show that ash dilution effects could explain such low fractional orders.

Some of the more recent apparent reaction rate models have Arrhenius parameters that describe the apparent reaction rate coefficients that depend on the composition of the parent coal [143] and some have parameters that depend on the extent of thermal annealing as well as the char precursor [114,128,138]. Apparent reaction rate models employing power-law kinetic expressions have also been applied to the carbon-carbon dioxide reaction (see [138,144-148]) as well as the carbon-steam gasification reaction (see [149,150]).

Recently, Ren *et al.* [151] presented an apparent kinetic model (AKM) that yields predictions that better agree with experimentally observed conversion rates of petroleum coke particles in high-temperature gasification environments than most apparent kinetic reaction rate models. The model uses a Boltzmann-based function to describe the gasification process that leads to the following expression for the carbon conversion (x_c) rate:

$$\frac{dx_c}{dt} = k_{AKM} x_c (1 - x_c). \tag{75}$$

The rate coefficient k_{AKM} is expressed in Arrhenius form. To facilitate comparison with the overall reaction rate and apparent reaction rate as given by Eqs. (71) and (73) above, Eq. (75) is equivalent to the following expression for the mass loss rate:

$$-\frac{1}{m}\frac{dm}{dt} = k_{AKM}(1 - m/m_0) = k_{AKM} x_c. \tag{76}$$

This form of the AKM model reveals that it predicts an instantaneous fractional mass loss rate that varies with conversion. The petroleum coke particles employed in experiments by Ren *et al.* [151] during development of the model exhibited smooth outer surfaces with few pores throughout conversion. Reaction occurs primarily at the periphery of the particles. Since the gasification behaviors of such petroleum coke particles differs from that of coal and biomass char particles, the applicability of this model to coal and biomass char gasification is unknown.

The Avrami-Erofeev [152] apparent reaction rate model has been employed to describe biomass char conversion rates that exhibit sigmoidal gasification behaviors, accelerating conversion rates during the initial stages of gasification and decelerating conversion rates during the final stages. For such chars, the conversion rate attains its maximum value at intermediate values of the extent of conversion. None of the apparent reaction rate models discussed above is capable of predicting such behavior. The Avrami-Erofeev reaction model for char conversion is expressed as

$$\frac{dx_c}{dt} = k_{AV\cdot ER} \cdot n''' \cdot (1 - x_c)[-\ln(1 - x_c)]^{(n''' - 1)/n'''} \tag{77}$$

where $k_{AV\cdot ER}$ is the apparent reaction rate constant (expressed in Arrhenius form) and n''' is referred to as a reaction order, dependent on the reaction mechanism. The classical Avrami-Erofeev equations [153] are usually applied to the analysis of isothermal reactions in solids with nuclei formation, growth and consumption, in particular, to the analysis of crystal aggregate growth. In such applications, the reaction order depends on the reaction mechanism: $n''' = 2$ for one-dimensional growth of nuclei, 3 for two-dimensional growth and 4 for three-dimensional growth. Bhatia and Perlmutter [81] indicate that the Avrami theory provides the underlying principle governing pore growth and pore overlap in their random pore model, which constitutes the basis of the model developed to describe the dependence of char internal surface area on char conversion (see Section 3.1.2). In Eq. (77), for $n''' \leq 1.0$, the conversion rate decreases from the onset of char conversion, however, for reaction orders greater than unity, the conversion rate initially increases with conversion before reaching a maximum and decreasing throughout the remainder of char conversion. A value of 2 for n''' has been employed to fit steam gasification conversion data [154]. With this value for the reaction order, the rate reaches a maximum at about 40% char conversion. Relatively few researchers have used the Avrami-Erofeev apparent reaction rate model in the analysis of their char conversion data. However, we recommend its use when data indicate a conversion rate that exhibits sigmoidal behavior.

Many studies concerned with modeling carbon particle behavior use apparent, overall particle conversion rates that employ power-law kinetics despite the fact that such models are limited in their applicability, being most accurate only in conditions of temperature, pressure and composition similar to the ones used in obtaining the data needed to evaluate model parameters. Carbon particle models that use intrinsic reactivity-based conversion rates are deemed to be more capable of accurately predicting carbon particle mass loss rates when particles are exposed to a wide range of conditions.

3.2.2. *Intrinsic reaction rate models*

Unlike apparent reaction rate models, which account both for chemical kinetics and internal diffusion, intrinsic reaction rate models do not account for diffusion. When developing intrinsic models, it is assumed that the reactive gas concentration to which the char is exposed is uniform over all char surfaces. Consequently, Zone I conversion is implicitly assumed throughout this subsection. For the resolved particle approach, this assumption is always satisfied for a given grid cell. For the point particle approach, however, the concept of the effectiveness factor, as discussed in Section 3.3.1, must be utilized in order to account for internal diffusion limitations, *i.e.*; Zone II or III conversion.

3.2.2.1. Intrinsic chemical reactivity. Many researchers define the intrinsic chemical reactivity of a carbon particle (R_c, in kg/m^2/s) as follows:

$$\frac{1}{m_c}\frac{dm_c}{dt} = -S_g R_c, \tag{78}$$

where S_g is the total internal, mass specific, surface area of the particle. (see Section 3.1.2 for more details on internal surface area.) This expression can be rewritten in terms of the conversion rate:

$$\frac{1}{(1-x_c)}\frac{dx_c}{dt} = S_g R_c. \tag{79}$$

Multiplying by $(1 - x_c)$ yields the following expression for the carbon conversion rate:

$$\frac{dx_c}{dt} = (1-x_c)\ S_g R_c = (1-x_c)\left[S_{g0}\sqrt{1-\psi\ \ln(1-x_c)}\right]\ R_c. \tag{80}$$

R_c is independent of any mass transport effects and depends solely on effects associated with the rates of the heterogeneous chemical reactions that occur at active sites on the carbonaceous, pore surfaces.

3.2.2.2. Power-law based intrinsic chemical reactivity models. Many researchers have expressed the intrinsic chemical reactivity of the carbonaceous particle material in oxidizing and gasifying environments in power-law form [56,89,96,97,147,148,155-171],

$$R_c = k_{int} P_{g,s}^m = A_{int}\ \exp\left(-E_{int}\ /\ \widehat{R}_u T_p\right)\ P_{g,s}^m, \tag{81}$$

where k_{int} is the intrinsic chemical reaction rate coefficient (in kg/m^2/s/atm^m), $P_{g,s}$ is the partial pressure of the reactive gas in contact with the carbon surface and m is the true (or intrinsic) reaction order with respect to the reactive gas partial pressure. The intrinsic chemical reaction rate coefficient is expressed on a unit total surface area basis. The true reaction order reflects the actual dependence of the intrinsic reaction rate on the reactive gas concentration. With coal and biomass chars, the true reaction order falls in the range zero to one.

To understand fractional reaction orders during char conversion, consider the following three-step adsorption/desorption reaction mechanism for carbon oxidation:

r1: $C_f + O_2 \rightarrow C(O) + O$
r2: $C_f + C(O) + O_2 \rightarrow CO_2 + C(O)$
r3: $C_b + C(O) \rightarrow CO + C_f$.

This three-step adsorption/desorption reaction mechanism for carbon oxidation is similar to the one considered by Hurt and Calo [172] but here, the products of the adsorption reaction differs and free and bulk carbons are shown in the reaction steps. Assuming a steady state for the adsorbed oxygen concentration during the course of reaction leads to the following expression for the intrinsic reactivity of carbon to oxygen in terms of reaction rate coefficients for reactions r1, r2 and r3 and the concentration of oxygen ([O_2]), (see Appendix A):

$$R_c = \widehat{M}_C\left\{\frac{k_1 k_3 \xi_n [O_2]}{(k_1[O_2]+k_3)}\left(1+\frac{k_2\xi_n[O_2]}{(k_1[O_2]+k_3)}\right)\right\}. \tag{82}$$

Analysis of this expression reveals how the rate limiting reactions and overall reaction order vary as temperature is increased. For the three reactions of concern, it is expected for the adsorption reaction to have the lowest activation energy and the desorption reaction to have the highest, *i.e.*, $E_1 < E_2 < E_3$. As a consequence, the rate of the adsorption reaction increases the slowest and the desorption reaction the fastest, as temperature is increased. At low temperatures, the rate of the adsorption reaction is the fastest of the three reactions and the rate of the desorption reaction is the slowest at the lowest temperatures. In the limit $k_1[O_2] > > k_3$, analysis of Eq. (82) reveals that $R_c \approx \widehat{M}_C k_3 \xi_n (k_1 + k_2\xi_n)\ / k_1$ – the reactivity is independent of the oxygen concentration ($m = 0$). This is a regime in which adsorption, complex-enhanced adsorption and desorption all influence char reactivity, although the overall reaction rate is limited by the rate of the desorption reaction, the slowest of the three. As temperature is increased to the low-to-moderate range, the rate of the desorption reaction becomes faster than that of the complex-enhanced adsorption reaction. In the limits $k_1[O_2] \gg k_3$ and $k_2\xi_n \ll k_1$, it can be shown that $R_c \approx \widehat{M}_C k_3 \xi_n$. The reactivity is also independent of the oxygen concentration ($m = 0$) in this regime and the desorption reaction controls char reactivity, although not the slowest of the three reactions. Whenever $k_1[O_2] \gg k_3$, char reactivity will exhibit near zeroth-order behavior and the desorption reaction will limit the overall reaction rate. Such behavior is expected at low to moderate temperatures.

As temperature is increased to the moderate-to-high range, the rate of the desorption reaction exceeds that of the adsorption reaction. It can be shown that in the limit $k_1[O_2] \ll k_3$, Eq. (82) can be approximated as follows: $R_c \approx \widehat{M}_C k_1 \xi_n [O_2](k_2\xi_n[O_2]+k_3)/k_3$. This expression reveals that reactivity is influenced by both adsorption and desorption in this regime. At moderate temperatures, when the rate of the complex-enhanced adsorption reaction is still faster than the adsorption reaction ($k_1[O_2] \ll k_3$ and $k_2\xi_n \ll k_1$), it can be shown that Eq. (81) reduces to $R_c \approx \widehat{M}_C k_1 \xi_n [O_2]$. At sufficiently high temperature, a point is reached when the desorption reaction proceeds at the fastest rate of all the three reactions. For the limiting case $k_1[O_2] \ll k_3$ and $k_2\xi_n[O_2] \ll k_3$, Eq. (82) also reduces to $R_c \approx \widehat{M}_C k_1 \xi_n [O_2]$. For this limit, char reactivity exhibits first-order behavior and adsorption controls the overall conversion rate. Thus, owing to the different temperature dependences of the rates of reactions r1, r2 and r3, the rate controlling step during carbon oxidation will vary as temperature varies. At low-to-moderate temperatures, zeroth order behavior will be exhibited and at moderate-to-high temperatures, first-order behavior will be exhibited. Since these limits are not actually reached, the reaction order would exhibit fractional values as temperature varies from low to high. Temperatures considered to be low, moderate and high depend on the char. A highly reactive char will have lower moderate and high values than a slowly reacting char.

It should be noted that different heterogeneous reaction mechanisms will yield different regimes for rate controlling reactions. Based on the three-step adsorption/desorption mechanism analyzed by Hurt and Calo [172], which differs from the mechanism just discuss by the adsorption reaction and its stoichiometry, the O_2-complex reaction controls at low temperatures, the desorption reaction at moderate temperatures and the adsorption reaction at high temperatures. No matter what the mechanism, the rate controlling steps will vary with temperature and oxygen concentration. If power-law kinetics are used to describe the reactivities predicted by the reaction mechanism, variations in reaction order would be required for accurate characterizations, and the order is likely to be fractional.

As already mentioned, the work of Hurt and Haynes [109] demonstrates that when distributions of activation energies are used to describe the rates of the adsorption and desorption reaction steps, power-law kinetics can adequately describe carbon particle reactivity. It should be emphasized, however, that this only holds when particles are undergoing conversion under steady-state conditions, when the particle temperature is relatively constant. Power-law kinetics can potentially yield inaccurate prediction of mass loss rates when carbon particles experience significant temperature gradients while burning. A power-law model that has a temperature-dependent reaction order would be needed for accurate predictions.

Power-law kinetic expressions have also been used to describe the intrinsic reactivities of carbon to CO_2 and carbon to H_2O. A simple adsorption/desorption Langmuir-Hinshelwood mechanism for the carbon-CO_2 reaction

r4: $C + CO_2 \rightleftarrows C(O) + CO$
r3: $C(O) \rightarrow CO$

yields the following expression for carbon reactivity to CO_2:

$$R_{CO_2,int} = \frac{k_a k_d P_{CO_2}}{k_a P_{CO_2} + k_d} \tag{83}$$

Here, k_a and k_d are the rate coefficients of the adsorption (r4) and desorption (r3) reactions presented above, respectively. When temperatures and pressures are in such ranges that the adsorption process is the rate limiting step ($k_d \gg k_a P_{CO_2}$), $R_{CO_2,int} \sim k_a P_{CO_2}$, and first-order rate behavior is observed. When the desorption process is the rate limiting step ($k_d \ll k_a P_{CO_2}$), $R_{CO_2,int} \sim k_d$, and zeroth-order rate behavior is observed. Since the activation energies of desorption reactions are usually greater than those of adsorption reactions, first-order behavior would be observed at high temperatures and zeroth-order at low temperatures. Fractional reaction order rate behavior is observed at moderate conditions of temperature. Note that at a fixed temperature, as the pressure is increased to the point where $k_a P_{CO_2} \gg k_d$, the observed rate would exhibit zeroth-order behavior. The carbon-steam reacting system behaves similarly, first-order behavior being observed at high temperature when the adsorption reaction limits the reactivity and near zeroth-order behavior at moderate to low temperatures and high pressure when the desorption step controls carbon reactivity. For gasification of an Australian bituminous coal at 0.5 MPa, Kajitani *et al.* [93] determined fractional reaction orders of 0.73 and 0.86 for CO_2 and H_2O, respectively, at 1300°C. At low temperatures, the reaction order for CO_2 gasification was found to be 0.54 at this pressure.

It should be noted that carbon particle temperature is needed in order to evaluate intrinsic reaction rate coefficients. When particle temperature is not specified, it must be calculated using the particle's energy balance, an equation that relates energy release rates via heterogeneous chemical reaction to the rates of energy loss from the particle via convection and radiation. As mentioned above, to properly account for energy release rates due to chemical reaction, the CO/CO_2 product ratio must be accurately described as a function of particle temperature.

3.2.2.2.1. The CO/CO_2 product ratio during char oxidation. Reaction rate models that employ power-law kinetics must be coupled with a submodel that describes the product distribution of the carbon oxidation reaction. As already mentioned, reaction products permit the determination of the ΔH_R of the global carbon consumption reaction and hence, permit the calculation of the particle temperature employing the particle's energy balance.

Both CO and CO_2 are the primary products of the carbon oxidation reaction and factors that govern the product ratio have been the subject of several experimental investigations [129-132, 173-175]. The ratio depends upon the formation rates of CO and CO_2 during the course of reaction. The formation rates of both these species increase with temperature, however, whereas CO_2 formation rates are first-order in the oxygen concentration, CO formation rates exhibit fractional order behaviors. Nearly all studies indicate that the CO/CO_2 ratio increases with increasing temperature and several studies indicate that the ratio decreases with increasing oxygen concentration. Phillips *et al.*, [131] and Laurendeau [176] hypothesized that these differences in CO and CO_2 formation rates stem from CO production occurring primarily at edge carbons of graphitic planes and CO_2 production at inorganic sites. As noted by Skokova [175], not only are temperature and oxygen concentration important in determining the CO/CO_2 ratio but other char characteristics that may impact this ratio include the sizes of carbon crystallites, pore structure, surface area, chemical composition and the nature of the functional groups on the surface. Foord [177] found that the CO/CO_2 ratio varies with heat treatment of the carbon. Increased heat treatment increases the extent of crystalline organization, creating a more ordered surface thereby facilitating surface diffusion. The higher the mobility of adsorbed oxygen complexes, the higher the rate of CO_2 formation. Consequently, increased mobility of adsorbed oxygen species owing to heat treatment should tend to decrease the CO/CO_2 product ratio. Therefore, the potential for devolatilization conditions to impact the product distribution during oxidation of coal and biomass chars exists.

Experiments performed to determine the product ratio of the carbon oxidation reaction must be done with care. Efforts must be taken to minimize mass transfer effects, thereby reducing the oxidation of CO as it leaves the carbon surface. Tognotti *et al.* [132] performed tests up to 1700 K in an electrodynamic balance and showed that at high temperatures, the measured CO/CO_2 ratio starts to be less than that predicted by the Arrhenius fit of data obtained at lower temperatures, a consequence of homogeneous oxidation of CO very close to the particle surface. The higher the temperature, the more likely homogeneous oxidation, which lowers the CO/CO_2 ratio of the gases diffusing from the surface of the particle.

The measured CO/CO_2 ratios are usually correlated in Arrhenius form, with several investigators multiplying the Arrhenius expression by $P_{O_2}^{n''}$ to capture the oxygen dependence, where n'' is the reaction order. Thus,

$$N_{CO} \Big/ N_{CO_2} = A_{CO} \exp(-E_{CO} / \widehat{R}_u T) \cdot P_{O_2}^{n''}.$$

The results of selected investigations that focused on the CO/CO_2 ratio are shown in Fig. 6. As noted, the CO/CO_2 ratio increases with increasing temperature. Arthur [129] was one of the first to investigate the CO/CO_2 product ratio during carbon oxidation and suggested the Arrhenius form to describe its temperature dependence. The dashed line labeled "1" in the figure represents the correlation by Arthur, which has been used in many char reaction rate models: $N_{CO}/N_{CO_2} = 10^{3.4} \exp(-(52\ \text{kJ/mol})/\widehat{R}_u T)$. Arthur employed an artificial graphite (99.8% fixed carbon) and a very low-volatile bituminous coal (94.2% fixed carbon) in his investigations, both yielding similar CO/CO_2 ratios during oxidation.

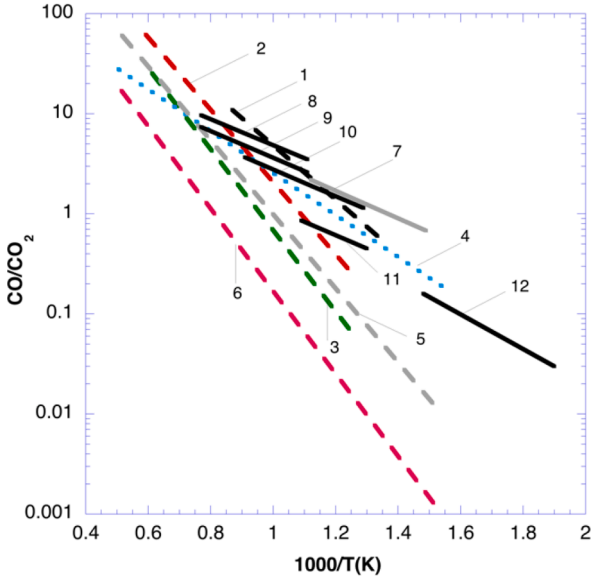

Fig. 6. Measured CO/CO_2 ratios during carbon oxidation 1) artificial graphite/coal char: E = 52 kJ/mol [129], 2) graphite 513EK: E = 60 kJ/mol [174], 3) graphite RW III: E = 78 kJ/mol [174], 4) cellulose char: E = 40 kJ/mol [175], 5) petroleum pitch char: E = 75 kJ/mol [175], 6) graphite: E = 77 kJ/mol [175], 7) soot: E = 27 kJ/mol, n''= 0.27 [130], 8) Spherocarb char, 5% O_2: E = 25 kJ/mol, n''= 0.21 [132], 9) Spherocarb char, 20% O_2: E = 26 kJ/mol, n''= 0.21 [132], 10) Spherocarb char, 100% O_2: E = 26 kJ/mol, n''= 0. 21 [132], 11) vitreous carbon, 1.6×10^{-2} % O_2: E = 25 kJ/mol, n''= 0.18 [173], 12) graphon, 1.3×10^{-3}-1.3×10^{-2} % O_2: E = 32-35 kJ/mol, n''= 0.22 [131].

Interestingly, the activation energies that describe the product distribution fall more or less into two major ranges, those in the range 50 - 80 kJ/mol (plotted as dashed lines 1, 2, 3, 5, and 6) and those in the range 25 - 35 kJ/mol (plotted as solid lines 7 - 12). Those carbons examined that yielded CO/CO_2 product ratios falling into the higher activation energy range are mostly graphitic or graphitizable materials. All of the materials examined by Skokova [175] had elemental carbon contents greater than 94%, and most of these carbons yielded CO/CO_2 ratios that fall into this higher activation energy range. Not all the data obtained by Skokova are shown, only data for graphite (line 6) and two chars produced at the same heat treatment temperature, one from a graphitizable precursor, petroleum pitch (line 5) and the other from a non-graphitizable precursor, cellulose (dotted line 4), which does not yield ratios in the higher activation energy range. Common to the carbons in the high activation energy range is their graphitic nature.

Those carbons examined that yielded CO/CO_2 product ratios falling into the lower activation energy range are soot (solid line 7), Spherocarb (solid lines 8, 9 and 10), a vitreous carbon (solid line 11), and graphon (solid line 12). Soot is an amorphous carbon that consists of agglomerations of nanoparticles having diameters less than about 30 nm. Spherocarb, a carbon molecular sieve, is a graphitized carbon having both micropores and macropores of the order 50 nm. Being a molecular sieve, it has a narrow, uniform porosity. Vitreous carbons (or glassy carbons) are non-graphitizable, microporous carbons widely used as electrode materials. Graphon is a conductive, graphitized carbon black having embedded heteroatoms such as oxygen and nitrogen and is produced from a polymer precursor. The embedded oxygen atoms have the potential to oxidize carbon atoms as the temperature is increased, decreasing the CO/CO_2 ratio. Although Spherocarb and graphon are graphitized carbons, they have low porosities and small pore sizes, the common characteristics of carbons having CO/CO_2 ratios described by activation energies in the lower range, 25 - 35 kJ/mol.

The data of Foord [177] (not shown) yielded activation energies for the CO/CO_2 product ratio of 45 kJ/mol for a graphite sample and 38 kJ/mol for a PVDC carbon, a porous carbon produced via carbonization of a polymer, polyvinylidene chloride. Like the cellulose char (dotted line 4 in Fig. 6) examined by Skokova [175], these activation energies fall into the range 35 - 45 kJ/mol, in between the high and low activation energy ranges already considered. There are few investigations of the product distribution during biomass char oxidation, hence the lack of results shown in Fig. 6 that potentially fall into this middle activation energy range.

It appears that the activation energies that describe the product distribution of the carbon oxidation reaction depend on a few characteristics of the carbonaceous material, amongst them the extent of graphitization, macro- and micro-porosity and pore size. Phillips *et al.* [131] hypothesized that the activation energy of the CO/CO_2 ratio may be independent of the types of carbon, being governed by the difference in the activation energies of the reactions releasing CO and CO_2 from the carbon surface. These researchers suggested that much of the observed variations in Arrhenius plots of the CO/CO_2 ratio should lie in differences in the pre-exponential factor A, which depends on many factors, amongst them surface oxide formation and the extent of conversion. This variation in A-factor is clearly demonstrated in the Arrhenius descriptions shown in Fig. 6.

Tests with Spherocarb were made at three different oxygen levels and the results indicate that at fixed temperature, the CO/CO_2 product ratio decreases with increasing oxygen concentration (see solid lines 8, 9 and 10 in Fig. 6). The reaction order with respect to the oxygen concentration was found to be 0.21. Reported reaction orders are in the range 0.18 - 0.27 for all the carbonaceous materials examined.

Hurt and Calo [172] considered a semi-global, three-step adsorption/desorption reaction mechanism to describe CO and CO_2 formation during carbon oxidation. Reaction rate coefficients were adjusted to provide predicted CO/CO_2 ratios that agree closely with the measurements of Arthur [129] as well as to provide a reasonable description of all the global behaviors of the CO/CO_2 ratio. Assuming steady state for adsorbed oxygen, their mechanism yields $N_{CO}/N_{CO_2} = k_3/(k_2 P_{O_2})$, where k_2 is the reaction rate constant for a complex-enhanced adsorption reaction (r2: $C(O) + O_2 \rightarrow CO_2 + C(O)$) and k_3 is the rate constant for the desorption reaction (r3: $C(O) \rightarrow CO$). Arrhenius parameters for the rate coefficients are $A_2 = 5.7 \cdot 10^{-4}$ bar^{-1}, $E_2 = 130$ kJ/mol and $E_3 = 180$ kJ/mol, all normalized to $A_3 = 1.0$. Employing the Arrhenius expression for the rate constants, the expression derived by Hurt and Calo [172] can be written as $N_{CO}/N_{CO_2} = 10^{3.24}\exp(-(50\ \text{kJ/mol})/\widehat{R}_u T)/P_{O_2}$, (with the oxygen partial pressure in bar), revealing that it yields predictions that fall into the high activation energy range. When the oxygen partial pressure is set to 1 bar, this mechanism and associate kinetic parameters yields predictions of CO/CO_2 ratios similar to those predicted using the expression of Arthur for graphitizable carbons. However, the experiments performed by Arthur [129] were at oxygen partial pressures of 0.05 and 0.25 atm. Consequently, in O_2/N_2 mixtures, the relation derived by Hurt and Calo [172] will yield CO/CO_2 ratios that are too high. The dependency of this ratio on the oxygen partial pressure predicted employing their relation is much stronger than that observed experimentally.

Like apparent reaction rate models, intrinsic models that employ power-law kinetics are most accurate in conditions of temperature, pressure and composition similar to the ones used in obtaining the data needed to evaluate model parameters. The influence of temperature and reactive gas partial pressure on reaction rates are reasonable well captured with such models but the separate effects of total pressure and reactive gas mole fraction are not. Power-law kinetics are not capable of describing the manner in which pressure alone controls chemical reaction rates. A heterogeneous reaction mechanism is required to capture the effects of total pressure as well as temperature and gas composition on char conversion rates.

3.2.2.3. Reaction mechanism-based intrinsic chemical reactivity models. Many studies have been undertaken that have the goal of developing heterogeneous reaction mechanisms that accurately describe the intrinsic chemical reactivity of carbonaceous materials. With reaction mechanisms, it is possible to account for the inhibiting effects of the reaction products. The overall reaction pathways for consuming the solid material, forming gaseous species, are

R01: $C(s) + H_2O \rightleftarrows CO + H_2$
R02: $C(s) + CO_2 \rightleftarrows 2\ CO$
R03: $C(s) + \frac{1}{2}\ O_2 \rightarrow CO$
R04: $C(s) + O_2 \rightarrow CO_2$
R05: $C(s) + 2\ H_2 \rightleftarrows CH_4$

The overall reaction mechanism describing the conversion of the solid carbonaceous material to gaseous products involves the buildup of adsorbed species on the solid surfaces, the migration of the adsorbed species on the surfaces and the desorption of these adsorbed species. Both the adsorption and desorption processes are characterized by broad distributions of activation energies, reflecting the heterogeneity of the surface sites. Inorganic material embedded in the solid has the potential

to catalyze the heterogeneous reactions that occur. No simple model is likely to capture all features of the overall process, but all realistic models should involve adsorption and desorption reactions, as proposed by Langmuir [178]. An example of such a heterogeneous reaction mechanism is shown in Table 1, the result of investigations undertaken in theses supervised by Mitchell [108,179,180] having the goal of deriving a heterogeneous reaction mechanism applicable to coal and biomass chars undergoing conversion in combustion, oxy-combustion and gasification environments. This type of model is oftentimes referred to as a turnover model [110], a model in which desorbing species yield new free sites available for adsorption. It builds on many previous mechanisms suggested for describing carbon conversion reactions, for example, see the review of Laurendeau [176]. The mechanism is capable of predicting overall char reactivity and off gas composition over a wide range of temperatures, pressures and gas compositions. In addition, the model is simple enough to be computationally tractable. Tilghman and Mitchell [181] present Arrhenius parameters and thermochemical data (ΔH_R and ΔS_R) for each reaction listed in Table 1 for a coal char and for a biomass char. The thermochemical data permit the calculation of reverse reaction rate coefficients that result in equilibrium at sufficiently long reaction times.

In Table 1, the species $C_2(O_2)$ denotes two adjacent carbon sites having adsorbed oxygen atoms. Also, the molar reaction rate of reaction i ($\widehat{\Re}_i$) is expressed in terms of the total surface concentration (ξ_n), the forward and reverse reaction rate constants (k_{if} and k_{ir}, respectively), the concentrations of reactive gas-phase species j ($[C_j]$), and the site fractions of adsorbed species m (θ_m), either O, H, OH, or CO. Here, θ_{O2} represents the fraction of adjacent sites having adsorbed oxygen atoms and θ_f represents the fraction of the sites that are free and hence, available for adsorption. A homogeneous reaction mechanism is used in conjunction with the heterogeneous reaction mechanism to determine the fates of the desorbed species and includes reactions leading to CH_4 from desorbed CH_2 and CH_3 species and to CO from desorbed HCO species.

Table 1
Reaction mechanism for carbonaceous solids exposed to H_2O, CO_2 and O_2 [107,108].

	Reaction	Reaction rate (mol/m^2-s)
R.1	$2C_f + H_2O \rightleftharpoons C(OH) + C(H)$	$\widehat{\Re}_1 = (\xi_n)^2\{k_{1f}[H_2O]\theta_f^2 - k_{1r}\theta_{OH}\theta_H\}$
R.2	$C(OH) + C_f \rightleftharpoons C(O) + C(H)$	$\widehat{\Re}_2 = (\xi_n)^2\{k_{2f}\theta_f\theta_{OH} - k_{2r}\theta_O\theta_H\}$
R.3	$C(H) + C(H) \rightleftharpoons H_2 + 2C_f$	$\widehat{\Re}_3 = (\xi_n)^2\{k_{3f}\theta_H^2 - k_{3r}[H_2]\theta_f^2\}$
R.4	$C(O) + C_b \rightarrow CO + C_f$	$\widehat{\Re}_4 = (\xi_n)\ k_{4f}\theta_O$
R.5	$C(OH) + C_b \rightleftharpoons HCO + C_f$	$\widehat{\Re}_5 = (\xi_n)\ \{k_{5f}\theta_{OH} - k_{5r}[HCO]\theta_f\}$
R.6	$C_b + C_f + C(H) + H_2O \rightleftharpoons CH_3 + C(O) + C_f$	$\widehat{\Re}_6 = (\xi_n)^2\{k_{6f}[H_2O]\theta_f\theta_H - k_{6r}[CH_3]\theta_f\theta_O\}$
R.7	$C_b + C_f + C(H) + H_2 \rightleftharpoons CH_3 + 2C_f$	$\widehat{\Re}_7 = (\xi_n)^2\{k_{7f}[H_2]\theta_f\theta_H - k_{7r}[CH_3]\theta_f^2\}$
R.8	$C_f + C(H) + CO \rightarrow HCO + 2C_f$	$\widehat{\Re}_8 = (\xi_n)^2\ k_{8f}[CO]\theta_f\theta_H$
R.9	$C(H) + C(H) \rightarrow CH_2 + C_f$	$\widehat{\Re}_9 = (\xi_n)^2\ k_{9f}\theta_H^2$
R.10	$CO_2 + C_f \rightleftharpoons C(O) + CO$	$\widehat{\Re}_{10} = (\xi_n)\ \{k_{10f}[CO_2]\theta_f - k_{10r}[CO]\theta_O\}$
R.11	$C_b + CO_2 + C(O) \rightarrow 2CO + C(O)$	$\widehat{\Re}_{11} = (\xi_n)\ k_{11f}[CO_2]\theta_O$
R.12	$CO + C_f \rightleftharpoons C(CO)$	$\widehat{\Re}_{12} = (\xi_n)\ \{k_{12f}[CO]\theta_f - k_{12r}\theta_{CO}\}$
R.13	$CO + C(CO) \rightarrow CO_2 + C_f + C_b$	$\widehat{\Re}_{13} = (\xi_n)\ k_{13f}[CO]\theta_{CO}$
R.14	$2C_f + O_2 \rightarrow C(O) + CO$	$\widehat{\Re}_{14} = (\xi_n)^2 k_{14f}[O_2]\theta_f^2$
R.15	$2C_f + O_2 \rightarrow C_2(O_2)$	$\widehat{\Re}_{15} = (\xi_n)\ \{(\xi_n)k_{15f}[O_2]\theta_f^2 - k_{15r}\theta_{O2}\}$
R.16	$C_f + C_b + C(O) + O_2 \rightarrow CO_2 + C(O) + C_f$	$\widehat{\Re}_{16} = (\xi_n)^2\{k_{16f}[O_2]\theta_f\theta_O - k_{16r}[CO_2]\theta_f\theta_O\}$
R.17	$C_f + C_b + C(O) + O_2 \rightarrow CO + 2C(O)$	$\widehat{\Re}_{17} = (\xi_n)^2 k_{17f}[O_2]\theta_f\theta_O$
R.18	$C_b + C_2(O_2) \rightarrow CO_2 + 2C_f$	$\widehat{\Re}_{18} = (\xi_n)\ k_{18f}\theta_{O2}$

3.2.2.3.1. Carbon oxidation. Many heterogeneous reaction mechanisms have been proposed to describe the overall carbon oxidation reaction, which leads to the formation of both CO and CO_2 [92,95,108,130,147,155,180,182-193]. Blyholder and Eyring [155] were among the first to apply dual-site adsorption to the carbon-oxygen system by considering the dissociative chemisorption of O_2 on carbon surfaces forming adsorbed oxygen atoms (C(O)) with the O-atoms able to migrate on the surface. It was assumed that an O-atom would hop along the surface until it forms a carbonyl type bond with a carbon atom. This carbonyl surface oxide can decompose, producing CO. Ma and Haynes [186], Brown *et al.* [193] and Sendt and Haynes [187] also suggested that dual-site adsorption of O_2 could result in the release of CO directly from the surface (see Reaction R.14 in Table 1). The work of Zhuang *et al*, [188] suggested that some carbon sites were more apt to desorb CO_2 rather than CO. Consequently, reactions involving the pseudo-adsorbed species $C_2(O_2)$, representative of two adjacent C(O) species (formed via Reaction R.15), denote carbon sites that preferentially yield CO_2 (see Reaction R.18). The work of Ahmed and Back [194], Du *et al.*, [130,184,195], Zhuang *et al.* [189,190] and Haynes and Newbury [185] lead to the inclusion of complex-enhanced desorption reactions, resulting from the interaction of a gaseous reactant and an adsorbed species (see Reactions R.16 and R.17). Such reactions lead to higher conversion rates at low temperatures than could be achieved without them. Several other researchers [130,179,180,184-187, 189,190,193] have included complex-enhanced adsorption in their carbon-oxygen reaction mechanisms. Migration of oxygen atoms has been demonstrated to take place on carbonaceous surfaces [175,179,187], however, Campbell [179] showed that neglecting migration did not significantly change calculated results. Consequently, the mechanism presented in Table 1 neglects migration with the benefit of reduced computational complexity. Reactions R.4 and R.14 - R.18 in Table 1 represent a carbon oxidation mechanism that predicts all experimental observations. In particular, the mechanism predicts (a) carbon conversion rates that increase with increasing temperatures, pressures and oxygen concentrations and (b) CO contents of the off gases that increase with increasing temperature. The predicted temperature dependence of the CO/CO_2 product ratio is in adequate agreement with previous determinations [129-132, 173-175, 177,191].

3.2.2.3.2. Carbon-carbon dioxide gasification. The heterogeneous reaction between carbon and carbon dioxide ($C + CO_2 \rightleftharpoons 2CO$) is commonly referred to as the Boudouard reaction, a reaction named after Octave Leopold Boudouard who studied the reaction in 1905. Many researchers [196-206] have proposed reaction mechanisms to describe the reaction pathways that reflect the Boudouard reaction, most notably Ergun [196,197] and Gadsby *et al.* [199]. Nearly all researchers propose oxygen exchange between CO_2 and the carbon surface forming C(O) and CO as the initial step in the mechanism, reaction R.10 in Table 1. Note that Reaction R.10 is reversible: The reaction does not proceed to completion but reaches an equilibrium state that depends on temperature and pressure. The adsorbed oxygen complexes desorb, forming CO (see reaction R.4).

Reactions R.4 and R.10 cannot describe observed gasification rates alone; consequently, research efforts have been focused on better characterizing the effects of CO, a species that slows the gasification rate when present. Gadsby *et al.* [199] hypothesized that inhibition was a consequence of CO molecules being adsorbed at sites on the carbon surface, preventing these sites from adsorbing species capable of removing a carbon atom from the bulk carbon. This is reflected by Reaction R.12 in Table 1. Many investigators support CO inhibition, and several reaction pathways that slow down carbon conversion rates in CO_2 environments have been proposed [198,200-202, 204-206]. Ingeme and Blackwood [200] noted that conversion rates at elevated pressures were better predicted if the concentration of adsorbed-CO species decreased as pressure increased, leading to the inclusion of Reactions R.12 and R.13 in the C-CO_2 mechanism. Laurendeau [176] and Shaw [205] suggested that complex-enhanced adsorption would lead to a

decrease in adsorbed-CO as pressure is increased, supporting the inclusion of Reaction R.13. Reactions R.4 and R.10 - R.13 in Table 1 represent a comprehensive carbon-CO_2 gasification mechanism that predicts all of the experimentally observed trends.

3.2.2.3.3. Carbon-steam gasification. The carbon-steam heterogeneous reaction has received considerable attention over the years [197-199, 203,207-212] and early attempts to define the mechanism were analogous to the carbon-carbon dioxide mechanism: Oxygen exchange between H_2O and the carbon surface forming C(O) and H_2 in a reversible reaction. Reactions R.1, R.2 and R.3 of Table 1 reflect the overall result of these early investigations, initiating the reaction sequence with the more likely dissociative chemisorption of H_2O on the surface, leading to adsorbed-OH and adsorbed-H, which undergo further reactions that lead to adsorbed-O with the release of H_2. Evidence for the existence of OH on carbonaceous surfaces was provided by Blackwood and McTaggart [213]. The adsorbed-OH can dissociate on the surface producing adsorbed-O and adsorbed-H (Reaction R.2) or desorb as HCO (after rearrangement), thereby removing a carbon atom from the bulk (Reaction R.5). Complexed-enhanced desorption of H-atoms can also lead to HCO formation via Reaction R.8, a reaction that couples the char-steam and char CO_2 systems of reaction. Following the lead of Laurendeau [176], adsorbed-H can result in methane formation (see Reactions R.6, R.7, R.9). Complex-enhanced desorption of H-atoms (Reactions R.6 and R.7) leads to increased methane production as pressure is increased, an observation of Blackwood and McGrory [214]. Other mechanisms have been postulated for methane formation resulting from adsorbed-H on the carbonaceous surface [215,216]; data validating such mechanisms are difficult to obtain.

3.2.2.3.4. Distributed activation energy approach for modeling the rates of desorption reactions. Owing to the presence of impurities within the carbon matrix and the inhomogeneity of the carbonaceous surface itself, the energies that bind adsorbed species to the surface differ for individual adsorbed complexes rendering differences in the desorption rates of similar adsorbed species. Consider adsorbed oxygen complexes for example, which desorb, removing carbon atoms from the carbonaceous matrix forming gas phase CO and CO_2. Because of the differences in binding energies, under the same gas-phase conditions the desorption rates are not the same for each adsorbed oxygen complex. As a consequence, the rate of the desorption reaction $C(O) + C_b \rightarrow CO + C_f$ depends not on the average binding energy (*i.e.*, $\frac{d[C(O)]}{dt} \neq -k[C(O)] = -A\cdot\exp(-E_{ave}/\widehat{R}_uT)\cdot[C(O)]$), but depends on the distribution of binding energies.

In the distributed activation energy (DAE) approach in modeling desorption reactions, each adsorbed species of binding energy E ($C_E(O)$) is assumed to desorb via a first-order, irreversible reaction:

$$C_E(O) + C_b \rightarrow CO + C_f$$

The desorption rate is given by

$$\frac{d[C_E(O)]}{dt} = -k_E[C_E(O)] = -A_E\cdot\exp(-E/\widehat{R}_uT)\cdot[C_E(O)] \tag{84}$$

Multiplying by dE and integrating over all E:

$$\int_0^\infty \frac{d[C_E(O)]}{dt}\cdot dE = -\int_0^\infty k_E\cdot[C_E(O)]\cdot dE \tag{85}$$

The left-hand-side of the above equation is the rate of change in the total adsorbed-O concentration; thus

$$\frac{d[C(O)]}{dt} = -\int_0^\infty k_E\cdot[C_E(O)]\cdot dE \tag{86}$$

Letting $f(E, t)$ denote the distribution function describing the distribution of adsorbed oxygen species on the carbonaceous surface at time t, (*i.e.*, $[C_E(O)] = f(E, t)\cdot[C(O)]$), the above equation can be rewritten as

$$\frac{d[C(O)]}{dt} = -\int_0^\infty k_E\cdot f(E,t)\cdot[C(O)]\cdot dE \tag{87}$$

or in terms of the Arrhenius parameters for k_E

$$\frac{d[C(O)]}{dt} = -\int_0^\infty A_E\cdot\exp(-E/\widehat{R}T)\cdot f(E,t)\cdot[C(O)]\cdot dE. \tag{88}$$

At the initial time ($t = 0$), a Gaussian distribution function is assumed for the adsorbed-O distribution function:

$$f(E,0) = \frac{1}{\sigma_d\sqrt{2\pi}}\cdot\exp\left(-\frac{(E-E_{ave})^2}{2\sigma_d^2}\right). \tag{89}$$

Here, E_{ave} is the mean value of the distribution and σ_d is the standard deviation. The evolution of $f(E, t)$ in oxygen-containing environments is quite complex and has not yet been accurately characterized. As the oxygen complexes desorb, underlying carbon atoms are exposed that differ in binding energy. Oxygen complexes adsorbed onto these newly formed carbon sites can have activation energies that span the entire activation energy range. At any time, the adsorbed-O distribution will depend on both the oxygen atoms that have been adsorbed over the time as well as those that have been desorbed. In most applications of DAE models in combustion and gasification environments, the distribution of activation energies on carbon surfaces is assumed to be invariant in time. Although the underlying carbon atom may not have the same binding energy as the carbon atom that desorbed, over the entire carbonaceous surface the initial distribution of binding energies ($f(E, t = 0)$) is assumed to be preserved as the adsorption/desorption process progresses. In addition, the pre-exponential factor A_E is assumed to be the same for all desorption reactions, (*i.e.*, $A_E = A_0$) in DAE applications to desorption reactions. With these assumptions, Eq. (88) can be rewritten as

$$\frac{d[C(O)]}{dt} = -\int_0^\infty A_0\cdot\exp(-E/\widehat{R}_uT)\cdot f(E,0)\cdot[C(O)]\cdot dE. \tag{90}$$

Employing the expression for the distribution function from Eq. (89) in the equation above results in

$$\frac{d[C(O)]}{dt} = -\int_0^\infty A_0\cdot\exp(-E/\widehat{R}_uT)\cdot\frac{1}{\sigma_d\sqrt{2\pi}}\cdot\exp\left(-\frac{(E-E_{ave})^2}{2\sigma_d^2}\right)\cdot[C(O)]\cdot dE \tag{91}$$

Defining an effective reaction rate coefficient as follows

$$k_{eff} = \int_0^\infty A_0\cdot\exp(-E/\widehat{R}_uT)\cdot\frac{1}{\sigma_d\sqrt{2\pi}}\cdot\exp\left(-\frac{(E-E_{ave})^2}{2\sigma_d^2}\right)\cdot dE, \tag{92}$$

the overall rate for the desorption reaction can be written as

$$\frac{d[C(O)]}{dt} = -k_{eff}\cdot[C(O)]. \tag{93}$$

Eq. (92) is used when determining the effective reaction rate coefficient for the desorption reaction when allowance is made for a distribution of energies binding adsorbed species to the carbonaceous surface.

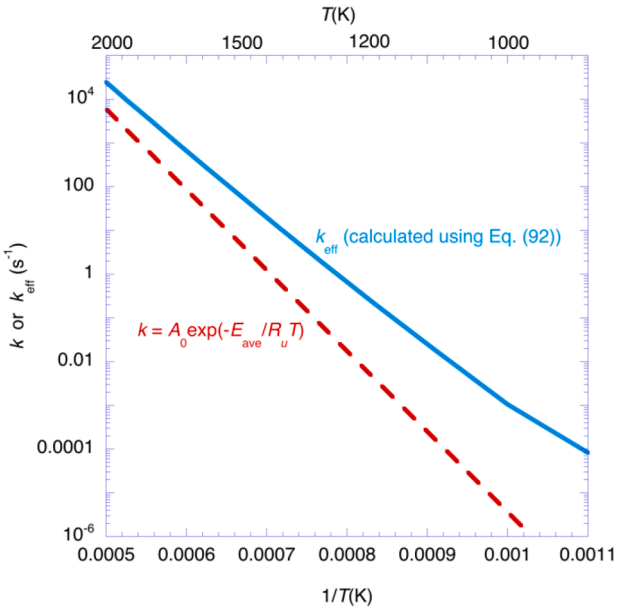

Fig. 7. Effective reaction rate coefficient for the desorption reaction C(O) + C_b → CO + C_f. The solid line represents a distributed activation energy approach, calculated using Eq. (92), with A_0 = 1x10^{13}, E_{ave} = 353 $\frac{kJ}{mol}$ and σ_d = 28 $\frac{kJ}{mol}$. The dashed line represents the rate coefficient calculated employing the average activation energy: k = A_0·exp(− E_{ave} /$\widehat{R}_u$T).

To help understand the consequences of the DAE approach, shown in Fig. 7 is a plot of k_{eff} versus temperature for the reaction C(O) + C_b → CO + C_f employing kinetic parameters determined by Tilghman and Mitchell [181] for the char of a bituminous coal: $A_0 = 1.0 \times 10^{13}$, E_{ave} = 353 kJ/mol and σ_d = 28 kJ/mol. For comparison, also shown is the reaction rate coefficient calculated employing the single, average activation energy ($k = A_0 \exp(E_{ave}/\widehat{R}_u T)$). The comparison clearly demonstrates that at all temperatures relevant to coal and biomass combustion, the DAE approach yields higher reaction rate coefficients and hence faster overall desorption rates when compared to the rates calculated assuming a single, average activation energy for the desorption reaction. This is a consequence of the faster release rates of adsorbed complexes having binding energies below E_{ave}. The differences are larger the lower the temperature since the lower the temperature the more important is the low energy tail of the distribution. For very high temperatures, however, the term within the exponent ($-E/\widehat{R}_u T$) will be close to zero for the entire width of the distribution, such that there will be no difference between the DAE and the average activation energy approach. The ratio k_{eff}/k decreases from 51.3 to 12.4 to 4.13 as temperature is increased from 1200 to 1500 to 2000 K. Calculations indicate that the broader the initial activation energy distribution (*i.e.,* the larger σ_d), the larger k_{eff} and hence, the faster the adsorbed-O desorption rate compared to the rate determined assuming a single, average activation energy for the desorption reaction.

Accurate assessment of the rates of desorption reactions requires that account is made for a distribution of binding energies on the char surface. When modeling char reactivity to oxygen, the DAE model should be applied to the adsorbed-O desorption reactions, C(O) + C_b → CO + C_f and $C_2(O_2)$ + C_b → CO_2 + C_f (see Table 1). When modeling char reactivity to steam, the DAE model should be applied to the adsorbed-OH desorption reaction, C(OH) + C_b → HCO + C_f and when considering CO inhibition in char reactivity to CO_2, the DAE model should be applied to the reverse rate of the CO adsorption reaction, CO + C_f⇌C(CO).

3.2.2.3.5. Reactivity. Based on the reactions presented in Table 1, the following expression can be derived for the intrinsic chemical reactivity of the carbonaceous particle material:

$$R_c = \widehat{M}_C\{\widehat{\Re}_4 + \widehat{\Re}_5 + \widehat{\Re}_6 + \widehat{\Re}_7 + \widehat{\Re}_9 + \widehat{\Re}_{11} + \widehat{\Re}_{13} + \widehat{\Re}_{14} + \widehat{\Re}_{16} + \widehat{\Re}_{17} + \widehat{\Re}_{18}\} \quad (94)$$

Here, $\widehat{\Re}_k$ is the net rate of Reaction R.k. In combustion environments, in which contributions from carbon-steam and carbon-carbon dioxide reactions are insignificant,

$$R_c = \widehat{M}_C\{\widehat{\Re}_4 + \widehat{\Re}_{14} + \widehat{\Re}_{16} + \widehat{\Re}_{17} + \widehat{\Re}_{18}\} \quad (95)$$

In oxy-combustion and gasification environments, all of the reactions should be considered in determining the conversion rate of the carbonaceous material. The high levels of CO_2 in the oxy-combustion environments enhances the importance of the carbon-carbon dioxide system of reactions and in gasification environments, the exothermicity of the carbon-oxygen system of reactions is key in providing sufficient energy as heat to drive the endothermic gasification reactions.

Many studies concerned with predicting carbon combustion and gasification behavior use heterogeneous reaction mechanisms that describe conversion rates as functions of oxidation and gasification conditions. In some of the studies, carbon conversion rate expressions were derived by assuming steady-state levels for the adsorbed species (see for example, [196-198, 200-203, 211,217-220]). In other studies, the laws of mass action as governed by the net rates of all the reactions in the proposed reaction mechanism are used to predict carbon conversion rates as reaction time progresses (for example, see [92,95,98,107,110, 147,181,192,221,222]). Several of the proposed reaction mechanisms include the impact of thermal annealing [92,95,147,192]. Reaction order varies with temperature, ranging from zero (at low temperatures when desorption reactions control reaction rates) to one (at high temperatures when adsorption reactions control reaction rates). Heterogeneous reaction mechanisms properly capture this change in reaction order as gas conditions change and hence, are deemed to be more reliable and accurate in predicting char conversion rates than power-law kinetic approaches in situations where gas conditions are expected to vary. As indicated earlier, heterogeneous reaction mechanisms also permit reliable predictions in cases where total pressure varies.

A summary of the different definitions used for apparent and intrinsic reaction rates is provided in Appendix B. Relationships between the different reaction rate models are also provided.

3.3. Sub-models for the point particle approach

In this Section, sub-models required for the point particle approach (*i.e.*, when the particle is not resolved) are presented. These models are needed in order to account for the unresolved spatial gradients both inside the particle itself and in the boundary layer around it.

The gas concentration in and around a reactive particle will in general not be spatially constant. Examples of the concentration profiles of carbon dioxide and steam around a gasifying particle are depicted in Fig. 8. Both steam and carbon dioxide are consumed by the gasifying char particle. In the example used for the figure, the concentration of steam in the bulk flow is higher, but due to the higher reactivity of char to steam, the concentration gradients of steam are steeper than the ones for carbon dioxide. This, together with the fact that the effective diffusivity inside the particle is lower than the one outside, results in a faster decrease of the reactant concentrations inside the particle than in the gas film surrounding the particle. The effect of the reactions and diffusion inside the porous char is discussed in Section 3.3.1 while the heat and mass transfer in the gas film surrounding the particle is discussed in Section 3.3.2.

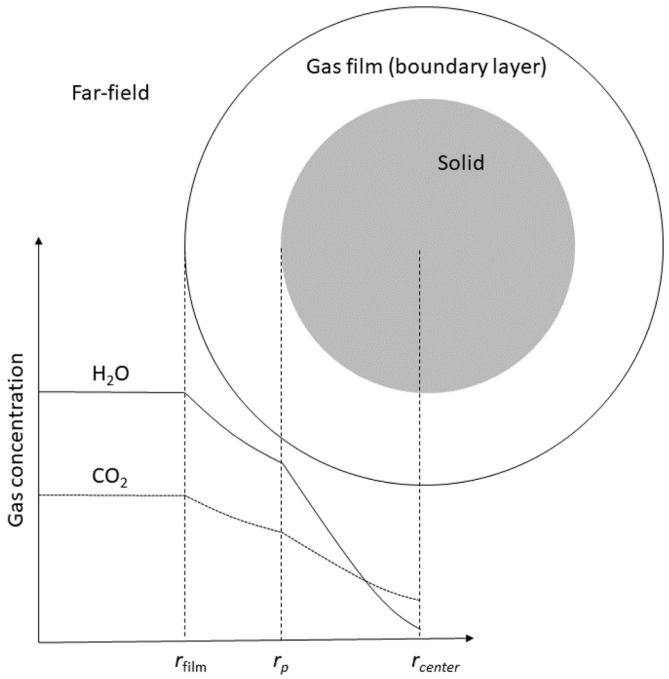

Fig. 8. Concentration profiles in and around a reactive particle in an ambient gas containing carbon dioxide and water.

3.3.1. Effectiveness factor

We will now assume a solid slab of char with thickness $2z_s$, where the fluid on both sides of the slab has the same properties (composition, pressure, temperature), and where the slab is penetrated by a straight pore of radius r_{pore}, as shown in Fig. 9. [This is also identical to assuming a slab of half this thickness where the lower boundary of the slab is sealed off.] The mass diffusion rate of reactant i along the length of the pore at position z is then given by

$$\dot{m}_{diff,i}(z) = A_{pore}\mathscr{D}_{pore,i,eff}C_g\frac{dX_i}{dz}\widehat{M}_i \tag{96}$$

where A_{pore} $(=\pi r_{pore}^2)$ is the cross sectional area of the pore, C_g is the gas concentration within the pore, X_i and $\widehat{M}_i$ are the mole fraction and molar mass, respectively, of reactant i and $\mathscr{D}_{pore,i,eff}$ is the effective diffusivity of species i within the pore when account is made both for bulk and Knudsen diffusion. It is expressed as

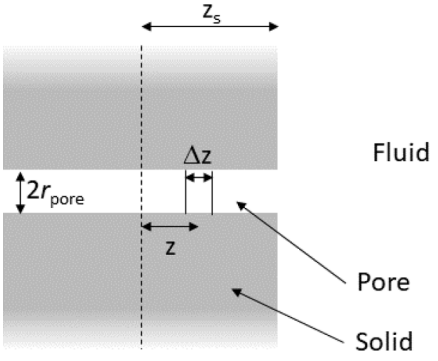

Fig. 9. Slab of char penetrated by a single straight pore.

$$\mathscr{D}_{pore,i,eff} = \left(\frac{1}{\mathscr{D}_i} + \frac{1}{\mathscr{D}_{Kn,i}}\right)^{-1}. \tag{97}$$

In contrast to the expression for $\mathscr{D}_{i,eff}$ in Eq. (18), which considers the diffusivity of a porous structure, $\mathscr{D}_{pore,i,eff}$ represents the diffusivity along a single pore of constant cross section. Hence, the tortuosity, constriction and porosity are not included in Eq. (97). From this, it is straight forward to calculate the difference in mass diffusion between two positions separated by Δz along the pore as

$$\Delta\dot{m}_{diff,i}(z) = \dot{m}_{diff,i}(z+\Delta z) - \dot{m}_{diff,i}(z) = A_{pore}\mathscr{D}_{pore,i,eff}\widehat{M}_i C_g\frac{d^2X_i}{dz^2}\Delta z. \tag{98}$$

Let us now assume that all relevant reactions are first order and that the product of one reaction is never the reactant of another reaction. This assumption is fulfilled employing the following set of global char conversion reactions:

R01: $C(s) + H_2O \rightleftarrows CO + H_2$
R02: $C(s) + CO_2 \rightleftarrows 2\,CO$
R03: $2C(s) + O_2 \rightarrow 2CO$

The mass consumption rate of reactant i (where i can refer to either CO_2, H_2O or O_2) within a thin element Δz around position z is then given by

$$\dot{m}_{reac,i}(z) = -2\pi r_{pore}\Delta z\widehat{R}_i\widehat{M}_i = 2\pi r_{pore}\Delta z\sum_{k=1}^{N_{reac}}k_k C_g X_i\widehat{M}_i = 2\pi r_{pore}\Delta z k_{k,i}C_g X_i\widehat{M}_i \tag{99}$$

where k_k is the rate constant of reaction k and $k_{k,i} = \widehat{R}_i/C_g X_i$ is the rate constant of the reaction that has species i as its reactant. In deriving this expression, Eqs. (7) and (10) were used together with the fact that all reactions are first order and that none of the products are the reactant of any of the other reactions. Since in steady state, the difference in mass diffusion between the inlet and the outlet of the thin element Δz must be due to reactions within the element, Eqs. (98) and (99) can be equated to obtain

$$\frac{d^2X_i}{dz^2} = \frac{2k_{k,i}}{r_{pore}\mathscr{D}_{pore,i,eff}}X_i = h_i^2 X_i \tag{100}$$

where

$$h_i = \sqrt{\frac{2k_{k,i}}{r_{pore}\mathscr{D}_{pore,i,eff}}}. \tag{101}$$

Setting the species boundary condition to $X_i = X_{i,s}$ at the external surface of the slab and $\frac{dX_i}{dz} = 0$ at its center ($z = 0$) (corresponding to the sealed off end for a slab with half thickness), integration of Eq. (100) yields

$$X_i = X_{i,s}\frac{\cosh\, h_i z}{\cosh\, h_i z_s}, \tag{102}$$

which gives the mole fraction of species i at position z in the pore. The total mass consumption rate of species i within the full half-length of the pore, $\dot{m}_{tot,i}$, when account is made for the fact that the reactant concentration decreases towards the center of the solid, equals the total mass diffusion rate at the pore inlet; such that

$$\dot{m}_{tot,i} = A_{pore}\mathscr{D}_{pore,i,eff}\widehat{M}_i C_g h_i\, X_{i,s}\tanh(h_i z_s)\,. \tag{103}$$

In order to obtain the above expression, Eq. (102) was used to find

the gradient of the mole fraction before Eq. (96) was evaluated at the solid surface. If the reactant concentration within the solid had been the same as it is at the solid surface, the total mass consumption rate would have been

$$\dot{m}_{tot,i,max} = 2\pi r_{pore} z_s \; k_{k,i} \; C_g X_{i,s} \widehat{M}_i. \tag{104}$$

An effectiveness factor for reactant i can now be defined as the ratio between its real consumption rate (Eq. (103)) and the rate that would have been experienced if the reactant concentration was constant throughout the solid (Eq. (104)), *i.e.*;

$$\eta_i = \frac{\dot{m}_{tot,i}}{\dot{m}_{tot,i,max}} = \frac{\tanh(h_i z_s)}{h_i z_s} = \frac{\tanh(\phi_{L,i})}{\phi_{L,i}}. \tag{105}$$

Since the effectiveness factor always contain the product of h_i and z_s, it is convenient to define the variable $\varphi_{L,i} = h_i z_s$. This variable is called the Thiele modulus, in honor of E. W. Thiele who was the first to calculate the effectiveness factor in a similar way in 1939 [141].

In the above calculation of the effectiveness factor, it was assumed that the solid contains one single pore with constant cross section that penetrates straight through the solid. What if this single pore were not straight but "tortuous" with a constant cross section and still penetrating the solid? The pore half-length in this configuration is $L = \tau z_s$, where τ is the tortuosity, and the Thiele modulus becomes

$$\phi_{L,i} = h_i \tau z_s = \tau z_s \sqrt{\frac{\rho_{char} S_g k_{k,i}}{\Theta(1-\Theta) f_r \; \mathscr{D}_{pore,i,eff}}} = z_s \sqrt{\frac{\rho_{char} S_g k_{k,i}}{\left(\Theta \; \mathscr{D}_{pore,i,eff} / \tau^2\right)}},$$

where we have used Eq. (57) to replace r_{pore} in Eq. (101).

The final expression on the right-hand-side was derived assuming $(1 - \Theta) f_r = 1$. The denominator of the square root term indicates how the effective pore diffusion coefficient is modified due to the tortuous path through the single pore. Since $\tau > 1$, this expression indicates that the tortuous path slows down the rate of diffusion in the pore, leading to a larger value of the Thiele modulus. A larger Thiele modulus yields a smaller effectiveness factor rendering a lower reactive gas consumption rate in the pore and a corresponding lower char consumption rate.

The case considered above is not reality, however, since there is typically a large network of pores that are not all straight and vary in cross-sectional area. In addition, the pores are inter-connected; a schematic of this can be seen in Fig. 10. If an element of thickness Δz across the entire slab is considered at a distance z from the slab mid-plane, all pores that cross the plane will contribute to diffusive flow into the elemental slab volume. The effective diffusion coefficient must reflect diffusion through all the pores in this case and is given by Eq. (18). Equations (96) and (98) apply but with $\mathscr{D}_{pore,i,eff}$ replaced by $\mathscr{D}_{i,eff}$ and the cross-sectional area of the pore replaced by the cross-sectional area

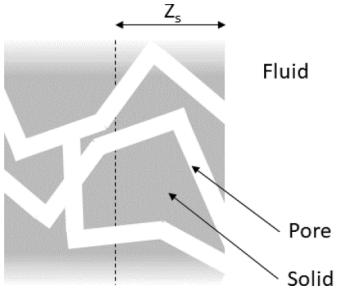

Fig. 10. Slab of char penetrated by multiple non-straight pores.

for diffusion into the slab (A_{slab}). Equation (99) also applies but with the surface of the pore wall within Δz replaced by the surface of all the pore walls of the slab within Δz (which equals $A_{slab}\Delta z \quad S_v$). This results in the following expression for the Thiele modulus for first-order reaction in a slab of thickness $2z_s$:

$$\phi_{L,i} = z_s \sqrt{\frac{k_{k,i} S_v}{\mathscr{D}_{i,eff}}} = z_s \sqrt{\frac{\rho_{char} S_g k_{k,i}}{\mathscr{D}_{i,eff}}}.$$

The effectiveness factor given in Eq. (105) still applies. This permits determination of the reactive gas consumption rate when flow through all pores is considered, no matter the tortuous path or variations in pore cross sections. When the molar reactive gas reaction rate evaluated at conditions at z_s is expressed as $\widehat{R}_{i,s}$, the Thiele modulus becomes

$$\phi_{L,i} = z_s \sqrt{\frac{\widehat{R}_{i,s} S_g \rho_{char}}{C_g X_{i,s} \mathscr{D}_{i,eff}}}. \tag{106}$$

The effectiveness factor used here is per reactant species. This means that the effectiveness factor will differ for oxygen and carbon dioxide, with the one for carbon dioxide being much closer to unity. Also, if a detailed reaction scheme is used, where the global reactions RO1-RO3 mentioned above are split into several sub-reactions, the sum of all sub-reactions that combines into a single global reaction must be used. Finally, if the product of one global reaction is the reactant of another global reaction, the analysis above is no longer formally applicable. For example, this is the case for

R04: $C(s) + O_2 \rightarrow CO_2$

where the product is the reactant of reaction RO2. Such issues can often be resolved by assuming that one of the reactions is much faster than the other. For example, reaction RO4 is much faster than reaction RO2. This means that as long as the effectiveness factor of oxygen is much smaller than unity, essentially all the CO_2 resulting from reaction RO4 is released close to the surface, such that the surface concentration of CO_2 can be used to determine the effectiveness factor of carbon dioxide in the regular way. If, on the other hand, the effectiveness factor of oxygen is close to unity, meaning that oxygen reactions are slow, reactions with carbon dioxide will be so slow that they can be neglected.

All of the above is for an infinitely large flat slab of char. Unlike coal-based chars, the permeability of a biomass char is anisotropic. The permeability in the cross-grain direction of a biomass char is much smaller than the permeability along the grains, such that the effectiveness factor of a flat slab can be used to approximate the biomass char. For coal chars, however, the pore structure is roughly isotropic, and the typical pulverized char particle is more spherical. By assuming a spherical geometry, the above exercise can be re-done to show that for spherical particles with isotropic permeabilities the effectiveness factor becomes

$$\eta_i = \frac{3}{\phi_{L,i}} \left(\frac{1}{\tanh(\phi_{L,i})} - \frac{1}{\phi_{L,i}} \right) \tag{107}$$

when z_s in Eq. (106) is replaced by r_p.

The effectiveness factor calculated above is correct only for first order reactions ($m = 1$). Mehta and Aris [223] have shown that approximate values of effectiveness factors for m^{th}-order reactions can be obtained by multiplying the Thiele modulus expression given in Eq. (106) by $\sqrt{(m+1)/2}$ to yield a modified Thiele modulus, $\varphi_{L,m,\,i}$,

$$\phi_{L,m,i} = z_s \sqrt{\frac{(m+1)\widehat{R}_{i,s} S_g \rho_{char}}{2\ C_g X_{i,s} \mathscr{D}_{i,eff}}}, \tag{108}$$

and then employing this modified Thiele modulus in the following expression for the effectiveness factor:

$$\eta_i = \sqrt{\frac{2}{(m+1)}}\left[\frac{3}{\phi_{L,m,i}}\left(\frac{1}{\tanh(\phi_{L,m,i})} - \frac{1}{\phi_{L,m,i}}\right)\right]. \tag{109}$$

For $0 < m < 2$, the errors in η_i are less than about 6.5% for a specified value of $\varphi_{L,m,\,i}$ and occur for values of $\varphi_{L,m,\,i}$ less than 8. For zeroth-order reactions, the effectiveness factor is 1.0 whenever the reactant concentration is finite at the particle center. Therefore, based on the numerical solution to the governing differential equation for zeroth-order reactions, when $\phi_{L,m,i} < \sqrt{6}$, the effectiveness factor is 1.0. For $\varphi_{L,m,\,i} = 3$, Eq. (109) yields $\eta_i = 0.95$ for zeroth-order reactions, about 5% error. For large values of the Thiele modulus ($\varphi_{L,m,\,i} > 20$), the expression agrees quite well with the numerical solutions for the $\varphi_{L,m,\,i}$-η_i relationship for zeroth and second order reactions.

Hong *et al.* [224] derived a correction function that when multiplied by Eq. (109) yields an η-$\varphi_{L,m}$ relationship that agrees quite well with numerical solutions for any specified value of reaction order. The correction function depends on the Thiele modulus and the reaction order and is expressed as

$$f_c(\phi_{L,m,i}, m) = \left(1 + \frac{\sqrt{0.5}}{\left(2\ \phi_{L,m,i}^2\ +\ 1\middle/2\ \phi_{L,m,i}^2\right)}\right)^{0.5(1-m)^2}.$$

For first-order reactions ($m = 1$), the correction function equals 1.0. With this correction function, the effectiveness factor is predicted with errors less than 2% when compared to the numerically determined values for m^{th}-order reactions. Equation (109) multiplied by the above correction function is recommended for determining the effectiveness factor when the intrinsic reactivity exhibits fractional order.

In this section, the effectiveness factor is defined as the ratio of the real reactant consumption rate to the rate experienced if the reactant concentration within the particle equaled its surface concentration. In order to be more pedagogical, however, Wheeler [80] refers to the effectiveness factor as the normalized available surface area inside the particle, while Laurendeau [176] sees it as the normalized average reactant concentration (which was also assumed in obtaining Eq. (30)). It is important to realize that these three definitions of the effectiveness factor are not equivalent if the reaction order differs from unity.

As noted by others (see for example, Laurendeau [176]), under Zone I conditions, when diffusion through the particle pores is much faster than the kinetics such that the reactive gas concentration is fairly uniform inside particles, the Thiele modulus is small ($\varphi_{L,m,\,i} < 0.5$) and $\eta \approx 1$. It was also noted that under Zone II conditions when pore diffusion limitations cause concentration gradients to exist inside particles, the Thiele modulus is greater than 6 and $\eta \approx 3/\varphi_{L,m,\,i}$.

It should be emphasized that the above expression for the effectiveness factor assumes that the internal structure of the char particle is uniform. However, owing to variations in the properties of different coals and biomass materials and the conditions particles experience during devolatilization, a broad range of possible internal structures exists inside char particles. Employing the three-category classification system put forth by Wu *et al.* [225] (which is based on the 12-category system proposed by Bailey, *et al.* [226]), highly porous, thin-walled char particles are group I type char particles. These particles fragment more frequently and burn faster than the other char types. Cenospheres fall into this group. Sahu *et al.* [165] found that the cenospheric char particles produced from the smaller coal particles were 10% to 15% more reactive than the char particles of equal size produced from the larger particles of the same coal. Group II type char particles have medium porosity and thicker walls than group I particles and contain three or more relatively large cavities inside their outer surfaces. Group III type char particles are relatively dense with low porosity. They fragment less frequently and take longer to reach 100% conversion than the other char types. Ma and Mitchell [227] developed overall particle reaction rate expressions and Thiele-modulus-effectiveness factor relationships for char particles in each group. Bailey *et al.*, [226], Cloke *et al.* [228] and Wu *et al.* [229] have also developed burnout models based on char morphology.

Equations (71),(73) and (78) can be combined to show that the overall particle reaction rate (R_{ov}) and the apparent (R_a) and intrinsic ($R_{C,int}$) reactivities are related as follows:

$$R_{ov} = \left(\rho_{char} d_p / 6\right)\ R_a^{'} = \left(\rho_{char} d_p / 6\right) S_g R_c = \left(\rho_{char} d_p / 6\right) S_g \eta R_{c,s} \tag{110}$$

Thus, under Zone II conditions when $\eta = 3/\varphi$, this can be written as follows when the intrinsic reactivity is expressed in power-law form

$$R_{ov} = \left(\rho_{char} d_p / 6\right) R_a^{'} = \left(\frac{\rho_{char} d_p}{6}\right) S_g \left(\frac{3}{\phi}\right) R_{c,s} = \left(\frac{2\widehat{M}_C D_{eff} \rho_{char} S_g}{(m+1)\nu_i \widehat{R}_u T_p}\right)^{\frac{1}{2}} k_{int}^{\frac{1}{2}} P_{i,s}^{\frac{(m+1)}{2}}. \tag{111}$$

In the final expression on the right-hand side, ν_i denotes the moles of reactant species i reacted per mole of char converted to gaseous species. Writing the overall reaction rate and apparent reactivity in power-law forms as given in Eqs. (72) and (74), the above equation becomes:

$$\begin{aligned} A_{ov} \exp\left(\frac{-E_{ov}}{\widehat{R}_u T_p}\right) P_{i,s}^{n} &= \left(\rho_p d_p / 6\right) A_a^{'} \exp\left(\frac{-E_a^{'}}{\widehat{R}_u T_p}\right) P_{i,s}^{n'} \\ &= \left(\frac{2\widehat{M}_C D_{eff} \rho_{char} S_g}{(m+1)\nu_i \widehat{R}_u T_p}\right)^{\frac{1}{2}} A_{int}^{\frac{1}{2}} \exp\left(\frac{-E_{int}}{2\widehat{R}_u T_p}\right) P_{i,s}^{\frac{(m+1)}{2}} \end{aligned} \tag{112}$$

Since the temperature and pressure dependences of the apparent and intrinsic rate expressions should be the same, the following relations between apparent and intrinsic (or true) kinetic parameters exist:

$$n = n^{'} = (m+1)/2 \qquad \text{and} \qquad E_{ov} = E_a^{'} = E_{int}/2 \tag{113}$$

The relations for the activation energies were derived assuming that the exponential terms in Eq. (112) were the dominant temperature-dependent terms. Note that an apparent reaction order of one-half implies a true order of zero, a value that indicates that the reaction rate is independent of the reactive gas concentration, and that an apparent reaction order of unity implies a reaction rate that is proportional to the reactive gas concentration. It should be emphasized that the relations given in Eq. (113) are only valid when the effects of pore diffusion are appreciable, when $\eta = (3/\phi_{L,m})\sqrt{2/(m+1)}$.

3.3.2. Heat and mass transfer between fluid and particle

For the point particle approach, where the particle is significantly smaller than the size of the numerical mesh, the transfer of heat and mass through the boundary layer around the particle must be modelled. Modeling heat and mass transfer is not a straightforward task, since a number of complicating factors may be present. The most relevant examples of such complications are: 1) homogeneous (gas-phase) reactions may occur within the boundary layer, 2) there is typically a net outward flow of gas from the particle surface (Stefan flow), 3) several reactant gases may be involved in the heterogeneous reactions and 4) there may be a non-zero relative velocity between the particle and the fluid.

Over the years, the two most popular models developed to describe the boundary layer of a burning char particle are the single-film and double-film models. In the single-film model, homogeneous chemical reactions are assumed to be negligible in the boundary layer surrounding the particle. Oxygen diffuses from the surrounding gas towards the particle surface where reaction takes place, producing CO and CO_2. The global reaction for char oxidation is characterized as

$$C + \left(1 - \frac{f}{2}\right) O_2 \rightarrow f\ CO + (1-f)\ CO_2$$

where f, the fraction of carbon converted to CO, increases with temperature. In the single-film model, any CO diffusing from the particle escapes the boundary layer before being converted to CO_2 via homogeneous reactions in the far-field. Consequently, none of the energy from the exothermic oxidation of CO influences the carbon particle temperature, directly. In the double-film model, as oxygen diffuses towards the particle it reacts with CO at a diffusion flame established in the boundary layer of the particle, producing CO_2. The overall course of reaction at the diffusion flame surface (modeled as an infinitely thin film) is $CO + ½\ O_2 \rightarrow CO_2$. All of the oxygen is consumed within the thin film; no oxygen reaches the carbon particle. The CO_2 produced in the thin film diffuses in both directions from the film. Due to this, char conversion now proceeds through CO_2 gasification. This means that the convective heat to the particle is less negative (or may even be positive) than for the single-film model. Hence, the essential differences between the two models are that for the single-film model: 1) the concentration of oxygen at the particle surface is higher, 2) the convective heat transfer from the particle to the fluid is higher and 3) the concentration of the gasifying agents at the surface (typically CO_2) is lower.

It is quite difficult to probe the small boundary layers surrounding oxidizing carbon particles while in hot environments and as a result, there is no direct evidence on the extent to which CO is oxidized in the boundary layers of pulverized coal or biomass char particles. Also, it is not known *a priori* how far from the particle surface the flame front should be placed. This means that even though there may indeed be a flame within the boundary layer for large particles, the double-film model may not represent it in an accurate way.

Studies have indicated that the single-film model is applicable to particles less than about 100 μm in diameter and that the double-film model is applicable to particles larger than 1000 μm. Field *et al.* [230] reported results of calculations that indicate that for a 25-μm diameter carbon particle exposed to a gas containing 0.1 atm O_2, 0.05 atm H_2O and the balance N_2 at 2000 K, about 8% of the CO is oxidized to CO_2 within a distance of two diameters from the particle's surface and for a 50 μm diameter particle, about 30% of the CO is converted to CO_2 within this distance from the surface. A significant fraction of CO is converted to CO_2 within a distance of two diameters from the surface of a 100 μm carbon particle. Sexana [231] reviewed several papers that considered the applicability of single- and double-film models to burning carbon particles, and most of these papers support the use of the single-film model for particles having diameters less than 100 μm undergoing oxidation at temperatures greater than about 1500 K. For particles larger than 100 μm exposed to high temperature oxidizing environments, CO oxidation occurs in the boundary layers surrounding the particles. The moving flame-front model developed by Zhang *et al.* [232] also supports the use of the single-film model for particles having diameters less than 100 μm. A continuous-film model [*e.g.* [233-237]] is needed for accurate prediction of particle temperatures and hence, for accurate prediction of carbon particle oxidation behavior during conversion. The CO, O_2 and CO_2 concentration profiles across the boundary layer are calculated in continuous-film models. The model developed by Caram and Amundson [235] supports the application of the single-film model for particles having diameters less than 50 μm and the application of the double-film model for particles having diameters greater than 5 mm. While studying anthracite particles in the range 60-1000 μm through detailed numerical simulations, Gonzalo-Tirado *et al.* [238] found the single-film model to fit the predictions reasonably well for all particle sizes (in particular for the pulverized size range), while the double-film model tended to overestimate particle temperatures and hence, conversion rates. Also for the case of oxyfuel combustion, when the effect of gasification reactions may be significant, Geier *et al.* [239] showed that the single-film model gave good results.

Based on the above, it is recommended to use the single-film model for all particles as long as they are not very large, say less than 250 μm in diameter. In the particular case when very large particles are of interest, *i.e.* when boundary layer flames are known to be controlling the heterogeneous reactions, the reader is advised to use the resolved particle approach instead of the point particle approach with the double-film model. The reason for this is two-fold; first of all, large particles may not be considered as isothermal, since the Biot number may be larger than 0.1, such that the point particle approximation should not be used. Secondly, for resolved particles the boundary layer flame is automatically correctly positioned. Note that for a large particle, both the particle and its boundary layer should be resolved.

3.3.2.1. Heat transfer. The heat transfer coefficient applicable for the single film model, which is required for Eq. (48), is given by [58]

$$H = H_0 \theta_{therm} \tag{114}$$

where H_0, the heat transfer coefficient for a spherical particle without a Stefan flow, is expressed as

$$H_0 = \frac{\mathrm{Nu}\ \lambda_{gas}}{d_p} \tag{115}$$

and θ_{therm}, a correction term that accounts for the effects of Stefan flow, is given by

$$\theta_{therm} = \frac{\phi_{Ste,t}}{e^{\phi_{Ste,t}} - 1}. \tag{116}$$

The Stefan flow constant, $\varphi_{Ste,t}$, is given by

$$\phi_{Ste,t} = \frac{1}{H_0} \frac{\dot{m}_{char} c_{pg}}{\pi d_p^2} \tag{117}$$

where $\dot{m}_{char}$ is the consumption rate of char and c_{pg} is the heat capacity of the gas in the Stefan flow.

3.3.2.2. Mass transfer. The general multi-reactant form of mass transfer for the single film model is given as [107]

$$\dot{n}_i - X_{i,s}\dot{n}_{total} = -k_{im}\left(X_{i,\infty} - X_{i,s}\right) \tag{118}$$

In this expression, the molar flux of gaseous species i at the external particle surface is expressed as

$$\dot{n}_i = \sum_{k=1}^{N_r} \dot{n}_{i,k}, \tag{119}$$

where the molar flux of species i due to reaction k is given as

$$\dot{n}_{i,k} = \frac{\left(\nu''_{i,k} - \nu'_{i,k}\right)\widehat{\Re}_{k,p} S_t}{A_p} \tag{120}$$

and N_r is the number of heterogeneous reactions occurring on the solid surface.

Also, the mass transfer coefficient is expressed as

$$k_{im} = \frac{C_g \mathscr{D}_i \mathrm{Sh}}{d_p} \tag{121}$$

where Sh is the Sherwood number. The mole fractions of species i at the particle surface and in the far field are given by $X_{i,s}$ and $X_{i,\infty}$,

respectively, while the net sum of all gaseous species being produced and consumed is given by

$$\dot{n}_{total} = \sum_{i=1}^{N_s} \dot{n}_i \tag{122}$$

where N_s is the number of gas-phase species. Due to the fact that $\widehat{\Re}_{k,p}$ is a function of $C_{i,p}$ and hence, $X_{i,s}$, the above set of equations is implicit and has to be solved numerically for $X_{i,s}$. This can be done by employing a Newton-Raphson solver, for example.

In order to avoid having to solve the implicit equation for $X_{i,s}$, account can be made for the effect of the Stefan flow by the use of a modified mass transfer coefficient, similar to what is done in Eq. (114). This means that Eq. (118) simplifies to

$$\dot{n}_i = -k_{im,corr}\left(X_{i,\infty} - X_{i,s}\right) \tag{123}$$

where

$$k_{im,corr} = k_{im}\ \theta_{spec}, \tag{124}$$

$$\theta_{spec} = \frac{\phi_{Ste,s}}{e^{\phi_{Ste,s}} - 1} \tag{125}$$

and

$$\phi_{Ste,s} = \frac{\dot{n}_{total}}{k_{im}}.$$

Eq. (123) can now be turned into an algebraic expression for $X_{i,s}$ as long as the properties of the previous time step is used to calculate $\dot{n}_i$ from Eqs. (119) and (120).

By assuming only a single heterogeneous reaction where carbon is oxidized by O_2, and by combining Eqs. (120) and (123) together with Eqs. (9) and (37) to solve for $X_{O2,s}$, it can be shown that

$$X_{O2,s} = \frac{k_{im,corr}X_{O2,\infty}}{k_{im,corr} + k_{reac}} \tag{126}$$

where

$$k_{reac} = \frac{k_{O2}S_t P_s \eta}{A_p \widehat{R}_u T_s} \tag{127}$$

The relation $P_{O_2,s} = P_s X_{O_2,s}$ was also used when deriving the above result.

With the above expressions, the molar reaction rate can be found analytically (instead of numerically), and the expression of Baum & Street [240] can be recovered:

$$\dot{n}_{O2} = -\frac{k_{im,corr}k_{reac}}{k_{im,corr} + k_{reac}}. \tag{128}$$

The above expression is commonly only used with first-order, apparent reaction models, in which k_{reac} is given by the apparent kinetic rate instead of Eq. (102).

For single heterogeneous reactions, a number of simulation tools approximate the mass transfer coefficient (Eq. (121)) with the approximation of Smith [1]:

$$k_{im,approx} = \frac{\mathscr{D}_{i,0}}{d_p}\frac{P_0}{P}\left(\frac{T}{T_0}\right)^{\zeta} \tag{129}$$

where the subscript *0* refers to the reference state. For this approximation, the Sherwood number has been assumed to be 2 (implying zero relative velocity between particle and fluid) and the temperature exponent $\zeta = 1.75$ (although based on the Chapman-Enskog theory, it should be 3/2). For all DNS and most LES simulation tools, where both the real particle Sherwood number and species diffusivities are readily evaluated, the more accurate Eq. (121) should always be used to determine the mass transfer coefficient instead of Eq. (129).

3.3.3. Mode of conversion

When a char particle is converted due to combustion or gasification reactions, this inevitably yields a reduction in its mass. Whether this mass reduction comes from changes in its apparent density or its radius, depends on the mode of conversion. For a particle that is reacting in Zone I, the mode of conversion will be to decrease its apparent density, while for Zone III the corresponding mode of conversion is a decrease in particle radius. For most cases, however, the process proceeds in Zone II, which means that the mode of conversion is non-trivial. A popular, but far from general, relation between apparent density (ρ_{char}) and particle diameter (d_p) as a function of total mass (m_p), is given by

$$\rho_{char} = \rho_{char,0}\left(\frac{m_p}{m_{p,0}}\right)^{\alpha} \tag{130}$$

and

$$d_p = d_{p,0}\left(\frac{m_p}{m_{p,0}}\right)^{\beta} \tag{131}$$

where subscript *0* refers to the initial condition and the ash fraction of the particle is assumed to be zero. This approach is used in many char particle conversion models, for example [1,121,241-243]. For a spherical particle, α must be between zero and one, while $\beta = \frac{1-\alpha}{3}$. Numerical approaches where these relations are used assume that both exponents are constant throughout conversion. This is typically *not* a valid assumption. In order to allow α and β to vary with time, the two above expressions should be re-written in a piecewise form. By employing a Taylor expansion and re-organizing the equations, one then arrives at [244]

$$\frac{d\rho_{char}}{dt} = \frac{\alpha}{V_p}\frac{dm_p}{dt} \tag{132}$$

and

$$\frac{dr_p}{dt} = \frac{1-\alpha}{4\pi r_p^2 \rho_{char}}\frac{dm_p}{dt} \tag{133}$$

where r_p is the radius of the particle. (Ash treatment will be discussed in Section 3.4.) In the limit of small time-steps and spherical particles, the above relations are general and exact. The issue is to find the correct value of α. It is clear that for the limiting cases of Zone I and Zone III conversion, $\alpha = 1$ and $\alpha \to 0$, respectively. Haugen *et al.* [244] have shown that these equations generally hold for all char conversion zones (Zones I, II and III), and for homogeneously porous particles

$$\alpha = \eta, \tag{134}$$

where η is the effectiveness factor. As long as the effectiveness factor is known, the general approach of Haugen *et al.* [244], as presented by Eqs. (132)- (134), is just as straight forward and easy to calculate as the traditional, but not general, approach given by Eqs. (130) and (131). The reader is therefore advised to use the general approach of Haugen *et al.* [244]. The same authors also found that for Zone II conversion, it will always take some time before the external radius of the particle starts to decrease, *i.e.,* one must wait some time before Eqs. (132)-(134) become active. The relevant time is large for large effectiveness factors and approaches zero for small effectiveness factors. (See Haugen *et al* [244] for more details.)

For the special case of cenospheric particles, where the char particle

consists of a thin carbonaceous shell surrounding a gaseous void, Eq. (134) is not strictly valid since a cenosphere is not a homogeneously porous particle. Since all the carbonaceous mass of a cenosphere is located in its thin outer shell, the reactant concentration within the pores of the particle will be essentially constant, which yields Zone I conversion and an effectiveness factor of unity. This means that it will always be the apparent density of the particle that is reduced, not its radius. Based on this, it is clear that Eq. (134) is applicable even for cenospheres.

For so-called mixed chars, which consist of solid carbonaceous material with several large voids spread throughout, no theory for its mode of conversion exist. But, since this type of particle can be considered as in-between the two limiting cases of solid and cenospheric char, which both adhere to Eq. (134), it is reasonable to assume that Eq. (134) is valid also for mixed chars.

It should be noted that Eq. (134) is only relevant for intrinsic reaction rate models. The effectiveness factor is not defined for apparent reaction rate models and hence, the value of α cannot be found. With apparent reaction rate models, it is customary to set α to unity for char conversion in the Zone I regime, to set α to a fraction for char conversion in the Zone II regime or to set α to zero for conversion in the Zone III regime. As examples, from observations of size and apparent density variations during char conversion in Zone II, several researchers [1,116,120,142,242] set α in the range 0.25 to 0.7 for reaction in oxygen; Gonzalo-Tirado *et al.* [245] set α to ~0.9 for reaction in CO_2.

3.4. Ash

The mineral matter in coals and biomass is classified as being either inherent or adventitious, where the inherent mineral matter was part of the plant materials from which the coal and biomass were derived and the adventitious mineral matter is from sources outside the decaying plants (*e.g.,* from the minerals in the swamps in which plant materials were submerged or from the sediments that deposited on coal seams during coalification or from nutrients in the soil that plants absorbed). Most of the inherent mineral matter chemically or colloidally combined with the organic material during the time the coal and biomass were being formed, becoming mineral inclusions in the carbonaceous matrix. The adventitious mineral matter is mostly trapped inside particle pores, although some does combine chemically or colloidally with the organic material over time. Although some mineral matter is released from the coal and biomass particles during grinding and size reduction of the raw materials as well as during devolatilization, a significant portion of the mineral matter remains in the carbonaceous char matrix as mineral inclusions. During the char conversion process, the mineral inclusions either vaporize or become a part of the particle's ash. Ash is the mineral matter residue remaining after complete conversion of the carbonaceous material.

The major clay minerals in coals are calcite, chlorite, dolomite, illite, kaolinite, montmorillonite, pyrite, quartz, and siderite (see Table 2 for examples of chemical formulas). When modeling mineral matter effects during char conversion, the oxides of the major minerals (*e.g.,* Al_2O_3, CaO, FeO, MgO, and SiO_2) are taken to be representative of the mineral species in coal chars. The major minerals in biomass are albite, anhydrite, calcite, gehlenite, and sandidine (examples of chemical formulas are also shown in Table 2), and in modeling efforts, the oxides of the major minerals (*e.g.,* Al_2O_3, CaO, K_2O, MgO, Na_2O, P_2O_5, and SiO_2), are taken to be representative of the mineral species in biomass chars.

There are wide variations in the mineral matter compositions of coals and biomass. For most coals, the alumino-silicate clay minerals and quartz usually account for 60% to 90% of the total mineral matter in the coal. Silicon is generally the most abundant component of the mineral matter (ranging from 1 to 4% of the dry, whole coal weight), followed by aluminum and iron (ranging from 0.3 to 2.5%), and then calcium (ranging from 0.3 to 2.5%) [246]. Less abundant components are magnesium, titanium and potassium. The concentration of inorganic sulfur ranges from trace amounts to 2% of the dry coal weight [246]. The mineral matter in coal is highly variable with many trace minerals having concentrations less than 0.1%. Many of the trace minerals dispersed in coals were brought into the coal seam by water flow. Coal seams laid down in areas subject to periodic flooding usually contain a great deal of mineral dispersion intimately mixed with the coal.

Table 2
Major minerals in coals and biomass.

Coal Minerals		
Name	**Chemical Formula**	**Mineral oxides**
Calcite/dolomite	$CaCO_3/CaMg(CO_3)_2$	CaO/MgO
chlorite	$(Mg,Fe)_3(Si,Al)_4O_{10}(OH)_2 \cdot (Mg,Fe)_3(OH)_6$	MgO, SiO_2, FeO, K_2O, Al_2O_3
illite	$(K,H_3O)(Al,Mg,Fe)_2(Si,Al)_4O_{10}[(OH)_2,(H_2O)]$	MgO, SiO_2, FeO, K_2O, Al_2O_3
kaolinite	$Al_2Si_2O_5(OH)_4$	SiO_2, Al_2O_3
montmorillonite	$(Na,Ca)_{0.33}(Al,Mg)_2(Si_4O_{10})(OH)_2 \cdot nH_2O$	Na_2O, CaO, Al_2O_3, MgO
pyrite	FeS_2	FeO
quartz	SiO_2	SiO_2
siderite	$FeCO_3$	FeO
Biomass Minerals		
Name	**Chemical Formula**	**Mineral oxides**
albite	$NaAlSi_3O_8$	Na_2O, Al_2O_3, SiO_2
anhydrite	$CaSO_4$	CaO
Calcite, calcium oxalate	$CaCO_3$, CaC_2O_4	CaO
gehlenite	$Ca_2Al[AlSiO_7]$	CaO, SiO_2, Al_2O_3
sanidine	$K(AlSi_3O_8)$	K_2O, Al_2O_3, SiO_2

For biomass, the alkali metals (Na and K), alkaline earth metals (Ca and Mg), P, S, and Cl constitute from 15 to 58% of the total weight of inorganics in the solid, depending on the plant type. Some biomass materials have from 50 to 93% silicon (*e.g.,* barley straw, rice husks and switchgrass) whereas the silicon contents of wood, bark, twigs, needles, shoots, and leaves are generally less than 10%. The major ash-forming minerals typical in woody biomass, in order of abundance, are Ca, K, Si, and Mg. In typical herbaceous biomass, the major ash-forming minerals in order of abundance are Si, K, and Ca, [247].

During char conversion, the solid mineral inclusions can become vapors due to either high temperatures or chemical reaction. For minerals with low boiling points (high vapor pressures) (see Table 3), the char conversion temperature is high enough to melt and then vaporize the minerals. The oxides of such elements as As, Hg, K, P, and Na have low enough boiling points to readily vaporize in this way and escape the char particle early in the char conversion process. On the other hand, oxides that have high boiling points (low vapor pressures) such as those containing Al, Ca, Fe, Mg, and Si can become vapor through reactions in the carbonaceous matrix with a reducing gas (H_2 or CO) to form reduced mineral vapor phase species. These volatile mineral species diffuse through the particle pores during the entire char conversion process.

Table 3
Melting (mp) and Boiling (bp) Points of Selected Metals and Mineral Oxides in Coal and Biomass.

Species	mp (K)	bp (K)	Species	mp (K)	bp (K)
Al_2O_3	2345	3250	K	336	1032
As_2O_3	585	738	MgO	3073	3873
CaO	2845	3123	Mg	923	1363
Ca	1115	1757	Na_2O	1405	2223
Fe_2O_3	1838	N/A (decomposes)	Na	371	1156
FeO	1650	3687	P_2O_5	Sublimes	633
HgO	773	N/A (decomposes)	SiO_2	1964	2503
Hg	234	630	SiO	1975	2150
K_2O	1010	N/A (decomposes)	TiO_2	2116	3245

Evidence for the transport of volatile mineral species through char particle pores is provided in the HTREM images of Lunden [248]. The extent of nucleation, condensation and coagulation of the volatile mineral species inside char particles is unknown. In the high temperature reducing environments inside particles, mineral vapors that homogeneously nucleate and condense or heterogeneously condense on mineral inclusions have the potential to re-vaporize or react with reducing gases to form volatile mineral sub-oxides and metals. The mineral vapors will undergo nucleation, condensation and coagulation processes that lead to the formation of ultra-fine particulate matter in the gaseous environment outside the char particle.

Since the primary metals in coals and biomass are Al, Ca, Fe, Mg, and Si, whose oxides have low vapor pressures, only a small fraction of the total mineral matter content of coal and biomass chars vaporizes and leaves the particle; most of the mineral matter remains with the char particle during the char conversion process and becomes ash, the oxidized form of the mineral matter. As the char particle size shrinks due to heterogeneous chemical reaction at the char particle periphery, the mineral matter in the receded particle volume can either (a) contribute to an ash layer that accumulates on the outer surface of the char particle, (b) diffuse back into the particle, or (c) be shed from the particle. Mineral matter shedding from char particles has been hypothesized to be a primary contributor to the particles in PM_{10} formation [249].

Mineral matter diffusion and accumulation on the outer particle surface can each reduce char conversion rates. The volatile minerals that diffuse into particle pores decreases the available carbon per unit surface area in the char thereby effectively reducing char conversion rates. This has been characterized as an "ash dilution" effect [55,97,163]. The mineral matter that accumulates on the particle outer surface can retard the diffusional rates of reactive gases to the internal surfaces of the char particles (an ash film effect), resulting in reduced char conversion rates. Except for the models developed by Shaddix and co-researchers [55,97,142,163,249] and Tian *et al.* [249], nearly all char conversion models have neglected mineral matter vaporization and diffusion effects.

It is also possible for there to be catalytic effects, where some mineral components influence the rates of heterogeneous char reactions [101,250-254]. Ash catalytic effects are most significant at low reaction temperatures and with low rank coals and biomass. In combustion tests performed in 10 vol-% O_2 at low temperatures (648 - 748 K), Cope *et al.* [255] found that the intrinsic oxidation rates of CaO-containing lignite char particles decreased as burnout increased and that increased burnout resulted in decreases in CaO surface areas, a consequence of sintering. From this observation, it was hypothesized that the decreased burnout was a result of CaO sintering with increased time of exposure in the low-temperature environments. Evidence for a correlation between low-temperature char oxidation rates and CaO surface areas was presented. As noted by Cope *et al.* [255], there have been no reports of CaO sintering during the high-temperature oxidation of lignite char particles.

The impact of mineral matter depends on its composition and as a consequence, coal and biomass char conversion rates are impacted differently by the presence of mineral matter. Tomita *et al.* [252] employed acid washing to demineralize coals in order to investigate mineral catalytic effects and found both increases and decreases in the gasification rates of the acid washed coal chars. Although changes in gasification rates were noted, it is difficult to attribute these changes to catalytic effects. Zolin *et al.* [254] found that the presence of inorganic material increases coal char reactivity significantly at heat treatment temperatures up to 1273 K but that above this temperature the catalytic activity of the inorganic materials is severely reduced. It is usually concluded that minerals in coals have little catalytic effect on char reactivity to oxygen at high temperatures during pulverized coal combustion.

Ash catalytic effects have the potential to become important in the late stages of char conversion as carbonaceous material becomes more and more surrounded by ash. Char conversion rates have been observed to decrease in the late stages of conversion, indicating that ash inhibits oxygen transport to the carbonaceous material during the late stages of the char conversion process. Catalytic effects are often neglected in char conversion models developed for use in pulverized fuel-fired entrained flow simulations, the mineral matter is treated as an inert solid having no direct impact on char conversion rates. It is likely that since kinetic parameters are extracted from experimental data employing ash-containing chars, the catalytic effects are implicitly accounted for when determining reaction rate coefficients for the specific coal or biomass char being considered.

In gasifiers, catalytic effects may become significant as char particle temperatures decrease during the gasification process owing to the endothermic char-H_2O and char-CO_2 reactions that become effective after consumption of the oxygen in the gasifier. Account should be made for such catalytic effects for accurate prediction of overall char conversion. It would be necessary to determine the reactivity of the ash-free carbonaceous material in char gasification experiments and then determine how the reactivity is enhanced as the ash-content of the char is increased. Owing to the differences in catalytic activity of the various ash components, tests would need to be performed with individual ash components. A char reactivity sub-model would then have to be developed that reflects the increases in char reactivity as functions of ash content and ash type.

3.4.1. Modeling the mineral-containing char particle

In char conversion models, the char particle is typically assumed to be spherical and initially to consist of a carbonaceous matrix containing mineral matter inclusions. Owing to the conditions that the coal and biomass particles undergo during devolatilization, the mineral matter is assumed to have transformed to stable, mineral oxide phases. At the high temperatures the char particles experience during heterogeneous reaction, some of the volatile matter vaporizes and escapes the particle. In addition, as the carbonaceous material is converted to gaseous species due to reaction, an ash layer accumulates at the particle periphery as the particle diameter recedes. The thickness of the ash layer depends on the extent to which the ash either diffuses back into the char particle core or is shed from the particle's outer surface. At any particular time t during char conversion, the char particle of diameter $d_{p,t}$ is considered to consist of a carbonaceous core of diameter $d_{pc,t}$ surrounded by an ash layer of thickness δ_t, where $\delta_t = (d_{p,t} - d_{pc,t})/2$.

The mineral oxide inclusions are assumed to be spherical and uniformly distributed within the core particle volume. In addition, any volatile mineral species are assumed to be distributed within the pore volume of the carbonaceous matrix. While both the char and the mineral inclusions have true and apparent densities, only the true and apparent densities of the char and apparent density of the inclusions are needed in deriving expressions that describe the internal structure of the char. Over the course of char oxidation, only a small fraction of the mass of mineral oxide inclusions vaporizes. Since the mineral oxide inclusions lose mass via vaporization from their outer surfaces, the porosities of the inclusions remain constant during the entire char conversion process. Thus, both the true and apparent densities of the mineral oxide inclusions are assumed to remain constant during char conversion.

The total volume of all the mineral oxide inclusions (V_{MO}), the volume occupied by the solid carbonaceous material ($V_{true,char}$) and the volume occupied by the pores in the char ($V_{char\ pores}$) constitute the total particle core volume. The total mass of mineral oxide inclusions (m_{MO}) and the mass of the char (m_{char}) constitute the total mass in the particle core (neglecting the mass of gas species in the char particle pores, which is insignificant when compared to that of the char and mineral oxide inclusions). Thus, at any time during the char conversion process, the volume and mass of material in the particle's core are given by

$$V_{pc,t} = V_{true,char,t} + V_{MO,t} + V_{char\,pores,t} = \pi d_{pc,t}^3 \Big/ 6 \text{ and } \quad m_{pc,t} = m_{char,t} + m_{MO,t} \tag{135}$$

where the volume occupied by the solid carbonaceous material can be

expressed in terms of the true density of the char, $\rho_{true\ \ char}$: $V_{true\ \ char} = m_{char}/\rho_{true\ \ char}$. Furthermore, the apparent densities of the char and mineral oxide inclusions in the core of the particle at time t can be expressed as

$$\rho_{char,t} = m_{char,t}/V_{pc,t} \text{ and } \quad \rho_{MO,t} = m_{MO,t}/V_{MO,t}. \tag{136}$$

The above relations can be combined to show that the apparent density of the ash-containing porous char particle core at any time satisfies the following expression:

$$\rho_{pc,t} = \frac{m_{char,t} + m_{MO,t}}{V_{pc,t}} = \rho_{char,t} + \frac{m_{MO,t}}{V_{pc,t}}. \tag{137}$$

Since $V_{pc,t} = m_{char,t}/\rho_{char,t}$, the above expression for the apparent density of the particle at time t can be rewritten as

$$\rho_{pc,t} = \rho_{char,t} + \rho_{char,t}\frac{m_{MO,t}}{m_{char,t}} = \rho_{char,t}\left(1 + \frac{Y_{MO,t}}{(1 - Y_{MO,t})}\right) = \frac{\rho_{char,t}}{(1 - Y_{MO,t})} \tag{138}$$

where $Y_{MO,t}$ is the mass fraction of the mineral matter in the core of the particle at the time. The apparent density of the mineral oxide inclusions is assumed to be constant, and the apparent density of the char is governed by the mode of char particle conversion sub-model, discussed in Section 3.3.3. As indicated, by specifying the reactivity of the char and relations for the effectiveness factor, the apparent density, diameter and volume of the carbonaceous material in the core of the char particle can be followed in time.

3.4.2. Ash layer thickness

As the diameter of the char particle core decreases, the mineral matter in the receded core volume has the potential to add to an ash layer on the char particle's outer surface. Assuming that the mineral inclusions are always uniformly distributed within the carbonaceous core of the particle, the fraction of mineral oxide inclusions in the core at time t that are still in the core at time $t + \delta t$ is given by the ratio $\frac{V_{pc,t+\delta t}}{V_{pc,t}}$ (which equals $d^3_{pc,t+\delta t}/d^3_{pc,t}$) and the fraction of mineral oxide inclusions in the core at time t that were in the receded core volume is given by $1 - \frac{V_{pc,t+\delta t}}{V_{pc,t}}$. The inclusions would have lost some of their mass over the time δt due to vaporization. The mass of mineral matter in the ash layer at time $t + \delta t$ must equal the mass of mineral matter already in the ash layer at time t plus the mass of that fraction of the un-vaporized mineral matter in the receded volume that adds to the ash layer. Thus,

$$m_{ash\ layer,\ t+\delta t} = m_{ash\ layer,\ t} + \left(1 - V_{pc,t+\delta t}/V_{pc,t}\right)\left[\rho_{pc,t}V_{pc,t}Y_{MO,t} - \dot{M}_{MOvap,t}\delta t\right]f_{MM} \tag{139}$$

where $\dot{M}_{MOvap,t}$ is the rate at which all the vaporized mineral species leave the char particle core at time t and f_{MM} is the fraction of the mass of mineral matter in the receded core volume that adds to the ash layer. A fraction of this ash is shed from the particle, f_{shed}, and a fraction diffuses back into the char particle core, $(1 - f_{MM} - f_{shed})$. The impact of f_{MM} and f_{shed} on ash layer development dynamics has yet to be addressed. These variables should be set to zero since there is no information available on their values.

If the apparent density of the mineral matter in the ash layer is ρ_{MM}, then the mass of mineral matter in the ash layer at time t is

$$m_{ash\ \ layer,\ t} = \rho_{MM}V_{ash\ \ layer,t} = \rho_{MM}\frac{\pi}{6}\left(d^3_{p,t} - d^3_{pc,t}\right) \tag{140}$$

and the mass of mineral matter in the ash layer of thickness δ at time $t + \delta t$ is

$$m_{ash\ layer,\ t+\delta t} = \rho_{MM}V_{ash\ layer,t+\delta t} = \rho_{MM}\frac{\pi}{6}\left[\left(d_{pc,t+\delta t} + 2\delta_{t+\delta t}\right)^3 - d^3_{pc,t+\delta t}\right]. \tag{141}$$

Expressing all volumes in terms of diameters, the above three equations can be combined to yield the following expression for the ash layer thickness at time $t + \delta t$:

$$2\delta_{t+\delta t} + d_{pc,t+\delta t} = \left(d^3_{pc,t+\delta t} + d^3_{p,t} - d^3_{pc,t} + \frac{6\left(1 - \frac{d^3_{pc,t+\delta t}}{d^3_{pc,t}}\right)\left[\rho_{pc,t}\left(\frac{\pi d^3_{pc,t}}{6}\right)Y_{MO,t} - \dot{M}_{MOvap,t}\delta t\right]f_{MM}}{\pi\rho_{MM}}\right)^{\frac{1}{3}}. \tag{142}$$

In this approach, the char particle diameter includes the thickness of the ash layer. Consequently, the diameter of the char particle at time $t + \delta t$ is given by

$$d_{p,t+\delta t} = d_{pc,t+\delta t} + 2\delta_{t+\delta t}. \tag{143}$$

Similar expressions for the ash layer thickness have been derived by others [55,97,142,163].

3.4.3. Modeling reactive gas diffusion to the carbonaceous core of char particles

Owing to the ash layer surrounding the carbonaceous core of the char particle, the fluxes of reactive gases to this core are decreased and the diffusional mass transfer coefficient is reduced. Accounting for Stefan flow, the molar flux of reactive gas i ($j_{i,r_{pc}}$) at the outer surface of the carbonaceous particle core can be expressed as follows:

$$j_{i,r_{pc}} = -\left(\frac{\mathscr{D}_i P}{\gamma \widehat{R}_u T_{BL}}\right)\frac{\left(r_p/r_{pc}\right)(Sh/2+1)/r_{pc}}{\left(1 + \left(\mathscr{D}_i/\mathscr{D}_{i,ash}\right)\left(T_p/T_{BL}\right)\left(\delta/r_{pc}\right)(Sh/2+1)\right)} \times \ln\left(\frac{1 - \gamma P_{i,r_{pc}}/P}{1 - \gamma P_{i,\infty}/P}\right). \tag{144}$$

In this equation, γ is the change in the volume of the gas upon reaction at the outer surface of the carbonaceous core, T_{BL} is the effective boundary layer temperature, Sh is the Sherwood number, $\mathscr{D}_i$ and $\mathscr{D}_{i,ash}$ are the bulk diffusion coefficients of species i across the boundary layer and ash layer, respectively, and $P_{i,r_{pc}}$ and $P_{i,\infty}$ are the partial pressures of species i at $r_{pc}$and in the free stream, respectively. The Sherwood number was used to relate the thickness of the boundary layer to the particle diameter ($\delta = d_p/Sh = 2r_p/Sh$). Chen and Kojima [256] recommend evaluating $\mathscr{D}_{i,ash}$ via the expression $\mathscr{D}_{i,ash} = (\Theta_{ash})^2\ \mathscr{D}_i$, where Θ_{ash} is the ash layer porosity. Others [166,257,258] have used similar expressions to determine gas diffusivities in ash layers, with slightly different exponents on the ash porosity term. The flux of species i at r_{pc} times $4\pi r^2_{pc}$ yields the molar flow rate of species i into the carbonaceous core and must equal the rate that the species is consumed via heterogeneous chemical reaction. This determines the value of $P_{i,r_{pc}}$. It is noted that the greater the ash layer thickness, the lower the flux of reactive gas to the carbonaceous particle core.

3.4.4. Mineral matter vaporization rates

Modeling the vaporization of the mineral inclusions in coals and biomass has been the subject of numerous investigations (see for example, references [259-271]). The mineral oxides within the carbonaceous matrix can react with CO to form volatile metal-containing species. The rates at which these gaseous species are released from the mineral oxide inclusions are limited by the rates that the volatile oxide species can diffuse from the mineral inclusions, entering the carbonaceous matrix surrounding the mineral inclusions. In a char particle, the vaporization rates of individual inclusions are not independent since the inclusions influence each other via the mineral vapor field established within the pores of the char particle as the mineral species diffuse. Employing the approach taken by Quann [260,261], the vaporization rate for a single inclusion of diameter d_{MO} embedded in a carbon matrix having an established mineral vapor field is approximated as follows:

$$\dot{M}_{MOvap(d_{MO})} = \frac{2\pi d_{MO}\widehat{M}_{MS_i}\mathscr{D}_{MS_i,eff}}{\widehat{R}_u T_p}\left(P^{eq}_{MS_i} - P_{MS_i}\right). \quad (145)$$

Here, $\widehat{M}_{MS_i}$ is the molecular weight of the volatile mineral species i, $\mathscr{D}_{MS_i,eff}$ is the effective diffusion coefficient of the volatile mineral species in the pores of the carbonaceous matrix, $\widehat{R}_u$ is the universal gas constant, T_p is the particle temperature, $P^{eq}_{MS_i}$ is the equilibrium partial pressure of the volatile mineral species at the surface of the mineral inclusion, and P_{MS_i} is the partial pressure of the volatile mineral species at the location of the mineral inclusion. This expression indicates that the vaporization rate of a mineral inclusion depends upon its position in the char particle, as reflected through the local partial pressure of the mineral oxide vapor, which is influenced by the vaporization rates of all the inclusions. The adequacy of such a vaporization expression depends on a quasi-steady reduced mineral oxide concentration profile established inside the char particle, a likely situation since the characteristic time for mineral matter diffusion is much shorter than the characteristic time for char combustion. Owing to the low volume fraction of inclusions in the char, Quann [260] applied a mean field approximation [272] to evaluate the mole fraction profile of mineral vapors in a porous char particle that results from generation of mineral vapors from a group of uniformly distributed inclusions, and determined a relation for the total vaporization rate from the single char particle. In this mean field approximation, although there can be an ash film, most of the mineral matter is distributed throughout the carbonaceous core – the mean field approximation approach is still applicable. Following the same approach, the instantaneous total vaporization rate (in kg/s) from a char particle having embedded mineral inclusions is given by

$$\dot{M}_{MOvap,t} = \eta_{vap} N_I \left(\dot{M}_{MOvap(d_{MO})}\right)^{isolated} = \eta_{vap} N_I \frac{2\pi d_{MO}\widehat{M}_{MS_i}\mathscr{D}_{MS_i,eff}}{\widehat{R}_u T_p} P^{eq}_{MS_i} \quad (146)$$

where N_I is the total number of inclusions in the char particle and η_{vap} is an effectiveness factor for vaporization, defined as the ratio of the total vaporization rate of a matrix of uniform inclusions vaporing under diffusion control with particles communicating (via mineral vapors in the pores) to the vaporization rate of N_I isolated inclusions. It is expressed as

$$\eta_{vap} = \frac{3}{\phi_I}\left[\frac{1}{\tanh(\phi_I)} - \frac{1}{\phi_I}\right]\left[1 - \frac{(\mathscr{D}_{MS_i}/\mathscr{D}_{O_2})}{\alpha_I(\mathrm{Sh}/2+1)}\left(\frac{T_{BL}}{T_p}\right)\left(\frac{\phi_I}{\tanh(\phi_I)} - 1\right)\right]^{-1}. \quad (147)$$

Here, $\mathscr{D}_{MS_i}$ and $\mathscr{D}_{O_2}$ are the bulk diffusivities of the diffusing mineral species and oxygen, respectively, and $\phi_I = ((d_P/d_I)\sqrt{3\varphi_I})$ is the Thiele modulus, where d_P and d_I are the diameters of the char particle and the mineral inclusions, respectively, and ϕ_I is the total volume fraction of inclusions inside the particle. The parameter α_I accounts for the effects of Stefan flow in the boundary layer surrounding the char particle and is expressed as follows:

$$\alpha_I = \frac{\ln\left[(1-\gamma P_{O_2}(r_p)/P)/(1-\gamma P_{O_2,\infty}/P)\right]}{1-\exp(\alpha')} \quad (148)$$

where in this expression

$$\alpha' = \left(\frac{\mathscr{D}_{O_2}(\mathrm{Sh}/2+1)}{\mathscr{D}_{MS_i}}\right)\frac{\ln\left[(1-\gamma P_{O_2}(r_p)/P)/(1-\gamma P_{O_2,\infty}/P)\right]}{\left[1+\left(\frac{\mathscr{D}_{O_2}}{\mathscr{D}_{O_2,ash}}\right)\left(\frac{T_p}{T_{BL}}\right)\left(\frac{\delta_{ash}(\mathrm{Sh}/2+1)}{r_{pc}}\right)\right]}. \quad (149)$$

The Thiele modulus φ_I is dependent solely on the volume fraction of inclusions and inclusion size for a given char particle. The vaporization effectiveness factor (η_{vap}) as a function of φ_I is shown in Fig. 11. Note that as φ_I increases, η_{vap} decreases. Also note that differences in the ratio $\mathscr{D}_{MS_i}/\mathscr{D}_{O_2}$ and the ash content of the char have relatively minor impact on the η_{vap}-φ_I relationship. Over the temperature ranges of interest to coal and biomass combustion processes, this ratio of diffusion coefficients is relatively insensitive to temperature and as such, the curves shown in the figure change little with change in temperature. The parameter φ_I increases with increasing volume fraction of mineral inclusions in the char, which increases with ash content. Hence, the higher the ash content of the char, the lower the effectiveness factor for vaporization. The higher the ash content of the char, the higher the mole fraction of the diffusing mineral species in the pore volume, which reduces the vaporization rates of the individual inclusions (as reflected in Eq. (145)).

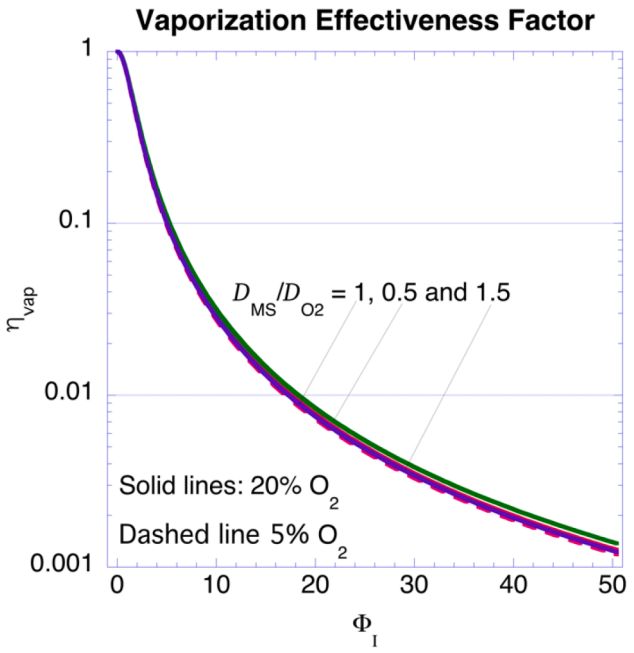

Fig. 11. Vaporization effectiveness factor as a function of φ_I calculated for a 100 μm diameter char particle undergoing combustion in 5% and 20% oxygen at 1750 K. The mineral vapor-to-O_2 diffusivity ratio, $\mathscr{D}_{MS_i}/\mathscr{D}_{O_2}$, is a parameter.

For a given ash content, the parameter φ_I increases with increasing ratio d_P/d_I. Consequently, the vaporization effectiveness factor decreases with a decrease in inclusion diameter. This is because the decreasing inclusion size increases the number of inclusions to maintain the given ash-content of the char particle. Smaller inclusion sizes result in higher overall vaporization rates for the char particle. As reported by Padia [265], the mineral matter in coals exists as either finely disseminated crystallites or inclusions nominally 2 μm or less in diameter. For char particle diameters in the range 50 to 100 μm having ash-contents in the range 5%-20%, values of φ_I are in the range 5 to 40. Expressions analogous to those above for the total mineral vaporization rate and vaporization effectiveness factor have been employed by others to describe mineral inclusion vaporization rates during coal char combustion (*e.g.*, [55,264,270,271]). Equations (146) – (149) simplify to the η_{vap}-φ_I relations derived by Quann [260] and employed by Niu *et al.* [163] when it is assumed that (i) char burning rates are diffusion-limited ($P_{O_2}(r_p) = 0$), (ii) CO is the sole product of the heterogeneous reaction ($\gamma = -1$) and (iii) the boundary layer surrounding the particle is quite large compared to the particle diameter ($\mathrm{Sh} = 0$).

Since the apparent density of the mineral inclusion is assumed to be constant during vaporization, the diameter of the inclusion can be followed as mineral vapors are released. Thus,

$$\frac{d}{dt}\left(m_{MO(d_{MO})}\right) = -\frac{\pi\rho_{MO}}{6}\frac{d}{dt}\left(d^3_{MO}\right) = \dot{M}_{MOvap(d_{MO})}. \quad (150)$$

Integrating from time t to time $t + \delta t$ and solving for the mineral oxide particle diameter at time $t + \delta t$ yields

$$d_{MO,t+\delta t} = \left(d_{MO,t}^2 - \frac{4\,\dot{M}_{MOvap(d_{MO})}}{\pi d_{MO,t}\rho_{MO}}\delta t \right)^{\frac{1}{2}}. \tag{151}$$

Note that since the coefficient of δt is not constant but depends on the size of the included particle, vaporization does not follow a d_{MO}^2-power law relationship.

The mineral species that leave the surfaces of the mineral inclusions transport through the carbonaceous matrix via diffusion. Due to the small diameters of the pores, Knudsen diffusion will be the primary mode of diffusion in the porous structure. Hence, the approach of Satterfield [50] can be used to determine the effective diffusion coefficient:

$$\begin{aligned}\mathscr{D}_{Kn,MS_i,eff} &= \frac{\theta_{eff}\theta_c \mathscr{D}_{Kn,i}}{\tau} = \frac{\theta_{eff}\theta_c}{\tau}\left(9,700\left(\frac{2\theta_{eff}}{S_g\ \rho_p}\right)\sqrt{\frac{T_p}{\widehat{M}_{MS_i}}}\right) \\ &= 19,400\left(\frac{\theta_c\theta_{eff}^2}{\tau\ S_g\ \rho_p}\right)\sqrt{\frac{T_p}{\widehat{M}_{MS_i}}}.\end{aligned} \tag{152}$$

When using this expression, the specific surface area (S_g) and apparent density (ρ_p) of the particle are in cm^2/g and g/mol, respectively, and the particle temperature is in K. The effective porosity of the carbonaceous matrix including the mineral oxide inclusions is calculated based on the fractions of the core volume that the carbonaceous material and mineral matter occupy:

$$\theta_{eff} = \frac{V_{char}}{V_{pc}}\theta_{char} + \frac{V_{MO}}{V_{pc}}\theta_{MO}. \tag{153}$$

Here, θ_{char} and θ_{MO} denote the porosities of the char and mineral oxide inclusions, respectively. The porosity of the char varies with char conversion and is discussed in Section 3.1.1. Considering the ash in the core of the particle, Eq. (19) should be modified, as follows, when determining the effective diffusion coefficient of any species i diffusing through the pores of the particle:

$$\mathscr{D}_{Kn,i,eff} = 19,400\left(\frac{\theta_c\ \theta_{eff}^2}{\tau\ S_g\ \rho_p}\right)\sqrt{\frac{T_p}{\widehat{M}_i}}.$$

A linear mixing rule is assumed for the specific surface area of the particle [179]:

$$S_{g,p} = Y_{MO}S_{g,MO} + (1 - Y_{MO})S_{g,char}. \tag{154}$$

Campbell [179] measured values of 5 ± 10 m^2/g for the ashes of both coal and biomass chars considered in his investigations. The specific surface area of the char also varies with char conversion and is discussed in Section 3.1.2. Often, the contribution of the specific surface area of the mineral matter is neglected in comparison to that of the char when determining the specific surface area of the particle. The question arises as to the extent to which mineral matter in the char impacts BET measurements of char specific surface area. Do BET specific surface area measurements using CO_2 or N_2 as adsorption gases include the specific surface areas of both the mineral matter and the char? To what extent do these gases adsorb onto mineral matter components? Could the specific surface area measurements performed by Campbell [179] using coal and biomass ashes be indicative of the specific surface areas of any residual carbonaceous materials remaining in the ash? These questions have not yet been definitively answered.

The parameters that define the effective diffusion coefficient for volatile mineral species transport through the carbonaceous matrix are evaluated at the conditions of the char at the time of interest. Similar approaches have been taken by others to determine the total mineral oxide vaporization rates from the mineral inclusions in the char when the physical characteristics of both the carbonaceous matrix and the mineral matter are considered [179,271].

In order to evaluate mineral oxide vaporization rates, it is necessary to determine the partial pressure of the volatile mineral oxide species at the surface of the mineral inclusion. When evaluating mineral oxide vaporization rates during char conversion, it is assumed that vaporization of isolated mineral inclusions (MO_n) in the char matrix occurs by chemical reduction to form volatile metal sub-oxides or fully reduced metals (MO_{n-1}). It is hypothesized that the mineral oxides are reduced by CO in the local conditions existing inside char particles via the following type reaction:

$$MO_n(s,l) + CO \leftrightarrow MO_{n-1}(g) + CO_2.$$

The equilibrium constant for this reaction can be expressed as

$$K_p = \exp\left(-\frac{\Delta\widehat{G}_R}{\widehat{R}_u T_p}\right) = \left[\frac{\left(\frac{P_{CO_2}}{P_{ref}}\right)\left(\frac{P_{MO_{n-1}}}{P_{ref}}\right)}{\left(\frac{P_{CO}}{P_{ref}}\right)a_{MO_n}}\right]_{eq} \tag{155}$$

where $\Delta\widehat{G}_R$ is the Gibbs function change for the reaction, a_{MO_n} is the activity of the solid (or liquid) mineral oxide and P_{ref} is the reference pressure (taken as 1 atm). Rearranging this expression, solving for the equilibrium partial pressure of the mineral sub-oxide yields

$$\left(\frac{P_{MO_{n-1}}}{P_{ref}}\right)^{eq} = a_{MO_n}K_p\left(\frac{P_{CO}}{P_{CO_2}}\right). \tag{156}$$

Note that the reduced volatile species partial pressure at the surface of the mineral oxide inclusion depends on the CO-to-CO_2 ratio in the gas phase at the position of the mineral inclusion. Also note that the larger the equilibrium constant of the mineral oxide reducing reaction, the greater the partial pressure of the reduced species at the surface of the mineral inclusion and hence, the faster the rate of vaporization. The activity of the mineral oxide is taken as unity in nearly all char models that have considered ash vaporization; consequently, the mineral oxide partial pressures determined are maximum values, rendering maximum values calculated for the vaporization rates. As noted by Neville *et al.* [269], reactions between acidic and basic constituents in the mineral inclusions can influence the activity of the vaporizing species.

Previous work by Quann and Sarofim [261] has indicated that the refractory oxides of aluminum, calcium, iron, magnesium, and silicon account for most of the submicron particulate matter formed during coal combustion. Modeling efforts indicated that at the high temperatures of interest, Ca, Fe, Mg, and Si vaporization is primarily in accord with the reduction reaction discussed above with the reactions being in equilibrium [261,273]. Key reactions are shown in Table 4 as reactions R.1 to R.4. Quann and Sarofim [261] considered other SiO_2 reduction reactions but reaction R.4 was found to be dominant during coal combustion. This was also the findings of Xu *et. al.*, [274], who considered SiO_2 reduction via H_2 and H_2O as well.

Table 4
Equilibrium Constants for Mineral Oxide Reduction Reactions.

	CO Reduction reaction	**Equilibrium constant, K_p**		
		1800 K	**2000 K**	**2200 K**
R.1	$CaO(s) + CO \leftrightarrow Ca(g) + CO_2$	$9.19e^{-10}$	$2.78e^{-08}$	$4.46e^{-07}$
R.2	$FeO(l) + CO \leftrightarrow Fe(g) + CO_2$	$3.86e^{-06}$	$4.05e^{-05}$	$2.70e^{-04}$
R.3	$MgO(s) + CO \leftrightarrow Mg(g) + CO_2$	$1.78e^{-07}$	$3.57e^{-06}$	$4.11e^{-05}$
R.4	$SiO_2(l) + CO \leftrightarrow SiO(g) + CO_2$	$5.50e^{-07}$	$1.53e^{-05}$	$2.26e^{-04}$
R.5	$Al_2O_3(s) + 2CO \leftrightarrow Al_2O(g) + 2CO_2$	$5.89e^{-17}$	$1.80e^{-14}$	$1.24e^{-13}$
R.6	$FeS(l) \leftrightarrow Fe(g) + 0.5S_2(g)$	$2.17e^{-06}$	$8.32e^{-05}$	$1.61e^{-03}$
R.7	$K_2O(l) + CO \leftrightarrow K_2(g) + CO_2$	$2.70e^{+00}$	5.95^{+00}	$1.09e^{+01}$
R.8	$Na_2O(l) + CO \leftrightarrow Na_2(g) + CO_2$	$9.65e^{-02}$	$2.72e^{-01}$	$6.07e^{-01}$
	H_2 Reduction reaction	**Equilibrium constant, K_p**		
		1800 K	**2000 K**	**2200 K**
R.9	$CaO(s) + H_2 \leftrightarrow Ca(g) + H_2O$	5.65^{-10}	$2.45e^{-08}$	$5.22e^{-07}$
R.10	$FeO(l) + H_2 \leftrightarrow Fe(g) + H_2O$	$2.37e^{-06}$	$3.56e^{-05}$	$3.16e^{-04}$
R.11	$MgO(s) + H_2 \leftrightarrow Mg(g) + H_2O$	$1.09e^{-07}$	$3.14e^{-06}$	$4.81e^{-05}$
R.12	$SiO_2(l) + H_2 \leftrightarrow SiO(g) + H_2O$	$3.38e^{-07}$	$1.35e^{-05}$	$2.65e^{-04}$
R.13	$Al_2O_3(s) + 2H_2 \leftrightarrow Al_2O(g) + H_2O$	$4.72e^{-18}$	$5.32e^{-15}$	$1.59e^{-12}$
R.14	$K_2O(l) + H_2 \leftrightarrow K_2(g) + H_2O$	$1.66e^{+00}$	5.25^{+00}	$1.28e^{+01}$
R.15	$Na_2O(l) + H_2 \leftrightarrow Na_2(g) + H_2O$	$5.93e^{-02}$	$2.39e^{-01}$	$7.11e^{-01}$

With aluminum inclusions, the reaction stoichiometry is slightly different with the likely vaporization reaction given by reaction R.5 in Table 4 [273]. The equilibrium partial pressure of the sub-oxide would be proportional to the square of the CO-to-CO_2 ratio.

With iron, there is uncertainty with respect to the governing vaporization reaction owing largely to the different forms of iron in the coal: siderite ($FeCO_3$), pyrite (FeS_2) and to a lesser extent, rozenite ($FeSO_4{\cdot}4H_2O$). The iron in both siderite and rozenite can likely be represented by FeO after heat treatment. Pyrite transitions at high temperatures could proceed through molten pyrrhotite (FeS) that vaporizes, yielding gaseous iron (Fe) and sulfur (S_2), as given by reaction R.6 in Table 4. For this reaction, the gaseous iron partial pressure at the surface of the molten pyrrhotite particle is inversely proportional to the square-root of the S_2 partial pressure. The higher the S_2 partial pressure, the lower the Fe partial pressure at the pyrrhotite inclusion surface and hence, the lower the pyrrhotite vaporization rate.

For biomass, the vaporization of the oxides of alkali metals should also be considered (see reactions R.7 and R.8 in Table 4). The partial pressures of the volatilized alkali metals at the surfaces of the inclusions satisfy the generalized expression given by Eq. (156).

Values of the equilibrium constants for reactions R.1 to R.8 at 1800, 2000, and 2200 K are shown in Table 4. Thermodynamic data were obtained from the literature [275,276]. The relatively high values of the equilibrium constants of the alkali metal reactions suggest that prior to significant char conversion, sodium and potassium inclusions would completely vaporize at such high temperatures. Aluminum inclusions, on the other hand, would hardly vaporize at all. All of the minerals in coals and biomass would vaporize to some extent over the course of char conversion owing to the high-temperature, reducing environments inside char particles. For multiple species vaporizing simultaneously, the total mineral matter vaporization rate as given by Eq. (146) would have to be modified to include contributions from the different types of mineral oxides present in the char.

In gasifying conditions, it is possible for mineral oxide inclusions to be reduced via reactions with hydrogen since the H_2 concentrations inside char particles may be significant, owing to the char-steam reaction ($C + H_2O \rightleftharpoons CO + H_2$). Mineral oxide reduction reactions that produce volatile sub-oxides or metals would have the form

$$MO_n(s) + H_2 \rightleftharpoons MO_{n-1}(g) + H_2O.$$

Equilibration of these type of reactions leads to the following expression for the sub-oxide partial pressure at the surface of the reacting mineral inclusion

$$\left(\frac{P_{MO_{n-1}}}{P_{ref}}\right)^{eq} = a_{MO_n} K_{p,R.9} \left(\frac{P_{H_2}}{P_{H_2O}}\right). \tag{157}$$

It is noted that the higher the H_2-to-H_2O ratio during the char conversion process, the greater the mineral oxide vaporization rate.

The equilibrium constants of mineral oxide reduction reactions with H_2 are also shown in Table 4 at 1800, 2000, and 2200 K. Nearly all are comparable to their analogs with CO as the reducing agent. These reactions are unimportant during combustion in air owing to the much lower values of P_{H_2}/P_{H_2O} compared to P_{CO}/P_{CO_2} at combustion temperatures however in gasification conditions, these reactions are likely to be significant contributors to mineral oxide vaporization and should be considered in char models if mineral matter vaporization rates are to be accurately predicted.

The impact of steam on mineral oxide vaporization rates during char combustion in O_2/CO_2 environments was demonstrated by Xu *et. al.*, [274] who found that vaporization rates were enhanced by the addition of steam. These investigators considered reactions between SiO_2 and H_2O and found that the equilibrium constants of all possible reactions were quite small. Based on the work of Filsinger and Bourrie [277] and Cheng and Cutler [278], the most likely reaction is $SiO_2(s) + 2\ H_2O \rightleftharpoons Si(OH)_4(g)$, and the equilibrium constant of this reaction at 2000 K is of the order 10^{-11}, seven orders of magnitude smaller than the equilibrium constants of SiO_2 reduction via CO and H_2. This suggests that SiO_2 vaporization via reaction with H_2O is negligible during char oxidation and can be neglected in char conversion models developed for oxidizing environments. However, as pointed out above, and also noted by Xu *et al.* [274] in $O_2/CO_2/H_2O$ environments, H_2 produced via the char-H_2O reaction promotes mineral oxide reduction, yielding volatile mineral sub-oxides and metals.

Only a small fraction of the mineral matter in chars vaporizes. In studies investigating ash vaporization during pulverized coal combustion, Quann [260] observed that a greater amount and percentage of ash vaporized during combustion of the low rank coals examined than for the bituminous coals. From 1% to 2% of the ash vaporized with bituminous coals and about 5% vaporized with low rank coals. A lignite from North Dakota exhibited the highest extent of ash vaporization with almost 9% of its ash vaporizing. The higher concentrations of the alkaline earth metals in the lower rank coals explain these observations.

Vaporization of the minerals in coals and biomass have been studied by many researchers. For examples of results employing several coals and different types of biomass, see references [260,264,278-282]. Nearly all support chemical reduction of the included mineral oxides to volatile mineral sub-oxides or metals. All support equilibration of the governing chemical reactions when CO is the reducing agent. It is quite likely that in gasifiers, the governing chemical reactions when H_2 is the reducing agent are also equilibrated. No char oxidation model has been developed to date that accounts for vaporization rates of different volatile mineral sub-oxides and metals released from different types of mineral inclusions as a consequence of their reactions with both CO and H_2 during the char conversion process. Multicomponent effects were discussed by Quann [260], who considered SiO_2, MgO and CaO as isolated pure phases existing inside the char particle. As noted, the equilibrium partial pressures at the surface of one inclusion influences the equilibria of another inclusion of different composition due to the products of the different mineral oxide reduction reactions. The partial pressures of CO_2 and H_2O will differ from their pure component cases.

3.4.5. Modeling the impact of mineral matter on char particle temperature

As noted, mineral matter vaporization, diffusion and ash layer buildup can influence char reactivity, which in turn will impact char particle temperatures. The char particle temperature is also impacted by the specific heat of the mineral matter in the char. Quite a few models include the impact of mineral matter on char particle temperature by accounting for the specific heats of the mineral oxides as well as that of the carbonaceous material when determining the effective specific heat of the particle (see for example, reference [179]):

$$c_{p,p} = Y_{MO} c_{p,MO} + (1 - Y_{MO}) c_{p,char} \tag{158}$$

where Y_{MO} is the mass fraction of the mineral oxides in the char particle at time t. The higher the ash content of the coal char particle, the lower the char particle temperature during char conversion.

3.4.6. Modeling mineral matter nucleation, condensation and coagulation

In the high-temperature reducing environments inside reacting char particles, the equilibrium partial pressures of the mineral sub-oxides and metals produced from chemical reduction of the mineral oxide inclusions are higher than their saturation pressures. This means that homogeneous nucleation is possible. The nucleated clusters could collide with the pore walls and stick, potentially hiding carbon sites. It is quite likely, however, that inside the carbonaceous core, the nucleated clusters re-vaporize before significant growth. Nucleation and re-vaporization rates are hypothesized to be nearly in balance inside char particles at high temperatures. In most char conversion models, the mineral matter that vaporizes during char conversion is assumed to escape the particle, leading to the formation of PM_{10} and smaller sized particles in the reactor volume. Any consequences of nucleation,

condensation and coagulation processes inside char particles during char conversion are usually neglected in char conversion models.

As the volatile reduced mineral vapors escape the char particle, diffusing into the surrounding environment, they react with gaseous species in the environment forming volatile mineral oxides. In combustors, the reduced mineral species react with oxygen and in gasifiers, with steam and carbon dioxide. At the lower temperatures outside particles, the volatile mineral oxides can homogeneously nucleate and condense, forming nano-sized particles that coagulate and coalesce. Since nano-size particle formation occurs outside of the char particle and does not significantly impact char particle conversion, discussion of modeling mineral matter nucleation, condensation and coagulation is confined to the Appendix, (see Appendix C). Niu and co-researchers [163,283,284] have developed char combustion models that account for mineral matter vaporization and vapor transport inside char particles as well as mineral vapor oxidation, nucleation, condensation, and coagulation in the boundary layers outside particles leading to particulate matter in flue gases.

3.5. Fragmentation

During the char conversion process, char particles fragment, producing a significant number of small particles differing in size and apparent density. Since char particle conversion rates depend on these physical properties, it is clear that fragmentation plays a role in determining the extent of overall mass loss and the time for overall char conversion to gaseous species during the char conversion process.

Fragmentation patterns fall into three categories: attrition, breakage and percolation. During attrition, very small char particles are shed from the peripheries of the fragmenting particles. The sizes of the parent, fragmenting particles remain relatively unchanged during attrition events. During breakage, char particles break into a few parts, say two or three, and during percolation, a distribution of fragment sizes are created, ranging from the smallest particles shed in attrition to nearly the sizes of the parent, fragmenting particles.

The apparent densities of the fragments produced can be lower or higher than the apparent density of the parent particles. For accurate prediction of mass conversion rates and times for complete char conversion, account must be made for the impact that fragmentation has on the variations in the size distribution and apparent densities of particles during the char conversion process.

When accounting for char fragmentation, the numbers of particles of all sizes and apparent densities must be tracked during char conversion. Particle population balance models have been developed to implement the process [13,212,285-288]. In such population balance models, the particle size distribution is described by a number of size bins, where each size bin is characterized by its upper and lower size cutoffs. The largest particles in the size distribution are contained in bin 1 (with upper and lower size cutoffs of d_1 and d_2, respectively) and the smallest particles in the size distribution are contained in bin n (with upper and lower size cutoffs of d_n and 0, respectively). In most cases, the upper and lower cutoffs of bin i are determined from the following expression:

$$\gamma = \frac{d_i}{d_{i+1}}. \tag{159}$$

This treatment yields evenly spaced size intervals in the log domain, which effectively resolves the size distribution in the small size range where particle number densities are high.

3.5.1. The fragmentation progeny matrix

The fragmentation progeny matrix, which defines the fragment size distribution for each pattern of fragmentation, is based on the work of Austin [285] who simulated the grinding of particles using a ball mill. The progeny matrix was later employed by Dunn-Rankin [287] in a kinetic model for simulating the evolution of particle size distributions during char combustion. The elements of the progeny matrix depend upon the type of fragmentation and are denoted by b_{ij}, where fragmenting particles in bin j produce fragments in bin i, where $j \le i$. The expressions presented below for the elements of the fragmentation progeny matrix were derived assuming that all fragments had the same apparent density as the fragmenting particle and hence, the volume of the fragmenting particle was conserved, *i.e.,*

$$d_{p,j}^3 = \sum_{i=j}^{n} b_{ij} d_{p,i}^3. \tag{160}$$

Here, a fragmenting particle of diameter d_j produces fragments of diameter d_i.

Attrition. Only a small fraction f (say, 0.1%) of the mass of the particle is lost during an attrition event. The fragmenting particle remains in bin j but may fall into bin j+1 if the particle size was already near the lower size cutoff of the bin. The attrited fragments fall into bins m_j to n, where the sizes of the largest attrited fragments (those falling into bin m_j) depend on the size of the fragmenting particle, the larger the fragmenting particle the larger the sizes of the attrited fragments. For char particles in the pulverized fuel size-range (say 100 μm), bin m_j may contain attrited particles nominally 0.05 μm in diameter whereas for millimeter size char particles, bin m_j may contain attrited particles nominally 0.5 μm in diameter. The elements of the attrition progeny matrix are as follows:

$$b_{ij} = \begin{cases} 0 & j+2 \le i \le m_j - 1 \\ \dfrac{f\gamma^{3(i-j)}}{n - m_j + 1} & m_j \le i \le n \\ \dfrac{(1-f)\gamma^3 - 1}{\gamma^3 - 1} & i = j \\ \dfrac{f\gamma^3}{\gamma^3 - 1} & i = j+1 \\ 0 & i < j \end{cases} \tag{161}$$

Breakage. Fragmenting particles only break into a few parts (say, two or three) during breakage type fragmentation, yielding relatively large fragments. Assuming that fragments produced when particles break fall only into the next m_l lower size classes, particles fragmenting in bin j produce fragments in bins j+1 to j+m_l. Care should be taken to ensure that bin j+m_l contains the smallest expected fragment sizes for the breakage of particles in bin j. For such a case, the elements of the breakage progeny matrix are as follows:

$$b_{ij} = \begin{cases} 0 & i \le j \\ \dfrac{\gamma^{3(i-j)}}{m_l} & i = j+1,\ j+m_l \\ 0 & i > j+1 \end{cases} \tag{162}$$

Percolation. Percolation fragmentation produces a distribution of fragment sizes. Austin [285] assumed that the same mass fraction of a fragmenting particle would fall into each logarithmically-spaced size bin and derived the following expression for elements of the percolation progeny matrix:

$$b_{ij} = \begin{cases} \dfrac{\gamma^{3(i-j)}}{n - j + 1} & i \ge j \\ 0 & otherwise \end{cases} \tag{163}$$

The elements of the progeny matrix, b_{ij}, represent the number of fragments generated that fall into bin i per particle fragmenting in bin j, *i.e.,* $b_{ij} = n_i/n_j$, where n_j represents the number of fragmenting particles in bin j and n_i, the number of fragments in bin i. It should be emphasized

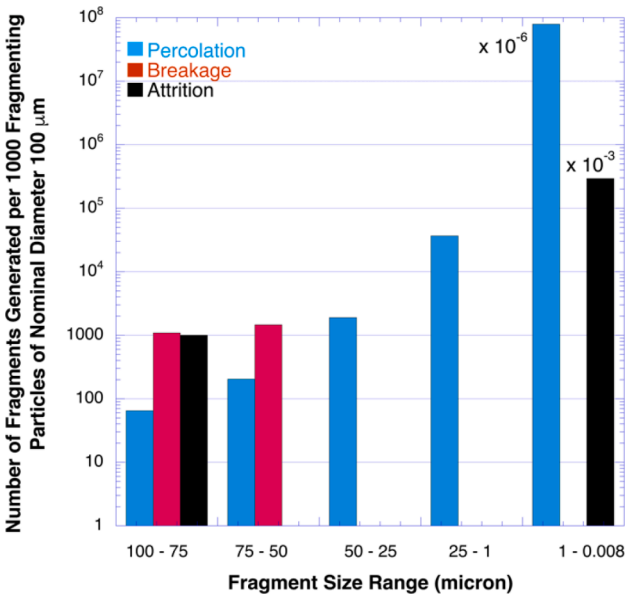

Fig. 12. Number of fragments generated per 1000 fragmenting particles in bin 1, with $d_1 = 100$ μm.

that bin j contains not only particles having diameter d_j, but particles having diameters between d_j and d_{j+1}. Shown in Fig. 12 are the numbers of fragments generated in selected size ranges when 1000 particles in bin 1, with $d_1 = 100$ μm, undergo fragmentation under the three different fragmentation scenarios, percolation, breakage and attrition. In the calculations, 100 size bins were considered ($n = 100$) with $\gamma = 1.1$, $d_2 \approx 91$ μm and $d_n = 0.008$ μm ($d_i = \gamma^{(j-i)} d_j$). Thus, the fragmenting particles were in the size range 91 – 100 μm. As noted in Fig. 12, when the 1000 particles in bin 1 undergo percolation fragmentation, fragments of all sizes are generated, and the number of particles in each size bin increases as the sizes of the fragments get smaller. Percolation results in quite a larger number of sub-micron size fragments. In the breakage fragmentation scenario, m_l was set to 5, *i.e.,* broken particles could yield fragments that fall into bins 2 to 5. Bin 5 has upper and lower size cutoffs of 68 and 62 μm, respectively, the expected size range for the smallest broken particles. With breakage fragmentation, the 1000 particles in bin 1 generated about 2,150 fragments, 1,365 of these having diameters between 75 and 91 μm and the remaining 785 fragments having diameters between 62 and 75 μm. The total number of particles resulting after breakage suggests that most particles broke into two parts, with some (150 of the 1000) breaking into three. As mentioned above, with breakage care must be taken in selecting m_l, the bin containing the smallest broken pieces for fragmentation in bin j. The larger m_l, the smaller the fragments in bin $j+m_l$ and hence, the larger the number of fragments in the bin. Thus, if the selected value of m_l is too large, particles would have to break into several pieces, more than the two or three parts assumed in breakage events. If the selected value is too small, then the total number of fragments generated would be less than twice the number of fragmenting particles in bin j, an impossibility since all of the particles in bin j are assumed to fragment into a smaller size range. With $\gamma = 1.1$ and $d_1 = 100$ μm, setting m_l to 6 would result in 2,555 fragments, with the smallest fragments in the size range 56 to 62 μm. Setting m_l to 4 would result in the generation of only 1,820 fragments, too few if all 1000 particles in bin 1 break into at least two parts. It is recommended to set m_l to the smallest value that yields at least twice the number of fragments as there are particles fragmenting in bin 1, the bin containing the largest particle sizes considered. In addition, it should be assumed that sub-micron size particles do not break. The breakage of such small particles are of little consequence and will not impact calculated mass loss profiles.

In the calculations assuming attrition fragmentation, the fraction of the volume lost to attrition was specified to be 0.1% (*i.e.*, $f = 0.001$) and the largest attrited fragment was specified to be 0.1 μm. The fragments generated during attrition were distributed into 26 size bins ranging from 0.1 to 0.008 μm. With attrition fragmentation, only 4 of the 1000 fragmenting particles in bin 1 lost sufficient volume to move to the next lower size bin, $d_2 = 91$ μm. A large number of sub-micron fragments were generated, but not as many as with percolation fragmentation. This is because the sum of the volumes of all the particles generated during attrition was limited to represent only 0.1% of the volume of the fragmenting particle. A larger fraction would yield a larger number of sub-micron size fragments.

Since there is relatively little mass in sub-micron size fragments, these results suggest that mass loss profiles calculated assuming attrition fragmentation during the char conversion process and neglecting fragmentation all together would yield similar mass loss profiles. However, since mass loss rates depend on particle size, mass loss calculations would differ assuming percolation or breakage fragmentation (or neglecting fragmentation). Mitchell and Akanetuk [13] show agreement between measured and calculated cumulative number distributions and mass loss profiles when percolation fragmentation is assumed to occur during char oxidation under zone II conditions. These researchers noted that it was not possible to get such agreement when either breakage or attrition fragmentation was assumed to occur during char conversion. Employing chars differing in porosity, these researchers also found that fragmentation rates increased with increasing char particle porosity.

To account for the different apparent densities of the fragments produced during fragmentation, Tilghman and Mitchell [212] considered apparent density classes and defined the tensor P to describe the variations in the apparent density distribution with fragmentation. Apparent density class k contained particles having an average apparent density of $\rho_{p,k}$. The elements of this tensor are $P_{i,j,k,m}$, where a particle in size bin j and apparent density class m fragments producing fragments in size bin i in apparent density class k. Assuming that most fragments will have an apparent density similar to that of their parent, fragmenting particle, a Gaussian distribution centered about the apparent density of the fragmenting particle was chosen to represent the fragment apparent density distribution. For such a scenario, elements of the P tensor are given by

$$P_{i,j,k,m} = \frac{1}{\sqrt{2\pi(\sigma_{ij})^2}} e^{-\left(\frac{(\rho_{p,m}-\rho_{p,k})^2}{2(\sigma_{ij})^2}\right)}. \tag{164}$$

In the work of Tilghman and Mitchell [212], the variance was taken as a piecewise factor having three values that depend on particle size, σ_1, σ_2 and σ_3, which were adjusted to provide agreement with data. The variance was calculated using the following relations

$$\sigma_{ij} = \begin{cases} \sigma_1 & if \quad i-j < N_{size}/5 \\ \sigma_2 & if \quad N_{size}/5 < i-j < N_{size}/2 \\ \sigma_3 & if \quad i-j > N_{size}/2 \end{cases} \tag{165}$$

where N_{size} is the number of size bins considered when describing the size distribution. The three values determined for the standard variances were 0.05, 0.08 and 0.12 g/cm^3 for σ_1, σ_2 and σ_3, respectively, for the char particles of a sub-bituminous coal from Wyoming, Wyodak coal. The variance increases with decreasing particle size.

As noted, the elements of the progeny matrix were determined under the assumption that all fragments produced by the fragmenting particles had the same apparent density as the fragmenting particle. This is valid for non-porous particles but becomes increasing less accurate as the fragmenting particle becomes more porous. The expression would violate the conservation of mass if the fragmenting particle had large voids within its outer surface or if it were a cenosphere. Since conservation of mass is the underlying principle, the following expression is more accurate but has yet to be employed in any model of char frag-

mentation:

$$\rho_{p,k} d_{p,j}^3 = \sum_{i=j}^{n} \sum_{m=1}^{N_{dens}} \rho_{p,m} P_{i,j,k,m} b_{ij} d_{p,i}^3. \quad (166)$$

In this approach, a fragmenting particle of diameter $d_{p,j}$ and apparent density $\rho_{p,k}$ produces fragments of diameter $d_{p,i}$ having apparent densities ranging from ρ_1 (the apparent density of the most dense particle in the population) to $\rho_{N_{dens}}$ (the apparent density of the least dense particles in the population), where N_{dens} is the number of apparent density classes used to describe the particle apparent density distribution.

3.5.2. The fragmentation rate

The fraction per unit time of particles of size $d_{p,i}$ and apparent density $\rho_{p,k}$ that fragment is denoted as $S_{i,k}$, and is given by

$$S_{i,k} = k_{frag} \left(\frac{\rho_{p,0}}{\rho_{p,k}} \right)^{\omega} d_{p,i}^{\omega^*}, \quad (167)$$

where $\rho_{p,0}$ is the mean initial density of all the particles, k_{frag} is the fragmentation rate constant (which gives the frequency of fragmentation events), and ω* and ω define the dependency of the fragmentation rate on particle size and inverse density, respectively. Values for these parameters are adjusted to provide agreement between experimental observations and calculations. For particles in the pulverized fuel size-range, a value of unity was used for ω* when all fragments were assumed to have the same apparent density ($\omega = 0$) [285,286]. Tilghman and Mitchell [212] employed values $\omega^* = 2$ and $\omega = 1$, when account was made for differences in the apparent densities of fragments.

As noted by Kleinhans *et al.* [247], the fragmentation rate depends on a number of factors, amongst them the initial char structure and particle size. The size dependence is captured explicitly in Eq. (167) whereas the initial char structure dependence is implicitly contained in k_{frag}. As indicated in the following section, it is the fragmentation rate that distinguishes the fragmentation patterns for a given char during conversion; the elements of the progeny matrix depend primarily on the number of size bins used to describe the fragment distribution and apply to all types of char particles. It is expected that k_{frag} depends on pressure since char particle morphology depends on pressure and fragmentation rates depend on char particle morphology [227]. For example, cenospheric type particles fragment more readily than low-porosity, dense char particles [225]. Kleinhans *et al.* [247] concluded that percolation was the primary type of fragmentation during combustion, that the number of fragments increased with particle size, and that char fragmentation depends on the type of char and its mineral composition.

A char fragmentation model has also been developed by Baxter [289] that relates the initial size distribution of the char to the final fly ash size distribution. The extent of char fragmentation as a function of initial char particle size was investigated using the model for char particles burning in 4% oxygen, by volume, at 1573 K. Results indicated that the extent of fragmentation was dependent on the initial char particle size and coal rank. With bituminous coals, model calculations indicated over 100 fragments per char particle for particles having initial sizes larger than about 80 μm and less than 10 fragments per particle for particles having initial sizes less than 20 μm. Lignite chars produced fewer fragments, less than 5 fragments per char particle for particles of all sizes.

3.5.3. Variations in particle size and apparent density distributions during char conversion

As char conversion progresses, the numbers of particles of a particular size and apparent density change due to the effects of heterogeneous reaction and fragmentation. The differential equation that describes the temporal variations in the number of particles in each size-density bin, $N_{i,k}$, can be expressed as follows:

$$\frac{dN_{i,k}}{dt} = -\left(C_{i,k} + D_{i,k} + S_{i,k}\right) N_{i,k} + C_{i-1,k} N_{i-1,k} + D_{i,k-1} N_{i,k-1} + \sum_{j=1}^{i} \sum_{m=1}^{N_{dens}} b_{ij} P_{i,j,k,m} S_{j,m} N_{j,m}. \quad (168)$$

Here, $C_{i,k}$ denotes the fraction of particles that leave the size bin per unit time owing to a reduction in diameter below the lower bin cutoff due to char reactivity, $D_{i,k}$ denotes the fraction of particles that leave the apparent density class per unit time owing to a reduction in apparent density due to char reactivity, and N_{dens} is the number of apparent density classes considered. Thus, the first bracketed term on the right-hand-side of the above equation represents the decrease in the number of particles in the size-density bin owing to char reactivity and fragmentation. The next two terms represent the increase in the numbers of particles as particles enter the bin from the adjacent bin containing larger diameter particles due to heterogeneous reaction at the outer surfaces of particles (which reduces particle diameter) and as particles enter the bin from the adjacent, higher density class due to heterogeneous reactions at the internal surfaces of particles (which reduces char apparent density). The last term on the right-hand-side of the above equation represents an increase in the number of particles in the size-density bin as a result of fragmentation of particles in larger size bins. The parameters $C_{i,k}$ and $D_{i,k}$ are evaluated via the following relations:

$$C_{i,k} = \frac{1}{(d_i - d_{i+1})} \left(\frac{dd_p}{dt} \right)_{i,k} = \frac{1}{(d_i - d_{i+1})} \left(\frac{2R_{ext}}{\rho_p} \right)_{i,k} \quad (169)$$

$$D_{i,k} = \frac{1}{(\rho_k - \rho_{k+1})} \left(\frac{d\rho_p}{dt} \right)_{i,k} = \frac{1}{(\rho_k - \rho_{k+1})} \left(\frac{6R_{int}}{d_p} \right)_{i,k} = \frac{\rho_k}{(\rho_k - \rho_{k+1})} \left(\eta S_g R_{ext} \right)_{i,k} \quad (170)$$

where R_{ext} is the intrinsic char reactivity evaluated at the conditions existing at the external surface of the char particle of diameter d_p and apparent density ρ_k and R_{int} is the intrinsic char reactivity evaluated at the conditions inside the particle, and expressed in terms of the effectiveness factor and reactivity at the external surface of the particle.

3.6. Modeling thermal annealing

Thermal annealing (or graphite formation) occurs when carbonaceous materials are subjected to high temperatures; it results in the loss in char reactivity under all combustion and gasification conditions. At high temperatures, edge carbons and dislocations in the carbon matrix (the most reactive of the carbon sites) can be lost due to surface reorganization induced by carbonization. During heat treatment, hydrogen is released from the carbonaceous matrix, which induces reordering of the turbostratic structures of coals and biomass, causing the char structures to become more graphitic and hence, less reactive since graphitization hinders oxygen accessibility and prevents the formation of surface oxide complexes. Thermal annealing induces sintering and phase transformations that lead to reductions in catalytic activity. All coal and biomass chars created at high temperatures experience some degree of thermal annealing during pyrolysis and devolatilization. During char conversion, the physical structures of coal and biomass chars change continuously owing to thermal annealing, adversely impacting char reactivity.

Reactivity loss has been attributed to loss of active carbon sites [124,165,168,290,291], loss of surface area [124,168,292], structural rearrangements associated with graphitization [104,105,125,145,146,157,159,291,293-296], and loss of catalytic activity [157,159,291,297]. Carbon and pyro-graphite rods [119,293,298], coal chars [105,114,124-128,138,143,145,146,157,159,165,290,294,297,299-301], biomass chars [150,302], cokes [128,300], and phenol-formaldehyde resin chars [127,168] have been investigated. Chars have been produced in heat treatment tests performed in thermogravimetric analyzers and heated strip reactors

[105,124-126, 128,138,146,157,168,290,300,302], electrically-heated wire-mesh and graphite sheet reactors [104,127,294,303], drop tubes and electrically-heated tubular furnaces [105,150,165,192,299], entrained flow reactors [114,159,296] as well as in packed and fluidized bed reactors [157,297]. Shock tubes [299] and hot jets of oxygen/nitrogen mixtures impinging on carbon surfaces [119,298] have also been used as methods for heat treatment. When monitoring char reactivity, combustion [104,114,119,124,127,128,150,157,159,165,168,290,291,293,294,297, 298,300,301,303], dry (CO_2) and wet (H_2O) gasification [17,125,138, 143,145,146,296,302] and oxy-combustion [92,105,143,245,302] environments have been considered as well as environments established in carbon-hydrogen-methane reacting systems [292]. Char precursors (*e.g.,* the type coal macerals, the nature of the parent material, whether a low-reactivity or high-reactivity char, type of inorganic matter present, as well as particle temperature-time history) were also found to impact the loss in reactivity owing to heat treatment [104,127,295]. For example, vitrinite-rich fractions of coals have been observed to deactivate more readily than inertinite-rich fractions [104]. All studies suggest that when modeling char conversion, it is important to account for the impact that thermal annealing has on char reactivity for accurate predictions.

Thermal annealing begins during the devolatilization process, as coals and biomass are initially heated to high temperatures. The impact of thermal annealing on char reactivity starts to become evident at temperatures higher than about 1000 K [105,150,292,296,297] and becomes increasingly important with increased temperature and duration of heat treatment. Several researchers [105,125,127,301] have used high-resolution transmission electron microscopy (HRTEM) to investigate the loss in reactivity and the development of structural anisotropy of char samples. It was noted that loss of char reactivity by thermal annealing and structural reorganization follow similar paths for coal and biomass [105,125,301,302]. It has been demonstrated that thermal annealing resulting from heat treatment of chars significantly affects both the extent and the accessibility of active sites available for the formation of surface oxides. The longer the heat treatment time and the higher the heat treatment temperature, the less the oxygen uptake (*i.e.,* the less oxygen adsorption at active carbon sites) by chars [290]. Nearly all studies conclude that the higher the peak temperature and the higher the heating rate and holding time at the peak temperature, the greater the adverse impact of thermal annealing on char reactivity.

It has also been observed that the extent of thermal deactivation in oxygen environments is more severe than it is in CO_2 environments [125,144], especially at high heat treatment temperatures. As hypothesized by Salatino and co-researchers [125,144], since CO_2 has a lower propensity to undergo micropore chemisorption than O_2 and since at high temperatures the accessibility of reactive sites is reduced by graphene layer stacking and rearrangement, chemisorption within micropores plays a more important role in gasification with oxygen than it does in gasification with CO_2.

Thermal annealing involves a number of individual processes having different temperature dependences that result in reactivity loss during coal and biomass combustion and gasification. At low temperatures ($T < \sim 1000$ K), cross-linking phenomena associated with hydrogen loss occur in the carbonaceous matrix and at higher temperatures, carbon structure reordering occurs. The reordering is associated with defect losses between carbon layers at intermediate temperatures (~1000 K to ~1800 K), with in-plane defect losses at higher temperatures (~1800 K to ~2300 K) and with crystallite growth at even higher temperatures ($T > 2300$ K) [125].

Despite the different temperature dependences, in most models developed to investigate thermal annealing, the overall process is lumped into a single deactivation step. In addition, two types of carbon sites are assumed to exist in the char, reactive type-A sites and less reactive type-B sites. The type-B sites are presumed to have been impacted by thermal annealing and hence, adsorb reactive gases at slower rates than the type-A sites. During the char conversion process, a number of the type-A sites undergo heterogeneous oxidation to produce gaseous product species while a number are converted to type-B sites, a consequence of thermal annealing during char conversion. The type-B sites are also involved in heterogeneous reactions, producing gaseous product species. It is usually assumed that the annealing reaction is irreversible and independent of both pressure and the composition of the environment. The annealing step is also assumed to be first-order with respect to the concentration of the type-A carbon sites. Many researchers [119, 138,145,293,298] have used variations of the following three-step reaction mechanism when accounting for thermal annealing:

$$\text{Untreated char} \xrightarrow{\text{heterogeneous reactions}} \text{Gaseous products}$$

$$\text{Untreated char} \xrightarrow{\text{thermal annealing}} \text{Deactivated char}$$

$$\text{Deactivated char} \xrightarrow{\text{heterogeneous reactions}} \text{Gaseous products}$$

The rate coefficient for the thermal annealing reaction is expressed in Arrhenius form: $k_d = A_d \quad \exp(-E_d/RT)$. A very wide range of activation energies has been reported for the annealing activation energy, E_d, from a low value near 13 kJ/mol (for a sub-bituminous coal) to a value as high as 730 kJ/mol (for graphite and carbonized filaments) [119,145,293, 297,298]. A variety of chars ranging from bituminous coal chars to lignite chars to biomass chars have been examined; no trends in activation energy of the deactivation reaction with char-type have been reported. It has been hypothesized that the activation energy of the deactivation reaction is independent of the carbon source [297], however, the available data found in the literature do not seem to support this hypothesis. Probably the most widely used value for the activation energy of the deactivation reaction is 97 kcal/mol (~407 kJ/mol), as found by Nagle and Strickland-Constable [298]. How the activation energy depends on the coal type, coal morphology and coal chemistry are still open questions. Wide variations in the determination of the activation energy of the annealing reaction are expected owing not only to coal properties but also to differences in heat treatment conditions, specifically, in coal particle heating rates, peak temperatures reached and residence times in heat treatment environments. These factors impact char specific surface area, porosity, extent of graphitization, and crystallite size [293], all of which impact the activation energy of the annealing reaction in ways not fully understood.

The pre-exponential factor of the annealing reaction depends on the particular char considered and the heat treatment conditions. Based on the results of Salatino *et al.,* [138], the activation energy of the annealing reaction is relatively constant for a variety of heat treatment conditions with the pre-exponential factor depending on heating rates and peak temperatures reached and the time the char spends in the heat treatment environments.

Simulations of the thermal annealing process indicate that there is not a sharp transition from the reactivity of the untreated char to that of the heat-treated char during the conversion process but a gradual transition. This could be a consequence of the time span over which annealing occurs being comparable to the time over which heterogeneous reactions consume the carbonaceous material. Early in char conversion, heterogeneous reaction occurs on both the active and deactivated carbon sites but once the active sites are depleted, char conversion rates are controlled by the conversion rates of the annealed char that was formed as the char conversion process proceeded. Senecca and Salatino [145] estimated a kinetic constant for annealing of 0.02

min^{-1} at 1173 K for untreated South African coal chars exposed to environments containing O_2 and CO_2. At temperatures below 1173 K, annealing rates were found to be less than the heterogeneous reaction rates with O_2 and CO_2. At about 1800 K, the rates of annealing and heterogeneous reaction in O_2 were observed to be comparable [304]. At higher particle temperatures, the time-scales for thermal annealing were found to be shorter than the characteristic time-scales for heterogeneous reaction, and at such high temperatures (>1800 K), it is quite likely that all carbon sites are impacted by thermal annealing before full char conversion. Murty *et al.* [267] suggested that at any temperature, annealing takes place over multiple time-scales, which makes it difficult to assess asymptotic behaviors of the annealing process.

In heat treatment studies with a lignin-rich biomass, Senecca *et al.* [302] observed that in oxy-combustion environments at temperatures exceeding 1473 K, the effects of thermal annealing are not monotonic. In the early stages of heat-treatment (t < 0.1 s), CO_2 was found to promote thermal annealing whereas at longer times (t > 1s), CO_2 was found to hamper thermal annealing. It appears that it is possible for some of the stable surface oxides that are formed on type-B carbon sites during the oxidation process to desorb, with the underlying carbon site having higher reactivity than the desorbed carbon site. In order to capture all the experimental observations, when predicting the conversion of coal and biomass chars, a realistic thermal annealing model must assume the production of both type-A and type-B carbon sites when a carbon atom desorbs from an annealed site. Such an annealing model was proposed by Blyholder *et al.* [293]:

$$\text{Carbon (Type-A site)} \xrightarrow[\text{desorption}]{\text{adsorption}} \text{reactions} \rightarrow \text{Carbon (Type-A site)} + \text{Gaseous products}$$

$$\text{Carbon (Type-A site)} \xrightarrow{\text{thermal annealing}} \text{Carbon (Type-B site)}$$

$$\text{Carbon (Type-B site)} \xrightarrow[\text{desorption}]{\text{adsorption}} \text{reactions} \rightarrow \text{Carbon (Type-A site)} + \text{Gaseous products}$$

$$\text{Carbon (Type-B site)} \xrightarrow[\text{desorption}]{\text{adsorption}} \text{reactions} \rightarrow \text{Carbon (Type-B site)} + \text{Gaseous products}$$

A three-component annealing model has also been proposed [192]. A reactive, hydrogenated pseudo-component of the char ($CHAR_H$) undergoes thermal annealing resulting in an amorphous, disorder char structure ($CHAR_C$) and an ordered, graphitic char structure ($CHAR_G$). Both $CHAR_H$ and $CHAR_C$ are formed during devolatilization - their relative amounts depending on coal rank. During the overall thermal annealing process, dehydrogenation reactions convert $CHAR_H$ (a char having a molar C/H ratio of 2/1, *e.g.* coronene, $C_{24}H_{12}$) to $CHAR_C$ and hydrogen ($CHAR_H \rightarrow 2CHAR_C + 0.5H_2$) and both $CHAR_H$ and $CHAR_C$ are converted to $CHAR_G$ ($CHAR_H \rightarrow CHAR_G$ and $CHAR_C \rightarrow CHAR_G$). Each of the char pseudo-components is involved in heterogeneous oxidation and gasification reactions, yielding gaseous products. In the heterogeneous reaction mechanism employed [192], $CHAR_H$ reacts with O_2, H_2O or CO_2 to yield $CHAR_C$ as well as gaseous CO and H_2. Arrhenius parameters for the three annealing reactions were determined by comparing predictions and experimental data on char reactivity obtained under a variety of test conditions. Overall, model predictions were in good agreement with the experimental data in terms of char conversion times and surface temperatures for both the chars of the bituminous coal and lignite that were investigated. The relative reactivities of the three char components at 1173 K were estimated to be ~40:20:1 for $CHAR_H$:$CHAR_C$:$CHAR_G$, reflecting the high reactivity of the hydrogen-containing char component and the low reactivity of the annealed char component. Compared to two-component annealing models, a three-component model can better reflect fast annealing rates early in char conversion with slower annealing rates during the later stages of char conversion, an experimental observation.

Thermal annealing models have also been developed that use a distribution of activation energies to describe the rate of the annealing reaction [114,128,143,168,291]. Such an approach is consistent with the viewpoint that thermal annealing involves numerous physical and chemical transformations having different temperature dependences. A continuous distribution of activation energies for the annealing reaction is hypothesized to better characterize the temperature dependence of the overall annealing process. In the approach pioneered by Suuberg [291], the number of active sites having activation energy in the range E_d to $E_d + dE_d$ is $F(E_d)dE_d$, and each of these active sites decays in accord with the first-order rate: $dF/dt = -k_dF$, where $-k_d$ is the rate coefficient for the annealing reaction: active sites → deactivated sites. Integration yields the number of the active sites that are still active after annealing for time t:

$$F(E_d) = F_0(E_d)\exp\left(\int_0^t (-k_d)\,dt\right) = F_0(E_d)\exp\left(-\int_0^t A_d \exp\left(-\frac{E_d}{\widehat{R}_u T}\right)dt\right) \tag{171}$$

In this approach, the initial distribution of the annealing activation energies is defined by the function $f(E_d)$, which is a specified function that satisfies $\int_{-\infty}^{\infty} f(E_d)dE_d = 1$. Letting S_0 denote the total number of active sites before significant annealing (or some measure of the initial number of active sites), the initial distribution of activation energies is given by

$$F_0(E_d) = S_0 f(E_d). \tag{172}$$

The total number of active sites at any time can be found by integrating $F(E_d)$ over all activation energies; thus,

$$S = \int_0^{\infty} F(E_d)\,dE_d \tag{173}$$

Combining the above equations results in

$$\frac{S}{S_0} = \int_0^{\infty} \exp\left(-\int_0^t A_d \exp\left(-\frac{E_d}{\widehat{R}_u T}\right)dt\right) f(E_d)\,dE_d, \tag{174}$$

which permits determination of the number of active sites that remain active after the char undergoes annealing for a time t from the onset of significant annealing, relative to an initial value for the number of active sites.

Suuberg and co-workers [168,291] employed a Gaussian distribution function for $f(E_d)$:

$$f(E_d) = \frac{1}{\sigma\sqrt{2\pi}}\exp\left[-\frac{(E_d - E_0)^2}{2\sigma^2}\right] \tag{175}$$

where E_0 and σ are the mean and standard deviation, respectively, of the distribution.

As noted by Suuberg *et al.* [168,291], the difficulty in identifying the number of active sites at time zero is overcome by assuming that the ratio expressed in Eq. (174) gives the number of active sites at two different temperatures, with the denominator, S_0, giving the number of sites at a temperature sufficiently low that thermal annealing is unimportant with respect to influencing char reactivity. Employing reactivity

data from a variety of coal chars, Suuberg *et al.* [168,291] searched the parameter space and found a best fit to the data: σ = 163 kJ/mol, E_0 = 151 kJ/mol and $A_d = 1 \times 10^{13}\ s^{-1}$. The annealing pre-exponent factor A_d was taken to be the same for all of the annealing reactions.

Suuberg and co-workers [168,291] observed that only the high activation energy annealing reactions contributed to the annealing process – annealing reactions having activation energies near the mean value or lower were essentially irrelevant, contributing little to annealing behavior at long times and high temperatures. They found that the effective annealing reactions have activation energies in the range 450 to just over 600 kJ/mol, corresponding roughly with the range of activation energies for aromatization and graphitization processes. Realizing that only the high activation energy end of the Gaussian distribution was active in impacting reactivity loss, the need to consider other distribution functions that exhibit declining numbers of sites with increasing activation energy for the initial distribution of active sites was emphasized. A log-normal distribution function [114,143] and a shifted gamma distribution function [128] have been considered. All such distribution functions are suitable; Zolin *et al,* [128] found that a shifted gamma distribution function yielded slightly better fits to their deactivation data than a log-normal distribution function.

Hurt *et al.* [114], slightly modified Suuberg's distributed activation thermal annealing model by incorporating a log-normal distribution function for annealing activation energies and coupling the annealing model to a char reactivity model adequate for char oxidation in the Zone II combustion regime. The log-normal distribution was expressed as

$$f(E_d, t_0) = \frac{1}{\sigma\sqrt{2\pi}} \exp\left[-\frac{(\ln(E_d) - \ln(E_0))^2}{2\sigma^2} \right] \tag{176}$$

where σ is the standard deviation of the $ln(E_d)$ distribution. This is the initially assumed distribution of the number of active sites and has the desired property, $\int_0^\infty f(E_d, t_0)\, dE_d = 1$. Since the active sites are lost at different rates due to differences in activation energies, the activation energy distribution function varies in time. By defining a normalized frequency distribution function for active sites at time t as follows

$$f(E_d, t) = \frac{F(E_d, t)}{S_0}, \tag{177}$$

and taking its time derivative, the following expression for the variation in the normalized frequency distribution function can be derived in light of Eq. (172) and the fact that $dF/dt = -k_d$:

$$\frac{df(E_d, t)}{dt} = -f(E_d, t) A_d \exp\left(-\frac{E_d}{\widehat{R}_u T_p} \right). \tag{178}$$

Separating variables and integrating results in:

$$\frac{f(E_d, t)}{f(E_d, t_0)} = \exp\left(-\int_0^t A_d \exp\left(-\frac{E_d}{\widehat{R}_u T_p} \right) dt \right). \tag{179}$$

Eqs. (173),(177) and (179) can be combined to yield the following expression for the total number of active sites in the char at time t relative to the total number of active sites in the char before significant annealing:

$$\frac{S}{S_0} = \int_0^\infty f(E_d, t)\, dE_d = \int_0^\infty f(E_d, t_0) \exp\left(-\int_0^t A_d \exp\left(-\frac{E_d}{\widehat{R}_u T_p} \right) dt \right) dE_d \tag{180}$$

For char particles undergoing oxidation in the Zone I combustion regime, char reactivity is proportional to the number of active carbon sites. Thus, at two different temperatures, both rendering Zone I conversion rates, the ratio of the overall particle reaction rates at the two temperatures is equal to the ratio of the number of active sites at the two temperatures, *i.e.*, $R_{ov}/R_{ov,0} = S/S_0$. However, as noted by Hurt *et al.* [114], for char particles undergoing oxidation in the Zone II combustion regime, the classical Thiele theory predicts that char reactivity is proportional to the square-root of the number of active sites *i.e.*, $R_{ov} \propto S^{\frac{1}{2}}$. Thus,

$$\frac{R_{ov}}{R_{ov,0}} = \left(\frac{S}{S_0} \right)^m = \left(\int_0^\infty \exp\left(-\int_0^t A_d \exp\left(-\frac{E_d}{\widehat{R}_u T} \right) dt \right) f(E_d, t_0)\, dE_d \right)^m \tag{181}$$

where $m = 1$ for combustion in Zone I and $m = 0.5$ for combustion in Zone II, the regime in which thermal annealing is more significant.

In the approach undertaken by Hurt and co-workers [114], for the Zone II combustion regime particle burning rates per unit external surface area were employed as measures of char reactivity, and these apparent reactivities were expressed as $R_{ov} = A\ exp(-E/\widehat{R}_u T_p) P_{O_2}^n$. The pre-exponential factor was treated as a variable dependent on char precursor and temperature-time history: $A = f(\text{precursor}, T(t))$. Based on data obtained in tests with ten vitrinite-rich coals of various ranks from the United States, Hurt *et al.* [114] determined rank-dependent correlations for initial char reactivity as a function of the dry, ash-free carbon content of the parent coal. The three parameters that define the distributed activation energy thermal annealing model (the natural logarithm of the pre-exponential factor, $\ln(A_d)$; the mean value of the ln (E_d) distribution, $\ln(E_0)$; and the standard deviation of the $\ln(E_d)$ distribution, σ) were also determined. The optimal parameters for the data set were found to be: $\ln(A_d) = 18.3$ ($\ln s^{-1}$), $\ln(E_0) = 2.8$ (ln kcal/mol), and σ = 0.46 (ln kcal/mol).

Since chars inherently undergo some extent of heat treatment during their formation, values for R_{ov} correspond to a hypothetical initial state. Hurt and co-workers [114] described a method for back-calculating R_{ov} from measurements of R_{ov}, knowing the temperature history the char particles experienced prior to and during the measurements. Employing apparent reactivities, their approach yields an initial value for the pre-exponential factor, A_0. Since prior heat treatment included pyrolysis, A_0 is reported as the pre-exponential factor for conversion of the raw coal.

Both the log-normal and gamma distribution functions yield low mean activation energies that result in considerable loss in char reactivity at temperatures as low as room temperature in very short periods of time. The low annealing activation energies are hypothesized to be associated with annealing processes that do not lead to reactivity loss since reactivity loss is not observed at such low temperatures. These distribution functions should be truncated at the low activation energy end when used. Holland *et al.* [143] argued that since there are essentially no data on deactivation processes that are possible at low temperatures that can be used to fit annealing model parameters, all low-temperature annealing processes should be included in the truncation of the activation energy distribution. Variations of the above distributed activation energy annealing model have been developed by others (*e.g.*, [138,222,305,306]) and shown to adequately describe the loss in char reactivity during both coal combustion and gasification.

As already discussed, when using the distributed activation energy annealing models, char reactivity loss must be modeled on a relative basis owing to the fact that there is no "initial char" for which the number of active sites is known, *i.e.*, S_0 is unknown. By the time a char has reached a temperature sufficiently high to induce reaction, appreciable annealing has already occurred. Because of this, in agreement with the approach of Hurt *et al.*, [114], Holland *et al.* [143] suggested that the annealing model be used in concert with a reactivity model when determining model parameters.

Holland *et al.* [143] extended the distributed activation energy annealing model pioneered by Suuberg [168,291] and modified by Hurt

[114] to include the impact of coal type, heating rate, peak temperature reached during heat treatment, and reactive gas. An elaborate optimization scheme was employed to determine the pre-exponential factor for the annealing reactions and the mean value and standard deviation of the distribution of annealing activation energies as functions of coal type, heating rate and peak temperature. In their approach the range of annealing activation energies considered was divided into a number of activation energy bins and Eq. (179) was used to determine $f(E_d,t)$ for each E_d-bin at time t. Summing over all activation energy bins yields the fraction of remaining reactivity. This fraction is initially unity and progressively decreases as the annealing time increases. At $t = 0$, $f(E_d,t)$ for each activation energy bin was determined from the log-normal distribution function, which was split into a bimodal distribution and renormalized to maintain the total number of initial active sites. The bimodal distribution reflected the low activation energies that were not associated with reactivity loss and the high activation energies that were associated with reactivity loss. Factors used to split the log-normal distribution were included in the optimization scheme. The pre-exponential factor for the annealing reaction was determined as a function of coal type (via an NMR-determined coal structural parameter) and heating rate (either greater than 10^4 K/s or less). A value for the structural parameter can be determined from correlations that employ the elemental analysis of the coal. The mean value of the log-normal distribution was determined as a function of coal type and peak temperature reached during annealing (either greater than 1500 K or less) and the standard deviation was determined as a function of coal type. A large experimental dataset for annealing effects on char reactivity in O_2, CO_2 and H_2O was used to determine the functional relationships in the work of Holland *et al.* [143]. Data were obtained in annealing tests employing several coals differing in rank, and reactivities were measured for annealed chars prepared under a wide range of conditions. As in the approach of Hurt *et al.* [114], an apparent rate was used as a measure of char reactivity. Along with the annealing parameters, an optimized value for the pre-exponential factor A was determined as a function of coal type and temperature history. The model put forth by Holland *et al.* [143] is the most sophisticated thermal annealing model developed to date. Considering all of the studies, thermal annealing is dependent on the time-temperature profile the char particle experiences during annealing, the particle heating rate and the peak temperature reached during heating, and the chemical structure of the parent coal. This model accounts for all of these dependences.

In char conversion models that use apparent rates as a measure of char reactivity, the effects of surface area changes are included in the rate. Consequently, the effects of changes in specific surface area are included with the losses in carbon and catalytic active sites in the distributed activation thermal annealing models discussed above.

No model has yet been developed that employs a distributed activation energy annealing sub-model coupled with a detailed heterogeneous reaction mechanism that describes the intrinsic chemical reactivity of the carbonaceous particle material and a specific surface area model that describes how the specific surface area of the char varies with conversion. In such models, the product of specific surface area and intrinsic chemical reactivity is proportional to the total number of active sites and hence from Eq. (11),

$$\frac{S_g \cdot R_c}{S_{g,0} R_{c,0}} = \int_0^\infty \exp\left(-\int_0^t A\exp\left(-\frac{E_d}{\widehat{R}_u T}\right) dt \right) f(E_d, t_0)\ dE_d \tag{182}$$

where S_g is the mass specific surface area of the char at time t and R_c is the intrinsic chemical reactivity of the carbonaceous particle material at the time. Note that intrinsic chemical reactivities apply to all conversion regimes and therefore, $m = 1$. Employing the specific surface area model (see Section 3.1.2), the instantaneous chemical reactivity relative to an initial intrinsic chemical reactivity is given as follows:

$$\frac{R_c}{R_{c,0}} = \frac{1}{\sqrt{1-\psi \ln(1-X(t))}} \left(\int_0^\infty \exp\left(-\int_0^t A\exp\left(-\frac{E_d}{\widehat{R}_u T}\right) dt \right) f(E_d,t_0)\, dE_d \right), \tag{183}$$

where ψ is the surface area structural parameter and X is char conversion. Here, the effects of microstructural changes in surface area on reactivity are included with the losses in carbon and catalytic active sites in the distributed activation thermal annealing sub-model. The effects of macrostructural changes in surface area associated with the opening of initially closed-off pores and pore coalescence are accounted for in the specific surface area sub-model.

3.7. Modeling non-spherical particles

Coal and biomass char particles are not spherical but have a variety of shapes. Since momentum, heat and mass transfer between gas and a particle are impacted by particle non-sphericity, so is the particle's reaction rate. Account is made for the effects of non-sphericity in many models by employing equivalent diameters and shape factors to describe the flow around the non-spherical particle. To account for non-sphericity effects on particle fluid dynamics, Tabet *et al.* [307] included a particle shape factor (defined as the ratio of the surface area of an equal-volume sphere to the actual surface area of the non-spherical particle) when defining the drag coefficient in the equation of motion for non-spherical coal and biomass particles in their CFD model for co-firing coal and biomass. Non-spherical particles tend to have larger surface areas and more porosity than spherical particles, which increases the oxygen fluxes inside particles and hence, enhances char particle conversion rates [307]. Yin *et al.* [308] introduced an enhancement factor into the diffusion equation that was intended to capture this non-spherical effect.

3.7.1. Volume-equivalent diameters for non-spherical particles

Non-spherical coal and biomass particles have been modeled as either oblate or prolate spheroids, the solid bodies formed by rotating an ellipse about its minor and major axes, respectively (See Fig. 13). Oblate and prolate spheroids are pictured in the figure below.

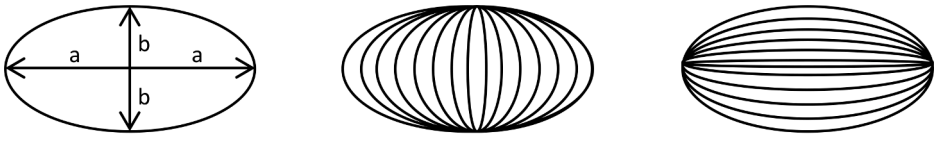

(a) An ellipse (b) An oblate spheroid (c) A prolate spheroid

Fig. 13. (a) An ellipse of major principal semi-axis a and minor principal semi-axis b. (b) Rotation of the ellipse about its minor axis forms an oblate spheroid. (c) Rotation of the ellipse about its major axis forms a prolate spheroid.

Numerically obtained velocity and temperature profiles established during the steady laminar flow past single spherical and non-spherical droplets and particles were analyzed by Comer and Kleinstreuer [309] to determine mean Nusselt numbers as functions of Reynolds numbers and aspect ratios A_R (re-defined here, as the ratio of the lengths of the particle's major (a) and minor (b) principal semi-axes ($A_R = a/b$) instead of the ratio of minor to major axis as done in the paper). Results indicated that for aspect ratios less than five, the average heat flux to the surface of a non-spherical particle that is modeled as an oblate spheroid is the same as the average heat flux to a sphere having the volume equivalent diameter of the oblate spheroid when this diameter is used to evaluate the Reynolds number, the drag coefficient and the Nusselt number. For an oblate spheroid having major principal semi-axis a and aspect ratio A_R, the volume equivalent diameter is $d_{equiv} = 2a/(A_R)^{1/3}$. A sphere having this diameter will have the same volume as the oblate spheroid. Results also indicated that the non-spherical particle will have higher overall heat transfer rate (in comparison to a spherical particle having the volume equivalent diameter), since it has more surface area. In light of the similarity between heat and mass transfer, the average reactant fluxes to the surfaces of non-spherical char particles will be adequately predicted if the non-spherical particles were modeled as spheres having volume equivalent diameters. The external surface area of a spherical particle having diameter d_{equiv} is smaller than the external surface area of the oblate spheroid. The higher the aspect ratio, the lower the surface area of the equivalent-volume sphere to that of the oblate spheroid. For an aspect ratio of three, the external surface area of the equivalent-volume sphere is about 80% of the external surface area of the oblate spheroid and falls to 63% for an aspect ratio of five.

While the previous paragraph was concerned with oblate spheroids, we will now focus on prolate spheroids. For a prolate spheroid having major principal semi-axis a and aspect ratio A_R, the volume equivalent diameter is $d_{equiv} = 2a/(A_R)^{2/3}$ and consequently, a sphere having this diameter will have the same volume as the prolate spheroid. Extending the results of Comer and Kleinstreuer [309] to prolate spheroids, the heat flux to the surface of a spherical particle having this diameter will be similar to the average heat flux to the surface of the prolate spheroid provided the Reynolds number, the drag coefficient and the Nusselt number are calculated using the volume equivalent diameter as the characteristic length. Again, in light of the similarities in mass and heat transfer, the average mass flux to the surface of a volume-equivalent diameter sphere will be similar to that of the non-spherical particle when modeled as a prolate spheroid. As with oblate spheroids, the surface area of the volume-equivalent sphere is less than the surface area of the prolate spheroid, and therefore the overall flow of reactive gas to the spherical particle will be less than that to the external surface of the prolate spheroid. For an aspect ratio of three, the external surface area of the equivalent-volume sphere is about 85% of the external surface area of the prolate spheroid and falls to 73% for an aspect ratio of five. Since the external surface areas of the prolate spheroid and the external surface area of its equivalent-volume sphere are more nearly the same than the external surface area of the oblate spheroid and the external area of its equivalent-volume sphere, it is recommended to model non-spherical coal and biomass char particles as prolate spheroids. As evidenced by the particles in the SEM images shown in Fig. 1, prolate spheroids reflect the shapes of the char particles more so than oblate spheroids. Note that the aspect ratios of most of the particles are less than three.

An external surface area ratio, $A_{ex,ratio}$, can be defined as the ratio of the external surface area of a prolate spheroid ($A_{ex,ps}$) to the external surface area of its volume-equivalent sphere ($A_{ex,ves}$): $A_{ex,ratio} \equiv A_{ex,ps}/A_{ex,ves} = 0.5\,(A_R)^{-2/3}\quad(1 + A_R \sin^{-1}(\varepsilon)/\varepsilon)$, where ε is the eccentricity of the prolate spheroid: $\epsilon = \sqrt{1 - b^2/a^2} = \sqrt{1 - (A_R)^{-2}}$. When modeling a non-spherical particle as a prolate spheroid and treating the particle as an equivalent-volume sphere, multiplying the external surface area of the equivalent-volume sphere by this surface area ratio will result in simulations having the correct average fluxes of heat and mass to the outer surface of the non-spherical particle and the correct external surface area associated with these average fluxes. As a consequence, in the simulations the diffusive flows of reactive gases to the non-spherical particle will be accurately assessed.

In a theoretical study on the combustion behaviors of non-spherical particles, Choi and Gavalas [310] found that when char conversion rates were diffusion-limited (the zone III conversion regime), pseudo-steady particle oxidation rates and temperatures are similar to those of spherical particles of equal volume and surface area. Their analyses indicated that as the extent of char conversion increased, non-sphericity increased. In addition, the simulations performed demonstrated that non-spherical particles burn faster than spherical particles of the same initial volume. Differences in times for complete conversion were less than 20% for initial aspect ratios between one and three. This finding is consistent with the results of Comer and Kleinstreuer [309]. Overall conversion times should scale with external surface area for diffusion-limited burning, and the external surface area of the spherical particle is from 15% to 27% less than that of the non-spherical particle.

3.7.2. Volume-equivalent shapes for non-spherical particles

Other approaches in modeling heat and mass transfer to non-spherical particles have been taken. In the approach taken by Baxter and co-researchers [311-313], heat and mass transfer at the outer boundary of the non-spherical particle are assumed to increase relative to that of a basic shape by the ratio of the particle's external surface area to that of a volume-equivalent particle of specific-shape, R_{SA}. For a nearly spherical particle, the characteristic surface area is the external surface area of the volume-equivalent sphere of radius r_p. Thus, for a near-spherical particle of external surface area $A_{ex,p}$, $R_{SA} = A_{ex,p}/(4\pi r_p^2)$. For a nearly cylindrical-shaped particle, the characteristic surface area is the external surface area of the volume-equivalent cylinder of aspect ratio A_R and radius r_p and therefore for such a cylinder-like particle, $R_{SA} = A_{ex,p}/(4\pi r_p^2 A_R)$. Flat plates of various aspect ratios were also considered and for a nearly flat plate-shaped particle (a flake-like particle), $R_{SA} = A_{ex,p}/(4r_p^2 A_R^2)$. These ratios were applied at the particle's boundary conditions. For example, in the models developed by Baxter and co-researchers [311-313] the heat flux at the outer surface of the non-spherical particle is given by:

$$\lambda_{eff} = \frac{\partial T_p}{\partial r}\Big|_{r=t,r_p} \theta_T h_{gas} R_{SA}\left(T_{gas} - T_p\right) + R_{SA}\varepsilon_p \sigma\left(T_w^4 - T_p^4\right),$$

where λ_{eff} is the effective particle thermal conductivity, h_{gas} is the heat transfer coefficient, θ_T is the blowing factor, and ε_p is the particle emissivity.

Mass and heat transfer coefficients developed for each specific shape (sphere, cylinder or flat plate) were employed in the model developed. Model calculations agreed with observations with respect to particle shape: near-spherical particles burn slower than less symmetrically shaped particles. The larger external surface areas and smaller thicknesses of cylinder-like and flake-like particles cause them to have higher heat and mass transfer rates. Calculations also indicated that the impact of shape on char particle behavior increases as the particle size increases. This model is claimed to be applicable to particles of all shapes.

3.7.3. Effectiveness factors for non-spherical particles

Aris [314] recommended calculating a characteristic dimension for the non-spherical particle from the ratio of its volume to its external surface area, V_p/A_p, when determining the relationship between the effectiveness factor and Thiele modulus. For first-order reaction, it was

shown that steady state solutions to the conservation equation governing simultaneous diffusion and reaction are largely independent of the particle shape when the Thiele modulus is evaluated using V_p/A_p as the characteristic dimension of a non-spherical particle. Instead of employing Eqs. (106) and (107) as expressions for the Thiele modulus for species i and its effectiveness factor, respectively, assuming first-order kinetics, Aris expressed the Thiele modulus for non-spherical particles (Λ) as

$$\Lambda_i = \left(\frac{V_p}{A_p}\right)\sqrt{\frac{k_{s,i}\ S_g\ \rho_{char}}{D_{i,eff}}}$$

and the effectiveness factor as

$$\eta_i = \frac{3\Lambda_i \coth(3\Lambda_i) - 1}{3(\Lambda_i)^2}.$$

In the expression for the Thiele modulus, $k_{s,i}$ is the reaction rate coefficient for the first-order reaction involving reactant species i. For spheres, employing the above equations yields the same value for the effectiveness factor when the sphere radius is used in Eq. (106) in the evaluation of the Thiele modulus and Eq. (107) is used when calculating the effectiveness factor. Consequently, as noted by Aris, there would be no dependence of the effectiveness factor on particle non-sphericity if only the volume-equivalent diameter were used as the characteristic dimension in the expression for the Thiele modulus. All non-spherical particles at the same temperature that have the same internal surface area and pore structure would have the same effectiveness factor. The penetration of reactive gases inside particles would be the same no matter the shapes of the particles, an unrealistic scenario. Table 5 shows values calculated for the effectiveness factor for various shaped particles for selected values of the Thiele modulus (Λ) employing the above equations. Particles are assumed to be in the shapes of prolate spheroids having semi-axis of 50 μm and aspect ratios ranging from one to five.

The top row of the table shows values calculated for $\varphi_{L,m}$ for spherical particles using Eq. (106) employing selected char properties and gas conditions and the second row shows values calculated for the corresponding value of $\eta(\varphi_{L,m})$ using Eq. (107). The same char properties and gas conditions used to determine each $\varphi_{L,m}$ were used to calculate Λ for non-spherical particles having selected aspect ratios; corresponding values for $\eta(\Lambda)$ were also calculated. Note that for the spherical particle ($A_R = 1$), $\eta(\varphi_{L,m}) = \eta(\Lambda)$. Values in the table indicate that for any selected value of $\varphi_{L,m}$, as the aspect ratio increases the Thiele modulus for the non-spherical particle (Λ) decreases and the effectiveness factor ($\eta(\Lambda)$), increases. Higher aspect ratio particles are thinner and as such, the penetration depth of reactive gases inside the particle increases (*i.e.*, the effectiveness factor is closer to unity). Also note that for any given particle shape, as φ increases, so does Λ, with corresponding decreases in $\eta(\Lambda)$– the higher the Thiele modulus, the lower the penetration depth of reactive gas no matter what the shape of the particle.

If the reaction rate is not first-order but m^{th}-order, the above equations for the Thiele modulus and effectiveness factor for the non-spherical particles can be modified as follows:

$$\Lambda_i = \left(\frac{V_p}{A_p}\right)\sqrt{\left(\frac{m+1}{2}\right)\frac{k_{s,i}\ S_g\ \rho_{char} C_s^{(m-1)}}{D_{i,eff}}}$$

and

$$\eta_i = f_c(\Lambda_i, m)\left(\sqrt{\frac{2}{m+1}}\right)\left(\frac{3\Lambda_i \coth(3\Lambda_i) - 1}{3(\Lambda_i)^2}\right)$$

where the correction function is expressed as

$$f_c(\Lambda_i, m) = \left(1 + \frac{\sqrt{0.5}}{\left(18\ \Lambda_i^2\ +\ 1/18\ \Lambda_i^2\right)}\right)^{0.5(1-m)^2}.$$

The above expressions are recommended for use when calculating the effectiveness factor for non-spherical particles. However, Aris [314] acknowledged that use of V_p/A_p as the characteristic dimension in the Thiele modulus expression is inadequate for transient problems.

3.8. Modeling char conversion at elevated pressures

Pressure influences overall char particle conversion rates primarily through the impact of pressure on species concentrations enhancing heterogeneous reaction rates and on coal and biomass devolatilization behaviors, which influences char particle morphology. The resistance to volatiles release increases with increased pressure and the effects of secondary reactions are promoted. As a consequence, the total yields of volatile matter, tars and gases decrease and the total char yields increase with increased devolatilization pressure. Pressure affects the thermoplastic properties of the coal during heating, and thermoplastic properties are highly rank dependent. Therefore, the effect of pressure on the char produced depends on the rank of the coal, the swelling behaviors of bituminous coals being the most impacted. High pressures favor the development of foam-type structures that lead to the formation of char particles having a variety of morphologies and apparent densities [315]. In general, if the coal swells, increasing the devolatilization pressure increases the yield of low density, anisotropic char particles.

At elevated pressures, intrinsic reaction rates are enhanced and diffusive transport rates in pores are decreased, and these influence char conversion rates. Whereas bulk diffusion coefficients decrease with increased pressure, Knudsen diffusion coefficients are independent of pressure. Consequently, Knudsen diffusion in pores becomes relatively more important as pressure is increased. Most models developed to predict the effects of pressure on char conversion rates accurately characterize the effects of pressure on transport properties and use a heterogeneous reaction mechanism to describe char reactivity [95,147,

Table 5
Thiele moduli (Λ) and effectiveness factors (η) for non-spherical particles. The Thiele modulus for spherical particles ($\varphi_{L,m}$) is calculated based on the volume-equivalent particle diameter.

	$\varphi_{L,m} = 1.5$ $\eta(\varphi_{L,m}) = 0.876$		$\varphi_{L,m} = 2.0$ $\eta(\varphi_{L,m}) = 0.806$		$\varphi_{L,m} = 3.0$ $\eta(\varphi_{L,m}) = 0.672$		$\varphi_{L,m} = 5.0$ $\eta(\varphi_{L,m}) = 0.480$		$\varphi_{L,m} = 10.0$ $\eta(\varphi_{L,m}) = 0.270$		$\varphi_{L,m} = 20.0$ $\eta(\varphi_{L,m}) = 0.143$		$\varphi_{L,m} = 30.0$ $\eta(\varphi_{L,m}) = 0.097$	
A_R	Λ	$\eta(\Lambda)$	Λ	$\eta(\Lambda)$	Λ	$\eta(\Lambda)$	Λ	$\eta(\Lambda)$	Λ	$\eta(\Lambda)$	Λ	$\eta(\Lambda)$	Λ	$\eta(\Lambda)$
1.0	0.500	0.876	0.667	0.806	1.000	0.672	1.667	0.480	3.333	0.270	6.667	0.143	10.000	0.097
1.1	0.499	0.877	0.665	0.807	0.998	0.672	1.663	0.481	3.327	0.270	6.654	0.143	9.981	0.097
1.3	0.496	0.878	0.661	0.808	0.992	0.675	1.653	0.483	3.305	0.272	6.610	0.144	9.915	0.097
2.0	0.464	0.891	0.619	0.826	0.929	0.698	1.548	0.507	3.096	0.288	6.192	0.153	9.287	0.104
2.5	0.443	0.899	0.590	0.839	0.885	0.716	1.475	0.525	2.950	0.301	5.901	0.160	8.851	0.109
3.0	0.423	0.907	0.564	0.850	0.846	0.731	1.410	0.542	2.820	0.313	5.641	0.167	8.461	0.114
4.2	0.386	0.921	0.515	0.870	0.773	0.761	1.288	0.576	2.576	0.338	5.152	0.182	7.727	0.124
5.0	0.366	0.928	0.488	0.881	0.732	0.778	1.220	0.597	2.440	0.354	4.880	0.191	7.321	0.130

222,227]. The impact of total pressure and reactive gas mole fraction on reactivity can be accurately characterized in this manner. This was demonstrated by Niksa *et al.*,[222] who used a three-step oxidation mechanism proposed by Hurt and Calo [172] to describe char oxidation kinetics in the model that was developed. Adjusting reaction rate coefficients to describe observed reaction conversion rates of each coal considered, the extent of char conversion at any selected reaction time and char particle temperatures were both predicted to increase with increasing pressure when burning is under zone II conditions, as experimentally observed with most coal chars.

In the coal combustion model developed by Niksa *et al.* [222] (CBK/E), account is made for thermal annealing and the pre-exponential factor of the annealing reaction is correlated with the carbon content of the coal. In addition, account is made for coal swelling during heat-up and devolatilization. The swelling index is correlated with total pressure and the swelling index at one atmosphere is correlated with the carbon content of the coal (see Section 4.2.5). This permits estimation of the initial size of the char particle at the onset of char conversion at elevated pressures.

Most of the studies that use power-law kinetics to describe high-pressure reaction rates have been concerned with char gasification at elevated pressures, with H_2O and CO_2 being the gasifying agents (see for example, references [93,94,164]). Roberts and Harris [164] found that activation energies were not significantly affected by pressure for the two coals investigated in their combustion and gasification studies, however, in other oxidation studies [162,316,317], activation energies were found to decrease with increased pressure.

If a power-law kinetics model is to be used to describe char reactivity at an elevated pressure, it is best to derive kinetic parameters using data obtained at the pressure of interest. Power-law models lack the underlying science that governs the influence of pressure on both rates of mass transport and rates of chemical reaction. For accurate predictions of char conversion rates at elevated pressures, heterogeneous reaction mechanisms are needed to accurately characterize the impact of total pressure on reaction rates. It is also necessary to accurately describe the pressure dependences of all diffusive mass transport coefficients.

3.9. Selecting char conversion models

The first step that must be taken in analyzing experimental char conversion data is the selection of an appropriate pore structure model, either the grain model, the random pore model or some other structural model. Most coal and biomass chars exhibit conversion rates that decelerate in time and both the grain and random pore models predict such behaviors. With proper adjustment of model parameters, both models can describe measured conversion rate data reasonably well. Morin *et al.* [89] found that activation energies and reaction orders are similar for both models. Some biomass chars exhibit conversion rates that initially accelerate with conversion and then decelerate, and for such sigmoidal behavior, an Avrami-Erofeev type model should be selected. It is up to the researcher analyzing the data to select the model that best describes the experimental observations. As already noted, the random pore model is recommended since it accounts for the non-monotonic evolution of the internal particle surface area, a phenomenon observed with most coal and biomass char particles.

When simulating thermochemical conversion of char, a reaction model has to be used. The choice of reaction model depends on the desired fidelity of the results and on which models are available for the char of interest. The model to use for the simulations is therefore often in the hands of those developing the reaction models. When developing a char reaction model, whether to select an apparent reaction rate model or an intrinsic reaction rate model depends on the experimental data available. If only mass loss data are available for particles of a given size, there is no choice except to use an apparent reaction rate model for such models only require information on gaseous conditions and the initial particle size. If initial apparent density and surface area data are available as well as mass loss data, then there is the choice of using an intrinsic reaction rate model.

Whether to employ power-law kinetics or a heterogeneous reaction mechanism is a choice that the researcher analyzing the data must make based on the experimental data available. The determination of reaction rate coefficients in heterogeneous reaction mechanisms requires more tests over a wider range of reaction conditions than the determination of power-law kinetic parameters. As noted previously, heterogeneous reaction mechanisms are applicable over wide ranges of temperature, pressure and reactive gas mole fraction whereas power-law kinetics are most accurate in the environments in which the data were obtained.

All char conversion models require information on the conditions of the char at the onset of char conversion, in particular information on the initial char particle size and apparent density. Initial char conditions are dependent on the properties of the parent material and on the particle's behavior during devolatilization, which depends on the heating rate and the final temperature reached during volatiles release. Both the initial particle size and apparent density will depend on the extent of swelling that occurs.

Char particle morphology is dependent on the properties of the parent material, particle size and operating conditions. Hence, different chars will exhibit different morphological features under the same gas conditions and heating rates. No two coals or biomass materials will behave in exactly the same manner. Studies have shown that char burnout profiles and temperature histories depend upon char morphology (see for example, [227,228]), therefore accurate predictions of char-particle behavior will depend upon knowing the morphology of the particles being modeled.

Macerals are the microscopic petrographic units in coal that are related to the coal's plant origin and these non-crystalline, organic substances play a role in establishing char particle morphology. The three major maceral groups are vitrinite (the most reactive units and derived from cell walls and woody plant tissue), liptinite (formerly referred to as exinite and derived from decayed leaf matter, spores, pollen, cuticle, and resin) and inertinite (the least reactive units and derived from degraded plant material). No two coals have the same maceral composition; this contributes to variations in coal char reactivities. The vitrinite content of the coal determines its plastic properties and the plastic properties govern, in large part, whether the char produced during devolatilization will have low or high porosity. In the char morphology studies undertaken by Bailey *et al.* [226], bituminous coals were noted to produce porous, anisotropic char particles while sub-bituminous coals were noted to produce mostly isotropic chars, almost exclusively at temperatures near 1273 K. Anisotropy is an indicator of cavities in the central portions of particles and is suggestive of the formation of medium- to high-porosity char particles. Isotropic particles are more uniform with thicker walls than anisotropic char particles and are likely to have lower porosities. The results of these researchers suggest that coals having high vitrinite contents have the potential to swell during heating thereby producing high-porosity char particles and that coals having relatively high inertinite contents have the potential to form low-porosity chars. The higher the vitrinite content of the coal, the greater the potential for metaplast formation and swelling, leading to the formation of high-porosity, low-density char particles. Low rank coals and biomass exhibit little plasticity during heating and hence, tend not to significantly swell. A commonly reported property of a coal is its swelling index (or swelling ratio), a measure of its increase in volume when the coal is heated under specified conditions. The higher the swelling index, the greater the potential for particles to swell during devolatilization producing high-porosity, low density char particles. The swelling index of most coals is equal to or greater than 1.0 whereas the swelling index for most biomass materials is less than 1.0 [2]. A correlation for the swelling index of a coal is presented in Section 4.2.5.

It should be emphasized that the impact of coal devolatilization on char morphology is quite important when there is particle swelling. The

extent of swelling depends not only on the rank of the coal and the pressure that the coal particles experience while losing volatile matter but also on the rates by which the coal particles are heated. A coal swelling model has been developed by Shurtz and co-workers [318,319] that predicts all of the trends observed during coal pyrolysis at atmospheric pressure and high heating rates. Particle shrinkage is predicted for lignites, while increasing swelling ratios are predicted as coal rank is increased from sub-bituminous to bituminous, and decreasing swelling ratios are predicted as coal rank is increased from low volatile bituminous to anthracite. The chemical structural parameters used in the swelling model depend on coal properties that are measured employing ^{13}C nuclear magnetic resonance (NMR) spectroscopy. Correlations for these structural parameters have been developed by Genetti *et al.* [6] that are based on the proximate and ultimate analyses of the coal of interest.

It is recommended to examine a scanning electron micrograph image of the char particles being analyzed to determine the morphological category in which the particles fall, whether group I, II or III (*i.e,* whether particles are mostly cenospherical, mixed or dense) and then use a Thiele modulus-effectiveness factor correlation that is appropriate for the morphological category (see Ma and Mitchell [227]). Expecting wide variations in morphology for bituminous coal chars, perhaps more accurate agreement between model predictions and measurements can be obtained by modeling one-third of the particles as cenospheres, one-third as mixed, medium porosity particles and one-third as dense, low-porosity particles.

In combustion tests of the chars of five coals, Cai *et al.* [303] found (i) that as pyrolysis/devolatilization temperatures increased, char reactivity decreased; (ii) that char reactivity increased with heating rate up to about 1000 K/s before leveling off at higher heating rates; (iii) that chars produced from higher rank coals were relatively insensitive to heating rate; and (iv) that char reactivity decreased as hydropyrolysis pressure increased. Thus, devolatilization conditions impact char particle initial conditions and the reactivity of the carbonaceous particle material.

Unfortunately, devolatilization models have not been improved to the extent that they are capable of predicting not only char yields but also the initial sizes, apparent densities and specific surface areas of the chars produced. It is necessary to measure the particle size distribution, the apparent density and the specific surface area of the char extracted from reactors as soon after devolatilization as possible for use as initial conditions. Model parameters should be evaluated using the mean of the particle size distribution as the characteristic particle diameter. It is recommended to perform sensitivity analyses to establish the sensitivity of kinetic parameters determined from conversion rate data to changes in initial char conditions. A particle population balance model should be employed to investigate the impact of the particle size distribution on the predicted overall char conversion rates.

4. Rank-based correlations for char reaction rates

No two coals have the same chemical composition or chemical structure and owing to the differences in these coal properties, no two coals that experience the same devolatilization conditions will yield char particles that are identical in composition and physical structure. Even pulverized particles of the same coal will produce char particles that differ in chemical and physical characteristics owing to particle-to-particle variations in composition and ash content. Experimentally obtained data will no doubt exhibit scatter, which may obscure trends in conversion behavior, making it difficult to formulate rank-dependent correlations that accurately describe the reactivities of a variety of coal chars.

Since mass transport effects start to influence char conversion rates at temperatures as low as 1200 K [169], specifics of heterogeneous reaction rates cannot be determined directly at temperatures exceeding 1200 K. The combined effects of heterogeneous reaction and pore diffusion limit overall reaction rates at such temperatures. Information on chemical kinetics must be back-calculated from experimental data after modeling mass transport effects. Uncertainties in the temperature dependences of transport properties, especially that of the effective diffusion pore coefficient, lead to uncertainties in the calculated high-temperature reaction rates and hence, uncertainties in activation energies determined for rate-limiting chemical reactions. Owing to (i) the influence of devolatilization on establishing the initial state of the char, (ii) the inherent differences in composition and physical structure of individual particles and (iii) the uncertainties associated with determining rates of rate-limiting heterogeneous reactions at high temperatures, the correlations relating char kinetic parameters to properties of the parent coal yield predictions for char behaviors that are only marginal for the chars of coals that were not in the dataset used to establish the correlation.

4.1. Inherent variations in coal and biomass char reactivities

Intrinsic reactivities can vary by several orders of magnitude for different types of carbons undergoing conversion in similar, high temperature environments. In general, the lower the rank of the coal, the higher the reactivity of its char. Data have been correlated with a wide range of intrinsic activation energies (from 100 to 289 kJ/mol) and reaction orders (from 0 to 1). An Arrhenius fit to all the data obtained in the char oxidation studies considered by Mulcahy and Smith [160,169] yielded a mean activation energy of 179.4 kJ/mol for a variety of carbons (petroleum and metallurgical cokes, lignite and coal chars, anthracite, soot, graphon, catalyzed and purified carbons, and selected graphites). More recent studies have yielded intrinsic activation energies for char oxidation that are within the above range, even for biomass chars. A relatively wide range of activation energies and reaction orders have been reported for the chars of coals having nearly the same rank undergoing conversion in similar environments (for example, see reference [115]). As noted by Mulcahy and Smith [169], a number of interdependent factors make Arrhenius parameters and reaction orders (A, E and n) difficult to determine at combustion temperatures, amongst them the atomic structure of the carbon and catalytic impurities. The values reported also depend on the Arrhenius parameters used to describe the CO/CO_2 ratio.

Consistent with the wide variations observed in the intrinsic reactivities of coal chars, there are wide variations in char apparent reaction rates, and wide variations in the kinetic parameters that describe them. Apparent activation energies range from 64 to 130 kJ/mol for the chars of the low volatile and high volatile bituminous coals used in the study of Hurt and Mitchell [115]. In the gasification studies considered by Gonzalo-Tirado *et al.* [245], apparent activation energies ranged from 97 to 236 kJ/mol for the chars of lignite and bituminous and sub-bituminous coals exposed to a range of CO_2 partial pressures at relatively high temperatures. Apparent reaction orders varied from 0.26 to 1. Shurtz and Fletcher [147] also reported wide variations in reactivity for chars produced from coals of similar ranks.

Besides the chemical reactivity of the carbonaceous particle material, a variety of factors can account for observed differences in coal and biomass char particle reactivities and many are associated with phenomena that occur during devolatilization. These factors influence the conditions of the char at the onset of heterogeneous reaction. In particular, the char particle's initial porosity, specific surface area and pore size distribution as well as the char's extent of thermal annealing are established during devolatilization. Along with variations in non-sphericity and ash content of individual coal particles, scatter in experimental reactivity data is inevitable, especially at high temperatures and pressures. Owing to the variations in the physical and chemical properties of coals and biomass and the factors that cause variations in char particle properties during devolatilization, it has been difficult to correlate char conversion rates with properties of the parent solid fuel.

4.2. Correlating char reactivities with properties of the parent material

Predictions of char reactivity based on coal elemental composition are scarce. There is no obvious mechanistic link between char reactivity and the composition of the coal, for coal composition alone does not provide information on the chemical structure of the char. It has been reported that coals with nearly the same elemental composition have quite different chemical structures [143] and therefore, burn differently. Nevertheless, a few correlations are available for char reactivity based on coal elemental composition.

4.2.1. Rank-dependent correlations for overall particle oxidation rates

Several investigators [114,115,143,149,157] have reported that char reactivity decreases with increasing carbon content of the parent coal, and this observation has guided the development of rank-dependent char conversion models. In the models developed by several researchers, the pre-exponential factor is correlated with the carbon content of the coal (see for example, references [114,143] and [147]). The adequacy of the correlation put forth by Hurt *et al.* [114] is demonstrated in the following paragraph.

Overall char particle burning rates and temperatures predicted for chars derived from several coals, a petroleum coke and Spherocarb are shown in Fig. 14. The particle burning rate, oxygen partial pressure at the outer surface of the particle and temperature were calculated using expressions for the overall particle conversion rate in power-law form (Eq. (72)), boundary layer diffusion (Eq. (144), neglecting Stefan flow and the steady-state form of the particle's energy balance (Eq. (45)). Kinetic parameters for the overall reaction rate coefficient and the CO/CO_2 ratio reported by the investigators for each char were used in the calculations. As noted in the published work, the kinetic parameters reported in each investigation yielded predictions of overall particle conversion rates that agreed with measurements for each char under the conditions tested.

The chars represented on the x-axis of Fig. 14 are arranged in the order of increasing rank of the char precursor: Char #1 was produced from a sub-bituminous coal and Char #12, from a petroleum coke. More information about the chars can be found in Table 6. The chars of the low rank coals are arranged in order of increasing heating value of the coal and the chars of the medium and high rank coals are arranged in order of increasing carbon content of the coal. Open symbols indicate calculations made assuming 6 vol-% oxygen at 1500 K and closed symbols indicated calculations made assuming 12 vol-% oxygen at 1500 K. The calculations shown in the left panel of Fig. 14 indicate that the kinetic parameters determined for the different coal chars do reflect the experimental observation that under the same ambient conditions, char reactivity decreases with increasing rank of the parent coal. The

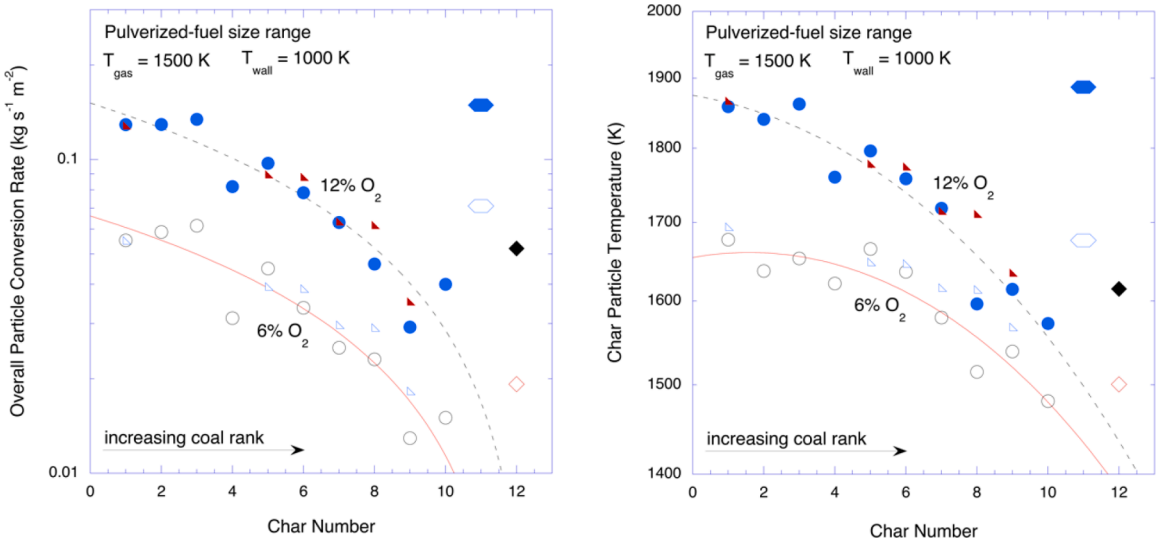

Fig. 14. Calculated overall particle conversion rates and temperatures for pulverized char particles exposed to 6% and 12% oxygen, by volume, at 1500 K with surrounding walls at 1000 K. Information about the different char particles (identified by the char number) is given in Table 6.

Table 6
Information about the different chars shown in Figure 14. Given the parameters in the table, the overall reaction rate of the individual chars are calculated as $R_{ov} = k_{ov}P_{O_2}^n$, when the rate coefficient is $k_{ov} = A_{ov}\exp(E_{ov}/\hat{R}_u T_p)$. Furthermore, the *CO* to CO_2 ratio is found as $N_{CO/CO_2} = A_C \exp(E_C/\hat{R}_u T_p)$.

Char #	Precursor	A_{ov}(kg m^{-2} s^{-1} atm^n)	E_{ov}(kJ/mol)	A_C(-)	E_C(kJ/mol)	n(-)	Reference
Char #1	SUBC	440	91.68	5.0×10^8	251.2	0.5	[115]
Char #2	brown coal	378	56.50	∞†	-	1.0	[123]
Char #3	Millmerran char	2590	86.66	∞†	-	0.5	[118]
Char #4	Low-rank, non-swelling	*	*	∞†	-	1.0	[111]
Char #5	HVCB	38	64.05	3.0×10^8	251.2	0.5	[115]
Char #6	HVCB	224	94.2	2.5×10^8	251.2	0.5	[115]
Char #7	HVAB	290	100.48	4.0×10^4	125.6	0.5	[115]
Char #8	LVB	105	85.82	∞††	-	0.5	[115]
Char #9	LVB	1140	125.6	3.0×10^8	251.2	0.5	[115]
Char #10	Semi-anthracite	200	79.54	∞†	-	1.0	[122]
Char #11	Spherocarb	2000	104.66	∞†	-	0.2	[120]
Char #12	pet coke:	200	76.19	∞†	-	1.0	[121]

† CO assumed to be the sole reaction product; A_C set to ∞
* $k_{ov} = -0.09 - 1.26 \times 10^{-4} T_p + 1.58 \times 10^{-7} T_p^2$

calculations shown in the right panel of Fig. 14 indicate that under the same ambient conditions, char particles produced from low rank coals will attain higher temperatures than those produced from high rank coals. Note that the chars produced from Spherocarb (Char 11) and petroleum coke (Char 12) do not follow the trends observed with the coal chars. The high overall particle conversion rate determined for Spherocarb is quite likely a consequence of its much higher specific surface area compared to coal char particles. Spherocarb is a carbon molecular sieve and as such, it is highly porous with a high porosity (~0.8) and uniform internal structure, unlike coal chars. Not much was mentioned about the petroleum coke employed in the study undertaken by Smith [121] except for the fact that it had a high surface area that was independent of particle size and extent of conversion, a feature not characteristic of coal chars burning in the zone II conversion regime. Smith [160] noted that at 1250 K, the intrinsic reactivity of the petroleum coke was 1000 times that of the brown coal (Char #2) examined. At 700 K, the reactivity of the petroleum coke particles was about 10 times that of the brown coal char particles.

The trend lines shown in the figures were determined from least-squares fits to the points shown for all the coal chars. The right-triangular points in the figure were calculated using the correlation of Hurt *et al.* [114], in which the activation energy is the same for all coal chars ($E_{ov} = 20$ kcal/mol) and the pre-exponential factor depends on the carbon content of the parent coal. Elemental content was known for only six of the coals represented in the figure. Using the correlation, overall particle conversion rates and particle temperatures are predicted that are in reasonably good agreement with the rates and temperatures calculated using the kinetic parameters for each of the coal chars for which the elemental carbon content was known. In the absence of measured conversion rate data, use of this rank-dependent correlation put forth by Hurt *et al.* [114], the Carbon Burnout Kinetics (CBK) model for char reactivity, is recommended. Expressions for the char oxidation rate and CO-to-CO_2 ratio employed in the model are presented below.

The CBK char oxidation model (uniform kinetics):

$$R_{ov,O_2} = -\frac{1}{A_p}\left(\frac{dm}{dt}\right)_{ov} = k_{ov} P_{O_2}^n,\ k_{ov} = A_{ov}\exp\left(E_{ov}/\widehat{R}_u T_p\right),\ \left(R_{ov,O_2}\text{in g cm}^{-2}\text{s}^{-1}\right)$$

$$E_{ov} = 20\ \text{kcal/mol}, \qquad n = 0.5$$

$$\ln(A_{ov}) = 10.82 - 0.0714\ C_{fc}, \qquad \left(A_{ov,O_2}\text{in g cm}^{-2}\text{s}^{-1}\ \text{atm}^{0.5}\right)$$

$C_{fc} \equiv$ the fixed carbon fraction of the coal (daf basis)

$N_{CO/CO_2} = 3 \times 10^8 \exp(E_C/\widehat{R}_u T_p)$ with $E_C = 60$ kcal/mol

Hurt *et al.* [114] indicate that the CBK model is applicable to chars whose parent coals are rich in vitrinite and have carbon contents from 60% to 90%, daf. The above correlation is for uniform kinetics, where consumption of all the carbonaceous particle material is assumed to be uniform. Hurt *et al.* [114] also provide rank-dependent correlations for statistical kinetics, where there is preferential consumption of the more reactive char components early in char conversion resulting in less reactive char later in conversion. These researchers also provide rank dependent correlations for the overall char conversion rate for use with a thermal annealing sub-model. In addition, the CBK model includes an ash inhibition sub-model option.

There have been several modifications to the CBK model. One version, the CBK8 [56], incorporates a rank-dependent correlation for the initial value for char oxidation reactivity in terms of the carbon content of the parent coal. In another version, CBK/E [222], the power-law kinetic expression was replaced with a three-step oxidation mechanism that reflects the variations in reaction order with temperature. This version permits the effects of pressure on char reactivity to be investigated (see Section 3.8). In yet another version, CBK/G [95], heterogenous reaction mechanisms for char gasification in CO_2 and H_2O environments were included. Each of these versions of CBK employs rank-dependent correlations for char kinetic parameters and each provides an option for including thermal annealing in the predictions.

4.2.2. Rank-dependent correlations for overall CO_2 gasification rates

Recent success in predicting devolatilization behavior is largely due to obtaining information about the chemical structure of the coal via NMR analyses. Such analyses have identified the size of aromatic clusters as indicators of char reactivity, the larger the cluster size the lower the reactivity. Large cluster sizes have a smaller fraction of carbon atoms on the edges of the clusters. Since the carbon atoms on the edges are most accessible to reactive gases, intrinsic reactivity should correlate with the fraction of carbon atoms found in the edge structures of the aromatic clusters. As noted by Shurtz and Fletcher [147], this is the closest mechanistic link between the *C/O* elemental ratio in the coal and the gasification reactivity of the char. As such, these researchers developed rank-dependent correlations for CO_2 gasification rate parameters based on the *C/O* ratio of the coal as well as on the aromatic cluster mass of the char produced, which requires NMR analysis of the char for relevant chemical properties. However, Shurtz and Fletcher [147] used correlations developed in devolatilization studies relating ^{13}C-NMR parameters to coal composition and correlated the appropriate NMR property (aromatic cluster mass) to char reactivity. Employing this information, the Char Conversion Kinetics (CCK) model for char CO_2 gasification was developed, which assumes first-order gasification kinetics.

CCK char gasification model correlations (first-order kinetics):

$$R_{ov,CO_2} = -\left(\frac{1}{A_p}\right)\frac{dm}{dt} = k_{ov,CO_2}\ P_{CO_2},\ \left(R_{ov,CO_2}\text{in g cm}^{-2}\ \text{s}^{-1}\right)$$

$$k_{ov,CO_2} = A_{ov,CO_2}\exp\left(E_{ov,CO_2}/\widehat{R}_u T_p\right),\ E_{ov,CO_2} = 123\ \text{kJ/mol}$$

$$\ln\left(A_{ov,CO_2}\right) = -0.51207(C/O) + 3.6505,\ \left(A_{ov,CO_2}\ \text{in g cm}^{-2}\ \text{s}^{-1}\ \text{atm}^{-1}\right)$$

or

$$\ln\left(A_{ov,CO_2}\right) = -0.039337(Char_{Ar}) + 8.3031,\ \left(A_{ov,CO_2}\ \text{in g cm}^{-2}\ \text{s}^{-1}\ \text{atm}^{-1}\right)$$

The aromatic cluster parameter, $Char_{Ar}$, is defined as $Char_{Ar} \equiv M_{cluster} - M_\delta(\sigma + 1)$, where $M_{cluster}$ is the average molecular weight per aromatic cluster, M_δ is the average side-chain molecular weight and $(\sigma + 1)$ is the average number of attachments per cluster. These three chemical structure properties ($M_{cluster}$, M_δ and $(\sigma + 1)$) can be measured by subjecting the char's precursor coal to ^{13}C-NMR analyses or they can be estimated from the composition of the precursor coal employing the following correlations derived by Genetti *et al.* [6].

$$NMR_{property} = c_1 + c_2\ X_C + c_3\ X_C^2 + c_4\ X_H + c_5\ X_H^2 + c_6\ X_O + c_7\ X_O^2 + c_8\ X_{VM} + c_9\ X_{VM}^2$$

Here, X_C, X_H and X_O represent the coal's carbon, hydrogen and oxygen contents on a dry, ash-free basis and X_{VM} is the ASTM volatile matter content (%) of the coal. Values for the coefficients in the equation are presented in Table 7. The better fit to the reaction rate parameters was obtained employing the correlation using the aromatic cluster parameter $Char_{Ar}$.

Table 7
Coefficients for ^{13}C-NRM Chemical Structure Properties [6].

	M_δ	$M_{cluster}$	$\sigma + 1$
c_1	4.220E+02	1.301E+03	5.2105E+01
c_2	-8.647E+00	1.639E+01	1.6387E+00
c_3	4.639E-02	-1.875E-01	-1.0755E-02
c_4	-8.473E+00	-4.548E+02	1.2369E+00
c_5	1.182E+00	5.171E+01	9.3194E-02
c_6	1.154E+00	-1.007E+01	-1.6567E-01
c_7	-4.340E-02	7.608E-02	4.0956E-03
c_8	5.568E-01	1.360E+00	9.2610E-03
c_9	-6.546E-03	-3.136E-02	-8.2672E-05

4.2.3. Rank- dependent correlations for intrinsic CO_2 gasification rates

An m^{th}-order model (CCK^N) was also developed by Shurtz and Fletcher [147] that better described gasification rates for more coal chars than the CCK model. Finding that a reaction order of 0.5 was adequate for all coal chars, the pre-exponential factor and activation energy were correlated with the *C/O* ratio and the aromatic cluster parameter, $Char_{Ar}$. However, the pre-exponential factor did not correlate very well with $Char_{Ar}$ for this model. The correlations employing the *C/O* ratio are presented below [147].

CCK^N char gasification model, *C/O* correlations:

$$R_{c,CO_2} = -\left(\frac{1}{m}\right)\frac{dm}{dt} = k_{int,CO_2}\left(P_{CO_2}/\widehat{R}_u T_p\right)^{0.5},$$

$$k_{int,CO_2} = A_{int,CO_2}\exp\left(E_{int,CO_2}/\widehat{R}_u T_p\right), \quad \left(R_{c,CO_2}\text{in s}^{-1}\right)$$

$$E_{int,CO_2} = 27.016 + 3.7296\ (C/O) - 0.3754\ (C/O)^2, \quad \left(E_{int,CO_2}\ \text{in kcal/mol}\right)$$

$$\ln\left(A_{int,CO_2}\right) = 14.778 + 0.5306\ (C/O) - 0.0908\ (C/O)^2, \quad \left(A_{int,CO_2}\ \text{in}\ \left(\text{mol cm}^{-3}\right)^{-0.5}\ \text{s}^{-1}\right)$$

Shurtz and Fletcher [147] admit that the CCK^N correlation based on the *C/O* ratio predicts the CO_2 gasification rates of lower rank coals better than those of higher rank coals. Both the CCK and CCK^N models are recommended for use in predicting CO_2 gasification rates in the absence of gasification reactivity data for the coal char of interest.

4.2.4. Rank-dependent correlation for overall intrinsic burning rates

Enhancements have been made to the original CBK model and in version 8 (CBK8) [56], intrinsic reaction rates expressed in power-law form are employed instead of the apparent reaction rates employed in CBK. Equation (78) can be multiplied by the particle mass m_c, to yield and expression for the overall mass loss rate of the particle in terms of the intrinsic reactivity of the char. Considering reaction on both external and internal surfaces of the particle yields the following expression for the overall intrinsic burning rate:

$$R^{int}_{ov,O_2} = -(dm_c/dt)_{external} - (dm_c/dt)_{internal} = \left(m_c\ S_g\ R_c\right)_{external} + \left(m_c\ S_g\ R_c\right)_{internal}$$

Now, $(m_c\ S_g)_{external}$ is the external surface area of the particle; thus, the above equation can be rewritten as

$$R^{int}_{ov,O_2} = A_p\ R_{c,s} + \left(m_c\ S_g\ R_c\right)_{internal}$$

where $R_{c,s}$ is the intrinsic reactivity evaluated at conditions existing at the external surface of the particle. Employing the effectiveness factor to relate the reactivity on internal surfaces to that at the external particle surface results in the following expression:

$$R^{int}_{ov,O_2} = A_p\ R_{c,s} + \eta\ m_c\ S_g\ R_{c,s}$$

Owing to the fact that $S_g \gg A_p$, the mass loss rate at the external particle surface is negligible compared to the loss on internal surfaces, except for when the effectiveness factor is quite small, in which case burning rates are diffusion-limited. In CBK8, mass loss on the external surface is neglected and the overall intrinsic burning rate is expressed as

$$R^{int}_{ov,O_2} = \eta\ m_c\ S_g\ R_{c,s} = \eta\ m_c\ S_g\ A_{int}\ \exp\left(-E_{int}/\widehat{R}_u T_p\right)\ P^m_{g,s}$$

where the intrinsic reactivity is written in power-law form. The product $S_g\ \ A_{int}$ is taken to be a single parameter in the model and is termed a *mass-specific intrinsic reactivity*. A rank-dependent correlation for this product was determined from the same data used in the development of CBK.

Expressions equivalent to Eqs. (108) and (109) are used for the Thiele modulus and effectiveness factor in CBK8. Evaluation of the Thiele modulus requires knowledge of the effective diffusivity for mass transport inside the particle owing to the combined effects of bulk and Knudsen diffusion. Instead of employing Eqs. (18) and (19) to determine $\mathscr{D}_{eff}$, the CBK8 model expresses the effective diffusivity as $\mathscr{D}_{eff} = \mathscr{D}_M\Theta/(\tau/f)$, where $\mathscr{D}_M$ is the molecular diffusivity, Θ is the porosity, τ is the tortuosity, and f is the fraction of the total porosity in the feeder pores. The ratio τ/f is a model parameter that characterizes pore structure, and it was observed that model predictions were sensitive to the value employed. Recommended parameters for the CBK8 model are presented below.

The CBK8 char oxidation model:

$$-dm_c/dt = R^{int}_{ov,O_2} = \eta\ m_c\ S_g\ A_{int}\ \exp\left(-E_{int}/\widehat{R}_u T_p\right)\ P^m_{g,s}$$

$$\log_{10}\left(S_g\ A_{int}\right) = 14.97 - 0.0764\ C_{fc},$$

S_g in $\text{cm}^{-2}\text{g}^{-1}$, A_{int} in g $\text{cm}^{-2}\ \text{s}^{-1}\ \text{atm}^{-m}$

where $C_{fc} \equiv$ wt-% carbon in the coal (daf basis)

$$E_{int} = 35\ \text{kcal/mol}, \quad m = 0.5, \quad \tau/f = 6$$

$$N_{CO/CO_2} = 200\exp\left(E_C/\widehat{R}_u T_p\right)\ \text{with}\ \text{E}_\text{C} = 9\ \text{kcal/mol}$$

In the absence of char intrinsic reactivity data, CBK8 is recommended for estimation of the *initial* overall intrinsic oxidation rate for the chars of pulverized fuels. With knowledge of the initial mass specific surface area of the char, S_{g0}, the *mass-specific intrinsic reactivity* can be decomposed to obtain the pre-exponential factor, A_{int}. Employing Eq. (66) for the variation of specific surface area with conversion permits the determination of char conversion as a function of time, subject to the value employed for the char structural parameter, ψ, and values specified for the gaseous conditions.

4.2.5. Rank-dependent correlation for coal swelling index

In one of the versions of the Carbon Burnout Kinetics model for char reactivity, CBK/E [222], a rank-dependent correlation for the coal swelling index (*SI*) was introduced that permits the evaluation of this ratio as a function of the carbon content of the parent coal and the total pressure of the reacting system. The correlation is for pulverized coal particles undergoing devolatilization under high-temperature, high--heating rate conditions and hence, can be used to estimate char particle sizes after devolatilization is complete. The correlation is presented below.

$$SI = \begin{cases} (SI_1)^{(0.7143+2.857\ P)}, & 0.1 \le P \le 0.8 \\ (SI_1)^{(3.5-0.625\ P)}, & 0.8 \le P \le 4.0 \end{cases}$$

where P is the total pressure (in MPa) and SI_1 is the swelling index at atmospheric pressure. It is correlated with the carbon content of the coal as follows:

$$SI_1 = \begin{cases} 8.67 - 0.0833\ C_{daf}, & 89 \le C_{daf} \le 92 \\ -0.0458 + 0.01459\ C_{daf}, & 72 \le C_{daf} < 89 \\ 1.0 & C_{daf} < 72 \end{cases}$$

Here, C_{daf} is the dry, ash-free carbon content of the coal (weight-%). The correlation indicates that at atmospheric pressure, as the carbon content of the coal increases from 72% to 89% the swelling index increases from 1.0 to about 1.26 and then decreases to 1.0 as the carbon content increases further to 92%. It also indicates that as the pressure is increased from 1 atm to 7.9 atm (~0.8 MPa), the swelling index increases, reaching a value about 3 times its atmospheric value at 7.9 atm. As the pressure is increased above 7.9 atm, the swelling index slowly decreases, falling to its atmospheric value at about 39.5 atm. As already noted, the swelling index is a measure of the increase in volume of the char after heating. Assuming that particles are spherical, the diameter of the char

particle formed subsequent to coal devolatilization can be approximated as $d_{char} \cong SI^{(1/3)} d_{coal}$.

4.2.6. Rank-dependent correlations for initial coal char surface areas

When char conversion occurs under zone I or zone II conditions, the surface areas of char particles vary during char conversion and therefore, the approach taken in the development of CBK8 (which assumes that the product of the surface area and *A*-factor associated with power-law kinetics is constant) does not permit heterogeneous reaction dynamics to be investigated. For such investigations, intrinsic reactivity models need information on the initial surface area of the char. Williams *et al.* [320] considered the measured initial surface areas of a number of coal chars that were produced during the rapid heating of the coal and correlated the initial surface areas with the fixed carbon content of the parent coal. The correlations obtained for N_2-BET and CO_2-BET surface areas are presented below:

$$N_2: \; S_{g0} = 1546.3 \; C_{fc}^2 - 2834.9 \; C_{fc} + 1301.7$$

$$CO_2: \; S_{g0} = 4764.2 \; C_{fc}^2 - 7324.9 \; C_{fc} + 2912.9$$

In the above expressions, S_{g0} is the initial surface area of the char particle (in m^2/g) and C_{fc} is the fixed carbon fraction of the parent coal (dry basis), as determined by a proximate analysis. The correlations predict increasing initial surface area with increasing coal rank, ranging from 97 m^2/g for a low-volatile bituminous coal having a fixed carbon content of 77% (dry) to 1020 m^2/g for a sub-bituminous C coal having a fixed carbon content of 33% (dry). These values are representative of reported measurements of the mass specific surface areas of chars produced from high rank coals undergoing high heating rate conditions. Values predicted for the chars of low rank coals are larger than measured values as are the values predicted for biomass chars. In the absence of surface area data, the above correlations can be used to estimate the surface area of the chars of high rank coals at the onset of char conversion.

Such correlations for the apparent and intrinsic reaction rates and surface areas of biomass char particles are not yet available. The overall oxidation rates of biomass chars were found not to be described by the CBK model, their gasification rates are not described by the CCK^N model, and their surface areas are not described by the correlations presented above for N_2- and CO_2-BET surface areas.

5. Challenges and future research directions

The sections above demonstrate that many of the processes that govern the behaviors of coal and biomass chars when exposed to hot environments containing O_2, CO_2 and H_2O have been characterized to the extent that mass loss rates, off-gas composition and char particle temperatures can be accurately predicted. Sub-models that correctly describe the physical and chemical processes that control char particle size, apparent density and reactivity have been developed. Ash models have been created that permit the vaporization rates of mineral inclusions to be characterized, permitting the rates that mineral vapors leave particles and hence, permitting the formation rates and size distributions of particulate matter to be predicted. Fragmentation models have been developed to the extent that the size distributions of char particles can be predicted when account is made for the combined effects of size reduction due to mass loss and fragmentation. Annealing models have also been developed that allow the prediction of the decrease in the reactivity of char exposed to high temperatures, which causes surface reorganization induced by carbonization.

Despite the advances made in modeling char particle behaviors, there are research areas that are still in need of consideration. Some challenges that remain to be overcome and future research directions aimed at extending char particle conversion modeling capabilities are indicated below, in no particular order of importance.

- Presently, the various heterogeneous reaction mechanisms that have been developed to describe char reactivity all differ in their descriptions of the key reaction pathways considered and all have used different coal and biomass chars in experiments undertaken to provide data needed to adjust rate coefficients. It has been difficult to obtain a full understanding of underlying rate-limiting processes that apply to all chars and to associate reaction rate coefficients with char properties. It would be quite useful if a single set of reaction pathways that govern char conversion in combustion and gasification environments were used to describe the reactivities for a variety of chars. The differences in the reactivities of different chars can then be associated with differences in the rate coefficients determined for the chars selected for examination. In this manner, it may be possible to associate rate coefficients with char properties, thereby enhancing model predictive capabilities. Such an effort has the potential to provide a means of better predicting the reactivities of untested chars.
- In most char heterogeneous reaction mechanisms that have been developed, the distribution of activation energies for desorption reactions is assumed to be invariant throughout char conversion, being described by the distribution at the onset of char conversion. This assumption needs to be assessed.
- Heterogeneous reaction rate models that allow for a distribution of activation energies for the adsorption reactions need to be considered.
- Char annealing models require the extent of annealing at the onset of char conversion. This requires describing the consequences of thermal annealing during coal/biomass particle heat-up and devolatilization. With coals, char conversion follows devolatilization. Models developed for annealing during devolatilization and during char conversion can be used without coupling. However with biomass, the potential for char conversion to start before the end of devolatilization is quite likely, especially for particle sizes greater than about 250 μm. Annealing models that are applicable to both devolatilization and char conversion processes need to be developed for such situations.
- Annealing models developed to date are useful in determining the decreases in char mass loss rates during char conversion and are adequate for use in point-particle calculations. However, for a complete understanding of the principles governing reactivity loss due to thermal annealing, a detailed heterogeneous reaction mechanism that accounts for the rate-limiting reaction pathways is needed that considers a distribution of activation energies for the carbon atoms that are exposed when carbon atoms desorb from annealed sites.
- Nearly all char conversion models have neglected mineral matter vaporization and diffusion effects. Future studies should be undertaken that include calculations of the release of mineral vapors containing not only silicon and magnesium but also aluminum, iron and calcium.
- Catalytic effects are important at low char particle temperatures and may become significant in gasifiers after oxygen consumption, when the endothermic char-H_2O and char-CO_2 reactions govern char conversion rates. Owing to the differences in catalytic activity of the various ash components, an ash-catalytic sub-model for use with a char gasification model needs to be developed that reflects the increases in char reactivity as functions of ash content and ash type.
- Besides carbon and oxygen, coal and biomass chars contain hydrogen, nitrogen and sulfur, however, few char conversion models account for the release rates of the H-, N- and S-containing species during the char conversion process. In oxidizing environments at high temperatures, reducing conditions still exist inside particles and H_2, N_2, NH_x, HCN, and H_2S are produced. As these species are released from the char particles, they are oxidized to H_2O, NO_x and SO_x. In gasification environments, H_2, N_2, NH_x, HCN, and H_2S are produced inside the particle, and undergo further reaction when

released from the particle as the gas phase approaches a state of equilibrium. More emphasis should be given to the development of char conversion models that predict pollutant formation during the conversion process.
- Hydrogen released from char can react with mineral oxide inclusions to produce mineral vapors. Few char conversion models include ash vaporization models that consider both CO and H_2 as reducing agents for mineral oxide inclusions. Such models should be developed in order to assess ash vaporization rates under the reducing conditions that actually exist inside char particles.
- To date, nearly all fragmentation models have been used in concert with particle population balance models. Point-particle calculations that include char particle fragmentation need to be undertaken.
- Most char conversion sub-models for point particles are designed assuming that the particles are spherical and isotropic. This is a reasonable assumption for pulverized coal char particles, but not for biomass char particles, which have more elongated shapes and are highly anisotropic. Corresponding sub-models for the point particle approximation should be developed.

6. Concluding remarks

Thermochemical char conversion is a collection of highly interconnected multiphase processes that depend on multicomponent thermodynamic, chemical kinetic, morphological mechanisms and parameters in addition to heat, mass and momentum transport. This work comprehensively reviewed numerical models and related experimental results involved in char conversion modeling. In addition to presenting the governing equations, the assumptions and boundary conditions underlying each model were examined.

Attention was given to an entire spectrum of approaches, from the most detailed simulation approach of fully resolved gas and char particles, to other more simplified computational approaches for both the gas and solid phases. Various sub models of char conversion were discussed to account for effects of turbulence, ash behavior, mode of conversion, particle fragmentation, and thermal annealing. Heterogeneous reaction kinetics were examined to find common ground, in principles and terminology, as well as important differences between the vast number of reaction rate models in the present literature. General classifications of these kinetic models were made for the reader to more clearly understand the various approaches surrounding apparent kinetic models and intrinsic mechanistic models.

To encourage the reader to explore the more relevant models of char conversion for a general application of interest, the following scenarios are presented. If one were interested in predicting overall combustor or gasifier performance with pulverized coal feed, then one might opt for a point particle approach with an apparent reaction rate model for the reacting particles. The fluid phase model, however, will depend on how the effects of turbulence are to be accounted for. The effects of turbulence are accounted for naturally if the relevant turbulent scales are resolved on the numerical mesh, as is the case for DNS, however, the scale of industrial sized operations is too large for a DNS simulation. Hence, one might consider a well-resolved LES model or potentially RANS simulation so long as the effects of turbulence on mass transfer are accounted for appropriately with additional models. Such a model will not be prohibitively demanding in computation, but it will yield char particle mass loss, off-gas composition, and temperature as it flows through the system. An ash model could be included if one wanted to predict ash vaporization rates so that particulate matter evolution inside the combustor could be characterized.

On the other hand, a resolved particle approach with a detailed heterogeneous reaction mechanism may be appropriate if one is interested in char particle conversion dynamics with a focus on characterizing underlying rate-limiting processes. Such a model would be extremely limited in scale but would provide additional information regarding particle density and radii evolution, rate-limiting reactions, concentration profiles within the particle, and details on the effectiveness factor. Furthermore, the results from fully resolved models can be used to inform other less resolved models in terms of the chemical kinetics of the point particles.

Ultimately, the present work aims to support the reader in understanding and development of future models. As presented, char conversion models must be designed based on the scope and scale of the system, including the most salient aspects to be modeled, and can be discretized to the highest degree that desired resolution or computational requirements permit. This work will aid the reader in referencing the vast body of literature and serve as a point of common reference for the principles and mathematics that have been developed thus far in char conversion models.

Declaration of Competing Interest

The authors declare that they have no known competing financial interests or personal relationships that could have appeared to influence the work reported in this paper.

Acknowledgements

The research leading to these results has received funding from the research projects: ‘CHEERS’, financed by the European Union’s Horizon 2020 research and innovation program (grant agreement No. 764697) and the research project ‘Gaspro’, financed by the Research Council of Norway (267916). The authors would like to thank Ewa Karchniwy for valuable input on the manuscript.

Appendix A. Char heterogeneous reaction mechanisms

A heterogeneous reaction mechanism consists of a number of adsorption and desorption reactions that describe the key reaction paths that occur when a solid is exposed to reactive gases. Of interest to combustion and gasification are the key reaction pathways when chars are subjected to environments containing O_2, H_2O and CO_2 as primary reactants. During combustion, the primary products are CO and CO_2 and during gasification, the primary products are H_2 and CO, with CH_4 being a minor product. For an adsorption reaction to occur, a free carbon site must be available to attract the reactant gas, leading to the formation of an adsorbed species. For example, during char combustion, a possible adsorption reaction is $C_f + O_2 \rightarrow C(O) + O$, where C_f represents the free carbon site and C(O) represents the adsorbed oxygen atom. When the adsorbed species leaving the carbon surface, extracting a carbon atom from the carbonaceous matrix in the process, a free carbon site is formed and the underlying bulk carbon atom is exposed. Such a desorption reaction is $C_b + C(O) \rightarrow CO + C_f$, where C_f represents the exposed carbon atom (a free carbon site available for adsorption). By showing the bulk carbon on the reactants side of the reaction, the reaction is balanced. This bulk carbon does not participate in the reaction and is shown solely to indicate mass conservation. In gasification environments, adsorption reactions can result not only in the formation of adsorbed-O, but also in adsorbed-H (C(H)), adsorbed-OH (C(OH)) and even adsorbed-CO (C(CO)). The heterogeneous reaction mechanism contains reactions for the formation of all the adsorbed species and for all the species that desorb from the carbon surface during the char conversion process.

Char reactivity based on heterogeneous reaction rates

Char reactivity is determined from the molar reaction rates of those reactions that release a gas phase species that contains a carbon atom extracted from the char surface. These are desorption reactions. If in desorption reaction k the molar mass of the desorbed species m is $\widehat{M}_m$, the mass fraction of carbon in the desorbed species is $\widehat{M}_C/\widehat{M}_m$ and therefore, the carbon mass loss rate due to reaction k (*i.e.,* char reactivity due to reaction k) is

$$R_{c,k} = (\widehat{M}_C / \widehat{M}_m)(\widehat{\Re}_k \widehat{M}_m) = \widehat{M}_C \ \widehat{\Re}_k \tag{184}$$

where $\widehat{\Re}_k$is the rate of reaction k (see (Eq. (7)). Summing over all desorption reactions yields overall char reactivity:

$$R_c = \sum_{k=1}^{N_{reac\_des}} R_{c,k} = \widehat{M}_C \sum_{k=1}^{N_{reac\_des}} \widehat{\Re}_k. \tag{185}$$

If all free and bulk carbons are shown in the heterogeneous reaction mechanism, then the desorption reaction will have a bulk carbon on the reactant side of the reaction. Since char reactivity is a measure of the rate that carbon atoms are removed from the carbonaceous matrix and for each carbon atom that is removed via desorption a bulk carbon is added as a reactant species to reflect mass conservation, it follows that char reactivity and the reactivity of the bulk carbons are the same. Thus,

$$R_c = \widehat{M}_C \sum_{k=1}^{N_{reac\_des}} \widehat{\Re}_k = -\widehat{M}_C \widehat{R}_{C_b} \tag{186}$$

where the molar reactivity of the bulk carbons is determined via Eq. (10).

The molar reactivities of all the species involved in the system of heterogeneous reactions must satisfy the following conservation of mass expression:

$$\sum_{i=1}^{N_{spec}} \widehat{R}_i \widehat{M}_i = 0 \tag{187}$$

where $\widehat{M}_i$ is the molar mass of species i, and the summation is over all the species in the mechanism, including the free and bulk carbons. Separating the summation into surface species (adsorbed species and free and bulk carbons) and gas-phase species yields

$$\sum_{i=1}^{N_{spec}} \widehat{R}_i \widehat{M}_i = \sum_{i=1}^{N_{spec\_surf}} \widehat{R}_i \widehat{M}_i + \sum_{i=1}^{N_{spec\_gas}} \widehat{R}_i \widehat{M}_i = 0. \tag{188}$$

Expanding the summation over the surface species and rearranging results in the following relationship for the reactivities of the free and bulk carbons:

$$\widehat{R}_{C_f} \widehat{M}_{C_f} + \widehat{R}_{C_b} \widehat{M}_{C_b} = -\left(\widehat{R}_{C(O)} \widehat{M}_{C(O)} + \widehat{R}_{C(H)} \widehat{M}_{C(H)} + \widehat{R}_{C(OH)} \widehat{M}_{C(OH)} + \widehat{R}_{C(CO)} \widehat{M}_{C(CO)}\right) - \sum_{i=1}^{N_{spec\_gas}} \widehat{R}_i \widehat{M}_i. \tag{189}$$

Grouping the summation of the reactivities of adsorbed species in the parenthesis and solving for the reactivity of the bulk carbon yields

$$\widehat{R}_{C_b} \widehat{M}_{C_b} = -\widehat{R}_{C_f} \widehat{M}_{C_f} - \sum_{i=1}^{N_{spec\_ads}} \widehat{R}_i \widehat{M}_i - \sum_{i=1}^{N_{spec\_gas}} \widehat{R}_i \widehat{M}_i. \tag{190}$$

Combining this equation with Eq. (186) yields the following expression for char reactivity:

$$R_c = \widehat{R}_{C_f} \widehat{M}_{C_f} + \sum_{i=1}^{N_{spec\_ads}} \widehat{R}_i \widehat{M}_i + \sum_{i=1}^{N_{spec\_gas}} \widehat{R}_i \widehat{M}_i. \tag{191}$$

Steady state

When during the course of reaction, an adsorbed species maintains a nearly constant concentration, the adsorbed species is said to be in "steady state." The formation and consumption rates of the adsorbed species are nearly equal and as such, for this adsorbed species, its molar reactivity is zero. Thus, for adsorbed species j in steady state during the course of char conversion, $\widehat{R}_j = 0$. When all the adsorbed species reach steady-state levels, the free carbon concentration also reaches a steady state. Thus, when all adsorbed species are at steady state,

$$(R_c)_{ss} = \sum_{i=1}^{N_{spec\_gas}} \widehat{R}_i \widehat{M}_i. \tag{192}$$

Many heterogeneous reaction mechanisms that have been developed support a quasi-steady state for adsorbed species, but unsteady calculations indicate that this occurs at char conversions greater than about 25%, after the adsorbed species have had sufficient time to build up to their steady-state concentrations.

Char reactivity in terms of reaction rate kinetic parameters

In order to demonstrate the above expressions for char reactivity, consider the following three-step adsorption/desorption reaction mechanism for carbon oxidation in which O-atoms are adsorbed via both an adsorption reaction (r1) and a complex enhanced adsorption reaction (r2). Both CO and CO_2 are released from the surface, CO_2 via the complex enhanced adsorption reaction and CO, via the desorption reaction, r3. This three-step adsorption/desorption reaction mechanism for carbon oxidation is an analog of the semi-global mechanism discussed by Hurt and Calo [172]. In this modification, account is explicitly made for free and bulk carbons.

r1: $C_f + O_2 \rightarrow C(O) + O$.
r2: $C_f + C_b + C(O) + O_2 \rightarrow CO_2 + C(O) + C_f$.
r3: $C_b + C(O) \rightarrow CO + C_f$.

Based on this mechanism, the right-hand-side of Eq. (186) can be expanded to yield the following expression for char reactivity:

$$R_c = \widehat{M}_C \sum_{k=1}^{N_{reac\_des}} \widehat{\Re}_k = \widehat{M}_C \ (\widehat{\Re}_2 + \widehat{\Re}_3). \tag{193}$$

The molar reaction rates of reactions r1, r2 and r3 are given by

$$\widehat{\Re}_1 = k_1 \ \xi_n \ (1-\theta_o) \ [O_2]$$

$$\widehat{\Re}_2 = k_2 \ \xi_n{}^2 \ (1-\theta_o) \ \theta_o \ [O_2]$$

$$\widehat{\Re}_3 = k_3 \ \xi_n \ \theta_o$$

where ξ_n is the total surface concentration of all carbon sites, θ_o is the fraction of the sites occupied by oxygen atoms and $[O_2]$ is the concentration of oxygen in the gas phase (in mol/m^3). The surface concentration of adsorbed oxygen atoms, [C(O)], equals $\xi_n\theta_o$ and since sites are either free or occupied by oxygen atoms, the surface concentration of free carbon sites, $[C_f]$, equals $\xi_n\theta_f = \xi_n \ (1-\theta_o)$. The carbonaceous solid material is assumed to behave as an ideal solid; consequently, the activity of bulk carbon is taken to be unity. Employing these reaction rates in Eq. (193) yields:

$$R_c = \widehat{M}_C \ \{k_2 \ \xi_n{}^2 \ (1-\theta_o) \ \theta_o \ [O_2] + k_3 \ \xi_n \ \theta_o\}. \tag{194}$$

The steady-state concentration for adsorbed-O (or the adsorbed-O site fraction) is found by setting its rate of change to zero:

$$\frac{d\theta_O}{dt} = \widehat{\Re}_1 - \widehat{\Re}_3 = \widehat{R}_{C(O)} = \xi_n\{k_1[O_2] - (k_1[O_2] + k_3)\theta_o\} = 0.$$

Solving for θ_O yields $(\theta_O)_{ss}$:

$$(\theta_O)_{ss} = \frac{k_1[O_2]}{k_1[O_2] + k_3}.$$

The fraction of free carbon sites at steady state is therefore

$$(\theta_f)_{ss} = 1 - (\theta_O)_{ss} = 1 - \frac{k_1[O_2]}{k_1[O_2] + k_3} = \frac{k_3}{k_1[O_2] + k_3}.$$

Employing these steady-state relations in Eq. (194) yields the following expression for char reactivity assuming adsorbed species in steady state:

$$R_c = \widehat{M}_C \sum_{k=1}^{N_{reac\_des}} \widehat{\Re}_k = \widehat{M}_C \left\{ k_2 \ \xi_n{}^2 \left(\frac{k_3}{k_1[O_2] + k_3}\right)\left(\frac{k_1[O_2]}{k_1[O_2] + k_3}\right)[O_2] + k_3 \ \xi_n \ \frac{k_1[O_2]}{k_1[O_2] + k_3} \right\}.$$

Simplifying results in

$$R_c = \widehat{M}_C \left\{ \frac{k_1 k_3 \xi_n [O_2]}{(k_1[O_2] + k_3)} \left(1 + \frac{k_2 \xi_n [O_2]}{(k_1[O_2] + k_3)}\right) \right\}. \tag{195}$$

The above equation gives char reactivity in terms of the reaction rate coefficients of the reactions in the mechanism. These are generally expressed in Arrhenius form.

Validation of Eq. (192)

The summation on the right-hand-side of Eq. (192) can be expanded to yield

$$(R_c)_{ss} = -\sum_{i=1}^{N_{spec,gas}} \widehat{R}_i \widehat{M}_i = \widehat{R}_{O_2}\widehat{M}_{O_2} + \widehat{R}_{CO_2}\widehat{M}_{CO_2} + \widehat{R}_{CO}\widehat{M}_{CO} + \widehat{R}_O\widehat{M}_O.$$

Based on the reaction mechanism, the molar reactivities of the species can be determined via Eq. (10).

$$\widehat{R}_{O_2} = -\widehat{\Re}_1 - \widehat{\Re}_2$$

$$\widehat{R}_{CO} = \widehat{\Re}_3$$

$$\widehat{R}_{CO_2} = \widehat{\Re}_2$$

$$\widehat{R}_O = \widehat{\Re}_1$$

Using these relations for species molar reactivity in the above expression for steady state char reactivity and simplifying results in

$$(R_c)_{ss} = (-\widehat{\Re}_1 - \widehat{\Re}_2)\widehat{M}_{O_2} + \widehat{\Re}_2\widehat{M}_{CO_2} + \widehat{\Re}_3\widehat{M}_{CO} + \widehat{\Re}_1\widehat{M}_O,$$

which can be rearranged to yield

$$(R_c)_{ss} = \widehat{\Re}_1(-\widehat{M}_{O_2} + \widehat{M}_O) + \widehat{\Re}_2(-\widehat{M}_{O_2} + \widehat{M}_{CO_2}) + \widehat{\Re}_3\widehat{M}_{CO}.$$

Since at steady state $\widehat{\Re}_1 = \widehat{\Re}_3$,

$$(R_c)_{ss} = \widehat{\Re}_3(-\widehat{M}_{O_2} + \widehat{M}_O + \widehat{M}_{CO}) + \widehat{\Re}_2(-\widehat{M}_{O_2} + \widehat{M}_{CO_2}).$$

Realizing that each parenthesis equals M_C, this expression can be rewritten as

$$(R_c)_{ss} = \widehat{\Re}_3(\widehat{M}_C) + \widehat{\Re}_2(\widehat{M}_C) = \widehat{M}_C(\widehat{\Re}_3 + \widehat{\Re}_2)$$

This agrees with Eq. (193), thereby validating Eq. (192) for the calculation of char reactivity when all adsorbed species are assumed to be in steady state.

CO-to-CO_2 product ratio

The CO-to-CO_2 product ratio can be calculated from the CO and CO_2 molar reactivities. The molar reactivities of the species are calculated via Eq. (10). Based on the reaction mechanism,

$$\widehat{R}_{CO} = \widehat{\Re}_3 = k_3\xi_n\theta_o$$

$$\widehat{R}_{CO_2} = \widehat{\Re}_2 = k_2(\xi_n)^2(1-\theta_o)\theta_o[O_2]$$

From the ratio of these reactivities,

$$\frac{N_{CO}}{N_{CO_2}} = \frac{\widehat{R}_{CO}}{\widehat{R}_{CO_2}} = \frac{k_3\xi_n\theta_o}{k_2(\xi_n)^2(1-\theta_o)\theta_o[O_2]} = \frac{k_3\xi_n}{k_2(\xi_n)^2(1-\theta_o)[O_2]}.$$

Employing the steady-state adsorbed-O site fraction:

$$\frac{N_{CO}}{N_{CO_2}} = \frac{(k_1[O_2] + k_3)}{k_2\xi_n[O_2]}$$

In agreement with experimental observations, this expression reveals that at fixed temperature, as the oxygen concentration is increased, the CO-to-CO_2 product ratio decreases, *i.e.,* more CO_2 is produced as the oxygen concentration is increased.

Appendix B. Summary of reaction rate models and relationships between them

The variety of models that have been developed to characterize the mass loss rates of char particles in oxidizing and reducing environments can be grouped into two categories: apparent reaction rate models and intrinsic reaction rate models. Apparent reaction rate models predict mass loss rates per unit external particle surface area (A_p) while intrinsic reaction rate models predict mass loss rates per unit internal surface area ($m_p \cdot S_g$) or per unit total surface area (internal plus external).

I. Overall/Apparent reaction rate models (see Section 3.2.1)

A. Overall particle reaction rate, R_{ov} (in kg/m^2/s)

$$R_{ov} \equiv -\frac{1}{A_p}\frac{dm}{dt} = -\left(\frac{1}{\pi d_p^2}\right)\frac{dm}{dt}$$

Employing power-law kinetics,

$$R_{ov} = k_{ov}\cdot P_{g,s}^{n} = A_{ov}\cdot\exp(-E_{ov}/\widehat{R}_u T_P)\cdot P_{g,s}^{n}$$

where k_{ov} is the overall reaction rate coefficient (in kg/m^2/s/atm^n), E_{ov} is the overall activation energy and n is the apparent reaction order. The reactive gas partial pressure is evaluated at the conditions existing at the outer surface of the particle, which is determined from a balance between the diffusive rate of flow of the reactive gas to the particle surface and its consumption rate at the surface due to heterogeneous chemical reaction.

B. Apparent reaction rates, R_a and $R_a^{'}$ (in 1/s)

$$R_a \equiv -\left(\frac{1}{m_0}\right)\frac{dm}{dt} \text{ or } R_a^{'} \equiv -\left(\frac{1}{m}\right)\frac{dm}{dt}$$

Employing power-law kinetics,

$$R_a = k_a\cdot P_{g,s}^{n'} = A_a\cdot\exp\left(-E_a/\widehat{R}_u T_p\right)\cdot P_{g,s}^{n'}$$

and

$$R_a^{'} = k_a^{'}\cdot P_{g,s}^{n'} = A_a^{'}\cdot\exp\left(-E_a^{'}/\widehat{R}_u T_p\right)\cdot P_{g,s}^{n'}$$

where k_a and $k_a^{'}$ are apparent reaction rate coefficients (in 1/atm^n/s), E_a and $E_a^{'}$ are apparent activation energies, and n' is the order of reaction.

C. Relationships between overall and apparent reaction rates

$$R_{ov} = \left(\rho_{char,0}\cdot d_{p,0}/6\right)\cdot\left(d_{p,0}/d_p\right)^2\cdot R_a = \left(\rho_{char}\cdot d_p/6\right)\cdot R_a^{'}$$

II. Intrinsic reaction rate models (see Sections 2.3 and 3.2.2)

The mass loss rate is expressed in terms of the intrinsic reactivity of the carbonaceous material, R_c (in kg/m^2/s).

$$\frac{1}{m_c}\frac{dm_c}{dt} = -S_g\cdot R_c$$

A. Power law-based models

$$R_c = k_{int}P_{g,s}^{m} = A_{int}\exp\left(-E_{int}/\widehat{R}_u T_p\right)P_{g,s}^{m}$$

where E_{int} is the intrinsic (or true) activation energy and m is the true reaction order.

B. Heterogeneous reaction mechanism-based models

Consideration is given to a heterogeneous reaction mechanism consisting of N_{reac} chemical reactions, some of which are desorption reactions that result in the formation of N_{spec} gas-phase species. Each of these species extracts a carbon atom from the carbon matrix when formed. The intrinsic chemical reactivity of the particle is given by

$$R_{c,p} = M_C\cdot\sum_{i=1}^{N_{spec}}\widehat{R}_{i,p}$$

where the overall molar reactivity of species i for the entire particle is expressed as

$$\widehat{R}_{i,p} = \sum_{k=1}^{N_{reac}}\widehat{\Re}_{k,p}\left(\nu_{i,k}^{''}-\nu_{i,k}^{'}\right).$$

The particle-averaged reaction rate of reaction k ($\widehat{\Re}_{k,p}$, in mol/m^2/s) is given by

$$\widehat{\Re}_{k,p} = k_{k,f}\Pi_{i=1}^{N_s}C_{i,p}^{\nu_{i,k}^{'}} - k_{k,r}\Pi_{i=1}^{N_s}C_{i,p}^{\nu_{i,k}^{''}} = \eta\cdot\left(k_{k,f}\Pi_{i=1}^{N_s}C_{i,s}^{\nu_{i,k}^{'}} - k_{k,r}\Pi_{i=1}^{N_s}C_{i,s}^{\nu_{i,k}^{''}}\right)$$

where the average reactant concentration in the particle ($C_{i,p}$, in mol/m^3) is evaluated as

$C_{i,p} = \eta \cdot C_{i,s}$,

$C_{i,s}$ being the reactant concentration at the surface of the particle.

C. Total char mass loss rate

$$\left(\frac{dm_c}{dt}\right)_{total} = \left(\frac{dm_c}{dt}\right)_s + \left(\frac{dm_c}{dt}\right)_{int} = -\left(1 + \frac{S_g \cdot \rho_{char} \cdot d_p \cdot \eta}{6}\right) \cdot A_p \cdot R_{c,s}$$

where $R_{c,s}$ is the intrinsic particle reactivity evaluated at conditions existing at the external surface of the particle.

D. Relationship between the overall particle reaction rate and the intrinsic particle reactivity

$$R_{ov} \equiv -\frac{1}{A_p}\frac{dm}{dt} = \left(1 + \frac{S_g \cdot \rho_{char} \cdot d_p \cdot \eta}{6}\right) \cdot R_{c,s}$$

Appendix C. Modeling mineral matter nucleation, condensation and coagulation

As the volatile reduced mineral species escape the char particle, diffusing into the surrounding environment, they react with gaseous species in the environment forming volatile mineral oxides. In combustors, the reduced mineral species react with oxygen and in gasifiers, with steam and carbon dioxide:

$$MO_{n-1}(g) + O_2 \rightarrow MO_n(g) + O$$

$$MO_{n-1}(g) + H_2O \rightarrow MO_n(g) + H_2$$

$$MO_{n-1}(g) + CO_2 \rightarrow MO_n(g) + CO$$

The rates of these bimolecular reactions are kinetically controlled. Globally, for reduced mineral species *i*:

$$R_{reaction,MO_n} = k_{O_2} P_{O_2} P_{MO_{n-1}} + k_{H_2O} P_{H_2O} P_{MO_{n-1}} + k_{CO_2} P_{CO_2} P_{MO_{n-1}} \tag{196}$$

where the reaction rate coefficients (k_{O_2}, k_{H_2O} and k_{CO_2}) are each expressed in modified Arrhenius form: $AT^n \exp(-E/RT)$. When considering the oxidation of magnesium metal vapors under simulated pulverized coal combustion conditions, Neville [268] estimated the rate coefficient using collision theory, as described by Laidler [321], and reported for the magnesium metal vapor oxidation reaction rate coefficient, k_{O_2}: $A = 4.44 \times 10^{18}$ m^3/mol/s, $n = 0.5$ and $E = 1.28 \times 10^5$ J/mol.

The partial pressure of the reduced mineral species at various distances outside the char particle are determined by integrating the following differential equation:

$$\frac{1}{r^2}\frac{d}{dr}\left(r^2 \frac{\mathscr{D}_{MO_{n-1}}}{\widehat{R}_u T_{BL}} \frac{dP_{MO_{n-1}}}{dr}\right) = -\dot{R}_{reaction,MO_n}. \tag{197}$$

Here, $\mathscr{D}_{MO_{n-1}}$ is the diffusion coefficient of the reduced mineral species (MO_{n-1}) in the boundary layer surrounding the particle and T_{BL} is the effective temperature in the boundary layer. At the radius of the char particle ($r = d_p/2$), $P_{MO_{n-1}} = P^s_{MO_{n-1}}$ and as $r \rightarrow \infty$, $P_{MO_{n-1}} \rightarrow 0$. Following the approach of Quann [260], the partial pressure of the reduced mineral oxide at the outer surface of the char particle is given by

$$P^s_{MO_{n-1}} = \left[\frac{\left(\frac{\mathscr{D}_{MO_{n-1}}}{\alpha_I \mathscr{D}_{O_2}}\right)\left(\frac{T_{BL}}{T_p}\right)\left(1 - \frac{\phi_I}{\tanh(\phi_I)}\right)}{1 + \left(\frac{\mathscr{D}_{MO_{n-1}}}{\alpha_I \mathscr{D}_{O_2}}\right)\left(\frac{T_{BL}}{T_p}\right)\left(1 - \frac{\phi_I}{\tanh(\phi_I)}\right)}\right] P^{eq}_{MO_{n-1}} \tag{198}$$

where φ_I is the Thiele modulus for vaporization ($\phi_I = (d_P/d_I)\sqrt{3\varphi_I}$, ϕ_I being the volume fraction of mineral inclusions inside the particle and d_I being the mean inclusion diameter) and α_I is defined in Eq. (148). Employing the above expressions, Neville [268] predicted that the magnesium metal vapors escaping a nominally 40 μm diameter char particle in 20% oxygen at 1750 K were completely re-oxidized to metal oxide vapors before the metal vapor had diffused nine particle radii from the particle surface. The simulations performed by Neville [268] also indicated that the re-oxidation reactions of calcium and iron metal vapors that escape the char particle are also fast at the high temperatures outside char particle surfaces and as a result, their partial pressures are significantly reduced in the boundary layers surrounding particles. The loss of the metal vapors via condensation processes are predicted to be inconsequential compared to the rates that the metal vapors are oxidized to metal oxides. However, the simulations performed by Neville also indicated that the re-oxidation of reduced silicon oxide (SiO) is relatively slow compared to that of the metal vapors. The partial pressure of SiO was calculated to be higher than that of volatile silicon oxide (SiO_2) as well as the SiO_2 saturation vapor pressure at distances from the char surface as great as 17 particle radii. It is likely that with volatile silicon oxides, the condensation of both SiO and SiO_2 need to be taken into account for accurate prediction of nanoparticle size distributions.

The volatile mineral oxides (MO_n) that are formed from the reduced metal oxides and metals can nucleate and then grow via heterogeneous condensation processes. The partial pressure (P_{MO_n}) of volatile mineral oxide species at various distances from the char particle is governed by the following differential equation:

$$\frac{1}{r^2}\frac{d}{dr}\left(r^2\frac{\mathscr{D}_{MO_n}}{\widehat{R}_u T_{BL}}\frac{dP_{MO_n}}{dr}\right) = \left(\dot{R}_{reaction} - \dot{R}_{nucleation} - \dot{R}_{condensation}\right)_{MO_n}. \tag{199}$$

Here, $\mathscr{D}_{MO_n}$ is the diffusion coefficient of the mineral oxide species in the gaseous mixture surrounding the char particle and the terms on the right-hand-side represent the rates of change (in mol/m^3/s) in the concentrations of the volatile mineral oxide species owing to chemical reaction, nucleation and heterogeneous condensation processes. At the high temperatures near the char surface, the partial pressures of the volatile mineral species are greater than their saturation pressures; consequently, there can be significant nucleation and condensation as particles grow via coagulation and coalescence processes.

As volatilized mineral oxide species diffuse, they tend to cluster. Based on the classical nucleation theory (CNT) (see for example, Reiss [322] and Karthika *et al.* [323]), nucleation will occur spontaneously as soon as a certain supersaturation level is achieved. This critical cluster size for volatile mineral oxide species is given by

$$d_{crit,MO_n} = \frac{4\sigma_{MO_n}\upsilon_{MO_n}}{k_B T \ln\left(P_{MO_n}/P^*_{MO_n}\right)} \tag{200}$$

Here, σ_{MO_n} is the specific surface tension of a droplet of the mineral oxide species having a molecular volume of υ_{MO_n}; P_{MO_n} and $P^*_{MO_n}$ are the partial and saturation pressures of the mineral oxide species, respectively; and k_B is the Boltzmann constant. The saturation pressure is taken as the partial pressure of the condensable species for equilibrium between liquid mineral oxide species with a planar interface and gaseous mineral species at temperature T. The ratio $P_{Mn}/P^*_{MO_n}$ is a measure of the extent of supersaturation. If there is no supersaturation ($P_{MO_n} < P^*_{MO_n}$), there is no homogeneous nucleation. For supersaturation ratios greater than about 5, homogeneous nucleation of submicron particles takes place [324]. The greater the extent of supersaturation, the smaller the critical cluster size, the initial size of the nucleated particles. For clusters of the critical size, growth rates (which lead to macroscopic size nano-particles) and decay rates (which cause clusters to shrink to the sizes of their monomers) are equal. The addition of just one more vapor molecule to a cluster of the critical size will cause nucleation. Shown in Fig. 15 are critical cluster sizes calculated for mineral species that may condense in a char particle's boundary layer for a supersaturation ratio of 5.

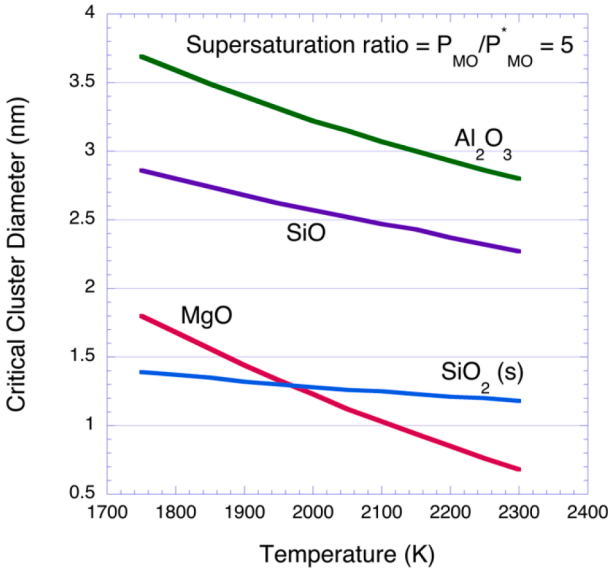

Fig. 15. Critical cluster diameter.

For temperatures between 1700 and 2300 K, critical cluster diameters are in between 0.5 and 4 nm, with Al_2O_3 vapors yielding the largest sizes and MgO, the smallest. Note that critical cluster sizes decrease with increasing temperature for a fixed extent of reaction. Of course, since the vapor pressures of the mineral species depend upon temperature, the same extent of supersaturation for each temperature implies different partial pressures for the mineral species vapors at the different temperatures. For a supersaturation ratio of 10, critical cluster sizes are about 30% smaller than they are for a saturation ratio of 5. Other researchers [324-326] have derived analogous expressions for the critical cluster size of condensing vapors based on the CNT.

The nucleation rate depends on the net number of clusters per unit time that grow larger than this critical size. Neville [268] applied the CNT to magnesium oxide vapors, and expressed the rate of homogeneous nucleation ($\dot{r}_{nucleation}$, in nuclei/m^3/s) of a spherical liquid MgO droplet from MgO vapors as follows:

$$\dot{r}_{nucleation,MO_n} = \frac{2\, a_C (P_{MO_n})^2 (\sigma_{MO_n})^{0.5} \upsilon_{MS_i}}{(2\pi m_{MO_n})^{0.5} (k_B T)^2} \exp\left(\frac{-16\pi (\sigma_{MO_n})^3}{3 k_B T (\Delta G_\upsilon)^2}\right) \tag{201}$$

where

$$\Delta G_\upsilon = \frac{k_B T}{\upsilon_{MO_n}} \ln\left(P_{MO_n} / P^*_{MO_n}\right) \tag{202}$$

Here, a_C is the condensation coefficient (assumed to be unity), m_{MO_n} is the molecular mass of the mineral oxide species (MgO), and ΔG_υ is the change in the Gibbs free energy for droplet formation per unit volume. Note that the greater the extent of supersaturation, the greater ΔG_υ and hence, the greater the mineral species nucleation rate. Analogous expressions for the rate of nucleation have been put forth by other researchers [324-326]. Shown in Fig. 16 are calculated nucleation rates for magnesium oxide and silicon oxide vapors as a function of temperature for specified values of the supersaturation ratio.

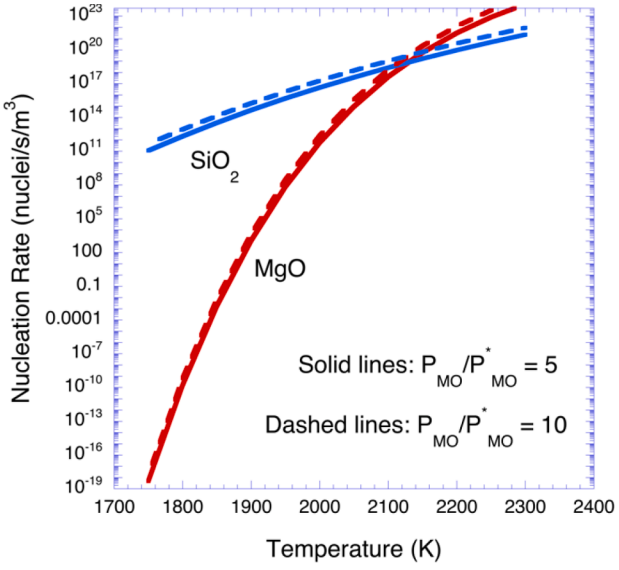

Fig. 16. Mineral oxide nucleation rates.

Nucleation rates are noted to increase with temperature, the rates being much more sensitive to temperature than to supersaturation ratio. For MgO vapors, at 2000 K, the nucleation rate is ~6.0×10^{11} nuclei/m^3/s for a supersaturation ratio of 5 and increases to ~2.4×10^{12} nuclei/m^3/s for a saturation ratio of 10, a factor of about four. The rate changes by over three orders of magnitude if the temperature is changed by only 50 K from 2000 K. The nucleation rates of SiO_2 vapors are not as sensitive to temperature as are the rates for MgO vapors. For a supersaturation ratio of 5, the nucleation rate of SiO_2 vapors increase from ~4.6×10^{16} nuclei/m^3/s at 2000 K to ~9.6×10^{19} nuclei/m^3/s at 2200 K, an increase by a factor of only about 2100 over a 200 K increase in temperature.

Initial droplet sizes could be as small as the critical cluster sizes. Helble and Sarofim [327] report that inorganic vapors homogeneously nucleate to form particles in the size range 0.01 to 0.03 μm (10 to 30 nm). It is quite likely that these particles could have already undergone some degree of coalescence. Assuming an initial mineral droplet size of $d_{MOn,it}$ the molar nucleation rate (in mol/m^3/s) is given by

$$\dot{R}_{nucleation,MO_n} = \frac{\pi d^3_{MO_n,init}}{6\upsilon_{MO_n} N_{AV}} \quad \dot{r}_{nucleation,MO_n} \tag{203}$$

where N_{AV} is Avogadro's number.

The nucleated mineral clusters grow in size owing to condensation of vapor molecules that collide with them. The heterogeneous condensation rate of vapor mineral species i depends on the Knudsen range of the stable mineral clusters and for the cluster sizes expected, the Knudsen number is in the transition range between flow in the free molecular ($Kn = \lambda / d_{cluster} >> 1$) and continuum ($Kn \ll 1$) regimes. Shown in Fig. 17 are calculated Knudsen numbers as functions of temperature for Al_2O_3, MgO and SiO_2, using the critical cluster size as the characteristic length. Note that Knudsen numbers increase with increasing temperature, especially for MgO, which exhibits the largest Knudsen numbers at temperatures greater than 1900 K. Aluminum oxide vapors, which have the largest critical cluster sizes have the smallest Knudsen numbers.

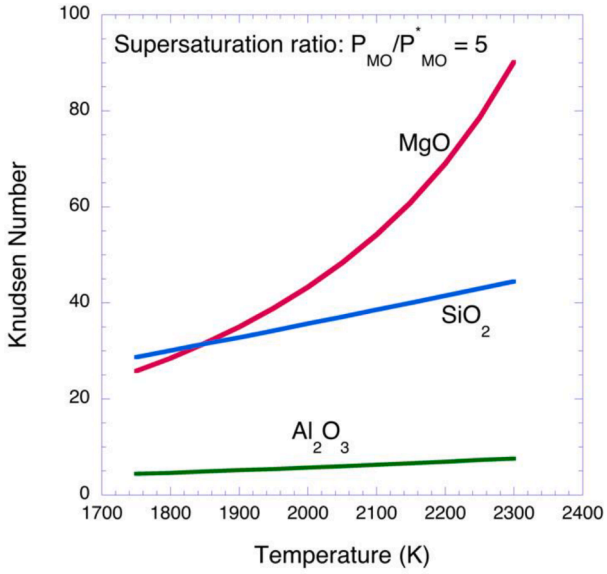

Fig. 17. Mineral oxide Knudsen numbers.

When Knudsen numbers are in the range for free molecular flow, collisions between the vapor molecules and the clusters will be random as the molecules travel in straight lines until they encounter another particle or hit a wall. For such particles, the condensation rate can be calculated using results from the kinetic theory of gases (*e.g.,* see Friedlander [328]):

$$\left(\dot{r}_{condensation,MO_n}\right)_{d_{MO_n}}^{free\ molecular} = \frac{\pi\left(d_{MO_n}\right)^2\alpha_c}{\left(2\pi m_{MO_n}k_BT\right)^{1/2}}\left(P_{MO_n}-P_{MO_n}^*\right). \tag{204}$$

This is the condensation rate for a particle of diameter d_{MO_n}. In the above expression, α_c is a mass accommodation factor and is assumed to be equal to unity. When Knudsen numbers are in the range for continuum flow, the vapor molecules are sufficiently large that they act as a continuous fluid flowing around each other and the clusters. Diffusion coefficients can be used to describe the relative motion between the vapors and clusters, and the condensation rate can be approximated using the following expression (*e.g.,* see [328]):

$$\left(\dot{r}_{condensation,MO_n}\right)_{d_{MO_n}}^{continuum} = \frac{2\pi d_{MO_n}\mathscr{D}_{MO_n}}{\widehat{R}_uT}\left(P_{MO_n}-P_{MO_n}^*\right). \tag{205}$$

In this expression, the diffusion coefficients are determined from $\mathscr{D} = \lambda\overline{\overline{\mathbf{u}}}/3$ where $\overline{\overline{\mathbf{u}}}$ is the mean speed of the particle: $\overline{\overline{u}} = \left(3\widehat{R}_uT/\widehat{M}\right)^{1/2}$.

In the transition flow regime, Kn ~ 1, the forces that particles experience as they flow is quite complex, rendering it necessary to use semi-empirical relations for the condensation rates for particles that have sizes the same order as their mean free paths. The following interpolation expression, due to Fuchs and Sutugin [329], has been used to describe the condensation rate over the entire Knudsen range:

$$\left(\dot{r}_{condensation,MO_n}\right)_{d_{MO_n}} = \left(\dot{r}_{condensation,MO_n}\right)_{d_{MO_n}}^{continuum}\left(\frac{1+\mathrm{Kn}}{1+0.377\mathrm{Kn}+\frac{4}{3\alpha_c}\left(\mathrm{Kn}+\mathrm{Kn}^2\right)}\right). \tag{206}$$

The above expression yields rates that match those for both the free molecular and continuum regimes when the mass accommodation factor is set to 0.461 and the Knudsen number is defined in terms of the particle diameter (Kn = λ/d), as in this work. When the Knudsen number is defined in terms of the particle radius (Kn = λ/d), as in the work of Fuchs and Sutugin [329], the accommodation factor takes the value 0.922, a value near their empirical value of unity. A graph showing the condensation rates for MgO particles at 2000 K for a supersaturation ratio of 5 is shown in Fig. 18. For Kn < 0.02, the condensation rates calculated via Eq. (206) are within 5% of the rates determined for the continuum regime and for Kn > 3, Eq. (206) yields rates that are within 5% of the rates determined for the free molecular regime. The range of Knudsen numbers covered in Fig. 18 ($2\times10^{-5} < \mathrm{Kn} < 3.4\times10^{3}$) corresponds to MgO particles in the size range 0.2 to 100 nm. It is concluded that Eq. (206) yields accurate prediction of condensation rates for all mineral oxide particles, for those as small as 0.2 nm in diameter (free molecular flow) to those as large as several microns (continuum flow).

Equation (206) gives the condensation rate per mineral oxide particle. It yields the flow of condensable mineral oxide vapors per unit time to the surface of a spherical mineral oxide particle of diameter d_{MO_n}. For MgO and SiO_2 particles near their critical cluster sizes, at 2000 K condensation rates are of the order 10^5 to 10^6 mol/s when the supersaturation ratio is in the range 5 to 10. The rates increase with increasing temperature and with increasing supersaturation ratio.

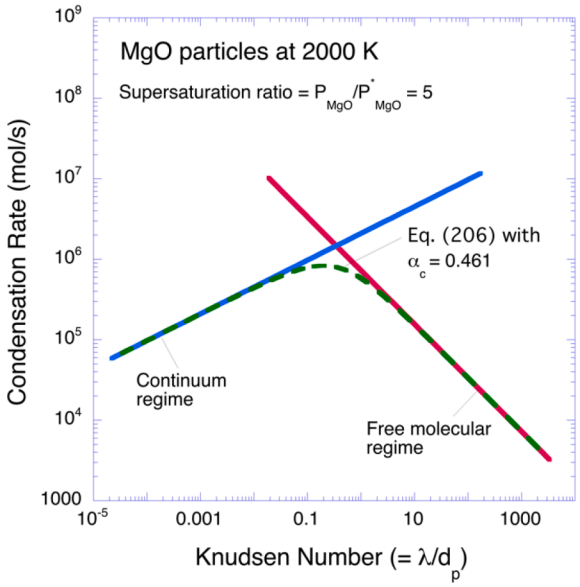

Fig. 18. Condensation rate as a function of Knudsen number for MgO particles at 2000 K. The dashed line corresponds to the results obtained when employing $\alpha_c = 0.461$ in Eq. (206).

The overall condensation rate is dependent on the number density and size distribution of the mineral oxide particles, and can be calculated as follows:

$$\dot{R}_{condensation,MO_n} = \int_0^\infty \left(\dot{r}_{condensation,MO_n}\right)_{d_{MO_n}} n(d_{MO_n}) dd_{MO_n} \tag{207}$$

where in the above expression, $n(d_{MO_n})$ is the number of particles of diameter d_{MO_n} at time t. As discussed below, the number distribution depends upon the extent of coagulation that occurs as the mineral oxides diffuse away from the outer surface of the char particle.

The above expressions for $\dot{R}_{reaction}$, $\dot{R}_{nucleation}$ and $\dot{R}_{condensation}$ are used in the governing differential equation for the partial pressure of the mineral oxide species outside the char particle surface, Eq. (199). When integrating, properties should be evaluated at the local gas temperature or some effective boundary layer temperature. The local gas temperature is estimated by solving the following differential equation governing heat conduction in the char particle's boundary layer:

$$\frac{1}{r^2}\frac{d}{dr}\left(r^2 \lambda_{gas}\frac{dT}{dr}\right) = 0. \tag{208}$$

Here, λ_{gas} is the effective thermal conductivity of the gas in the boundary layer.

At the conditions of interest, the CNT predicts the formation of a large number of nuclei with critical diameters of the order 1 nm. As they diffuse away from the char particle surface, they collide and stick, resulting in the formation of a large number of spherical nano-particles. Coagulation of these particles accounts for the reduction in their total numbers and coalescences accounts for the increase in the average size of the particles produced.

Many different approaches have been taken to account for coagulation of mineral vapors during char combustion (for example, see references [163,324]) or of aerosols (for example, see references: [325,328,330-335]). Following the lead of Friedlander [328], an expression for the rate of coagulation can be determined by considering the collision frequency of particles in Brownian motion in a uniform flow field, employing the results of kinetic theory to determine the collision frequency factor for collisions among molecules that behave as rigid, elastic (non-interacting) spheres. The number of collisions (z_{ij}) between particles having volumes u and v, per unit time per unit volume is given by

$$z_{ij} = \beta(u,v)n(u)n(v) \tag{209}$$

where the collision frequency function $\beta(u, v)$ is the rate of collisions per particle per unit volume, $n(u))$ is the number of volatile mineral oxide particles per unit volume having volume u and $n(v)$ is the number having volume v. These collisions result in the formation of new particles having volume $u + v$. The newly formed particles also undergo collisions with all the other particles. The net rate of change in the number of newly formed particles of volume v can be expressed as

$$\frac{dn(v)}{dt} = 0.5\int_0^v \beta(u, v-u)\ n(u)\ n(v-u)du - \int_0^\infty \beta(u, v)\ n(u)\ n(v)du \tag{210}$$

where the first term on the right-hand side represents the rate of formation of particles of volume v from collision between particles of volume u and smaller (*i.e.,* particles having volumes $v-u$) and the second term on the right represents the rate of loss of the newly formed particles of volume v due to collisions with all other particles. This is the partial integro-differential equation governing particle coagulation. Solutions yield the size distributions of the mineral oxide particles in time.

The form of the collision frequency function depends upon the flow regime, the limits being the continuum regime (Kn $= \lambda/d_p \ll 1$) and free molecular regime (Kn $>>1$, $d_p \ll \lambda$). When particles are larger than the mean free path (Kn $\ll 1$), a concentration gradient of condensable mineral species exists around each mineral oxide particle, rendering a diffusion-governed heterogeneous condensation rate. For the continuum regime,

$$\beta(u, v) = \frac{2k_B T}{3\mu}\left(\frac{1}{(u)^{\frac{1}{3}}} + \frac{1}{(v)^{\frac{1}{3}}}\right)\left((u)^{\frac{1}{3}} + (v)^{\frac{1}{3}}\right) \tag{211}$$

where μ is the gas viscosity. When particles are much smaller than the mean free path, flow is in the free molecular regime and no steady concentration gradient is established around particles. For flow in the free molecular regime,

$$\beta(u, v) = \left(\frac{3}{4\pi}\right)^{\frac{1}{6}}\left(\frac{6k_B T}{\rho_{MO}}\right)^{\frac{1}{2}}\left(\frac{1}{u} + \frac{1}{v}\right)^{\frac{1}{2}}\left((u)^{\frac{1}{3}} + (v)^{\frac{1}{3}}\right)^2 \tag{212}$$

where μ is the mass density of the condensing species, the volatile mineral oxide. In some approaches, the collision frequency in the free molecular regime is multiplied by a factor (taking a nominal value of 2), to account for the enhancement in the collision frequency due to dispersion forces (see for example Neville [268] and Graham and Homer [331]).

Integration of Eq. (210) with collision frequency functions given by either Eq. (211) or (212) is rather complicated for a distribution of initially sized particles. However, approximate solutions can be derived by assuming that the evolving particle size distribution exhibits self-preserving characteristics, becoming invariant in time and independent of the initial particle size distribution. This was demonstrated by Friedlander and Wang [330] for coagulation in the continuum regime and by Lai *et. al* [332] for coagulation in the free molecular regime. In the approach, the self-preserving particle size distribution function is expressed in terms of the variable η, defined as the ratio of the particle volume v to the average particle volume concentration $\overline{v}$. This average volume concentration is calculated as the ratio of the total particle volume at time t per unit volume of gas, V ($m^3$of particles)/(m^3 of gas), to the particle number concentration, N (#particles/m^3). Thus, at time t,

$$\eta = v/\overline{v} \qquad \text{and} \qquad \overline{v} = V/N. \tag{213}$$

where

$$V = \int_0^\infty v\ n(v)\ dv \quad \text{and} \quad N(t) = \int_0^\infty n(v)\ dv. \tag{214}$$

In terms of η, the particle size distribution is defined in non-dimensional form as ψ(η), where

$$\psi(\eta) = n(v)V/N^2. \tag{215}$$

When these variables are employed in either Eq. (211) or (212), a solution to Eq. (210) for Brownian coagulation in either the continuum or free molecular regime can be obtained that is particle size distribution invariant in time and dependent only on the collision frequency function. The function ψ(η) is an asymptotic solution to Eq. (210) towards which all systems having homogeneous collision frequency functions converge. The collision frequency functions given in Eqs. (211) and (212) for the continuum and free molecular flow regimes are homogeneous functions of particle volume. Shown in Fig. 19 are curves obtained for the self-preserving number size distributions for particles in the continuum and free molecular regimes (see references [330] and [332], respectively). The curves were plotted from the numerical results provided in tables in the two publications. Analytical expressions are provided in the papers for the lower ($\eta \to 0$) and upper ($\eta \to \infty$) ends of the spectrum. For specified η, ψ(η) can be obtained for each regime. Other researchers have shown that self-preserving distribution functions are also obtained for aerosol coagulation in the continuum and free molecular regimes even when expressed in the forms of logarithmic volume distribution functions (see Lehtinen and Zachariah [335], for example).

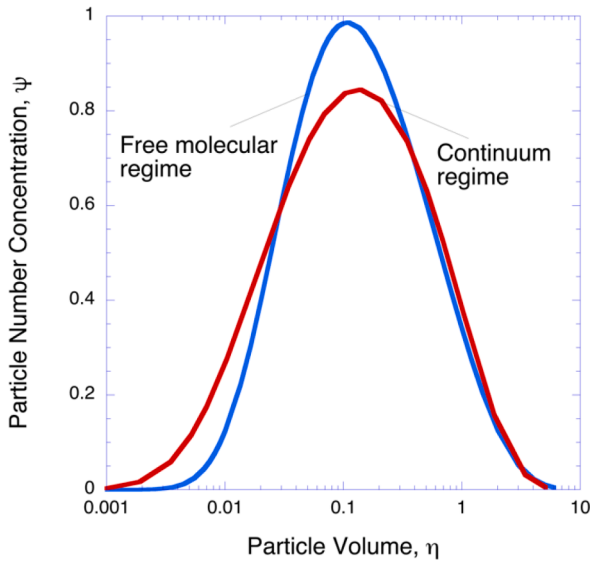

Fig. 19. Self-preserving particle number concentration distributions. The plots were prepared from data presented in the tables put forth by Friedlander and Wang [330] for the continuum regime and by Lai et al. [332] for the free molecular regime.

For coagulation in the continuum regime, the total particle concentration is found by integration of the following differential equation:

$$\frac{dN}{dt} = -\frac{2k_B T}{3\mu}(1+ab)N^2 \tag{216}$$

The parameters a and b are defined as the following integrals:

$$a = \int_0^\infty \eta^{\frac{1}{3}}\psi(\eta)\, d\eta \qquad \text{and} \qquad b = \int_0^\infty \eta^{-\frac{1}{3}}\psi(\eta)\, d\eta \tag{217}$$

and are constants obtained by integration of the self-preserving particle size distribution function in the continuum regime (see Friedlander and Wang [330]). Assuming constant properties in the char particle's boundary layer over the time period t to $t+\delta t$, piecewise integration of Eq. (216) yields:

$$N_{t+\delta t} = N_t\left(1 + \left(\frac{2(1+ab)k_B T}{3\mu}\right)_t N_t \delta t\right)^{-1} \tag{218}$$

where at time $t = 0$, the total particle number density takes its initial value of N_0. Having determined the total number density at time $t+\delta t$, the particle size distribution at the time can be calculated via Eqs. (213) and (215) using the η- ψ(η) relationship for the self-preserving particle size distribution function determined for the continuum regime and the value of V calculated from the initial mineral oxide particle size distribution. This assumes that all of the mineral oxide particles remain in suspension from the time they escape the char particle up to time $t+\delta t$, rendering V constant.

For coagulation in the free molecular regime, the total particle concentration is found by integration of the following equation put forth by Lai *et al.* [332]:

$$\frac{dN}{dt} = -\frac{\chi}{2}\left(\frac{3}{4\pi}\right)^{\frac{1}{6}}\left(\frac{6k_B T}{\rho_{MO}}\right)^{\frac{1}{2}} V^{\frac{1}{6}} N^{\frac{11}{6}} \tag{219}$$

where the parameter χ is defined as the following double integral:

$$\chi = \int_0^\infty \int_0^\infty \left(\eta^{\frac{1}{3}} + \tilde{\eta}^{\frac{1}{3}}\right)^2 \left(\frac{1}{\eta} + \frac{1}{\tilde{\eta}}\right)^{\frac{1}{2}} \psi(\eta)\psi(\tilde{\eta}) d\eta\, d\tilde{\eta}. \tag{220}$$

By integration of the η-ψ(η) relationship for the self-preserving particle size distribution function in the free molecular regime, Lai *et al.* [332] found χ to have the value 6.67. For constant properties in the char particle's boundary layer over the time period t to $t+\delta t$, Eq. (219) can be integrated, assuming that all particles remain suspended, to yield:

$$N_{t+\delta t} = \left[\frac{1}{(N_t)^{\frac{5}{6}}} + \left(\frac{5}{6}\right)\left(\frac{\chi}{2}\right)\left(\frac{3}{4\pi}\right)^{\frac{1}{6}}\left(\left(\frac{6k_B T}{\rho_{MO}}\right)^{\frac{1}{2}} V^{\frac{1}{6}}\right)_t \delta t\right]^{-\frac{6}{5}}. \tag{221}$$

Having evaluated $N_{t+\delta t}$, the number of particles at time $t+\delta t$ having volume v can be determined from Eqs. (213) and (215) and the self-preserving distribution function calculated for the free molecular regime along with the value of V determined from the initial size distribution.

Since $v = V/N$, Eq. (221) can be rearranged to yield the following expression for the average particle volume at time $t+\delta t$ in terms of the average particle volume at time t:

$$\overline{v}_{t+\delta t} = \frac{V}{N_{t+\delta t}} = \left[(\overline{v}_t)^{\frac{5}{6}} + \left(\frac{5}{6}\right)\left(\frac{\chi}{2}\right)\left(\frac{3}{4\pi}\right)^{\frac{1}{6}}\left(\frac{6k_BT}{\rho_{MO}}\right)^{\frac{1}{2}} V\delta t \right]^{\frac{6}{5}}. \tag{222}$$

The volume-mean particle diameter at time $t+\delta t$ can therefore be expressed as

$$\overline{d}_{p,t+\delta t} = \left(\frac{6\overline{v}_{t+\delta t}}{\pi}\right)^{\frac{1}{3}} = \left(\frac{6}{\pi}\right)^{\frac{1}{3}}\left[(\overline{v}_t)^{\frac{5}{6}} + \left(\frac{5}{6}\right)\left(\frac{\chi}{2}\right)\left(\frac{3}{4\pi}\right)^{\frac{1}{6}}\left(\frac{6k_BT}{\rho_{MO}}\right)^{\frac{1}{2}} V\delta t \right]^{\frac{2}{5}}. \tag{223}$$

Neville [268] showed that the primary submicron particles produced during combustion of nominally 50 μm diameter particles of Montana lignite at 1700 K in 15%, 20% and 40% oxygen were well represented by particle sizes calculated using an approximate form of the above equation. Samples of submicron particles were collected at selected distances from the point of coal injection. Measurements indicated rapid changes in particle number density and size as the small particles collide and coalesce, in agreement with the calculations. The number density decreased from 2.76 x 10^{11} particles/cm^3 at 3.81 cm from the injection point to 6.24 x 10^{10} particles/cm^3 at 6.35 cm while the volume-mean diameter increased form 3.4 nm to 13.9 nm.

Recently, Niu and co-researchers [163,283,284] implemented versions of the above equations to predict the particle size distributions of particulate matter during coal combustion. In the models developed, account is made for re-oxidation of the mineral sub-oxides and metals that escape char particles and for nucleation, condensation, coagulation, and coalescence of these particles to form fine ash particles.

In order to accurately predict the size distribution of the nano-sized particles produced during char oxidation and gasification, it is necessary to consider vaporization followed by nucleation, condensation and coagulation of all the minerals in the coal and biomass chars. In nearly all condensation and coagulation sub-models developed to date, the interactions of various kinds of vapor species originating from different mineral inclusions in the coal char are neglected. MgO and SiO_2 have been taken to be representative of all types of mineral inclusions in the coal and biomass chars. Besides consideration of the refractory metals, account should also be made for the vaporization of mercury, arsenic and selenium species during coal char conversion and for sodium, potassium, and phosphorus species during biomass char conversion. Evidence exists for the deposition of such volatile mineral species on ash particles as they cool in exhaust gases [278].

References

[1] Smith IW. The combustion rates of coal chars: a review. In: Nineteenth Symposium (International) on Combustion; 1982. p. 1045–65.
[2] Li J, Paul MC, Younger PL, Watson I, Hossain M, Welch S. Prediction of high-temperature rapid combustion behaviour of woody biomass particles. Fuel 2016;165:205–14.
[3] Anthony DB, Howard JB. Coal devolatilization and hydrogasification. AIChE Journal 1976;22:625–56.
[4] Falcitelli M, Biagini E, Tognotti L. Development of the advanced biomass and coal devolatilization (ABCD) model. In: 10th Conference on Energy for a Clean Environment; 2009.
[5] Fletcher TH, Kerstein AR, Pugmire RJ, Grant DM. Chemical Percolation Model for Devolatilization .2. Temperature and Heating Rate Effects on Product Yields. Energ Fuel 1990;4:54–60.
[6] Genetti D, Fletcher TH, Pugmire RJ. Development and application of a correlation of C-13 NMR chemical structural analyses of coal based on elemental composition and volatile matter content. Energ Fuel 1999;13:60–8.
[7] Kobayashi H, Howard JB, Sarofim A. Coal devolatilization at high temperatures. In: Proceedings of the Combustion Institute. 16; 1976. p. 411–25.
[8] Niksa S, Kerstein AR. Flashchain Theory for Rapid Coal Devolatilization Kinetics 1. Formulation. Energ Fuel. 1991;5:647–65.
[9] Sheng CD, Azevedo JLT. Modeling biomass devolatilization using the chemical percolation devolatilization model for the main components. In: Proceedings of the Combustion Institute. 29; 2002. p. 407–14.
[10] Solomon PR, Hamblen DG, Carangelo R, Krause JL. Coal thermal decomposition in an entrained flow reactor: Experiments and theory. In: Proceedings of the Combustion Institute. 19; 1982. p. 1139–49.
[11] Sommariva S, Maffei T, Migliavacca G, Faravelli T, Ranzi E. A predictive multi-step kinetic model of coal devolatilization. Fuel 2010;89:318–28.
[12] Xing JK, Wang HO, Luo K, Wang S, Bai Y, Fan JR. Predictive single-step kinetic model of biomass devolatilization for CFD applications: A comparison study of empirical correlations (EC), artificial neural networks (ANN) and random forest (RF). Renew Energ 2019;136:104–14.
[13] Mitchell R, Akanetuk J. The impact of fragmentation on char conversion during pulverized coal combustion. In: Twenty-sixth symposium (International) on Combustion; 1996. p. 3137–44.
[14] Mitchell RE, Hurt RH, Baxter LL, Hardesty DR. Compilation of Sandia coal char combustion data and kinetic analysis. Sandia National Laboratory Report; 1992.
[15] Hirschfelder JO, Curtiss CF, Bird RB. Molecular Theory of Gases and Liquids. New York: Chapman & Hall, London: Wiley; 1954.
[16] Chabane AM, Truffin K, Nicolle A, Nicoud F, Cabrit O, Angelberger C. Direct numerical simulation of combustion near a carbonaceous surface in a quiescent flow. Int J Heat Mass Tran 2015;84:130–48.
[17] Dierich F, Richter A, Nikrityuk P. A fixed-grid model to track the interface and porosity of a chemically reacting moving char particle. Chem Eng Sci 2018;175:296–305.
[18] Farazi S, Sadr M, Kang S, Schiemann M, Vorobiev N, Scherer V, et al. Resolved simulations of single char particle combustion in a laminar flow field. Fuel 2017;201:15–28.
[19] Gomez MA, Porteiro J, Chapela S, Miguez JL. An Eulerian model for the simulation of the thermal conversion of a single large biomass particle. Fuel 2018;220:671–81.
[20] Ha MY, Choi BR. A numerical study on the combustion of a single carbon particle entrained in a steady flow. Combust Flame 1994;97:1–16.
[21] Jayawickrama T, Chishty MA, Babler M, Umeki K, Haugen NEL. The effect of Stefan flow on the drag coefficient of reactive spherical particles in a gas flow. International Journal of Multiphase Flow 2019;117:130–7.
[22] Lee J, Tomboulides AG, Orszag SA, Yetter RA, Dryer FL. A transient two-dimensional chemically reactive flow model: Fuel particle combustion in a nonquiescent environment. Twenty-Sixth Symposium (International) on Combustion 1996;2:3059–65.
[23] Luo K, Mao CL, Fan JR, Zhuang ZY, Haugen NEL. Fully resolved simulations of single char particle combustion using a ghost-cell immersed boundary method. Aiche Journal 2018;64:2851–63.
[24] Nikrityuk PA, Gabner M, Kestel M, Meyer B. Numerical study of the influence of heterogeneous kinetics on the carbon consumption by oxidation of a single coal particle. Fuel 2013;114:88–98.
[25] Pan YY, Kong SC. Simulation of biomass particle evolution under pyrolysis conditions using lattice Boltzmann method. Combust Flame 2017;178:21–34.
[26] Richter A, Nikrityuk PA, Meyer B. Three-dimensional calculation of a chemically reacting porous particle moving in a hot O_2/CO_2 atmosphere. Int J Heat Mass Tran 2015;83:244–58.
[27] Richter A, Vascellari M, Nikrityuk PA, Hasse C. Detailed analysis of reacting particles in an entrained-flow gasifier. Fuel Process Technol 2016;144:95–108.
[28] Sayadi T, Farazi S, Kang S, Pitsch H. Transient multiple particle simulations of char particle combustion. Fuel 2017;199:289–98.
[29] Schulze S, Kestel M, Nikrityuk PA, Safronov D. From detailed description of chemical reacting carbon particles to subgrid models for CFD. Oil Gas Sci Technol 2013;68:1007–26.
[30] Schulze S, Nikrityuk P, Compart F, Richter A, Meyer B. Particle-resolved numerical study of char conversion processes in packed beds. Fuel 2017;207:655–62.
[31] Tufano GL, Stein OT, Kronenburg A, Frassoldati A, Faravelli T, Deng L, et al. Resolved flow simulation of pulverized coal particle devolatilization and ignition in air- and O_2/CO_2 atmospheres. Fuel 2016;186:285–92.
[32] Tufano GL, Stein OT, Kronenburg A, Gentile G, Stagni A, Frassoldati A, et al. Fully-resolved simulations of coal particle combustion using a detailed multi-step approach for heterogeneous kinetics. Fuel 2019;240:75–83.

[33] Tufano GL, Stein OT, Wang B, Kronenburg A, Rieth M, Kempf AM. Coal particle volatile combustion and flame interaction. Part II: Effects of particle Reynolds number and turbulence. Fuel 2018;234:723–31.
[34] Tufano GL, Stein OT, Wang B, Kronenburg A, Rieth M, Kempf AM. Coal particle volatile combustion and flame interaction. Part I: Characterization of transient and group effects. Fuel 2018;229:262–9.
[35] Vascellari M, Xu H, Hasse C. Flamelet modeling of coal particle ignition. In: Proceedings of the Combustion Institute. 34; 2013. p. 2445–52.
[36] Wittig K, Nikrityuk PA, Schulze S, Richter A. Three-dimensional modeling of porosity development during the gasification of a char particle. AIChE Journal 2017;63:1638–47.
[37] Xue ZC, Guo QH, Gong Y, Xu JL, Yu GS. Numerical study of a reacting single coal char particle with different pore structures moving in a hot O_2/CO_2 atmosphere. Fuel 2017;206:381–9.
[38] Zhang W, Tainaka K, Ahn S, Watanabe H, Kitagawa T. Experimental and numerical investigation of effects of particle shape and size distribution on particles' dispersion in a coaxial jet flow. Adv Powder Technol 2018;29:2322–30.
[39] Zhang W, Watanabe H, Kitagawa T. Direct numerical simulation of ignition of a single particle freely moving in a uniform flow. Adv Powder Technol 2017;28:2893–902.
[40] Fong GH, Jorgensen S, Singer SL. Pore-resolving simulation of char particle gasification using micro-CT. Fuel 2018;224:752–63.
[41] Lee JC, Yetter RA, Dryer FL. Transient numerical modeling of carbon particle ignition and oxidation. Combust Flame 1995;101:387–98.
[42] Zhang H, Luo K, Haugen NEL, Mao C, Fan J. Drag force for a burning particle. Combust Flame 2020;217:188–99.
[43] Zhang LH, Liu K, You CF. Fictitious domain method for fully resolved reacting gas-solid flow simulation. J Comput Phys 2015;299:215–28.
[44] Hecht ES, Shaddix CR, Geier M, Molina A, Haynes BS. Effect of CO_2 and steam gasification reactions on the oxy-combustion of pulverized coal char. Combust Flame 2012;159:3437–47.
[45] Hecht ES, Shaddix CR, Molina A, Haynes BS. Effect of CO_2 gasification reaction on oxy-combustion of pulverized coal char. In: Proceedings of the Combustion Institute. 33; 2011. p. 1699–706.
[46] Mitchell RE, Ma LQ, Kim B. On the burning behavior of pulverized coal chars. Combust Flame 2007;151:426–36.
[47] Haberle I, Haugen NEL, Skreiberg O. Simulating thermal wood particle conversion: Ash-layer modeling and parametric studies. Energ Fuel 2018;32:10668–82.
[48] Haberle I, Haugen NEL, Skreiberg O. Combustion of thermally thick wood particles: A study on the influence of wood particle size on the combustion behavior. Energ Fuel 2018;32:6847–62.
[49] Hermansson S, Thunman H. CFD modelling of bed shrinkage and channelling in fixed-bed combustion. Combust Flame 2011;158:988–99.
[50] Satterfield CN. Mass transfer in heterogeneous catalysis. Cambridge Massachusetts: MIT Press; 1970.
[51] Usseglio-Viretta FLE, Finegan DP, Colclasure A, Heenan TMM, Abraham D, Shearing P, et al. Quantitative Relationships Between Pore Tortuosity, Pore Topology, and Solid Particle Morphology Using a Novel Discrete Particle Size Algorithm. J Electrochem Soc 2020:167.
[52] Hamann T, Zhang L, Gong YH, Godbey G, Gritton J, McOwen D, et al. The Effects of Constriction Factor and Geometric Tortuosity on Li-Ion Transport in Porous Solid-State Li-Ion Electrolytes. Adv Funct Mater 2020:30.
[53] Münch B, Holzer L. Contradicting Geometrical Concepts in Pore Size Analysis Attained with Electron Microscopy and Mercury Intrusion. Journal of the American Ceramic Society 2008;91:4059–67.
[54] Stenzel O, Pecho O, Holzer L, Neumann M, Schmidt V. Predicting Effective Conductivities Based on Geometric Microstructure Characteristics. Aiche Journal 2016;62:1834–43.
[55] Niu YQ, Liu SQ, Shaddix CR, Hui SE. An intrinsic kinetics model to predict complex ash effects (ash film, dilution, and vaporization) on pulverized coal char burnout in air (O_2/N_2) and oxy-fuel (O_2/CO_2) atmospheres. In: Proceedings of the Combustion Institute. 37; 2019. p. 2781–90.
[56] Sun JK, Hurt RH. Mechanisms of extinction and near-extinction in pulverized solid fuel combustion. In: Proceedings of the Combustion Institute. 28; 2000. p. 2205–13.
[57] Simons GA. The Role of Pore Structure in Coal Pyrolysis and Gasification. Progress in Energy and Combustion Science 1983;9:269–90.
[58] Bird RB, Stewart WE, Lightfoot EN. Transport Phenomena. New York: John Wiley and Sons; 1961.
[59] Fatehi H, Bai XS. A comprehensive mathematical model for biomass combustion. Combustion Science and Technology 2014;186:574–93.
[60] Haberle I, Skreiberg Ø, Lazar J, Haugen NEL. Numerical models for thermochemical degradation of thermally thick woody biomass, and their application in domestic wood heating appliances and grate furnaces. Progress in Energy and Combustion Science 2017;63:204–52.
[61] Brosh T, Patel D, Wacks D, Chakraborty N. Numerical investigation of localised forced ignition of pulverised coal particle-laden mixtures: A direct numerical simulation (DNS) analysis. Fuel 2015;145:50–62.
[62] Hara T, Muto M, Kitano T, Kurose R, Komori S. Direct numerical simulation of a pulverized coal jet flame employing a global volatile matter reaction scheme based on detailed reaction mechanism. Combust Flame 2015;162:4391–407.
[63] Luo K, Wang HO, Fan JR, Yi FX. Direct numerical simulation of pulverized coal combustion in a hot vitiated co-flow. Energ Fuel 2012;26:6128–36.
[64] Bai Y, Luo K, Qiu K, Fan J. Numerical investigation of two-phase flame structures in a simplified coal jet flame. Fuel 2016;182:944–57.
[65] Farazi S, Hinrichs J, Davidovic M, Falkenstein T, Bode M, Kang S, et al. Numerical investigation of coal particle stream ignition in oxy-atmosphere. Fuel 2019;241:477–87.
[66] Rieth M, Kempf AM, Kronenburg A, Stein OT. Carrier-phase DNS of pulverized coal particle ignition and volatile burning in a turbulent mixing layer. Fuel 2018;212:364–74.
[67] Wan K, Vervisch L, Xia J, Domingo P, Wang Z, Liu Y, et al. Alkali metal emissions in an early-stage pulverized-coal flame: DNS analysis of reacting layers and chemistry tabulation. In: Proceedings of the Combustion Institute. 37; 2019. p. 2791–9.
[68] Wen C, Luo K, Wang H, Luo Y, Fan J. Analysis of pulverized coal flame stabilized in a 3D laminar counterflow. Combust Flame 2018;189:106–25.
[69] Kruger J, Haugen NEL, Lovas T. Correlation effects between turbulence and the conversion rate of pulverized char particles. Combust Flame 2017;185:160–72.
[70] Rieth M, Proch F, Rabacal M, Franchetti BM, Cavallo Marincola F, Kempf AM. Flamelet LES of a semi-industrial pulverized coal furnace. Combust Flame 2016;173:39–56.
[71] Karchniwy E, Haugen NEL, Klimanek A, Langørgen Ø. The effect of turbulence on mass transfer in solid fuel combustion: RANS model. Combust Flame 2021;227:65–78.
[72] Haugen NEL, Kruger J, Mitra D, Lovas T. The effect of turbulence on mass transfer rates of small inertial particles with surface reactions. Journal of Fluid Mechanics 2018;836:932–51.
[73] Karchniwy E, Klimanek A, Haugen NEL. The effect of turbulence on mass transfer rates between inertial particles and fluid for polydisperse particle size distributions. Journal of Fluid Mechanics 2019;874:1147–68.
[74] Kruger J, Haugen NEL, Mitra D, Lovas T. The effect of turbulent clustering on particle reactivity. In: Proceedings of the Combustion Institute. 36; 2017. p. 2333–40.
[75] Jayawickrama TR, Haugen NEL, Babler MU, Chishty MA, Umeki K. The effect of Stefan flow on Nusselt number and drag coefficient of spherical particles in non-isothermal gas flow. International Journal of Multiphase Flow 2021:140.
[76] Schiller L, Naumann A. Über die grundlegenden Berechnungen bei der Schwerkraft aufbereitung. Z Verein Deutsch Ing 1933;77:318–20.
[77] Wen CY, Yu YH. Mechanics of Fluidization. Chemical Engineering Progress 1966;62:100–11.
[78] Ming-yan G, Ming-chuan Z, Juan Y, Wei-dong F. Feng-guo T. Numerical study on the spatial distribution of energy release during char combustion. Appl Energ 2008;85:1060–70.
[79] McConnell J, Goshayeshi B, Sutherland JC. An evaluation of the efficacy of various coal combustion models for predicting char burnout. Fuel 2017;201:53–64.
[80] Wheeler A. Reaction Rates and Selectivity in Catalyst Pores. Advances in Catalysis 1951;3:249–327.
[81] Bhatia SK, Perlmutter DD. A random pore model for fluid-solid reactions: 1. Isothermal, kinetic control. AIChE Journal 1980;26:379.
[82] Mendoza E, Cunningham RE, Ronco JJ. Oxidation of zinc sulfide pellets - application of a model of diffusion with simultaneous reaction under effective diffusivity and surface area profiles. Journal of Catalysis 1970;17:277–86.
[83] Gavalas GR. A random capillary model with applications to char gasification at chemically controlled rates. AIChE Journal 1980;26:577–85.
[84] Su J-L, Perlmutter DD. Effect of pore structure on char oxidation kinetics. AIChE Journal 1985;31:973–81.
[85] Wang G, Zhang J, Geng W, Shao J. A modified random pore model for gasification kinetics of coal char and biomass char. In: TMS 2015 144th Annual Meeting & Exhibition; 2015. p. 841–8.
[86] Ishida M, Wen CY. Comparison of zone-reaction model and unreacted-core shrinking model in solid-gas reactions—I Isothermal analysis. Chem Eng Sci 1971;26:1031–41.
[87] Dutta S, Wen CY. Reactivity of coal and char. 2. In oxygen-nitrogen atmospheres. Ind Engng Chem Process Des Dev. 1977;16:31–7.
[88] Dutta S, Wen CY, Belt RJ. Reactivity of coal and char. 1. In carbon dioxide atmospheres. Ind Engng Chem Process Des Dev. 1977;16:20–30.
[89] Morin M, Pecate S, Masi E, Hemati M. Kinetic study and modelling of char combustion in TGA in isothermal conditions. Fuel 2017;203:522–36.
[90] Raghunathan K, Yang RYK. Unification of coal-gasification data and its applications. Ind Eng Chem Res 1989;28:518–23.
[91] Feng B, Bhatia SK. Variation of the pore structure of coal chars during gasification. Carbon 2003;41:507–23.
[92] Holland T, Fletcher TH. Global sensitivity analysis for a comprehensive char conversion model in oxy-fuel conditions. Energ Fuel 2016;30:9339–50.
[93] Kajitani S, Hara S, Matsuda H. Gasification rate analysis of coal char with a pressurized drop tube furnace. Fuel 2002;81:539–46.
[94] Kajitani S, Suzuki N, Ashizawa M, Hara S. CO_2 gasification rate analysis of coal char in entrained flow coal gasifier. Fuel 2006;85:163–9.
[95] Liu GS, Niksa S. Coal conversion submodels for design applications at elevated pressures. Part II. Char gasification. Progress in Energy and Combustion Science 2004;30:679–717.
[96] Mitchell RE. An intrinsic kinetics-based, particle-population balance model for char oxidation during pulverized coal combustion. In: Proceedings of the Combustion Institute. 28; 2000. p. 2261–70.
[97] Niu YQ, Shaddix CR. A sophisticated model to predict ash inhibition during combustion of pulverized char particles. In: Proceedings of the Combustion Institute. 35; 2015. p. 561–9.

[98] Tilghman MB, Haugen NEL, Mitchell RE. Comprehensive char particle gasification model adequate for entrained-flow and fluidized-bed gasifiers. Energ Fuel 2017;31:2164–74.
[99] Fermoso J, Arias B, Pevida C, Plaza MG, Rubiera F, Pis JJ. Kinetic models comparison for steam gasification of different nature fuel chars. J Therm Anal Calorim 2008;91:779–86.
[100] Lu GQ, Do DD. Comparison of structural models for high-ash char gasification. Carbon 1994;32:247–63.
[101] Duman G, Uddin MA, Yanik J. The effect of char properties on gasification reactivity. Fuel Process Technol 2014;118:75–81.
[102] Tsuge M, Hama T, Kimura Y, Kouchi A, Watanabe N. Interactions of Atomic and Molecular Hydrogen with a Diamond-like Carbon Surface: H-2 Formation and Desorption. Astrophys J 2019;878.
[103] Brenner DW, Shenderova OA. Theory and modelling of diamond fracture from an atomic perspective. Philos T R Soc A 2015:373.
[104] Beeley T, Crelling J, Gibbins J, Hurt R, Lunden M, Man C, et al. Transient high-temperature thermal deactivation of monomaceral-rich coal chars. In: Twenty-Sixth Symposium (International) on Combustion. 2; 1996. p. 3103–10.
[105] Senneca O, Salatino P, Masi S. The influence of char surface oxidation on thermal annealing and loss of combustion reactivity. In: Proceedings of the Combustion Institute. 30; 2005. p. 2223–30.
[106] Ooi N, Rairkar A, Adams JB. Density functional study of graphite bulk and surface properties. Carbon 2006;44:231–42.
[107] Haugen NEL, Mitchell RE, Tilghman MB. A comprehensive model for char particle conversion in environments containing O_2 and CO_2. Combust Flame 2015;162:1455–63.
[108] Tilghman MB. A consistent reaction mechanism and model for the combustion and gasification of coal and biomass, and the co-firing thereof. Stanford University; 2017.
[109] Hurt RH, Haynes BS. On the origin of power-law kinetics in carbon oxidation. In: Proceedings of the Combustion Institute. 30; 2005. p. 2161–8.
[110] Haynes BS. A turnover model for carbon reactivity I. Development. Combust Flame. 2001;126:1421–32.
[111] Field MA. Rate of combustion of size-graded fractions of char from a low-rank coal between 1200 K and 2000 K. Combust Flame 1970;14:237–52.
[112] Field MA, Gill DW, Morgan BB, Hawksley PGW. Combustion of pulverised coal. Leatherhead: The British Coal Utilization Research Association; 1967.
[113] Gulbransen EA, Andrew KF, Brassart FA. The oxidation of graphite at temperatures of 600 to 1500°C and at pressures of 2 to 76 torr of oxygen. Journal of Electrochemical Society 1963;110:476–83.
[114] Hurt R, Sun JK, Lunden M. A kinetic model of carbon burnout in pulverized coal combustion. Combust Flame 1998;113:181–97.
[115] Hurt RH, Mitchell RE. Unified high-temperature char combustion kinetics for a suite of coals of various rank. In: Proceedings of the Combustion Institute. 24; 1992. p. 1243–50.
[116] Mitchell RE. On the products of the heterogeneous oxidation reaction at the surfaces of burning coal char particles. In: Proceedings of the Combustion Institute. 22; 1988. p. 69–78.
[117] Mitchell RE. Variations in the temperatures of coal-char particles during combustion: A consequence of particle-to-particle variations in ash-content. In: Proceedings of the Combustion Institute. 23; 1990. p. 1297–304.
[118] Mitchell RE, McLean WJ. On the temperature and reaction rate of burning pulverized fuels. In: Proceedings of the Combustion Institute. 19; 1982. p. 1113–22.
[119] Walls JR, Strickland-Constable RF. Oxidation of carbon between 1000 and 2400 °C. Carbon 1964;1:333–8.
[120] Waters BJ, Squires RG, Laurendeau NM, Mitchell RE. Evidence for formation of CO_2 in the vicinity of burning pulverized carbon particles. Combust Flame 1988;74:91–106.
[121] Smith IW. Kinetics of combustion of size-graded pulverized fuels in the temperature range 1200–2270 K. Combust Flame 1971;17:303–14.
[122] Smith IW. The kinetics of combustion of pulverized semi-anthracite in the temperature range 1400 - 2000 K. Combust Flame 1971;17:421–8.
[123] Thomas GR, Stevenson AJ, Evans DG. Ignition of coal particles without temperature jump. Combust Flame 1973;21:133–6.
[124] Radovic LR, Walker PLJ, Jenkins RG. Importance of carbon active sites in the gasification of coal chars. Fuel 1983;62:849–56.
[125] Senneca O, Salatino P. Loss of gasification reactivity toward O_2 and CO_2 upon heat treatment of carbons. In: Proceedings of the Combustion Institute. 29; 2002. p. 485–93.
[126] Senneca O, Salatino P. Overlapping of heterogeneous and purely thermally activated solid-state processes in the combustion of a bituminous coal. Combust Flame 2006;144:578–91.
[127] Shim HS, Hurt RH. Thermal annealing of chars from diverse organic precursors under combustion-like conditions. Energ Fuel 2000;14:340–8.
[128] Zolin A, Jensen A, Dam-Johansen K. Kinetic analysis of char thermal deactivation. In: Proceedings of the Combustion Institute. 28; 2000. p. 2181–8.
[129] Arthur JR. Reactions between Carbon and Oxygen. Trans Faraday Soc 1951;47:164–78.
[130] Du Z, Sarofim A, Longwell JP, Tognotti L. The CO/CO_2 ratio in the products of the carbon-oxygen reaction. editors. In: Lahaye J, Ehrburger P, editors. Fundamental Issues in Control of Carbon Gasification Reactivity. Kluwer Academic Publishers; 1991. p. 91–106.
[131] Phillips R, Vastola FJ, Walker Jr PL. The effect of oxygen pressure and carbon burn-off on the product ratio of the carbon-oxygen reaction. Carbon 1969;7:479–85.
[132] Tognotti L, Longwell JP, Sarofim A. The products of the high temperature oxidation of a single char particle in an electrodynamic balance. In: Proceedings of the Combustion Institute. 23; 1990. p. 1207–13.
[133] Day RJ, Walker Jr PL, CC Wright. The carbon-oxygen reaction at high temperatures and high gas flow rates. In: Conference on Industrial Carbon & Graphite Soc Chem Ind (London); 1958. p. 348–70.
[134] Hamor RJ, Smith IW, Tyler RJ. Kinetics of combustion of a pulverized brown coal char between 630 and 2200 K. Combust Flame 1973;21:153–62.
[135] Harris DJ, Smith IW. Intrinsic reactivity of petroleum coke and brown coal char to carbon dioxide, steam and oxygen. In: Proceedings of the Combustion Institute. 23; 1990. p. 1185–90.
[136] Smith IW, Tyler RJ. The reactivity of a porous brown coal char to oxygen between 630 and 1812 K. Combustion Science and Technology 1974;9:87–94.
[137] Fletcher TH, Sawaya RJ, Allen JW, Hecker WC, Smoot LD. Kinetics of high-pressure char oxidation. Abstr Pap Am Chem S 1999;218:U641.
[138] Salatino P, Senneca O, Masi S. Assessment of thermodeactivation during gasification of a bituminous coal char. Energ Fuel 1999;13:1154–9.
[139] Smith IW, Tyler RJ. Internal burning of pulverized semianthracite: the relation between particle structure and reactivity. Fuel 1971;51:312–21.
[140] Suuberg EM, Wojtowicz M, Calo JM. Reaction order for low temperature oxidation of carbon. In: Proceedings of the Combustion Institute. 22; 1988. p. 79–87.
[141] Thiele EW. Relation between catalytic activity and size of particle. Ind Engng Chem 1939;31:916–20.
[142] Murphy JJ, Shaddix CR. Effect of reactivity loss on apparent reaction order of burning char particles. Combust Flame 2010;157:535–9.
[143] Holland T, Bhat S, Marcy P, Gattiker J, Kress JD, Fletcher TH. Modeling effects of annealing on coal char reactivity to O_2 and CO_2, based on preparation conditions. Energ Fuel 2017;31:10727–44.
[144] Salatino P, Senneca O, Masi S. Gasification of a coal char by oxygen and carbon dioxide. Carbon 1998;36:443–52.
[145] Senneca O, Russo P, Salatino P. The role of carbonization in the evolution of coal char gasification reactivity. Abstr Pap Am Chem S 1996;211:11. Fuel.
[146] Senneca O, Russo P, Salatino P, Masi S. The relevance of thermal annealing to the evolution of coal char gasification reactivity. Carbon 1997;35:141–51.
[147] Shurtz RC, Fletcher TH. Coal char-CO_2 gasification measurements and modeling in a pressurized flat-flame burner. Energ Fuel 2013;27:3022–38.
[148] Tremel A, Spliethoff H. Gasification kinetics during entrained flow gasification - Part I; devolatilisation and char deactivation. Fuel 2013;103:663–71.
[149] Linares-Solano A, Mahajan OP, Walker Jr PL. Reactivity of heat-treated coals in steam. Fuel 1979;58:327–32.
[150] Septien S, Valin S, Peyrot M, Dupont C, Salvador S. Characterization of char and soot from millimetric wood particles pyrolysis in a drop tube reactor between 800 degrees C and 1400 degrees C. Fuel 2014;121:216–24.
[151] Ren LW, Wei RD, Zhu TC, Xin J. Novel Kinetic Model for Petcoke Gasification at High Temperature. Energ Fuel 2019;33:10638–50.
[152] Vyazovkin S, Burnham AK, Criado JM, Perez-Maqueda LA, Popescu C, Sbirrazzuoli N. ICTAC Kinetics Committee recommendations for performing kinetic computations on thermal analysis data. Thermochim Acta 2011;520:1–19.
[153] De Bruijn TJW, De Jong WA, Van Den Berg PJ. Kinetic parameters in Avrami-Erofeev type reactions from isothermal and non-isothermal expreiments. Thermochim Acta 1981;45:315–25.
[154] Prestipino M, Galvagno A, Karlstrom O, Brink A. Energy conversion of agricultural biomass char: Steam gasification kinetics. Energy 2018;161:1055–63.
[155] Blyholder G, Eyring H. Kinetics of graphite oxidation II. J Phys Chem 1959;63:1004–8.
[156] Essenhigh RH. Chemistry of Coal Utilization. New York: John Wiley and Sons; 1981.
[157] Jenkins RG, Nandi SP, Walker Jr PL. Reactivity of heat-treated coals in air at 500°C. Fuel 1973;52:288–93.
[158] Kurylko L, Essenhigh RH. Steady and unsteady combustion of carbon. In: Proceedings of the Combustion Institute. 14; 1973. p. 1375–86.
[159] Radovic LR, Walker PLJ, Jenkins RG. Effect of lignite pyrolysis conditions on calcium oxide dispersion and subsequent char reactivity. Fuel 1983;62:209–12.
[160] Smith IW. The intrinsic reactivity of carbons to oxygen. Fuel 1978;57:409–14.
[161] Young BC, Smith IW. The kinetics of combustion of petroleum coke particles at 1000 to 1800 K: The reaction order. In: Proceedings of the Combustion Institute. 18; 1981. p. 1249–55.
[162] Monson CR, Germane GJ, Blackham AU, Smoot LD. Char oxidation at elevated pressures. Combust Flame 1995;100:669–83.
[163] Niu YQ, Wang S, Shaddix CR, Hui SE. Kinetic modeling of the formation and growth of inorganic nano-particles during pulverized coal char combustion in O_2/N_2 and O_2/CO_2 atmospheres. Combust Flame 2016;173:195–207.
[164] Roberts DG, Harris DJ. Char gasification with O_2, CO_2, and H_2O: Effects of pressure on intrinsic reaction kinetics. Energ Fuel 2000;14:483–9.
[165] Sahu R, Levendis YA, Flagan RC, Gavalas GR. Physical properties and oxidation rates of chars from three bituminous coals. Fuel 1988;67:275–83.
[166] Sotirchos SV, Amundson NR. Dynamic behavior of a porous char particle burning in an oxygen-containing environment. AIChE Journal 1984;30:537–49.
[167] Sotirchos SV, Amundson NR. Diffusion and reaction in a char particle and in the surrounding gas phase. Two limiting models. Ind Eng Chem Fundam 1984;23:180–91.
[168] Suuberg EM, Wojtowicz M, Calo JM. Some aspects of the thermal annealing process in a phenol-formaldehyde resin char. Carbon 1989;27:431–40.
[169] Mulcahy MFR, Smith IW. Kinetics of combustion of pulverized fuel: a review of theory and experiment. Reviews of Pure and Applied Chemistry 1969;19:81–108.

[170] Zhang Z, Li ZS, Cai NS. Reduced-order model of char burning for CFD modeling. Combust Flame 2016;165:83–96.
[171] Zhou ZJ, Chen LP, Guo LZ, Qian B, Wang ZH, Cen KF. Computational modeling of oxy-coal combustion with intrinsic heterogeneous char reaction models. Fuel Process Technol 2017;161:169–81.
[172] Hurt RH, Calo JM. Semi-global intrinsic kinetics for char combustion modeling. Combust Flame 2001;125:1138–49.
[173] Otterbein M, Bonnetain L. Combustion d'un carbone vitreux sous basses pressions d'oxugene. Carbon 1968;6:877–85.
[174] Rossberg M. Experimentelle Ergebnisse über die Primärreaktionen bei der Kohlenstoffverbrennung (Experimental results on the primary reactions in carbon combustion). Z Elektrochem 1956;60:952–6.
[175] Skokova KA. Selectivity in the carbon-oxygen reaction: The Pennsylvania State University; 1997.
[176] Laurendeau NM. Heterogeneous kinetics of coal char gasification and combustion. Progress in Energy and Combustion Science 1978;4:221–70.
[177] Foord AD. The carbon-oxygen reaction. University of Newcastle upon Tyne; 1972.
[178] Langmuir I. The adsorption of gases on plane surfaces of glass, mica, and platinum. Journal of the American Ceramic Society 1918;40:1361–403.
[179] Campbell PA. Investigation into the roles of surface oxide complexes and their distributions in the carbon-oxygen heterogeneous reaction mechanism. Stanford University; 2005.
[180] Ma L. Combustion and gasification of chars in oxygen and carbon dioxide at elevated pressure. Stanford University; 2006.
[181] Tilghman MB, Mitchell RE. Coal and biomass char reactivities in gasification and combustion environments. Combust Flame 2015;162:3220–35.
[182] Laine NR, Vastola FJ, Walker Jr PL. The role of the surface complex in the carbon-oxygen reaction. In: Fifth Conference on Carbon; 1961. p. 211–7.
[183] Walker Jr PL, Vastola FJ, Hart PJ. Oxygen-18 tracer studies on the carbon-oxygen reaction. New York: Fundamentals of Gas-Surface Interactions; 1967. p. 307–17.
[184] Du ZY, Sarofim AF, Longwell JP, Mims CA. Kinetic measurement and modeling of carbon oxidation. Energ Fuel 1991;5:214–21.
[185] Haynes BS, Newbury TG. Oxyreactivity of carbon surface oxides. In: Proceedings of the Combustion Institute. 28; 2000. p. 2197–203.
[186] Ma MC, Haynes BS. Surface heterogeneity in the formation and decomposition of carbon surface oxides. In: Proceedings of the Combustion Institute. 26; 1996. p. 3119–25.
[187] Sendt K, Haynes BS. Density functional study of the chemisorption of O_2 on the armchair surface of graphite. In: Proceedings of the Combustion Institute. 30; 2005. p. 2141–9.
[188] Zhuang QL, Kyotani T, Tomita A. DRIFT and TK/TPD analyses of surface oxygen complexes formed during carbon gasification. Energ Fuel 1994;8:714–8.
[189] Zhuang QL, Kyotani T, Tomita A. Desorption behavior of surface oxygen complexes on carbon in an inert gas and in O_2-gasification atmosphere. Energ Fuel 1996;10:169–72.
[190] Zhuang QL, Kyotani T, Tomita A. Dynamics of surface oxygen complexes during carbon gasification with oxygen. Energ Fuel 1995;9:630–4.
[191] Bonnetain L, Duval X, Letort M. On the role of surface oxides in the graphite-oxygen reaction. In: Proceedings of the Fourth Carbon Conference. Oxford: Pergamon Press; 1960. p. 107–14.
[192] Maffei T, Khatami R, Pierucci S, Faravelli T, Ranzi E, Levendis YA. Experimental and modeling study of single coal particle combustion in O_2/N_2 and oxy-fuel (O_2/CO_2) atmospheres. Combust Flame 2013;160:2559–72.
[193] Brown TC, Lear AE, Haynes BS. Oxygen chemisorption on carbon. In: Proceedings of the Combustion Institute. 24; 1992. p. 1199–206.
[194] Ahmed S, Back MH. The role of the surface complex in the kinetics of the reaction of oxygen with carbon. Carbon 1985;23:513–24.
[195] Du ZY, Sarofim AF, Longwell JP. Activation-energy distribution in temperature-programmed desorption - modeling and application to the soot-oxygen system. Energ Fuel 1990;4:296–302.
[196] Ergun S. Kinetics of the reaction of carbon with carbon dioxide. Journal of Phys Chem 1956;60:480–5.
[197] Ergun S. Kinetics of the reactions of carbon dioxide and steam with coke, 598. Bulletin: US Bureau of Mines; 1962.
[198] Gadsby J, Hinshelwood CN, Sykes KW. The kinetics of the reactions of the steam-carbon system. In: Proceedings of the Royal Society. 187; 1946. p. 129–51.
[199] Gadsby J, Long FJ, Sleightholm P. The mechanism of the carbon dioxide-carbon reaction. In: Proceedings of the Royal Society A. 193; 1948. p. 357–76.
[200] Ingeme AJ, Blackwood JD. The reaction of carbon with carbon dioxide at high pressure. Australian Journal of Chemistry 1960;13:194–209.
[201] Koenig PC, Squires RG, Laurendau NM. Evidence for two-site model of char gasification by carbon dioxide. Carbon 1985;23:531–6.
[202] Koenig PC, Squires RG, Laurendau NM. Char gasification by carbon dioxide: Further evidence for a two-site model. Fuel 1986;65:412–6.
[203] Long FJ, Sykes KW. The mechanism of the steam-carbon reaction. Proceedings of the Royal Society 1948;193:377–99.
[204] Menster M, Ergun S. A study of the carbon dioxide-carbon reaction by oxygen exchange, 664. Bulletin: Bulletin of Bureau of Mines; 1973. p. 1–42.
[205] Shaw JT. Theoretical work on reaction sequences in the gasification of coke by carbon dioxide and by steam in conditions remote from equilibrium. Fuel 1977;56:134–6.
[206] Tsai NK. Influence of high carbon monoxide concentration on the carbon dioxide gasification of a selected coal char. Stanford University; 1999.
[207] Biederman DL, Miles AJ, Vastola FJ, Walker Jr PL. Carbon-carbon dioxide reaction: kinetics at low pressures and hydrogen inhibition. Carbon 1976;14:351–6.
[208] Bjerle I, Eklund H, Linne M, Svensson O. Thermogravimetric analysis of Swedish shale char. Kinetics of the steam-carbon and carbon dioxide-carbon reactions. Ind Eng Chem Process Des Dev. 1982;21:141–9.
[209] Johnstone HF, Chen CY, Scott DS. Kinetics of the steam-carbon reaction in porous graphite tubes. Ind Eng Chem 1952;44:1564–9.
[210] Schmal M, Montiero JLF, Toscani H. Gasification of high ash content coals with steam in a semibatch fluidized bed reactor. Ind Eng Chem Process Des Dev. 1983;22:563–70.
[211] Strickland-Constable RF. Some comments on the work of Key on the reactions between coke and carbon dioxide and between coke and steam. J Chem Phys 1950;47:356–60.
[212] Tilghman MB, Mitchell RE. Characterizing char particle fragmentation during pulverized coal combustion. In: Proceedings of the Combustion Institute. 34; 2013. p. 2461–9.
[213] Blackwood JD, McTaggart FK. Reactions of carbon with atomic gases. Australian Journal of Chemistry 1959;12:533–42.
[214] Blackwood JD, McGrory F. The carbon-steam reaction at high pressure. Australian Journal of Chemistry 1958;11:16–33.
[215] Blackwood JD. The kinetics of the system carbon-hydrogen-methane. Australian Journal of Chemistry 1962;15:397–408.
[216] Gorin E, Zielke C. Kinetics of carbon gasification - interaction of hydrogen with low temperature char at 1500 to 1700 F. Ind Eng Chem 1955;47:820–5.
[217] Botero C, Field RP, Herzog HJ, Ghoniem AF. Impact of finite-rate kinetics on carbon conversion in a high-pressure, single-stage entrained flow gasifier with coal-CO_2 slurry feed. Appl Energ 2013;104:408–17.
[218] Hedden K, Lowe A. Uber die vergasung von reaktorgraphit mit kohlendioxid und wasserdampf. Carbon 1967;5:339–53.
[219] Kapteijn F, Meijer R, Moulijn JA. Transient kinetic techniques for detailed insight in gas solid reactions. Energ Fuel 1992;6:494–7.
[220] Muhlen H-J, van Heek KH, Juntgen H. Kinetic studies of steam gasification of char in the presence of hydrogen, carbon dioxide and carbon monoxide. Fuel 1985;64:944–9.
[221] Campbell PA, Mitchell RE. The impact of the distributions of surface oxides and their migration on characterization of the heterogeneous carbon-oxygen reaction. Combust Flame 2008;154:47–66.
[222] Niksa S, Liu GS, Hurt RH. Coal conversion submodels for design applications at elevated pressures. Part I. devolatilization and char oxidation. Progress in Energy and Combustion Science 2003;29:425–77.
[223] Mehta BN, Aris R. Communications on the theory of diffusion and reaction - VII The isothermal pth order reaction. Chem Eng Sci 1971;26:1699.
[224] Hong JH, Hecker WC, Fletcher TH. Improving the accuracy of predicting effectiveness factors for mth order and Langmuir rate equations in spherical coordinates. Energ Fuel 2000;14:663–70.
[225] Wu HW, Wall T, Liu GS, Bryant G. Ash liberation from included minerals during combustion of pulverized coal: The relationship with char structure and burnout. Energ Fuel 1999;13:1197–202.
[226] Bailey JG, Tate A, Diessel CFK, Wall TF. A char morphological system with applications to coal combustion. Fuel 1990;69:225–39.
[227] Ma LQ, Mitchell R. Modeling char oxidation behavior under Zone II burning conditions at elevated pressures. Combust Flame 2009;156:37–50.
[228] Cloke M, Wu T, Barranco R, Lester E. Char characterisation and its application in a coal burnout model. Fuel 2003;82:1989–2000.
[229] Wu T, Lester E, Cloke M. A burnout prediction model based around char morphology. Energ Fuel 2006;20:1175–83.
[230] Field MA, Gill DW, Morgan BB, Hawksley PGW. Combustion of pulverised coal. Leatherhead: The British Coal Utilization Research Association; 1967.
[231] Saxena SC. Devolatilization and combustion characteristics of coal particles. Progress in Energy and Combustion Science 1990;16:55–94.
[232] Zhang J, Zhang MC, Yu J. Extended Application of the Moving Flame Front Model for Combustion of a Carbon Particle with a Finite-Rate Homogenous Reaction. Energ Fuel 2010;24:871–9.
[233] Annamalai K, Durbetaki P. Combustion behavior of char/carbon particles. In: Proceedings of the Combustion Institute. 17; 1979. p. 169–78.
[234] Basu P, Broughton J, Elliott DE. Combustion of single particles in fluidized beds. In: London: Inst. Fuel Symposium Series, Inst. of Fuel;; 1975.
[235] Caram HS, Amundson NR. Diffusion and reaction in a stagnant boundary layer about a carbon particle. Ind Engng Chem Fund 1977;16:171–81.
[236] Mitchell RE, Kee RJ, Glarborg P, Coltrin ME. The effect of CO conversion in the boundary layers surrounding pulverized-coal char particles. In: Proceedings of the Combustion Institute. 23; 1990. p. 1169–76.
[237] Makino A, Law CK. Quasi-steady and transient combustion of a carbon particle: theory and experimental comparisons. Proc Combust Inst 1986;21:183–91.
[238] Gonzalo-Tirado C, Jimenez S, Johansson R, Ballester J. Comparative study of four alternative models for CO oxidation around a burning coal char particle. Combust Flame 2014;161:1085–95.
[239] Geier M, Shaddix CR, Davis KA, Shim HS. On the use of single-film models to describe the oxy-fuel combustion of pulverized coal char. Appl Energ 2012;93:675–9.
[240] Baum MM, Street PJ. Predicting the combustion behaviour of coal particles. Combustion Science and Technology 1971;3:231–43.
[241] Essenhigh RH. An integration path for the carbon-oxygen reaction with internal reaction. In: Proceedings of the Combustion Institute. 22; 1988. p. 89–96.
[242] Essenhigh RH. Influence of initial particle density on the reaction mode of porous carbon particles. Combust Flame 1994;99:269–79.

[243] Hurt RH, Mitchell RE. On the combustion kinetics of heterogeneous char particle populations. In: Twenty-Fourth Symposium (International) on Combustion. 24; 1992. p. 1233–41.
[244] Haugen NEL, Tilghman MB, Mitchell RE. The conversion mode of a porous carbon particle during oxidation and gasification. Combust Flame 2014;161:612–9.
[245] Gonzalo-Tirado C, Jimenez S, Ballester J. Gasification of a pulverized sub-bituminous coal in CO2 at atmospheric pressure in an entrained flow reactor. Combust Flame 2012;159:385–95.
[246] Meyers RA. Coal Handbook. Inc. New York; 1981.
[247] Kleinhans U, Wieland C, Frandsen FJ, Spliethoff H. Ash formation and deposition in coal and biomass fired combustion systems: Progress and challenges in the field of ash particle sticking and rebound behavior. Progress in Energy and Combustion Science 2018;68:65–168.
[248] Lunden MM, Yang NYC, Headley TJ, Shaddix CR. Mineral-char interactions during char combustion of a high-volatile coal. In: Twenty-Seventh Symposium (International) on Combustion, Vols 1 and 2; 1998. p. 1695–702.
[249] Tian C, Lu QY, Liu YX, Zeng HB, Zhao YC, Zhang JY, et al. Understanding of physicochemical properties and formation mechanisms of fine particular matter generated from Canadian coal combustion. Fuel 2016;165:224–34.
[250] Degroot WF, Kannan MP, Richards GN, Theander O. Gasification of agricultural residues (biomass) - influence of inorganic constituents. J Agr Food Chem 1990; 38:320–3.
[251] Sekiguchi Y, Shafizadeh F. The effect of inorganic additives on the formation, composition, and combustion of cellulose char. J Appl Polymer Sci 1984;29: 1267–86.
[252] Tomita A, Mahajan OP, Walker PLJ. Catalysis of char gasification by minerals. American Chemical Society, Division of Fuel Chemistry, Preprints 1977;22:4–6.
[253] Umeki K, Moilanen A, Gomez-Barea A, Konttinen J. A model of biomass char gasification describing the change in catalytic activity of ash. Chem Eng J 2012; 207:616–24.
[254] Zolin A, Jensen A, Jensen PA, Frandsen F, Dam-Johansen K. The influence of inorganic materials on the thermal deactivation of fuel chars. Energ Fuel 2001;15: 1110–22.
[255] Cope RF, Arrington CB, Hecker WC. Effect of Cao Surface-Area on Intrinsic Char Oxidation Rates for Beulah Zap Chars. Energ Fuel 1994;8:1095–9.
[256] Chen C, Kojima T. Single char particle combustion at moderate temperature: Effects of ash. Fuel Process Technol 1996;47:215–32.
[257] Hampartsoumian E, Pourkashanian M, Williams A. Combustion rates of chars and carbonaceous residues. J I Energy 1989;62:48–56.
[258] Sadhukhan AK, Gupta P, Saha RK. Analysis of the dynamics of coal char combustion with ignition and extinction phenomena: Shrinking core model. Int J Chem Kinet 2008;40:569–82.
[259] Yu D, Xu MH, Liu X, Huang J, Li G. Mechanisms of submicron and residual ash particle formation during pulverized coal combustion: A comprehensive review. Dev Chem Eng Mineral Process 2005;13:467–82.
[260] Quann RJ. Ash vaporization under simulated pulverized coal combustion conditions. Massachusetts Institute of Technology; 1982.
[261] Quann RJ, Sarofim A. Vaporization of refractory oxides during pulverized coal combustion. In: Proceedings of the Combustion Institute. 19; 1982. p. 1429–40.
[262] Desrosiers RE, Riehl JW, Ulrich GD, Chiu AS. Submicron fly-ash formation in coal-fired boilers. In: Proceedings of the Combustion Institute. 17; 1979. p. 1395–403.
[263] Flagan RC. Submicron particles from coal combustion. In: Proceedings of the Combustion Institute. 17; 1979. p. 97–104.
[264] Kazanc F, Levendis YA, Maffei T. Chemical composition of submicrometer particulate matter (PM1) emitted from combustion of coals of various ranks in O_2/N_2 and O_2/CO_2 environments. Energ Fuel 2013;27:4984–98.
[265] Padia A. The behavior of ash in pulverized coal under simulated combustion conditions. Massachusetts Institute of Technology; 1976.
[266] Senior CL, Flagan RC. Synthetic chars for the study of ash vaporization. In: Proceedings of the Combustion Institute. 20; 1984. p. 921–9.
[267] Murty HN, Biederman DL, Heintz EA. Kinetics of graphitization – I. Activation energies. Carbon 1969;7:667–81.
[268] Neville M. Formation of inorganic submicron particles under simulated pulverized coal combustion conditions. Massachusetts Institute of Technology; 1982.
[269] Neville M, Quann RJ, Haynes BS, Sarofim AF. Vaporization and condensation of mineral matter during pulverized coal combustion. In: Proceedings of the Combustion Institute. 18; 1981. p. 1267–74.
[270] Sui JC, Xu MH, Qiu JH, Qiao Y, Yu Y, Liu XW, et al. Numerical simulation of ash vaporization during pulverized coal combustion in the laboratory-scale single-burner furnace. Energ Fuel 2005;19:1536–41.
[271] Zeng TF, Sarofim AF, Senior CL. Vaporization of arsenic, selenium and antimony during coal combustion. Combust Flame 2001;126:1714–24.
[272] Felderhof BU, Deutch JM. Concentration dependence of the rate of diffusion-controlled reactions. J Chem Phys 1976;64:4551–8.
[273] Lee CM, Davis KA, Heap MP, Eddings E, Sarofim A. Modeling the vaporization of ash constituents in a coal-fired boiler. In: Proceedings of the Combustion Institute. 28; 2000. p. 2375–82.
[274] Xu YS, Liu XW, Zhou ZJ, Sheng L, Wang C, Xu MH. The role of steam in silica vaporization and ultrafine particulate matter formation during wet oxy-coal combustion. Appl Energ 2014;133:144–51.
[275] Barin I. Thermochemical Data of Pure Substances. VCH Verlagsgeselischaft mbH; 1995.
[276] Binnewies M, Milke E. Thermochemical Data of Elements and Compounds. Wiley-VCH Verlag GmbH; 1999.
[277] Filsinger DH, Bourrie DB. Silica to silicon - key carbothermic reactions and kinetics. Journal of the American Ceramic Society 1990;73:1726–32.
[278] Cheng M-C, Cutler IB. Vaporization of silica in steam atmosphere. J Am Ceram Soc 1979;62:593–6.
[279] Haynes BS, Neville M, Quann RJ, Sarofim AF. Factors governing the surface enrichment of fly ash in volatile trace species. J Colloid Interface Sci 1982;87: 266–78.
[280] Senior CL, Flagan RC. Ash vaporization and condensation during combustion of a suspended coal particle. Aerosol Sci Tech 1982;1:371–83.
[281] Wen C, Xu MH, Yu DX, Sheng CD, Wu HW, Zhang PA, et al. PM10 formation during the combustion of N_2-char and CO_2-char of Chinese coals. In: Proceedings of the Combustion Institute. 34; 2013. p. 2383–92.
[282] Xu MH, Yu DX, Yao H, Liu XW, Qiao Y. Coal combustion-generated aerosols: Formation and properties. In: Proceedings of the Combustion Institute. 33; 2011. p. 1681–97.
[283] Niu YQ, Liu X, Wang S, Hui SE, Shaddix CR. A numerical investigation of the effect of flue gas recirculation on the evolution of ultra-fine ash particles during pulverized coal char combustion. Combust Flame 2017;184:1–10.
[284] Niu YQ, Yan BK, Liu SQ, Liang Y, Dong N, Hui SE. Ultra-fine particulate matters (PMs) formation during air and oxy-coal combustion: Kinetics study. Appl Energ 2018;218:46–53.
[285] Austin LG, Klimpel RR, Luckie PT. Process engineering of size reduction: Ball milling. New York: Society of Mining Engineers; 1984.
[286] Dunn-Rankin D, Kerstein AR. Numerical simulation of particle size distribution evolution during pulverized coal combustion. Combust Flame 1987;69:193–209.
[287] Dunn-Rankin D. Kinetic-Model for Simulating the Evolution of Particle-Size Distributions during Char Combustion. Combustion Science and Technology 1988;58:297–314.
[288] Syred N, Kurniawan K, Grifths T, Gralton T, Ray R. Development of fragmentation models for solid fuel combustion and gasification as subroutines for inclusion in CFD codes. Fuel 2007;86:2221–31.
[289] Baxter LL. Char Fragmentation and Fly-Ash Formation during Pulverized-Coal Combustion. Combust Flame 1992;90:174–84.
[290] Senneca O, Salatino P, Menghini D. The influence of thermal annealing on oxygen uptake and combustion rates of a bituminous coal char. Proceedings of the Combustion Institute 2007;31:1889–95.
[291] Suuberg EM. Thermally induced changes in reactivity of carbons. In: Lahaye J, Ehrburger P, editors. Fundamental Issues in Control of Carbon Gasification Reactivity. Dordrecht Kluwer Academic Publishers; 1991.
[292] Blackwood JS, Cullis BD, McCarthy DJ. Reactivity in the system carbon-hydrogen-methane. Australian Journal of Chemistry 1967;20:1561–70.
[293] Blyholder G, Binford JS. Eyring H. A kinetic theory for the oxidation of carbonized filaments. J Phys Chem 1958;62:263–7.
[294] Russell NV, Gibbins JR, Man CK, Williamson J. Coal char thermal deactivation under pulverized fuel combustion conditions. Energ Fuel 2000;14:883–8.
[295] Senneca O, Salatino P, Masi S. Microstructural changes and loss of gasification reactivity of chars upon heat treatment. Fuel 1998;77:1483–93.
[296] Weeda M, Rutte E, Kapteijn F, Moulijn JA. The development of coal char reactivity during CO_2 gasification. In: Proceedings of the International Conference on Coal Science; 1991. p. 448–51.
[297] McCarthy DJ. Changes in oxy-reactivity of carbons due to heat treatment and pre-hydrogenation. Carbon 1981;19:297–301.
[298] Nagle J, Strickland-Constable RF. Oxidation of carbon between 1000 and 2000°C. Proc Fifth Conf Carbon 1961;1:154–64.
[299] Lightman P, Street PJ. Microscopical examination of heat treated pulverized coal particles. Fuel 1968;47:7–28.
[300] McCarthy DJ. Some effects of overheating and carbon burn-off on the performance of fluidized-bed combustors. Fuel 1982;61:298–302.
[301] Senneca O, Salatino P, Masi S. Heat treatment-induced loss of combustion reactivity of a coal char: The effect of exposure to oxygen. Exp Therm Fluid Sci 2004;28:735–41.
[302] Senneca O, Apicella B, Russo C, Cerciello F, Salatino P, Heuer S, et al. Pyrolysis and Thermal Annealing of Coal and Biomass in CO_2-Rich Atmospheres. Energ Fuel 2018;32:10701–8.
[303] Cai HY, Guell AJ, Chatzakis IN, Lim JY, Dugwell DR, Kandiyoti R. Combustion reactivity and morphological change in coal chars: Effect of pyrolysis temperature, heating rate and pressure. Fuel 1996;75:15–24.
[304] Senneca O, Salatino P. A semi-detailed kinetic model of char combustion with consideration of thermal annealing. In: Proceedings of the Combustion Institute. 33; 2011. p. 1763–70.
[305] Feng B, Jensen A, Bhatia SK, Dam-Johansen K. Activation energy distribution of thermal annealing of a bituminous coal. Energ Fuel 2003;17:399–404.
[306] Zolin A, Jensen A, Dam-Johansen K. Coupling thermal deactivation with oxidation for predicting the combustion of a solid fuel. Combust Flame 2001;125: 1341–60.
[307] Tabet F, Gokalp I. Review on CFD based models for co-firing coal and biomass. Renew Sust Energ Rev 2015;51:1101–14.
[308] Yin CG, Rosendahl L, Kaer SK, Condra TJ. Use of numerical modeling in design for co-firing biomass in wall-fired burners. Chem Eng Sci 2004;59:3281–92.
[309] Comer JK, Kleinstreuer C. Computational Analysis of Convection Heat-Transfer to Nonspherical Particles. Int J Heat Mass Tran 1995;38:3171–80.
[310] Chol MK, Gavalas GR. A Theoretical-Study of Combustion of Nonspherical Particles. Combustion Science and Technology 1993;89:9–26.
[311] Lu H, Ip E, Scott J, Foster P, Vickers M, Baxter LL. Effects of particle shape and size on devolatilization of biomass particle. Fuel 2010;89:1156–68.

[312] Lu H, Robert W, Peirce G, Ripa B, Baxter LL. Comprehensive study of Biomass particle combustion. Energ Fuel 2008;22:2826–39.
[313] Lu H, Scott J, Echols K, Foster P, Ripa B, Farr R, et al. Effects of particle shape and size on black liquor and biomass reactivity. In: Proceedings of the 2004 Conference on Science in Thermal and Chemical Biomass Conversion; 2004.
[314] Aris R. On shape factors for irregular particles .1. The steady-state problem. Diffusion and reaction (Reprinted from Chem Engng Sci, vol 6, pg 262-268, 1957). Chem Eng Sci. 1995;50:3899–903.
[315] Yu JL, Lucas J, Wall T, Liu G, Sheng CD. Modeling the development of char structure during the rapid heating of pulverized coal. Combust Flame 2004;136:519–32.
[316] Croiset E, Mallet C, Rouan JP, Richard JR. The influence of pressure on char combustion kinetics. In: Twenty-Sixth Symposium (International) on Combustion, Vols 1 and 2; 1996. p. 3095–102.
[317] MacNeil S, Basu P. Effect of pressure on char combustion in a pressurized circulating fluidized bed boiler. Fuel 1998;77:269–75.
[318] Shurtz RC, Hogge JW, Fowers KC, Sorensen GS, Fletcher TH. Coal Swelling Model for Pressurized High Particle Heating Rate Pyrolysis Applications. Energ Fuel 2012;26:3612–27.
[319] Shurtz RC, Kolste KK, Fletcher TH. A coal swelling model for CFD applications at high heating rates. Energ Fuel 2011;25:2163–73.
[320] Williams A, Backreedy R, Habib R, Jones JM, Pourkashanian M. Modelling coal combustion: the current position. Fuel 2002;81:605–18.
[321] Laidler KJ. Chemical Kinetics. New York: McGraw-Hill; 1965.
[322] Reiss H. The statistical mechanical theory of irreversible condensation. I J Chem Phy 1952;20:1216–27.
[323] Karthika S, Radhakrishnan TK, Kalaichelvi P. A review of classical and nonclassical nucleation theories. Cryst Growth Des 2016;16:6663–81.
[324] McNallan MJ, Yurek GJ, Elliot JF. The formation of inorganic particulates by homogeneous nucleation in gases produced by the combustion of coal. Combust Flame 1981;42:45–60.
[325] Mulholland GW, Samson RJ, Mountain RD, Ernst MH. Cluster size distribution for free molecular agglomeration. Energ Fuel 1988;2:481–6.
[326] Zhang LF, Pluschkell W, Thomas BG. Nucleation and growth of alumina inclusions during steel deoxidation. Steel Proc 2002;85:463–76.
[327] Helble JJ, Sarofim AF. Factors determining the primary particle-size of flame-generated inorganic aerosols. J Colloid Interf Sci 1989;128:348–62.
[328] Smoke Friedlander SK. Dust and Haze, Fundamentals of Aerosol Behavior. New York: John Wiley and Sons; 1977.
[329] Fuchs NA, Sutugin AG. Highly-Dispersed Aerosols. Topics in current aerosol research, international reviews in aerosol physics and chemistry. Ann Arbor 1971:1.
[330] Friedlander SK, Wang CS. The self-preserving particle size distribution for coagulation by Brownian motion. J Colloid Interface Sci 1966;22:126–32.
[331] Graham SC, Homer JB. Coagulation of molten lead aerosols. Faraday Symp 1973:85–96.
[332] Lai FS, Friedlander SK, Pich J, Hidy GM. The self-preserving particle size distribution for Brownian coagulation in the free molecular regime. J Colloid Interface Sci 1972;39:395–405.
[333] Lee KW, Chen H. Coagulation rate of polydisperse particles. Aerosol Sci Tech 1984;3:327–34.
[334] Lee KW, Chen J, Gieseke JA. Log-normally preserving size distribution for Brownian coagulation in the free-molecule regime. Aerosol Sci Tech 1984;3:53–62.
[335] Lehtinen KEJ, Zachariah MR. Self-preserving theory for the volume distribution of particles undergoing Brownian coagulation. J Colloid Interf Sci 2001;242:314–8.

Nils Erland L. Haugen Haugen is a senior research scientist at SINTEF Energy Research with more than 20 years of experience within numerical simulations of turbulent flows, both with and without reacting particles. He develops high fidelity CFD tools and is currently the chair of the steering committee of the Pencil Code, which is an open multi-purpose DNS code. Haugen has supervised a number of PhD and master students within the field of char conversion. Some of these students were the first to show the effect of turbulence on pulverized char conversion. On the other side of the scientific spectrum, Haugen is the leader of an intercontinental demonstration projects that is currently building the world's largest Chemical Looping Combustion (CLC) demonstration plant.

Brandon Ka Yan Loong Brandon Ka Yan Loong is a doctoral graduate student at Stanford University in the department of chemical engineering. His research experience is focused in modeling the chemical dynamics of char particles and associated ash vaporization processes. He also has experience in new materials development for novel electrochemical approaches to coal and biomass conversion. His graduate teaching experience includes courses in chemical kinetics, thermodynamics, and combustion science for both undergraduate and graduate students.

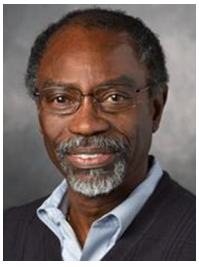

Reginald E. Mitchell Reginald E. Mitchell is a Professor of Mechanical Engineering, Emeritus at Stanford University in Palo Alto, California and has over 45 years of experience dedicated to research in combustion science, focusing on laminar methane/air diffusion flame chemistry and structure and coal and biomass char reactivity. His experimental and modeling studies have provided the information needed to enhance our fundamental understanding of the chemical and physical processes that govern the rates of fuel consumption. Besides studies on understanding and predicting coal and biomass combustion and gasification conversion phenomena, his studies have also involved research on the development of coal and biomass conversion technologies that facilitate CO_2 capture. Of particular interest has been research devoted to developing fuel cells that run on coal and biomass. During Professor Mitchell's twenty-nine years at Stanford, he taught undergraduate and graduate courses in thermodynamics, heat transfer and combustion fundamentals and applications and served as an advisor and mentor to many undergraduate and graduate students. He is the author of numerous technical papers and has given several presentations on the results of his research at universities, conferences, symposia, and other professional meetings.